

Cardiff University

**School of Engineering
Centre for Research in Energy Waste and the Environment
(CREWE)**

**Performance assessment of a Horizontal Axis
Tidal Turbine in a high velocity shear
environment**

**A Thesis submitted to Cardiff University,
for the Degree of Doctor of Philosophy**

By

Allan Mason-Jones

UMI Number: U585299

All rights reserved

INFORMATION TO ALL USERS

The quality of this reproduction is dependent upon the quality of the copy submitted.

In the unlikely event that the author did not send a complete manuscript and there are missing pages, these will be noted. Also, if material had to be removed, a note will indicate the deletion.



UMI U585299

Published by ProQuest LLC 2013. Copyright in the Dissertation held by the Author.
Microform Edition © ProQuest LLC.

All rights reserved. This work is protected against
unauthorized copying under Title 17, United States Code.



ProQuest LLC
789 East Eisenhower Parkway
P.O. Box 1346
Ann Arbor, MI 48106-1346

DECLARATION

This work has not previously been accepted in substance for any degree and is not being concurrently submitted in candidature for any degree

Signed *A. Mason-Jones* (Allan Mason-Jones)
Date *11/9/09*

STATEMENT 1

This thesis is being submitted in partial fulfilment of the requirements for the degree of PhD.

Signed *A. Mason-Jones* (Allan Mason-Jones)
Date *11/9/09*

STATEMENT 2

This thesis is the result of my own investigations, except where otherwise stated. Other sources are acknowledged by footnotes giving explicit reference. A detailed reference list is included.

Signed *A. Mason-Jones* (Allan Mason-Jones)
Date *11/9/09*

STATEMENT 3

I hereby give consent for my thesis, if accepted, to be available for photocopying and for inter-library loan, and for the title and the summary to be made available to outside organisations.

Signed *A. Mason-Jones* (Allan Mason-Jones)
Date *11/9/09*

Director of studies:

Signed *DMJ O'Sherty* (Dr. D.M. O'Doherty)
Date *10/03/10*

Acknowledgments

I would like to take this opportunity to thank my thesis supervisors Dr. Tim O'Doherty and Dr. Daphne. M. O'Doherty for giving me invaluable guidance and encouragement throughout the work undertaken in this thesis.

I would like to thank Chris Wooldridge, Paul Evans and Ian Fryett from the Cardiff School of Earth, Ocean and Planetary Sciences, Cardiff University for their ADCP and SWATH measurements along with the dissemination of the methods and procedures used during the surveys.

I would also like to thank Dr. Carl Byrne for his help with the development of test equipment and the staff of the engineering and electrical workshops for their help and support. A thank you is also extended to the University of Liverpool for the use of their water flume and the help provided over the test duration. Finally, I would also like to thank Dean Lloyd and Tom Milne for their assistance in the CFD analysis.

I will also forever be in debt to Rachel, Rowan and Toby for their encouragement, support and patience.

ABSTRACT

The main focus of this thesis was to assess the performance of a full scale Horizontal Axis Tidal Turbine (HATT), using the CFD package, FluentTM, and measured high shear tidal profiles. Two sites are considered: the Anglesey Skerries and a site in the Severn Estuary, both off the Welsh coast. In order to achieve this aim a number of key steps were performed including the use of an existing laboratory scale prototype HATT to establishing the optimum blade pitch angle and provide an experimental data set. Once established the HATT CFD model was used to scale up from the laboratory scale to 30 m diameter. By the use of non-dimensionalised characteristics of power, thrust and torque coefficients, it was shown that the HATT was scaleable and independent of Reynolds number. Using these findings a suitable turbine diameter was determined for site specific analysis. Velocity profiles from the two sites were obtained via vessel mounted Acoustic Doppler Current Profiler (ADCP) surveys. These data were used to define a high velocity shear environment. When non-dimensionalised these data were found to also collapse onto the scaling curves provided a true average for the velocity, across the swept area, is used.

In addition, when the HATT was ‘positioned’ at varying depths down the water column the power extraction was shown to reduce considerably with depth. When positioned close to the seabed, the cyclic torque, power and axial thrust loads were studied with and without a stanchion positioned downstream of the turbine. The presence of a stanchion was also shown to significantly increase the amplitude of the cyclic torque, power and axial thrust during rotation. The findings of this thesis suggest that the complexity of the dynamic torque, power and axial thrust, along with the wake profile, are influenced by the HATT’s interaction with the ocean seabed. These complexities are therefore of prime importance when considering a deep water application which encompasses all or part of a high velocity shear regime.

The work presented in the thesis shows that it is possible to predict a turbine’s performance (for a given geometry) for any scale and velocity profile, from a single diameter. When positioned lower in the water column, the downstream wake also showed a high level of asymmetry which was also shown to influence the upstream flow field.

CONTENTS

1	Introduction.....	1
1.1	Background.....	1
1.2	UK 2020 renewable energy.....	2
1.3	Turbine blade technology.....	2
1.4	Aims of the study.....	3
1.5	Thesis objectives.....	3
2	Literature review – technology drivers and current technology.....	4
2.1	Overview of literature review.....	4
2.1.1	Growth in energy demand.....	5
2.1.2	Global warming.....	6
2.1.3	Renewable and nuclear energy.....	7
2.2	Marine energy resources.....	8
2.2.1	Tidal barrage and lagoons.....	9
2.2.2	Tidal stream.....	14
2.2.3	Horizontal Axis Tidal Turbines (HATTs).....	15
2.2.4	Tidal stream resource distribution.....	19
2.3	Energy extraction from tides.....	23
2.3.1	Number of turbine blades.....	24
2.3.2	Scaled prototype HATT testing.....	26
2.3.3	Scaled flume testing.....	30
2.3.4	Wake length.....	31
2.3.5	Surface interaction.....	35
2.3.6	Stanchion and turbine interaction.....	39
2.4	Summary of background review	43
3	Literature review – modelling and ADCP measurement techniques.....	44
3.1	Blade Element Momentum (BEM) Theory.....	44
3.2	Computational Fluid Dynamics (CFD).....	45

3.2.1	RANS viscous models.....	47
3.2.2	K- ϵ viscous model.....	48
3.2.3	Reynolds Stress Model (RSM).....	50
3.2.4	Near wall functions.....	52
3.3	Acoustic Doppler Current Profiler (ADCP) measurements.....	55
3.3.1	ADCP advantages.....	55
3.3.2	ADCP disadvantages.....	56
3.4	Literature summary.....	56
4	Numerical study of turbine performance.....	57
4.1	2D blade profile for BEM.....	58
4.1.1	2D lift and drag coefficients.....	59
4.1.2	Blade Element Momentum (BEM) theory and MatLab code.....	60
4.1.3	Input parameters for BEM MatLab code.....	63
4.2	3D CFD models of prototype HATT.....	64
4.2.1	Prototype reference CFD geometry preparation in Gambit.....	64
4.2.1.1	Geometry preparation and meshing for turbine volume.....	64
4.2.1.2	Geometry preparation and meshing for rectangular channels.....	66
4.2.1.3	Meshing schemes for reference, site and flume MRF volumes.....	67
4.2.1.4	Geometry preparation and meshing of site turbine volume.....	69
4.2.1.5	Geometry preparation and meshing of site rectangular volume.....	69
4.2.1.6	Geometry preparation and meshing of flume turbine volume.....	70
4.2.1.7	Geometry preparation and meshing of flume rectangular volume.....	70
4.3	Boundary conditions applied to the reference, site and flume models.....	72
4.3.1	Quasi-static approach to HATT modelling.....	72
4.3.2	Application of Moving Reference Frame (MRF).....	73
4.3.3	Momentum and continuity equations in MRF model.....	74
4.3.4	Power and wake sensitivity to MRF grid resolution.....	75
4.3.5	Power and wake length sensitivity to MRF length.....	75
4.3.6	Suitability of viscous model.....	76
4.3.7	Turbulence specification method.....	77

4.4	Determination of turbine power.....	79
4.4.1	Force on turbine blades.....	79
4.4.2	User Defined Function (UDF) for torque, power and axial thrust load calculations for all CFD models.....	80
4.4.3	Manual input of user defined variables for all models.....	80
4.4.4	Code read input variables to CFD models... ..	81
4.4.5	Execution of On-Demand UDF.....	82
4.4.6	Generation of torque, power and axial thrust curves.....	84
4.5	Scaling for estuarine and oceanic application.....	84
4.5.1	Non-dimensional analysis of CFD and measured flume data	85
4.5.2	Scaling of a HATT	88
4.5.3	Peak power calculation using scaling.....	88
4.6	Optimisation of a deep water 10 m diameter turbine reference CFD model with plug flow.....	89
4.7	10 m diameter site turbine reference CFD model with plug flow.....	91
4.8	Power attenuation in 35 m depth reference CFD model (Severn data).....	92
4.9	Power attenuation in 50 m depth reference CFD model (Severn data).....	94
4.10	Velocity profile survey at 3 locations within the Anglesey Skerries.....	95
4.11	Turbine stanchion loading.....	95
4.12	Effect of stanchion geometry on HATT performance.....	96
4.13	Effect of blade position on turbine performance with and without stanchion.....	97
5	Recirculation water flume and ADCP measurements.....	98
5.1	Validation of prototype design using water flume.....	98
5.1.1	Servomotor and control system.....	99
5.1.2	Coupling servomotor drive to prototype HATT.....	101
5.1.3	Programming and servomotor control for flume tests.....	102
5.1.4	Setting optimum blade pitch angle on prototype HATT.....	103
5.1.5	Prototype HATT and re-circulating water flume placement.....	105
5.1.6	Verification of optimal blade pitch angle using water flume.....	106
5.2	Acoustic Doppler Current Profiler (ADCP) velocity profiler.....	107

5.3	ADCP data for profiled flow analysis at Severn Estuary and Anglesey locations.....	108
5.4	Severn Estuary and Anglesey site SWATH Measurements.....	109
6	HATT and velocity profile characteristion using water flume and ADCP survey.....	110
6.1	Re-circulating flume test results.....	110
6.2	Use of the flexible and solid drive couplings.....	118
6.2.1	Drive coupling effects on torque and power curves.....	118
6.2.2	Measured torque and power curves with blade pitch variation.....	120
6.3	ADCP and SWATH surveys.....	123
6.3.1	ADCP measurements in Severn Estuary.....	124
6.3.2	Depth averaged ADCP velocity profiles at proposed Severn site.....	126
6.3.3	Proposed site CFD model using depth averaged velocity profile (SevernEstuary).....	129
6.3.4	Comparison of depth averaged velocity profiles between the Severn Estuary and Anglesey sites.....	132
7	CFD modeling.....	137
7.1	First order approximation for TSR and optimum blade pitch angle using simplified BEM model.....	137
7.2	Validation of CFD models.....	139
7.2.1	Characteristics of prototype turbine reference CFD model.....	140
7.2.2	Effect of MRF on torque, power and axial thrust load.....	144
7.2.3	Effect of MRF on wake velocity recovery rates.....	145
7.2.4	Effect of inlet turbulence intensity on peak power extraction.....	150
7.3	Optimisation of flume model.....	150
7.3.1	CFD flume model torque, power and wake deficit results.....	153
7.3.1.1	Convergence monitoring for CFD models.....	159
7.4	Comparison of flume CFD model and measured flume results.....	160
7.4.1	Effect of stanchion dam on power measurements.....	163

7.5	Summary of flume measurements and CFD validation.....	166
8	Scaling from 0.5 m diameter prototype turbine.....	168
8.1	Geometric scaling of prototype turbine.....	168
8.2	Non-dimensional analysis of CFD and flume data.....	170
8.2.1	Comparison of non-dimensional study for reference CFD models with increasing turbine diameter and upstream water velocity (Plug).....	171
8.2.2	Depth average velocity (V_{av}) calculation using velocity profile and volumetric flow rate calculation across turbine diameter (Severn Estuary data)...	174
8.2.3	Non-dimensionalised turbine performance characteristics using the average of the upstream velocity profile (Severn Estuary data).....	175
8.2.4	Non-dimensional study for reference CFD models with changes in blade pitch angle.....	177
8.2.5	Comparison of Non-dimensionalised turbine performance characteristics using flume CFD and measured flume data.....	180
8.3	Performance charts for prototype HATT design.....	182
8.3.1	Peak power calculations.....	188
8.3.2	10 m diameter reference frame CFD model with plug flow.....	188
8.3.3	Tidal velocity effects on peak power.....	193
8.4	Wake recovery for 10 m diameter reference frame CFD model plug flow.....	194
8.5	Summary of turbine scaling.....	200
9	Power attenuation through depth using Severn Estuary ADCP data.....	202
9.1	Upstream velocity and power definition using Severn Estuary data.....	203
9.1.1	Power comparison between the Severn Estuary and Anglesey site 2 data.....	205
9.2	Contour of wake z-axis velocity with plug flow for 50 m depth CFD model.....	207
9.2.1	Contour of wake z-axis velocity with plug flow for 35 m depth CFD model.....	208
9.2.2	Contour of wake z-axis velocity with profiled flow (Severn data) for 50 m depth CFD model.....	212
9.2.3	Contour of wake z-axis velocity with profiled flow (Severn data) for 35 m depth CFD model.....	214

9.2.4	Comparison of wake vortex with plug and profiled flow.....	217
9.3	Turbine stanchion interaction.....	219
9.3.1	Effect of stanchion on HATT power under site conditions.....	226
9.3.2	Performance curves through 360° of rotation (no stanchion) with profiled flow...	227
9.3.3	HATT performance curves through 360° of rotation (with stanchion) and profiled flow.....	234
9.3.4	Combined performance curves with and without stanchion.....	239
9.3.5	Contour plots of asymmetric flow.....	242
9.4	Example of possible asymmetric wake interaction for a modular array.....	245
9.5	Summary for power attenuation.....	248
10	Conclusions and recommendations.....	250
10.1	Conclusions.....	250
10.2	Specific Observations.....	252
10.3	Recommendations and future work.....	253

References

APPENDICES

Appendix.1: Blade Element Momentum code

Appendix.2: Table of Blade pitch angles for BEM.

Appendix.3: Power User Defined Function (UDF)

Appendix.4: Measured flume data.

List of Figures

Chapter 1

Figure 1.1 Historic and projected renewable generation capacity, 2007 and 2020.....1

Chapter 2

Figure 2.1	Millennial Northern Hemisphere (NH) temperature reconstruction.....6
Figure 2.2	Installed capacity of renewable energy technologies between 1997 And 2006.....7
Figure 2.3	UK Tidal range resource.....10
Figure 2.4	Picture of the La Rance tidal barrage.....11
Figure 2.5	Schematic of the La Rance tidal barrage showing the power plant at the centre.....11
Figure 2.6	Long list of proposed barrages, lagoons and tidal fences.....13
Figure 2.7	Tidal lagoons evaluated as part of the Severn Barrage Programme.....13
Figure 2.8	Oxford University's THWAT horizontal axis turbine.....15
Figure 2.9	Selection of tidal turbine technologies.....18
Figure 2.10	UK Tidal stream resource.....21
Figure 2.11	Power coefficient curves for wind turbines with increasing blade numbers.....26
Figure 2.12	Experimental variation of power coefficient with TSR.....27
Figure 2.13	Power output with respect to flow velocity.....28
Figure 2.14	River trials for a 4 bladed 5.5m turbine with a flow speed of 0.9 m/s.....29
Figure 2.15	Comparison of CFD and experimental power for a 5.5 m diameter turbine in a 0.9 m/s tidal flow.....29
Figure 2.16	Power coefficient (C_p) and axial thrust coefficient (C_T) calculated from measurement.....31

Figure 2.17	Correlation between measured and calculated power coefficient (C_p) curves.....	31
Figure 2.18	Predicted downstream vortex development (a) and downstream velocity profiles (b).....	33
Figure 2.19	Poor diffusion of vorticity in the downstream wake of the rotor blades.....	34
Figure 2.20	Up and downstream surface interaction with energy extraction using 2D VOF model (a) no extraction (b) with extraction.....	36
Figure 2.21	Measured water surface elevation for 1.8 m/s (a) and 2.35 m/s (b) flow velocity.....	38
Figure 2.22	Support structures for marine current turbines.....	39
Figure 2.23	Velocity attenuation with depth using $1/7^{\text{th}}$ law.....	42

Chapter 3

Figure 3.1	Near wall turbulence represented by the ‘law of the wall’.....	53
------------	--	----

Chapter 4

Figure 4.1	2D cross section of 0.5 m diameter laboratory turbine.....	59
Figure 4.2	Comparison between FX 63-137 and prototype turbine profile.....	59
Figure 4.3	Lift and drag coefficients for Wortmann FX 63-137 profile.....	60
Figure 4.4	(a) Unconnected B1 and hub, (b) Blade B1 copied at 120° to B2 and 240° to B3, (c) blades B1, B2 and B3 connected to hub.....	65
Figure 4.5	Central rectangular channel with MRF removed.....	67
Figure 4.6	Volume creation and meshing of channel volume	67
Figure 4.7	Mesh pattern for meshing scheme 4 column 1, Table 4.3.....	68
Figure 4.8	Central rectangular channel with MRF removed (Site model).....	69
Figure 4.9	Volume creation and meshing of channel volume (Site model).....	70
Figure 4.10	Geometry of flume CFD model.....	71
Figure 4.11	(a) Non-conformal volume interface and support bar,	

	(b) Prototype turbine without support, (c) turbine with support bar, (d) Flume model velocity inlet and pressure outlet boundaries.....	74
Figure 4.12	Power sensitivity to MRF lengths δZ_{DS} & δZ_{US}	76
Figure 4.13	UDF blade force components.....	83
Figure 4.14	Dimensions of deep water reference CFD model.....	90
Figure 4.15	Dimensions of 35 m depth site CFD model.....	92
Figure 4.16	Proposed HATT sites along transect line within the Anglesey Skerries.....	95
Figure 4.17	Stanchion geometries for axial thrust load study.....	96
Figure 4.18	Distance between turbine blades and stanchion.....	97

Chapter 5

Figure 5.1	Schematic of re-circulating water flume at The University of Liverpool....	98
Figure 5.2	BALDOR AC servomotor.....	99
Figure 5.3	Schematic of connection summary - recommended wiring for servomotor and control system.....	100
Figure 5.4	Final servomotor assembly showing 1k Ω load resistor.....	101
Figure 5.5	Flexible and solid drive shaft couplings.....	101
Figure 5.6	Torque macro for servomotor flume tests.....	102
Figure 5.7	0.5 m diameter prototype HATT.....	104
Figure 5.8	Angled precision blocks with 60 block aligned with blade tip.....	105
Figure 5.9	Turbine positioned in circulating water flume at the University of Liverpool.....	106
Figure 5.10	ADCP and bathymetric survey aboard the CodaOctopus Guiding Light...	109

Chapter 6

Figure 6.1	Turbine during testing at 1 m/s showing wake from support bar.....	110
Figure 6.2	Angular velocity as a percentage of maximum servomotor velocity at each sample period over the test duration.....	112

Figure 6.3	Measured servomotor current (A) at each sample period over the test duration.....	112
Figure 6.4	Combined angular velocity (%) and servomotor current (A) showing average point and error band for each sample period.....	113
Figure 6.5	Average angular velocity (%) with error bars and linear curve fit.....	114
Figure 6.6	Measured turbine torque at 1 m/s water velocity.....	114
Figure 6.7	CFD and measured power curve at 1 m/s water velocity using 0.5 m HATT: combined solid and flexible drive coupling data	115
Figure 6.8	Averaged servomotor torque vs TSR: Test 1; combined solid and flexible drive coupling data	116
Figure 6.9	Power curve for Test 1 vs angular velocity with error bars.....	117
Figure 6.10	Variation in torque (a) and power (b) measurement when using solid and flexible drive couplings also CFD flume model data.....	119
Figure 6.11	Torque curves from flume tests with blade pitch angles of 3°, 6° and 9° using flexible drive coupling only.....	121
Figure 6.12	Power curves from flume tests with blade pitch angles of 3°, 6° and 9° using flexible drive coupling only.....	122
Figure 6.13	Alternative velocity profiles normalised with depth and velocity.....	124
Figure 6.14	SWATH of surveyed area and turbine location.....	125
Figure 6.15	3D SWATH of survey area showing turbine location, velocity vectors and water surface (Severn Estuary).....	126
Figure 6.16	Depth averaged ADCP Velocity profiles (Severn Estuary).....	127
Figure 6.17	Depth averaged velocity profile at HWS+2 referenced to metres CD (Severn Estuary).....	128
Figure 6.18	Depth averaged velocity profile at HWS+3 referenced to metres CD (Severn Estuary).....	128
Figure 6.19	Depth averaged velocity profile at HWS+6 referenced to metres CD (Severn Estuary).....	129
Figure 6.20	Site CFD model upstream velocity profile with 1/7 th power law and	

	Plug flow (Severn Estuary).....	130
Figure 6.21	ADCP and 1/7 th power law velocity profiles for proposed site and reference CFD model (Severn Estuary).....	131
Figure 6.22	Bathymetry showing proposed HATT sites along transect line Within the Anglesey Skerries.....	133
Figure 6.23	Comparison between rescaled Severn Estuary data and 1/5 th , 1/7 th and 1/10 th power law.....	134
Figure 6.24	Comparison between rescaled Anglesey site 2 data and 1/5 th , 1/7 th and 1/10 th power law.....	134
Figure 6.25	Peak velocity 3 m below water surface through tidal cycle.....	136
Figure 6.26	Velocity difference across turbine diameter.....	136
 Chapter 7		
Figure 7.1	Correlation between CL curve Figure 4.3 and curve fit Equation 4.1.....	138
Figure 7.2	Power coefficient (C _p) with blade pitch variation using BEM to the base of Tip Speed Ration (TSR).....	138
Figure 7.3	Peak power coefficient (C _p) with blade pitch angle (θ) variation.....	139
Figure 7.4	Tetrahedral MRF and quadrilateral channel mesh with non-conformal interface.....	141
Figure 7.5	Cell count grid dependency peak power checks for reference domain prototype model.....	142
Figure 7.6	Limitation of blockage effects from boundary walls.....	144
Figure 7.7	Effect of MRF length on 0.5 m diameter HATT using reference domain..	145
Figure 7.8	Axial wake velocity recovery with a 0.07L MRF length Z _{DS}	147
Figure 7.9	Axial wake velocity recovery with a 0.47L MRF length Z _{DS}	148
Figure 7.10	Comparison of axial wake velocity recovery with MRF length at 0.07L and 0.47L Z _{DS}	148
Figure 7.11	Peak power reduction with increasing turbulence intensity (I%).....	150
Figure 7.12	Normalised power variation with blade pitch variation.....	152

Figure 7.13	Power coefficient variance with blade pitch angle.....	152
Figure 7.14	Flume CFD model using different viscous models at 1 m/s	156
Figure 7.15	Flume CFD model using different viscous models at 1 m/s to calculate power vs angular velocity (rad/s).....	157
Figure 7.16	Flume CFD model using different viscous models at 1 m/s to calculate axial thrust (N) vs angular velocity (rad/s).....	158
Figure 7.17	Upstream and downstream velocity deficit with different viscous models (a and b) and velocity deficit induced by a porous disc.....	158/9
Figure 7.18	Downstream axial velocity convergence monitoring.....	160
Figure 7.19	Torque curves generated from CFD flume model with various viscous models and measured from the flume tests while using both the flexible and solid drive couplings.....	161
Figure 7.20	Power curves generated from CFD flume model with various viscous models and measured from the flume tests while using both the flexible and solid drive couplings.....	161
Figure 7.21	Measured and calculated power coefficient (C_p) with varying blade pitch angle.....	162
Figure 7.22	Normalised velocity profile of upstream tower dam effect.....	165
Figure 7.23	Normalised relative distance (Z_{us}) upstream of stanchion Dam (circular cross section).....	165
Chapter 8		
Figure 8.1	Combined power coefficient (C_p) vs TSR with increasing turbine diameter and upstream water velocity	172
Figure 8.2	Combined torque coefficient (C_{Torq}) vs TSR with increasing turbine diameter and upstream water velocity	172
Figure 8.3	Combined axial thrust coefficient (C_T) vs TSR with increasing turbine diameter and upstream water velocity	173
Figure 8.4	Comparison between profiled and plug volumetric flow rate across turbine area	174

Figure 8.5	Power coefficient (C_p) vs TSR with increasing upstream water velocity (plug) and average (V_{av}) profiled flow across the turbine diameter175
Figure 8.6	Torque (C_{Torq}) coefficient (C_{Torq}) vs TSR with increasing upstream water velocity (plug) and average (V_{av}) profiled across the turbine diameter....176
Figure 8.7	Thrust coefficient (C_T) vs TSR with increasing upstream water velocity (plug) and average (V_{av}) profiled across the turbine diameter176
Figure 8.8	Effect of blade pitch angle on C_p with changes in blade pitch angle179
Figure 8.9	Effect of blade pitch angle on C_{Torq} with changes in blade pitch angle179
Figure 8.10	Effect of blade pitch angle on C_T with changes in blade pitch angle180
Figure 8.11	Combined C_p curves for reference CFD and flume models. Also non-dimensionalised data from flume model and volumetric velocity profile average181
Figure 8.12	Combined C_{Torq} curves for reference CFD and flume models. Also non-dimensionalised data from flume model and volumetric velocity profile average..... 181
Figure 8.13	Extrapolated power curves from 6 m diameter HATT and calculated using scaled CFD.....185
Figure 8.14	Design specific Peak power curves with increasing diameter and tidal velocity..... 186
Figure 8.15	Design specific Peak power curves with increasing diameter and tidal velocity with a maximum tidal velocity of 3.08 m/s..... 187
Figure 8.16	Power curves with blade pitch variation for 10 m diameter turbine189
Figure 8.17	Performance characteristics for 10 m diameter HATT plug flow with a $V = 3.08$ m/s190
Figure 8.18	Performance characteristics for 10 m diameter HATT to the base TSR ...191
Figure 8.19	Variation in C_T and C_p with blade pitch angle (θ).....191
Figure 8.20	Pathlines coloured with axial velocity at peak torque TSR = 2.1 [A].....192
Figure 8.21	Pathlines coloured with axial velocity at peak power TSR = 3.6 [B].....192
Figure 8.22	Pathlines coloured with axial velocity at freewheeling TSR = 6.7 [C].....192
Figure 8.23	Peak power with blade pitch and tidal velocity193
Figure 8.24	Power curves for 10 m diameter turbine showing peak power, Betz limit and available power to the base of angular velocity194

Figure 8.25	Downstream axial velocity recovery with pitch angle variation for 10 m diameter turbine	196
Figure 8.26:	Downstream axial velocity recovery with increasing axial thrust CT For 10 m diameter turbine.....	197
Figure 8.27:	Wake recovery and vortex diameter across X-plane of reference domain with a blade pitch angle of 0°	198
Figure 8.28:	Wake recovery and vortex diameter across X-plane of reference domain with a blade pitch angle of 6°	199
Figure 8.29:	Wake recovery and vortex diameter across X-plane of reference domain with a blade pitch angle of 12°	199

Chapter 9

Figure 9.1	Normalised power (Pn) attenuation through water column with plug and profiled upstream velocity profiles for the site and reference CFD models	202
Figure 9.2	Power and torque curves for reference and site domains with plug and Profiled flows.....	204
Figure 9.3	Dependency of power coefficient on upstream flow definition.....	204
Figure 9.4	Torque and power curves for Severn and Anglesey site 2.....	205
Figure 9.5	Comparison between Anglesey, Severn and 1/7 th power law.....	206
Figure 9.6	Velocity magnitude for reference domain z-axis velocity profile along central depth plane with plug -flow at velocity-inlet boundary (m/s).....	207
Figure 9.7	Velocity magnitude for site domain z-axis velocity profile along central depth plane with plug flow at velocity-inlet boundary (m/s).....	209
Figure 9.8	Centre plane velocity deficit profiles; Chilworth (A) and IFREMER (B)..	211
Figure 9.9	Wake deficits for Reference and site CFD models with plug and profiled flow. Plus contour plot coloured with axial velocity for reference CFD model with plug flow.....	212

Figure 9.10	Wake deficits for Reference and site CFD models with plug and profiled flow. Plus contour plot coloured with axial velocity for reference CFD model with profiled flow.....	212
Figure 9.11	Velocity magnitude for reference domain z-axis velocity profile (Velocity magnitude) along central depth plane with profiled flow at velocity-inlet boundary (m/s).....	213
Figure 9.12	Velocity magnitude for site domain z-axis velocity profile along central depth plane with profiled flow at velocity-inlet boundary (m/s).....	214
Figure 9.13	Wake deficits for Reference and site CFD models with plug and profiled flow. Plus contour plot coloured with axial velocity for site CFD model with plug flow.....	215
Figure 9.14	Wake deficits for Reference and site CFD models with plug and profiled flow. Plus contour plot coloured with axial velocity for site CFD model with profiled flow.....	216
Figure 9.15	Stable downstream vortices with upstream plug flow.....	218
Figure 9.16	Disrupted downstream vortices with upstream profiled flow.....	218
Figure 9.17	Pathlines coloured by velocity magnitude with elliptical stanchion cross section.....	219
Figure 9.18	Plan view of Pathlines coloured by velocity magnitude with elliptic cross section.....	220
Figure 9.19	Pathlines coloured by velocity magnitude with profiled stanchion cross section.....	220
Figure 9.20	Plan view of Pathlines coloured by velocity magnitude with profiled cross section.....	221
Figure 9.21	Plan view of Pathlines coloured by velocity magnitude with circular cross section.....	221
Figure 9.22	Plan view of Pathlines coloured by velocity magnitude with circular cross section.....	222
Figure 9.23	Pathlines coloured by velocity magnitude with diamond stanchion cross section.....	222

Figure 9.24	Plan view of Pathlines coloured by velocity magnitude with diamond cross section.....	223
Figure 9.25	Pathlines coloured by velocity magnitude with square cross section.....	223
Figure 9.26	Plan view of Pathlines coloured by velocity magnitude with square cross section.....	223
Figure 9.27	Effect of stanchion geometry on turbine power extraction with increasing stanchion axial thrust.....	225
Figure 9.28	Turbine and stanchion axial thrust variation with stanchion geometry.....	225
Figure 9.29	Torque variation for B1, B2 and B3 through 360° with no stanchion.....	228
Figure 9.30	Power variation for B1, B2 and B3 through 360° with no stanchion.....	229
Figure 9.31	Axial thrust variation for B1, B2 and B3 through 360° with no stanchion.....	229
Figure 9.32	Example of current velocity profile and turbine rotation.....	229
Figure 9.33	Individual blade and total power and thrust curves through 360° of rotation.....	230
Figure 9.34	Pathlines coloured by velocity magnitude Case.1 right view.....	232
Figure 9.35	Pathlines coloured by velocity magnitude for Case.1 left view.....	232
Figure 9.36	Pathlines coloured by velocity magnitude for Case.1 reduced wake.....	233
Figure 9.37	Pathlines coloured by velocity magnitude for Case.1 increased wake.....	233
Figure 9.38	Upstream pathline contacting B3 wake along a plain at 32 m depth coloured with velocity magnitude and B1 at 263° rotation angle.....	235
Figure 9.39	Upstream pathline missing B1 and B2 wake along a plain at 32 m depth coloured with velocity magnitude and B1 at 263° rotation angle.....	235
Figure 9.40	Pathlines coloured by velocity magnitude with downstream stanchion.....	236
Figure 9.41	Pathline plain at 32 m depth coloured with velocity magnitude with B1 at 263° rotation angle.....	236
Figure 9.42	Torque variation for B1, B2 and B3 through 360° with stanchion.....	238
Figure 9.43	Power variation for B1, B2 and B3 through 360° with stanchion.....	238
Figure 9.44	Axial thrust variation for B1, B2 and B3 through 360° with stanchion.....	239

Figure 9.45	Combined torque variation for Case.1 and Case.2.....	240
Figure 9.46	Combined power variation for Case.1 and Case.2.....	240
Figure 9.47	Combined axial load variation for Case.1 and Case.2.....	241
Figure 9.48	Contours coloured with velocity magnitude at (a) 6 m and (b) 8 m upstream of the HATT.....	242/3
Figure 9.49	Contours coloured with velocity magnitude at (a) 1 m upstream and (b) 0.5 m downstream of the HATT.....	244
Figure 9.50	Downstream contour planes coloured with velocity magnitudes.....	245
Figure 9.51	Iso contour (1.3 m/s) with flow entering at the apex frame base (a) and at the apex (b).....	247
Figure 9.52	contours of velocity magnitude entering frame apex.....	248

List of Tables

Table 2.1	Summarised existing and proposed tidal range projects.....	11
Table 2.2	Black and Veatch UK tidal resource by depth (key resource highlighted)...	20
Table 4.1	Dimensions and boundary conditions for CFD models.....	58
Table 4.2	Coordinates for prototype blade divided into 11 segments (tip pitch = 6°).....	63
Table 4.3	Cell count for all CFD models.....	68
Table 4.4	Rotational axis depth for 10 m turbine in 35 depth.....	93
Table 4.5	Rotational axis depth for 10 m turbine in 50 depth.....	94
Table 5.1	BALDOR AC servomotor Specifications.....	99
Table 5.2	Coordinates for proposed HATT sites.....	107
Table 6.1	Summarised results for flume tests using both flexible and solid drive shafts.....	117
Table 7.1	Summary of results for CFD flume model using different viscous models.....	154
Table 8.1	HATT diameter with water depth.....	169
Table 8.2	Reynolds number (millions) for CFD and flume tests.....	177
Table 9.1	Dimensions of flume facilities A and B.....	209

Nomenclature

A = Swept area of turbine, m^2

A_x = Area vector of the face in x-component, m^2

a = Axial induction factor

a' = Rotational induction factor

B = Number of blades

c = Chord length, m

C_p = Power coefficient

C_{p,max} = Maximum theoretical power coefficient (Betz limit)

C_T = Thrust coefficient

C_E = Electrical power generation coefficient

CL = Coefficient of lift

CD = Coefficient of drag

C_{ij} = Convective transport

D_{ij}^μ = Viscous diffusion term

D_{ijk}^t = Turbulent diffusion term

D = Diameter, m

D_H = Hydraulic diameter, m

E_K = Available kinetic energy. Also see Pa, W

E_P = Potential energy in tidal range, W

F_x = Force vector in x-component (sum of shear force and static pressure force), N

F_y = Force vector in y-component (sum of shear force and static pressure force), N

Fr = Froude Number

F = Total force, N

F_s = Shear force, N

FT = Axial thrust force, N

F_p = Static pressure force, N

F_{p,x} = Force due to static pressure in x-component, N

$I\%$ = Turbulence Intensity percentage
 $I\%$ = Percent of servomotor current
 I = Servomotor current, A
 I = Turbulence intensity,
 I_{bT} = Turbulence intensity relative to chord length at blade tip
 I_{bD} = Turbulence intensity relative to turbine diameter
 K = turbulent kinetic energy, m^2/s^2
 ℓ = Turbulence length scale, m
 N = Total number of faces
 N_e = Ensemble average of experiments
 n = Face number
 P = Turbine power extraction, W
 P_p = Peak power extraction, W
 P_a = Available power upstream of turbine, W
 P_{ij} = Stress production rate
 P = Static pressure acting on the element, N/m^2
 P_{CFD} = Power predicted using CFD, W
 $P_{scaling_law}$ = Power calculated using scaling law, W
 P_s = Mechanical shaft power, W
 PE = Electrical power, W
 P_n = Normalised power
 Re = Reynolds number,
 R_{ij} = Reynolds stresses, N/m^2
 r = Radius, m
 r_x = Distance in x-component, m
 r_y = Distance in y-component, m
 \vec{r} = Position vector in rotating reference frame, m
TSR = Tip speed ratio at blade tip
 TSR_r = Tip speed ratio at radius r
 TSR_0 = Tip speed ratio at blade base
 t = Time, s

T = Torque, Nm
 T_p = Peak torque, Nm
 u' = Velocity fluctuation, m/s
 u_{\bullet} = Velocity average, m/s
U = Mean Velocity, m/s
 \bar{u}_r = Relative velocity in MRF, m/s
 u_r = Friction velocity and typical velocity turbulence length scale
V = Up stream water velocity, m/s
 V_{msp} = Mean Spring peak velocity, m/s
 V_{Ri} = Resultant incident flow velocity at blade segment (i), m/s
 V_{def} = Downstream wake velocity deficit
 V_o = Axial water velocity upstream of HATT, m/s
 V_w = Axial water velocity downstream of HATT, m/s
 y_{nw} = distance from wall boundary and turbulence length scale
 Y_i = Power generated at segment (i) along the blade radius, W
 y^+ = Near wall flow resolution factor (local Reynolds number)
 y^* = Near wall flow resolution factor
Zus = Distance upstream of stanchion, m

Greek Symbols

α = Incident or attack angle, Degrees
 β = Relative flow angle, Degrees
 δZ_{DS} = Axial distance between hub rear and downstream MRF face, m
 δZ_{US} = Axial distance between hub apex and upstream MRF face, m
 ε = Turbulence dissipation rate, m^2/s^2
 ε = turbulent dissipation term,
 Φ_{ij} = source/sink due to pressure/strain correlation
 γ = Blade twist angle between tip and base, degrees
 μ_t = Turbulent viscosity

μ = Fluid dynamic viscosity, kg/ms
 ν = Kinematic viscosity, m²/s
 θ = Blade pitch angle, degrees
 θ_p = optimum blade pitch angle, degrees
 ρ = Density of fluid, kg/m³
 σ' = Local solidity factor, $Bc/2\pi r$
 $\bar{\Omega}$ = Angular velocity of MRF, rad/s
 ω = Angular velocity of turbine, rad/s
 ω_s = Specific dissipation rate, 1/s
 ψ = Tip loss factor

Acronyms

ADCP: Acoustic Doppler Current Profiler
BEM: Blade Element Momentum theory
BERR: Department for Business Enterprise and Regulatory Reform
BDC Bottom Dead Centre
BWEA: British Wind Energy Association
CCC: Committee on Climate Change
CD: Chart Datum
CFD: Computational Fluid Dynamics
DNS: Direct Numerical Simulation
DTI: Department of Trade and Industry
EIA: Energy Information Administration
EMEC: European Marine Energy Centre
ETSU: Energy Technology Support Unit
EVM: Eddy Viscosity Models

GDP:	Gross Domestic Product
HATT:	Horizontal Axis Tidal Turbine
HAWT:	Horizontal Axis Wind Turbine
HAT:	Highest Astronomical Tide
HWS:	High Water Spring
IPCC:	International Panel for Climate Change
LAT:	Lowest Astronomical Tide
LES:	Large Eddy Simulation
LMG:	Permanent Magnet Generator
MCT:	Marine Current Turbines
NOAA:	National Oceanic and Atmospheric Administration
NIA:	Nuclear Industry Association
N-S:	Navier-Stokes equations
RANS:	Reynolds Averaged Navier-Stokes
RNG:	Renormalized Grouping
RSM:	Reynolds Stress Model
SDC:	Sustainable Development Commission
TDC:	Top Dead Centre
THGL:	Tidal Hydraulic Generators Ltd
THWAT:	Transverse Horizontal Axis Water Turbine
UDF:	User Defined Function
UKWED:	UK Wind Energy Database
VATT:	Vertical Axis Tidal Turbine

VOF: Volume Of Fluid

WHOI: Woods Hole Oceanographic Institution

1 Introduction

1.1: UK 2020 renewable energy

Following the installation of the first wind farm which was built at Delabole, Cornwall in 1991, wind power generating capacity by 2007 had surpassed that of hydropower. The UK now plans to install up to 30 GW of mostly offshore wind capacity as part of efforts to reach its 20 % of energy from renewable by 2020 (BERR, 2006). Currently the UK is set to reach 5 GW by early 2010 (Nakanishi, 2009). The Committee on Climate Change (CCC), December 2008 stated that 30 % of the UK's electricity supply would be from onshore and offshore wind by 2020. The magnitude of the contribution required from renewable technologies by 2020 is shown in Figure 1.1. By far the largest contribution is from onshore and offshore wind. The next largest increase is from tidal stream/range which does not exist in the 2007 data. Over the next 10 years around 4 GW of tidal stream/range generation capacity as to be installed to meet the 2020 target. This is a challenging task to undertake considering tidal stream is in its infancy with very little contribution to the grid. Moreover, in the UK large tidal barrage/lagoons have not even got past the consultation stages.

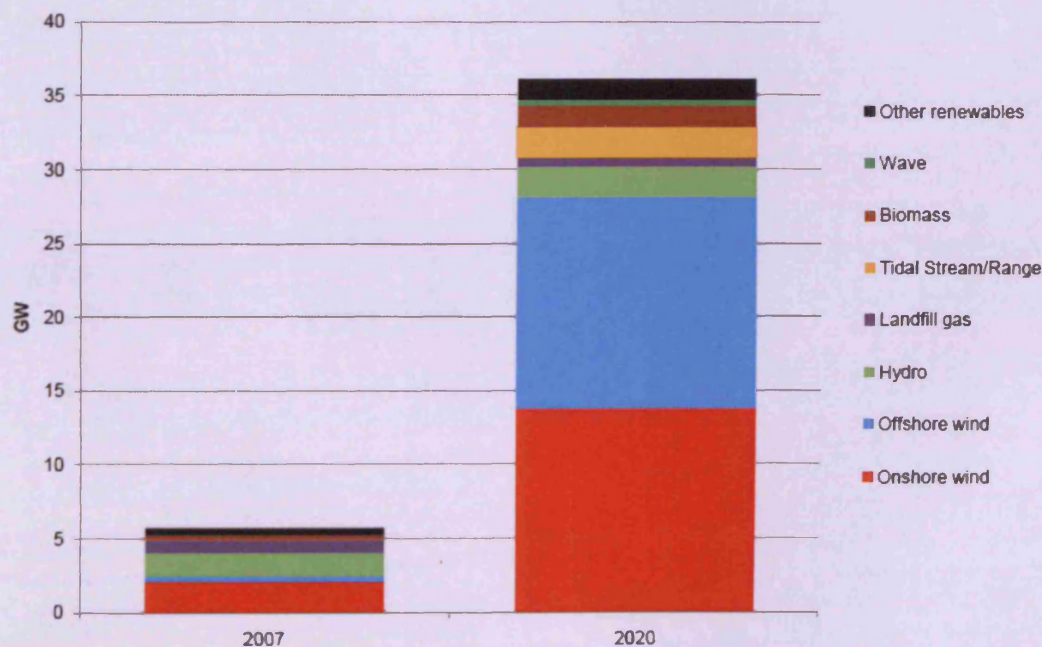


Figure 1.1: Historic and projected renewable generation capacity, 2007 and 2020

Source: CCC, 2008

1.2: Applications of marine turbines

Horizontal Axis Tidal Turbine (HATT) technology is currently at the full scale prototype phase with much of the technology adapted from the wind industry. HATT technology, however, has barely started to touch the target of 4 GW by 2020, shown in Figure 1.1. The challenges that face HATT development are complicated by the medium in which they operate, such as depth and high currents. This requires them to possess a higher degree of robustness than Horizontal Axis Wind Turbines (HAWTs), with the ability to operate with limited maintenance schedules. Higher structural loading and the addition of biological fouling from marine life with increased material corrosion from salts are also just some of the operational issues. Others include concept economics and embedded CO₂ associated with manufacture, installation, decommissioning and shore-to-site transportation (Douglas et al, 2007), (Carbon Trust, 2006). HATTs are initially being developed in waters between 30 m and 40 m deep due to the cost and accessibility of such technology. It is known that at depths of 30 m and 40 m depths the total UK resource is around 16%. However, it is estimated that approximately 80% of the total tidal stream resource is actually in depths greater than 40 m where potentially future development will expand (Black and Veatch, 2005). At depths > 50 m seabed mounting configurations used for depth < 40 m are no longer viable in terms of economics and installation and therefore will require other options to be investigated (Fraenkel, 2004).

If UK tidal stream technology is to play a significant role in meeting the 2020 target, with or without a contribution from tidal range technology, it will have to quickly expand to include deep water applications, > 50 m.

1.3: Turbine blade Technology

Much of the fundamental technology associated with the development of aerofoil sections is contained in reports written for the National Advisory Committee for Aeronautics (NACA), which later in 1958 became the National Aeronautics and Space Administration (NASA). Although others exist, the NACA blade profiles are still an excellent source for the lift and drag properties for a wide range of aerofoil cross sections used in the development of helicopter blades and aircraft wings. Over the last 30 years they have been utilised in the development of wind turbine blades which has now grown into a major global energy supply. Like HAWTs the performance of a

HATT is governed by many parameters, which range from the near-field hydrodynamic physics, such as lift and drag forces at the blade surface, to the creation of the downstream vortex, its far field expansion and associated velocity deficit along its axial length. The magnitude of the torque and resulting power generated from the blade hydrodynamics is governed by its profile, profile variation along its length and the amount of twist applied between the tip and its base. These features are fundamental to the efficient operation of the device and as such are the fundamental design parameters to be considered.

1.4: Aim of the thesis

The work of this thesis uses an existing blade profile and angle of twist of a prototype 0.5 m diameter HATT.

The aim of this work was to use the CFD package Fluent™ to investigate the performance (power, torque and axial thrust) of a full scale HATT in a high shear environment based on site velocity profile data.

1.5: Thesis objectives

- Using the existing laboratory scale prototype HATT to measure its performance characteristics within a calibrated water flume. Using these data to validate CFD models.
- To develop an economical CFD model of the prototype HATT. Economical, both in terms of memory and computational time, while maintaining its ability to capture the measured performance of the physical prototype device.
- To scale the prototype design to dimensions with economic power extraction (upto 30 m). Also to include velocity scaling from 2 – 6 knots (1 - 3.08 m/s)
- To use realistic velocity profiles through the water column at a site to assess turbine performance and wake characteristics. Data provided by a vessel mounted Acoustic Doppler Current Profiler (ADCP).
- To use an economic, quasi-static approach to capture the dynamic interaction between the rotating blades and support stanchion for a scaled model positioned within the lower 25% of the water column while subjected to an upstream velocity profile derived from the ADCP data.

2: Literature Review – technology drivers and current technology

In the light of the rapid technology development and application expansion required to meet the 2020 target discussed in Section 1.1, Chapter 2 considers some of the past and current technology drivers that have led to the current needs of energy supply. It will also cover some of the more published tidal technologies.

2.1: Overview of technology drivers

This chapter is intended to give a brief overview on the events that have led to current energy demand and, for some, the ostensible threat of accelerated anthropological global warming. The main focus will be on renewable energy resources, specifically marine, with a greater emphasis on tidal stream and how the UK resource compares with European and the broader Global resource. Tidal range and stream locations and their associated resources are discussed for the UK with some examples of proposed barrage and lagoons, also prototype tidal stream devices that are currently sited around the UK. To help develop an overall picture on tidal stream energy for the UK, resource estimates such as that presented by (Black and Veatch, 2005) and tidal stream resource variability between sites (Carbon Trust, 2005) will be discussed.

2.1.1: Growth in energy demand

Following the move away from a worker based industry in the late 17th century and with the advent of steam and railway in the latter part of the 18th century the western industrial revolution gave way to a greater growth in energy consumption (Ashton, 1998). With increasing personal wealth and the desire for better standards of living, energy demand from the domestic market also increased during the 19th century. Most of this resource was in the form of high energy density fuels originating from organic matter diagenesis such as coal, gas and oil (Miller, 2005). The energy stored in these fuels made them economically attractive to industry and the transport sector alike, both then and now. To date the global demand for energy is set to increase with accelerated growth in developing countries such as China and India. It has been stated that between 1980 and 2005 their combined share of

the world's total energy consumption increased from 8% to 18% and is set to double to one quarter of the global consumption between 2005 and 2030 (EIA, 2008). The same source also estimated that global energy consumption will grow by 53% between the period 2005 to 2030 if laws and policies associated with energy usage remain unchanged, resulting in an increase of 68300 TWh for the same period. The world is now faced with legacies associated with past and present energy consumption and its impact through the possibility of accelerated global warming.

2.1.2 Global Warming

The first large scale reaction to the global warming phenomenon was the Kyoto agreement of 1997 where each country that ratified the agreement would agree to “reduce its greenhouse gas emissions by 5% from 1990 levels by 2010” (Kyoto, 1997). The protocol however suffered a major set back when in 2001 US President George. W. Bush argued that the Kyoto protocol would be bad for the U.S. economy. This resulted in the USA's refusal to ratify the agreement, limiting the protocol's global impact (Maslin, 2004). However, 186 other countries did agree with the findings of the environmental treaty, which was eventually ratified in 2005 (CBC News, 2005). There were however other obstacles on the road to an outright acceptance of the phenomenon as disputes were still raging between sceptics of global warming accelerated by anthropogenic emissions and those that advocated it. The most famous of the controversies surrounded the well documented “Hockey Stick graph” presented by E.M. Mann et al, 1999. Taken by many to be proof of anthropogenic global warming, the graph showed relatively even temperature fluctuations with a slight downward trend in temperatures. This is followed by a sharp rise in global temperature towards the beginning of the 19th century (Watson, 2001), Figure 2.1, which coincides with the onset of the industrial revolution. The economic cost of not taking action to mitigate the consequences of global warming however had not been considered until the publication of the Stern Review, which had a significant impact world wide (Stern, 2005). The report indicated that damages resulting from unmitigated global warming could be 5% of global GDP each year, or as much as 20% GDP in the worst case scenario put forward by the report. In contrast, the cost could be limited to 1% of global GDP each year if prompt action was taken to reduce greenhouse emissions. Placing the

impact of global warming in terms of economics greatly increased global attention. In addition to the 1997 Kyoto protocol, during early 2007 the European Commission published a communication outlining a target to reduce green house gas emissions by at least 20% by 2020 compared to 1990 levels with a further stipulation of 30%, provided there was comprehensive international agreement (Russ et al., 2007). With the inauguration of USA President Barack Obama in January 2009 and his pledge:

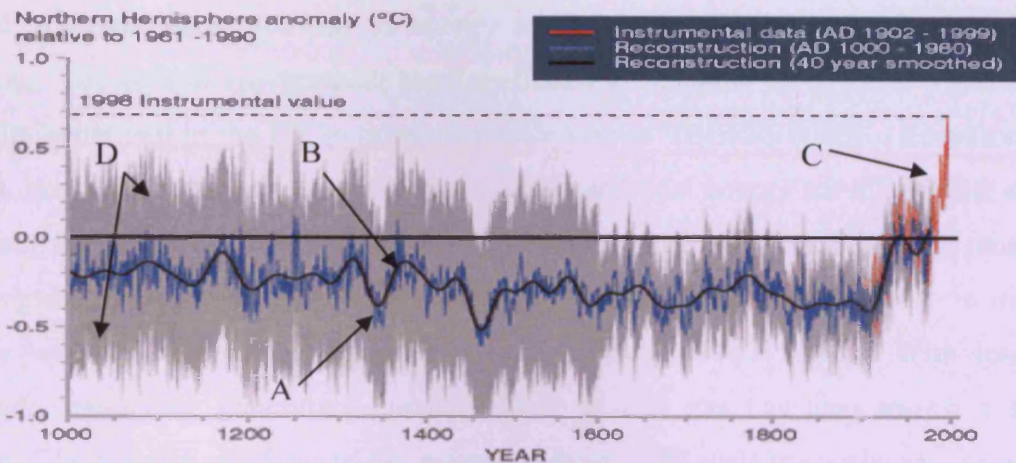


Figure 2.1.: Millennial Northern Hemisphere (NH) temperature reconstruction (A) tree rings, corals, ice cores, historical records (AD 1000 to 1999), a smoother version (B) and instrumental data (C) and two standard error limits (D) are shown.

Source: IPCC Third Assessment Report

“To protect our climate and our collective security, we must call together a truly global coalition” (Collinson, 2009), optimism for the EU’s successor to the Kyoto protocol has increased (Harrison, 2009). The nature of the new ‘global coalition’ however has yet to be realised. In the UK the government had already taken an aggressive route and announced a tougher target for the reduction of CO₂ emissions in its Climate Change Bill (Anderson, 2007). However, the reduction of 60% from 1990 levels by 2050 did not match the global targets set out in the Stern Review. It was suggested that the UK might have to make an 80% cut in CO₂ emissions from 1990 levels by 2050 to meet this far reaching target (Environmental Audit Committee, 2007),(Summers et al, 2008). Budget plans to meet the 60% CO₂ reduction to the 1990 level target will be put forward by the UK parliament with independent advice from the Climate Change Committee (CCC) before June 2009. The CCC has also been asked to report on the 80% reduction target (BERR, 2008). This elucidates the need for other forms of energy production such as that delivered by renewable technologies and nuclear to help mitigate greenhouse gas emission. The full

scope of other energy schemes, such as nuclear, is far reaching and encompasses such levels of detail as to warrant a separate literature review, which is beyond the scope of this thesis.

2.1.3 Renewable and nuclear energy

In order for greenhouse gas reduction to succeed, energy sources other than fossil fuels are required and renewable sources of energy are a viable option for assisting with the reduction. The British Government has “confirmed a timetable up to 2020 when 20% of electricity generated in the UK is from renewable source” (BERR, 2006). Resources such as wind, landfill gas, biomass, hydroelectric, wave and tidal energy are all feasible options with many in current use. Figure 2.2 shows the installed capacity for a range of renewable technologies. Between the years 1997 and 2006 wind had the largest growth in installed capacity with an increase of approximately 5 times its 1997 value. With less of a magnitude, electricity generating capacity from landfill gas has also shown a similar increase. The proportion of electricity generated from small scale hydroelectric and sewage sludge digestion has remained relatively constant, between the years 1996 and 2006 (BERR, 2008). Although, not shown, large scale hydro capacity has remained relatively constant at around 1.4 GW. In 2006, 4.7% of electricity generated in the UK was from a combination of renewable energy resources, (Defra, 2008). It was suggested that to meet the 2020 target of 15 %, of all energy from wind power generation, the existing capacity would have to increase by a factor of 10 (Arnott, 2008).

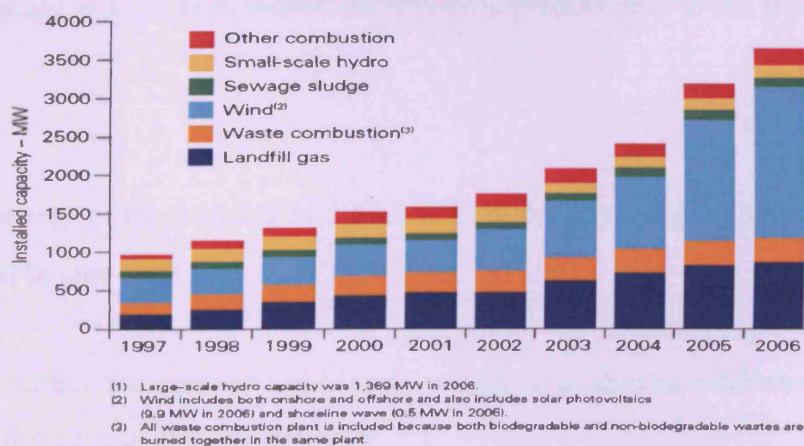


Figure 2.2: Installed capacity of renewable energy technologies between 1997 and 2006.
 Source: BERR, 2008

During 2008 it was stated that wind power alone now produces 3 GW of electricity for the UK. Current figures, suggested by UKWED at the end of 2009, put wind energy production at 4.03 GW with a total of 2741 sited turbines. The UKWED database, in late 2009, shows that there are 665 turbines under construction with a total power of approximately 0.057 GW with a further 3642 turbines in planning with total power of approximately 0.421 GW (BEWA, 2009). It is therefore likely that by the end of 2010 wind energy production will be between 5 GW and 6 GW. Another considerable source of alternative energy, not included in Figure 2.2 is tidal stream and range. Given resource estimates from various sources there is now a breed of new technologies emerging within this area of marine energy that, if developed, could make a significant contribution to the UK electricity supply. Although most of the methodology associated with these devices is not new, the application of new materials and technologies has given them the potential to survive the harsh operational environment that has historically eluded economic power extraction. Examples of new materials and technologies include sealing, bearings and composite materials used for blade construction.

2.2: Marine energy resources

One of the emerging technologies is tidal energy where two very different approaches exist, namely tidal range and tidal stream. Electricity can either be generated through impoundment schemes, such as barrages and lagoons, or directly from the tidal stream using devices such as tidal turbines and reciprocating hydrofoils. Barrages and lagoons use the potential energy at high tide, where the energy is proportional to the square of the tidal height.

$$E_p = \frac{1}{2} \rho A g h^2 \quad (2.1)$$

Where: A is the area of the basin, ρ is the water density, g is the gravitational acceleration and h is the tidal height.

Tidal turbines extract the sum of the kinetic energy available in tidal streams, which is proportional to the cube of the tidal velocity.

$$E_k = \frac{1}{2} \rho A v^3 \quad (2.2)$$

Where: A is the swept area of the turbine and v is the upstream water velocity.

Most of the largest tidal ranges and streams are generated from the gravitational attraction and rotation of the moon and to a lesser extent the sun. This interaction produces a rhythmic rise and fall in ocean levels allowing accurate temporal and spatial prediction. Over many years, typically at shallow waters along coastal lines, tide gauges have been used in conjunction with Harmonic and Response methods to predict local tide levels with an extremely high level of accuracy (NOAA, 2008). Other mechanisms such as salinity or temperature gradients can also generate tidal streams; in some locations these can approach a constant velocity (Thomas, 2007). The Mediterranean is one location where this type of phenomenon is noted, such as in the straits of Dardanelles and in Greek waters through the straits of Samos, Kafirea, Kea and Kithos (Non Nuclear Energy – JOULE II, 1996). Another example includes streams generated from barotropic flows and salinity gradients as brackish water such as when the Baltic Sea mixes with the Atlantic Ocean. Some of the strongest streams associated with this type of flow have been reported along the Danish coast (Nielsen, 2005). The UK is also well situated to take advantage of such resources (Black and Veatch, 2005)

2.2.1: Tidal barrage and lagoons

Impoundment schemes utilise the potential energy associated with a high vertical tidal range by storing water at high tide and releasing it through turbines as the tide ebbs or floods depending on the turbine arrangement. The technology however requires large civil works to either partially or totally block off the channel. It is predicted that such impoundment schemes have the potential of creating up to 600 MW of power (Baker et al, 2006). This represents around half the power from a conventional power station. The UK has the second highest tidal range in the world with the Severn Estuary and Mersey being the main areas of interest with regards to tidal range, Figure 2.3. Of the two, the Severn Estuary alone has 90% of the UK's tidal range resources and the Mersey around 7.5% (BERR¹, 2008). Although, estuaries such as the Severn have large potential for electricity

generation, for the last 40 years the only large scale tidal barrage has been operating at La Rance in France, Figures 2.4 and 2.5. The La Rance barrage is around 710 m long with a four lane road running across the top. It has a total generating capacity of 240 MW from 24, 10 MW Bulb turbines and is capable of generating energy during ebb and flood tides. However, it is mainly operated on ebb only, due to the better power generation economics, via the use of pumping during flood tide, which increases the release height post high tide (Kerr, 2006) and (ETSU, 1990).

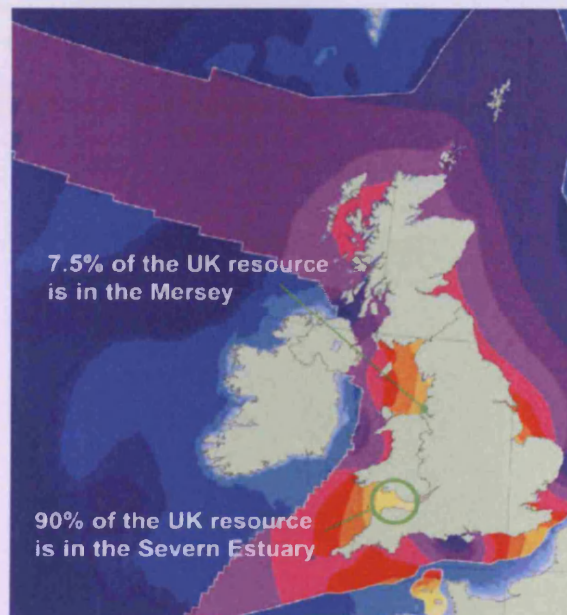


Figure 2.3: UK Tidal range resource.
Source: BERR, 2008.

There are, however, a number of smaller schemes in operation such as the 20 MW power plant situated at Annapolis Royal on the Nova Scotia side of the Bay of Fundy, Canada. This scheme was completed in 1984 at a cost of \$55 million, Canadian (~£31 million: using 2009 exchange rate). The 4 MW power plant at Jiangxia, China and the experimental 0.4 MW plant at Kislaya Guba, Russia are some of the smaller scale tidal range devices (ReVelle and ReVelle, 1992). The location, power rating and energy production of these and other future tidal range plants were summarized by Kerr (2006) as given by Table 2.1. One thing that is clear from Table 2.1 is the scale of future proposals, with the Russian Mezan Bay and Tigr power rating being around 117 times larger than the current La Rance scheme. Of the proposed schemes the UK has the second largest yearly energy production with the combined output of the Severn Estuary and Mersey locations.

Table 2.1: Summarised existing and proposed tidal range projects. Source: Kerr, 2006)

Country	Location	Power (MW)	Energy (TWh/yr)
<i>Operational</i>			
France	La Rance	240	0.5
Canada	Annapolis Royal	20	0.04
China	Jiangxia	3.9	0.01
Russia	Kislaya Gula	0.4	0.001
<i>Proposals</i>			
Canada	Bay of Fundy, Cumberland Basin	1400	3.3
China	Various	1000	2.5
Russia	Mezan Bay and Tigur	28000	31.0
Korea	Siwha and Garolim	740	1.4
India	Khambat	1800	3.9
Australia	Secure Bay and Cape Keraudren	600	1.1
Argentina	San Jose/Neuvo	600	1.8
UK	Severn Estuary and Mersey	9300	18.5



Figure 2.4: Picture of the La Rance tidal barrage

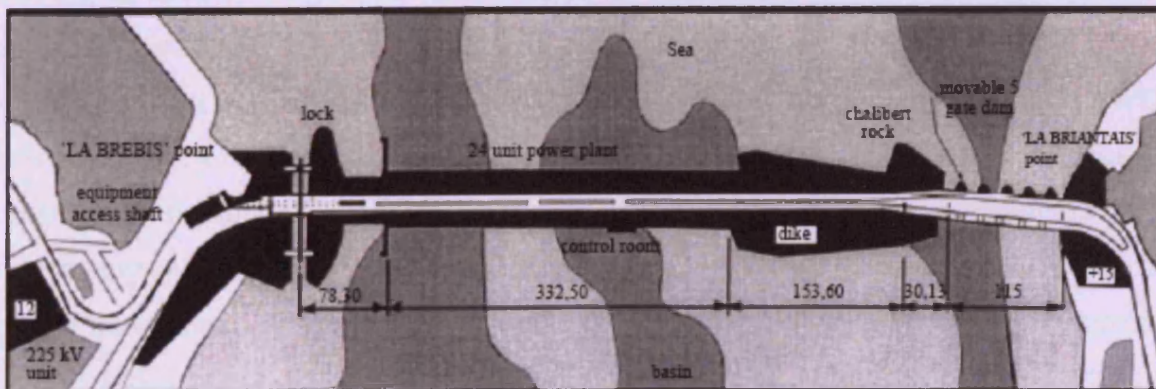


Figure 2.5: Schematic of the La Rance tidal barrage showing the power plant at the centre

There are three major schemes being considered for the Severn Estuary, the most discussed is the Cardiff-Western (A) impoundment, which according to the Sustainable Development Commission, (2007), would be comprised of 216 turbines along a length of 16.1 km with a generating capacity of 8.64 GW, Figure 2.6. The document also states that it is estimated to have an annual electrical output of 17 TWh/yr, which represents around 4.4 % of the UK electricity demand. This revised value is around 1.5 TWh/yr lower than that previously presented in Table 2.1 by Kerr, (2006) for the Severn and Mersey combined. The 4.4% however still indicates that the Cardiff-Western barrage is a significant potential resource. The second is the Shoots with a length of 4.1 km and 30 turbines and an annual average electricity output of 2.77 TWh/y. This second case (The shoots) (B) has the potential to generate 0.7% of the UK electricity demand (Sustainable Development Commission¹, 2007). The third is the largest of the proposed barrages known as the Outer Barrage (C) which has the potential to produce 25 TWh/y, which is around 6.5% of the UK electricity demand with a capital cost of £29bn. Figure 2.6, also shows the long list of potential sites for both tidal range lagoons as presented in Volume 1 of the DECC, 2008. Some of the lagoons included in the same study were the Russell Lagoon (1) with an estimated output of 2.3 TWh/y and capital cost of £3.1bn (Parsons Brinckerhoff, DECC, 2008).

One of the first tidal lagoon projects was the 30 MW scheme proposed for Swansea Bay, South Wales by Tidal Electric Ltd (TEL). Just over two square miles of sea off the coast would be impounded by the scheme producing an average output of about 15 MW (Friends of the Earth, 2004). A more recent proposal by TEL is for a 60MW lagoon at Swansea bay covering an area of 5 km² and an embankment length over 9 km long. TEL estimate a capital cost of £81.5 million for the Swansea Bay scheme. However, reviews by the Department of Trade and Industry (DTI) and the Welsh Development Agency (WDA) showed significantly higher construction and running costs for the same project. The total construction cost for the same site, by the two reviews, was estimated to be around £234M with an energy cost 4 times that of the TEL figure of 3.5p/kWh (Baker et al. 2006). To date none of these proposals are in the construction stages. It is interesting to note a comparison made by Baker et al (2006) on the construction cost of the Cardiff Bay barrage, which was completed in 1999, and the Swansea lagoon. The cost of the Cardiff barrage was £220M with a length of 1.1km. This gives a realistic insight to what the potential costs for a 9 km

lagoon may cost and credibility to the total cost proposed by the DTI and WDA for the Swansea lagoon. In another study the energy cost of three lagoons in the upper Severn Estuary, Figure 2.7 was compared with the Severn barrage (Cardiff–Weston). The energy cost for the three lagoons was found to be 40% higher than for the barrage (DTI³, 2006), this was mainly due to the large construction costs of the impoundment walls. The focus of this thesis is on tidal stream technologies and therefore tidal range will not be covered in any further detail.

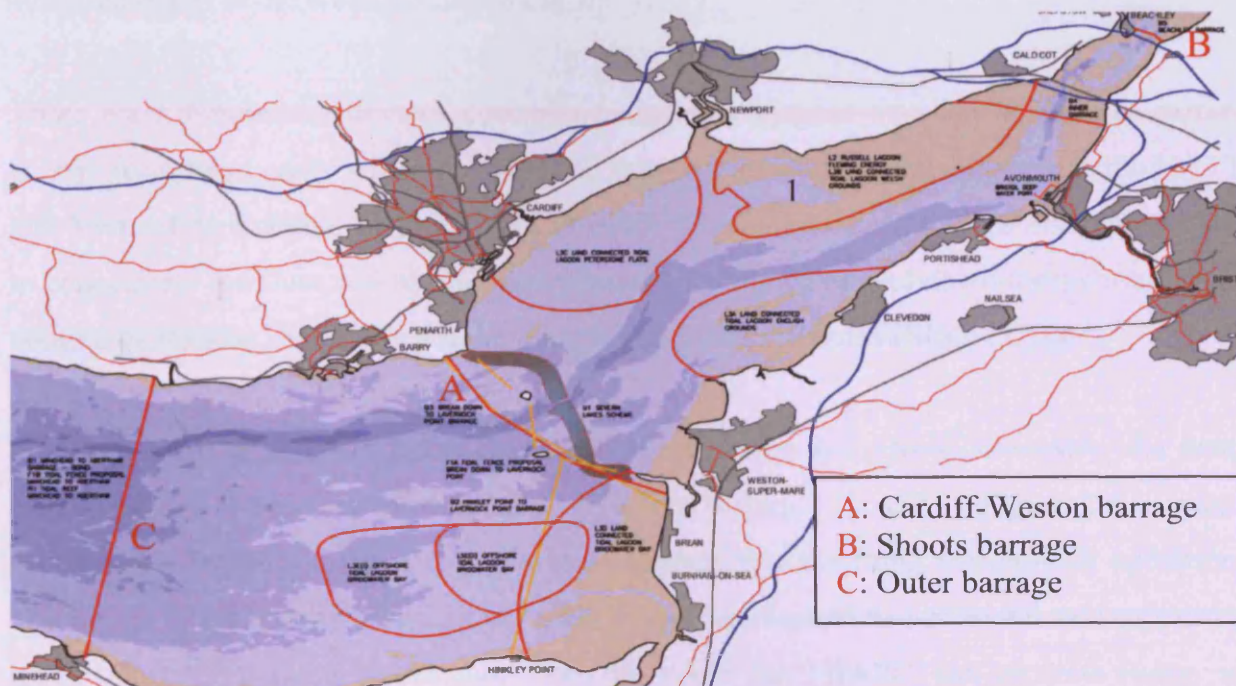


Figure 2.6: Long list of proposed barrages, lagoons and tidal fences.
Source: DECC, 2008

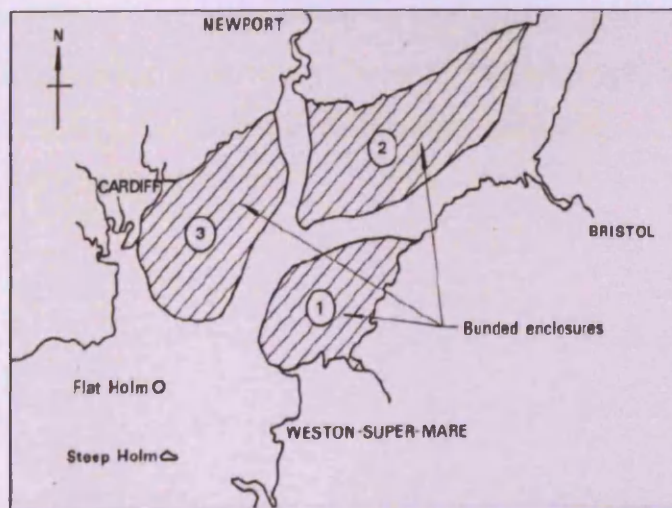


Figure 2.7: Tidal lagoons evaluated as part of the Severn Barrage Programme. Source: DTI³, 2006

2.2.2: Tidal stream

In contrast to barrage and tidal lagoons, tidal stream turbines use the kinetic energy of the tide directly and, unlike the impoundment schemes, tidal stream turbines allow the water to pass through and around them and do not require the storage of water. They are normally also fully submerged below the water level and thus do not offer a visual obstruction to the seascape. They can be seabed mounted for example via a pile driven stanchion or floated at a desired depth in the water column using buoyancy.

There are a number of devices currently under development that can be used to extract energy from local energy fluxes. These fall into two general categories, such as the HATT and Vertical Axis Tidal Turbine (VATT). Others include venturi devices that can be used to concentrate the flow and oscillating hydrofoils that move up and down through the water column generating electricity via the pumping of hydraulic fluids (SDC, 2007).

A more recent design has been developed by engineers at Oxford University, the team claim that the Transverse Horizontal Axis Water Turbine (THAWT), Figure 2.8, is more robust, efficient and cheaper to build and maintain than anything currently in operation. The device is essentially a cylindrical rotor that rotates around its horizontal axis supported by two concrete posts at either end. Like the VATT the THAWT can generate energy in both flow directions with an estimated power generation of 12 MW from a 10 m diameter and 60 m long rotor (Jha, 2008). According to McCulloch, head of the electrical power group at Oxford's engineering department the manufacturing and maintenance costs are about 60% and 40% lower, respectively than other horizontal devices currently under development (Kumar, 2008).

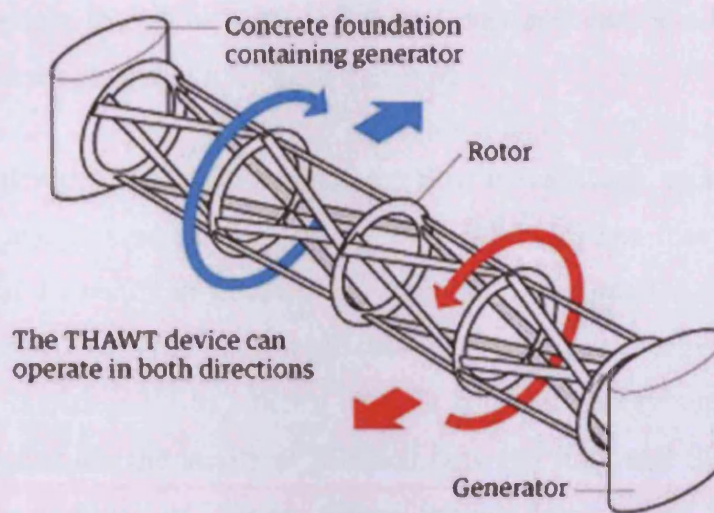


Figure 2.8: Oxford University's THAWT horizontal axis turbine.

Source: Kumar, (2008). THWAT: Next generation underwater turbines from Oxford.

There are numerous publications and websites that discuss the various aspects of these technologies and therefore they will not be discussed in detail. The previously cited independent report covers the relative performance of differing types of marine energy conversion technologies in comprehensive detail (SDC, 2007). Since the work contained within this thesis concentrates on HATTs a detailed comparison between other marine technologies, which includes wave, will not be discussed here.

2.2.3: Horizontal Axis Tidal Turbines (HATTs)

Local tidal velocity, turbulence, bathymetry, water column velocity profile and depth, sea bed mounting, local shipping requirements combined with concerns associated with marine fish and mammals are just some of the key issues that need to be considered for the successful development of tidal stream devices. Much of the fundamental technology associated with HATTs is derived from the wind industry which in some respects circumvents much of the early developments phases, such as blade profile testing and the basics of the ensuing hydrodynamics. However, the medium in which they operate produces higher structural loading, when compared with air driven turbines. This is in addition to biological fouling from marine life, increased material corrosion from salts and the possibility of blade cavitation at shallower water depths (Douglas et al, 2007). As a result the design criterion for a HATT requires a high degree of robustness with a limited

maintenance schedule to reduce both operational cost and embodied CO₂ emissions from increased material usage and site to shore transport.

By placing such devices at locations where the flow is restricted, such as through channels, between islands and around peninsulas, the high tidal currents that naturally occur there have the potential to result in high energy extraction. Examples of these include bays, fjords and harbours. This type of flow possesses a significant energy resource which could make a valuable contribution to either a local or national energy supply. Global areas of potential interest include the straits of Messina between Italy and Sicily and concentrated flows between the Indonesian islands. Others include Long Island Sound and New York Harbour, New York, USA (Pugh, 2004). A North American study by the Electrical Power Research – Institute (EPRI) included sites within Alaska, Washington, California, Massachusetts, Maine, New Brunswick and Nova Scotia. The total available energy from these sites was estimated to be 1.65 GW, with a 15 % extractable power of approximately 248 MW (based on 90 % power take-off efficiency), (Bedard et al, 2006). Using the same 15 % extractable energy assumption, seven sites in the Bay of Fundy, Canada were estimated to give a total extractable energy of 830 MW (Hagerman, 2006). Along the European coastline, around 106 sites have been identified for electricity generation (Non Nuclear Energy – JOULE II, 1996). The UK in particular has a significant domestic Tidal Stream Resource, representing around half of the European resource and around 10-15% of the known global resource (Black and Veatch, 2005). However, for the year 2006 the measurable energy contributions from tidal stream simply do not exist, indicating that the technology has yet to reach the supply radar. The motivation for the technology however is clear, of the 382.5 TWh/yr of electricity demand in the UK (SDC, 2007), it is estimated that the extractable tidal stream resource has the potential to generate 15.6 TWh/yr, which is approximately 4% of the UK's electricity demand (Black and Veatch, (2005). However, according to Black & Veatch, (2005), the figure is slightly reduced to 12 TWh/yr by the so called 'significant impact factor' (SIF). The SIF uses the flux approach that allows for a change in flow characteristics at a site, which result from energy extraction at another location. This means that only a finite proportion of the total energy in the flow can be extracted without significantly affecting flow speeds, and possibly the surrounding

environment (Carbon Trust, 2009). It should be noted however, that other studies have also focused on localised and array based potential energy extraction. These studies have used variables such as the SIF, average operational efficiency, turbine down-time (maintenance), minimum stream velocity for efficient energy extraction, the ratio between first and second tides and for array based farms, spacing of individual turbines (Strathclyde, 2009). In contrast to Black and Veatch, (2005), the following surveys have quoted figures of 58 TWh/yr (DTI, 2003), 22 TWh/yr (Soerensen et al, 2003) and 27 TWh/yr (ABP mer, 2007) for the total potential extractable energy. The latter energy figures illustrate the difficulties involved in estimating a 'reliable' value for the UK's tidal energy resource. Moreover, research by Salter, (2007) suggests that the potential energy of a tidal wave resultant from the vertical displacement of water could increase the previously quoted potential energies by a factor of 20 times (ABP mer, 2007) and (Salter, 2007). With the addition of data obtained from the installation of arrays, it is likely that procedures used to estimate the suitability of potential sites will improve. The addition of site specific data to the current evaluation calculations would increase confidence for further investment and expansion. Although in its infancy, UK tidal stream technology has resulted in a number of installed full scale devices. Marine Current Turbines (MCT) introduced the world's first offshore tidal stream turbine, The Seaflow, Figure 2.9 (a). It was built into the seabed 1.5 km off shore from Lynmouth, Devon with a total cost of £3.2 million. It comprises an 11 m diameter twin bladed turbine and is capable of producing 300 kW of electricity at a tidal flow of about 2.8 m/s (5.5 knots) (DTI, 2006). The Seaflow generator was never connected to the grid. With around £4.27m worth of grant from the DTI, MCT has also developed the more recent 1.2 MW SeaGen project at Strangford Lough off the coast of Northern Ireland, Figure 2.9 (b). The SeaGen project will supply up to 1000 homes with electricity with a total project cost estimated at £8.4m (SDC, 2007). MCT have also commenced studies for a small array of 10 turbines off the Skerries, North Wales.

Resulting from recommendations made by the House of Commons Science and Technology Select Committee in 2001 the European Marine Energy Centre (EMEC) with its five tidal stream test sites was established. EMEC is situated 2km offshore at the Fall of Warness, off Eday, Orkney and is fast becoming a major centre for the testing of tidal

stream and wave devices. The EMEC site was selected out of a possible 18 due to the existence of a national grid connection and excellent tide and wave resource (SDC, 2007). The Dublin based OpenHydro Group Ltd have installed a 250kW prototype Open centre turbine at the site, Figure 2.9 (c) as part of their plans to develop a deep sea application, Figure 2.9 (d).



(a) SeaFlow, turbine near Lynmouth



(b) SeaGen, twin turbines near Strangford Lough



(c) OpenHydro at EMEC Orkeny



(d) OpenHydro concept with seabed mounting

Figure 2.9: Selection of tidal turbines technologies

Image Sources: (a) www.compositesworld.com (b) www.peakenergy.blogspot.com (c) & (d) www.newenergyfocus.com



A clear advantage of tidal stream turbines is that they can be sized to suit the requirements of the local environment, i.e. coastal restrictions, tidal flow, tidal range, seabed topography, etc., and can be placed on either an individual or ‘farm’ configuration. As such, no large civil works are required and this method would therefore be less disruptive to wildlife,

marine activity (and possibly the coastline) and would not present a significant barrier to water transport as in the case of lagoons and barrages. It has been stated that the ideal site for a tidal stream turbine is to be within 1 km of the shoreline and at a depth of 20 m to 30 m (Fujita, 2000). The ideal tidal speed is 2 to 3 m/s (between approx. 4 and 6 knots) as higher speeds can lead to blade loading problems (Soares, 2004). The Pentland Firth however will play a significant part in testing these figures since local tidal velocities can reach 4 m/s. Moreover, since around 53% to 58% of the UK tidal stream resource is estimated to come from the Pentland region (Black & Veatch, 2005) and (Carbon Trust, 2005) designing marine devices to operate at tidal velocities of these magnitudes maybe an absolute requirement if the full resource is to be taken advantage of.

2.2.4: Tidal stream resource distribution

A recent survey on the extractable tidal resource distribution by depth, Table 2.2, suggests that 63% of the total resource is at depths greater than 40 m with a Mean-Spring-Peak velocity (V_{msp}) range between 2.5 m/s and 5.5 m/s and above. Although more challenging to deploy and maintain there is considerable resource at depths greater than 40 m where the resource is estimated to be 28% with a V_{msp} of 5.5 m/s and above. Between 30 m and 40 m depth the V_{msp} ranges between 2.5 m/s and 3.5 m/s with an extractable resource of 18%, (Black and Veatch, 2005). It is within this latter velocity and depth range that tidal turbines are initially being developed, such as those previously discussed. It is unlikely that attention will be given to depths less than 25 m as the peak resources is estimated to be around 3.4%.

Table 2.2: Black and Veatch UK tidal resource by depth (key resource highlighted)

	Red: >20% of total resource
	Orange: 10–20% of total resource

B&V 2005 Extractable Resource Distribution by depth / velocity (%)						
Depth Range (m)	V_{msp} Velocity Range (m/s)					Total
	<2.5	2.5–3.5	3.5–4.5	4.5–5.5	>5.5	
<25	0.2	3.4	0.9	0.0	0.0	4.4
25–30	0.1	2.3	0.0	0.0	0.0	2.5
30–40	8.8	18	3.5	0.0	0.0	30
>40	11	3.3	11	10	28	63
Total	20	27	15	10	28	100

Although tidal stream technology has the advantage of good temporal and spatial predictability of tides from hourly to monthly and yearly cycles, there is still significant resource variability between all the UK sites. These are currently identified by their tide phase differences. If the UK is to take advantage of its tidal stream resources it is essential that this combined variability be considered. As previously stated the Pentland region has over half the UK resource and thus will have significant influence to its electrical supply. Figure 2.10, gives some idea of the resource variability between four of the locations (BERR, 2008), ranging from 3.7% at the Mull of Galloway to a more desirable 15% around Alderney. The resource availability of the Severn is not shown in Figure 2.10 however estimates have been published on the variability for UK sites combined into regions (Carbon Trust, 2005). The report splits the UK into 5 resource regions such as The Channel Islands, Northern Islands, North West, Pentland and South West. The total energy yield from each of these sites is 3.017 TWh/y, 1.045 TWh/y, 2.033 TWh/y, 8.12 TWh/y and 1.229 TWh/y, respectively. For the South West, which includes four locations within the Bristol Channel, namely Barry, Foreland Point and South and North Lundy the total energy yield from these four locations is 712 GWh/y, representing around 58% of the total energy yield from the South West region and around 5% of the total UK tidal stream resource.

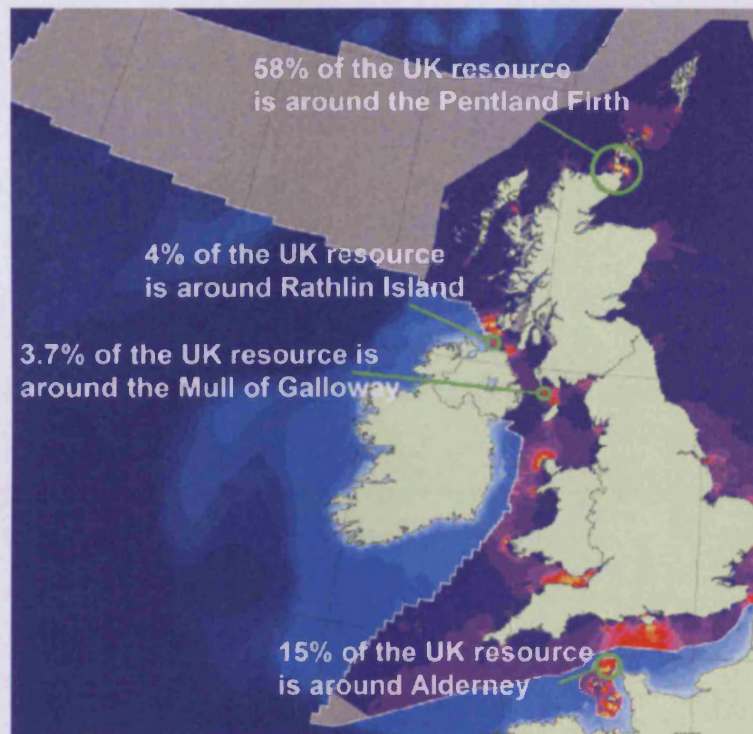


Figure 2.10: UK Tidal stream resource. Source: BERR¹, 2008.

This not only makes the Bristol Channel a viable energy source it goes beyond the direct requirement for energy extraction as it also has the potential to attenuate the variability in supply between the regions, specifically the large phase differences between the Pentland Firth and other resource locations.

Given the tidal stream resource data published by the DTI, the actual energy availability at an identified site is, however, limited due to local shipping routes, bathymetry and the upstream tidal velocity magnitude and profile. These features will have a major influence on the performance of individual turbines whether sited individually or in arrays. Moreover, wake interaction between turbines will further influence bathymetric positioning and turbine spacing. Although, this is extremely site specific it will have a significant effect on performance and, once fully developed, on the UK tidal stream resource estimate of 12 TWh/y. The location of the turbine through the water column can be influenced by local shipping requirements and or the local bathymetry within the vicinity of the turbine or turbine arrays. In the case where the turbine occupies a significant proportion of the water column the upstream velocity profile, depending on its nature, could have the potential to

introduce asymmetric loading across the turbine diameter, which not only affects the turbine's ability to extract energy effectively, it also can have a detrimental influence on structural components through mean stress/strain fatigue. Areas of main concern would be the blades, blade to hub connection and main drive components such as the driveshaft, bearings and seals.

Long term performance and reliability is a key issue if the technology is to be expanded to the implementation of arrays at all the potential UK sites. Since tidal stream technology is at such an early stage it is unclear what the actual nature of site specific resource is and or what the final availability for the UK will be. Early indications from prototypes, such as those previously discussed, indicate that the devices are meeting or exceeding the predicted energy capture (Kerr, 2006). Given that very little site-specific performance data is available for tidal stream devices, localised site specific data is still needed to understand the performance of a given turbine design, and how key operational parameters might change under varying conditions. In a detailed study on the implementation of tidal stream turbines within the Alderney races around the Channel Islands, Bahaj and Myers (2004) and Myers and Bahaj (2005) showed that with an appropriately positioned array of turbines an energy yield in excess of 7.4 TWh/yr could be realised, which was stated to be equivalent to 2 % of the UK requirements for the year 2000. It was also observed that although the energy resource was totally predictable, the power production was observed to be uneven. This latter point elucidates the complexity of individual sites as knowledge is increased on tidal patterns and the potential for down time or generation redundancy between sites. Further work on the effects of bathymetry and water column velocity profile and the time phase difference between sites is therefore required. Using the information gained from phase differences, bathymetry and velocity profiles a fundamental picture on performance characteristics of a given design can be gleaned. When compared to an idealised operational environment, such as during laboratory testing and mathematical modelling, the power extraction between site and theoretical models can be compared.

The potential to mitigate supply intermittency and generation redundancy was shown to be possible with careful choice of six phase-locked tidal stream power installations (Hardisty,

2007). The aforementioned research indicated that by installing devices in the Severn Estuary, Menai Straits, Mersey, Clyde, Tyne and Humber with power capacities of 45, 20, 40, 20, 55 and 25 MW, respectively, an overall rate of about 45 MW throughout the UK tidal cycle could be realised with the potential to stabilise the total supply. This though would require large portions of these locations to be dedicated to power generation, which could potentially cause major disruption to local shipping lanes. This is especially the case for the Severn Estuary as large cargo vessels are commonplace with vessel drafts up to 14 m (Auld, 2008). With such large drafts the operational depth of tidal stream devices would therefore be severely restricted to deeper depths. This however places the device in the lower boundary of the water column which could potentially exhibit high rates of shear.

Due to the velocity profile through the water column, it would be undesirable to locate a HATT at a depth whereby its swept area occupies a portion of the water column that equates to around 25 % of the overall depth (Bryden et al, 1998). However, if a stable electrical contribution to the UK supply is to be realised then some form of compromise would be required either in local shipping or the operational size and/or depth for HATT placement. If the latter option were to be considered then the performance of a HATT within the lower 25 % boundary would need to be investigated with an aim to establish its effects on key performance characteristics such as power extraction, torque and axial thrust loads. To achieve a true representation of this a site measured velocity profile would be required. Moreover, as given by Table 2.2 with 63 % of the total V_{msp} in depths > 40 m it maybe the case that modular arrays could potentially occupy the lower 25 % of the water column, placing the rotors in a high shear velocity field. This latter case will be discussed later in Chapter 9.

2.3: Energy extraction from tides

The principle of energy extraction from moving water is the same as that applied to air and energy extraction from wind. There are however fundamental differences with regard to density, compressibility and boundary conditions. The density of seawater is 1025 kg/m^3 , depending on parameters such as temperature and salinity, whereas air has a density of 1.225 kg/m^3 , again depending on temperature (Encyclopaedia Britannica, 1965). This

means that seawater has a density approximately 840 times that of air allowing a HATT to operate at much lower angular velocities but with higher axial thrust loading. Unlike a HATT application, HAWTs operate within the shear boundary of the Earth's atmosphere with no upper boundary affecting the near field velocity profile directly above the turbine. However, for a HATT the water surface has a direct effect on the depth velocity profile from factors such as surface wave height and wake to surface interaction.

In a detailed study on the energy yield potential from the Alderney Race in the Channel Islands Bahaj and Myers, (2004) also suggested that the lowest point of the swept area should not fall inside a depth band of 25% of the overall depth (h) if high levels of cyclic power generation and blade loading from the high shear rates were to be avoided. Based on nominal operating depths they suggest that the distance between the seabed and rotational centre of the hub should nominally be 50 % of the overall depth leaving around 7 m between the water surface and the top of the swept area and nominally 8 m between the seabed and the lower swept area. However, as the technology is expanded into regions where restrictions from local shipping apply this optimal depth may be considerably restricted. As discussed in 2.2.4 the variability of supply from tidal phase differences between regions sites such as the Severn Estuary would play a vital role in the balance of this variability. However, due to the existence of major ports such as Newport and Bristol there is a large number of shipping lanes which could pass through potential energy extraction sites requiring the turbine to be positioned closer to the seabed. With the requirement for a better understanding of the operational conditions and the ensuing performance of the HATT, both structurally and hydrodynamically, it is essential to build a better picture of the key performance characteristics of the design.

2.3.1: Number of turbine blades

The optimum number of blades is dependent on both economics and the rate of energy increase with increasing blade count (Hau, 2006). Figure 2.11 shows power coefficient (C_p) curves to the base of TSR with an increasing number of rotor blades from 1 to 4 for a wind turbine. What is evident in Figure 2.11 is that the peak power extraction is tending towards an asymptotic value of $C_p = 0.48$ with 4 blades reducing economic gain verses

additional blade numbers. Moreover, as the turbine diameter increases the operational range of the device is also reduced for a rated wind speed. Along with higher noise generation due to the higher rotational speeds the asymmetric visual aspect of both the single and two bladed wind turbine designs has made them less popular with proponents of the 3 bladed design (Cotrell, 2002). However, this was mainly the case for the more visual HAWT. Although it is ultimately dependent on construction design and overall numbers, as the number of blades is increased the cost associated with manufacture also increases, however, as seen this is accompanied by decreasing returns in energy extraction. It is also stated by Hau, 2006 that the increase in power extraction between 1 and 2 bladed turbines is around 10 % and 3 % to 4 % between a 2 and 3 blade design. However, between 3 and 4 blades this drops to around a 1 % to 2 % increase in the power extracted.

As previously discussed, although there are differences in the medium in which wind and tidal stream turbines operate they share the same fundamental energy extraction physics. Unlike wind turbines, tidal stream turbines are not subject to the same visual constraints of onshore wind turbines, although noise generation may still be an issue for marine life (DTI, 2007). The 'acceptable' level of noise generation between 2 and 3 bladed marine turbines will therefore be a result of theoretical prediction and experimental measurement both laboratorial and from on site full scale prototypes. It is likely that, much like onshore wind turbines, the number of blades for a marine turbine will be influenced by noise, power extraction efficiencies and inevitably the economics of these constraints.

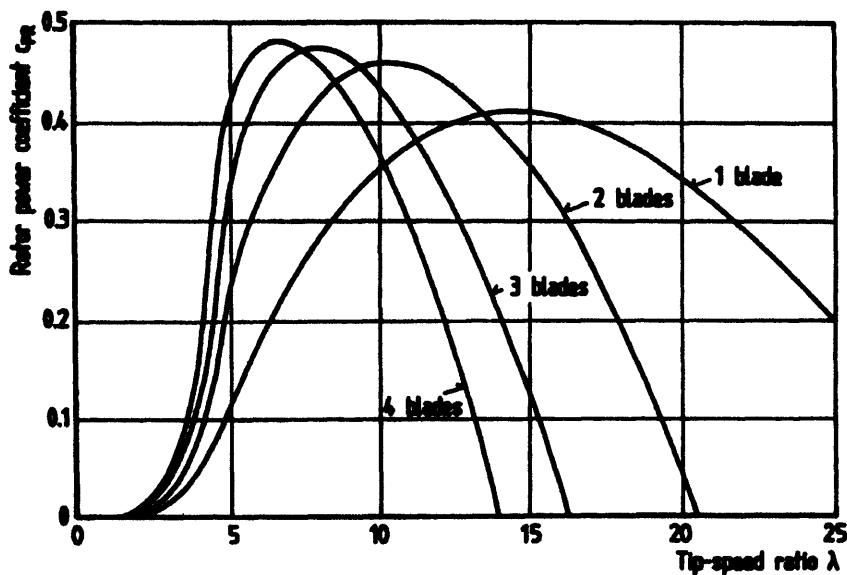


Figure 2.11: Power coefficient curves for wind turbines with increasing blade numbers.

Source: Hau, 2006

With very limited information from full scale prototype devices, data relating to the potential interaction between tidal turbine blades and marine animals is at best speculative. However, with time and technological dissemination some gaps in this information may be covered with the SeaGen project of Strangford Lough. MCT, the installers of the two rotor design, shown in Figure 2.9 (b), have undertaken a comprehensive environmental monitoring programme managed by a leading environmental consultancy, Royal Haskoning who are also working in partnership with Queen's University Belfast and the St Andrews University Sea Mammals Research Unit (MCT, 2008). The programme was also overseen by an independent body, chaired by David Erwin a former Chief Executive of the Ulster Wildlife Trust (Abuelsamid, 2007).

2.3.2: Scaled prototype HATT testing

Attachment to moving vessels and the placement in fast flowing rivers, re-circulating water flumes and towing tanks include some of the methodologies that have been used for the testing of small to medium scale HATTs. During the validation of their Permanent Magnet Generator (PMG) prototype HATT, Swansea University used a series of towed experiments via the use of their research vessel R.V. Noctiluca (Orme and Masters., 2004). The hydrodynamic and electrical efficiencies of the 1 m diameter, 3 bladed HATT, were tested

over a range of flow speeds and varying angular velocities. The 12 m long twin-hulled shallow draft vessel provided enough spacing between its hulls to allow a channel of water clear of wake and propeller disturbances. The 1 m diameter turbine was designed to operate in flows between 1.8 m/s and 2.83 m/s with power and speed ratings of 1.5kW and 200 rpm, respectively. Figure 2.12 gives C_p to the base of TSR for mechanically loaded and electrically loaded runs. The results clearly show a peak C_p of around 0.45 at a TSR of around 3.8.

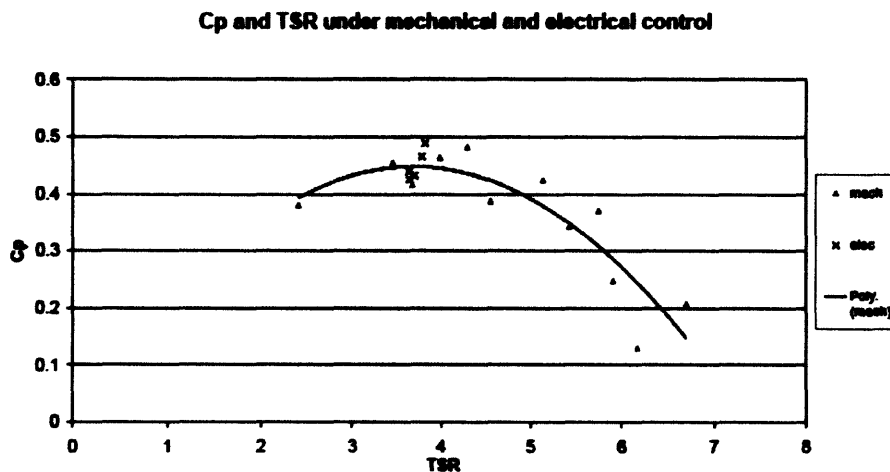


Figure 2.12: Experimental variation of power coefficient with TSR.
Source: (Orme and Masters, 2004)

Also given in the same study was the mechanical shaft (P_s) and electrical power (P_E) output of the turbine with varying flow velocity, Figure 2.13. Orme and Masters, (2004) also give an estimate of the turbine output using the Blade Element Momentum (BEM) theory with an initial C_p of 0.5. One interesting feature of this study was the final electrical power generation efficiency (coefficient) C_E which included friction and generation losses. Orme and Masters showed that due to losses a C_E of 0.24 was finally realised.

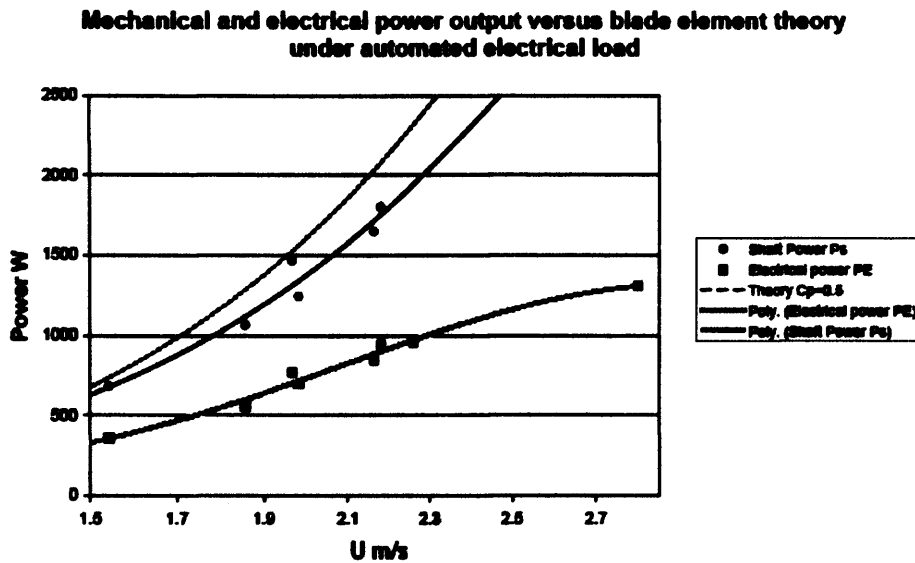


Figure 2.13: Power output with respect to flow velocity.
Source: (Orme and Masters, 2004)

In 2002 Tidal Hydraulic Generators Ltd (THGL) carried out trials on a 4 bladed 5.5 m diameter prototype turbine on the Cleddau River near Milford Haven in Pembrokeshire, UK, Figure 2.14, with a flow speed of 0.9 m/s. From the physical tests the peak performance of the turbine was found by varying its angular velocity via mechanical loading. A peak C_p of approximately 0.3 was obtained at a TSR of 3 from the river trials. No electrical loading was included in the report. However, to aid future research and development into HATT design, the experimental results of this study were later correlated with data generated from a CFD model of the same turbine (Egarr et al, 2004).



Figure 2.14: River trials for a 4 bladed 5.5m turbine with a flow speed of 0.9 m/s
Source: Egarr et al, 2004

This work was also extended to include CFD modelling of a 4 bladed turbine while using the same blade design parameters. The experimental power curve combined with that of the CFD model show similar trends and peak extraction limit, Figure 2.15. There is however a slight shift in the angular velocity at which peak C_p occurs. A peak C_p of 0.31 was obtained from the CFD model at a TSR of approximately 2.3.

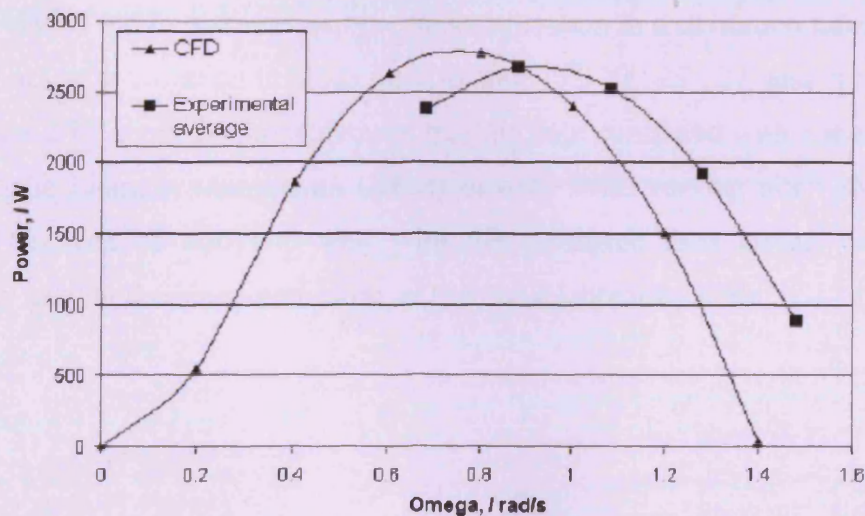


Figure 2.15: Comparison of CFD and experimental power for a 5.5 m diameter turbine in a 0.9 m/s tidal flow.

Source: (Egarr, et al., 2004)

While river and towing tests can give valuable insight to the performance of such devices there is little control over the operational environment. The accuracy of measurement is, to varying orders of magnitude, affected by riverbed topography, upstream turbulence intensity, interference from the proximity of the vessel hull and velocity profile through the water column. However, via the use of controlled flume testing, these issues can be circumvented forming a better base from which correlations can be made with mathematical modelling techniques, such as BEM theory and CFD.

2.3.3: Scaled flume testing

In an attempt to overcome the phenomena discussed in Section 2.3.2, a series of controlled experiments using re-circulating water flumes and towing tanks have been carried out by Myers and Bahaj, (2005) and Bahaj et al, (2007). The results of these studies have produced reliable data on the physical performance of such devices and a valuable tool for the quantitative evaluation of data obtained via theoretical methods such as CFD and BEM theory. Along with the key performance characteristics such as the power coefficient (C_p) and axial thrust coefficient (C_T) they also investigated stall characteristics, changes in Reynolds number and the possible occurrence of cavitation, which typically occurs towards the blade tip. Figure 2.16 (a) and (b) gives C_p and C_T values calculated from measured data for a 3 bladed 0.8 m diameter turbine under operation in a cavitation tunnel, also given are best fit lines with variation in blade pitch angles, 15° , 20° , 25° , 27° and 30° (Batten et al, 2006). Figure 2.17 gives the same data set but this time compared with a theoretical study using the Blade Element Momentum (BEM) theory. With varying pitch angle the BEM theory can be seen to correlate well with the measured data giving validity to the methodology used in the characterisation, at least on a laboratory scale.

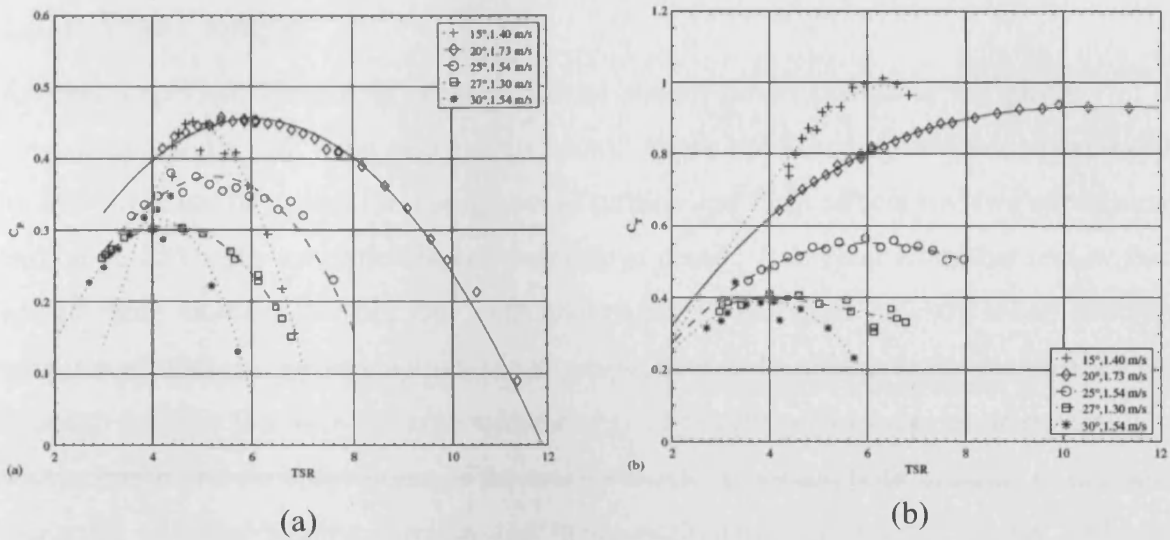


Figure 2.16: (a) Power coefficient (C_p) and (b) axial thrust coefficient (C_T) calculated from measurement. Source: Batten, et al., 2006

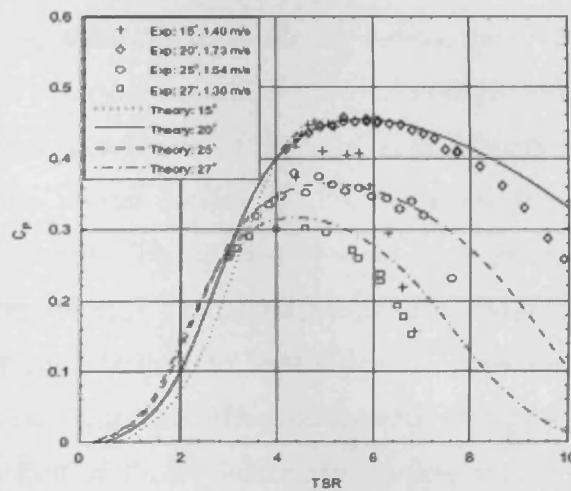


Figure 2.17: Correlation between measured and calculated power coefficient (C_p) curves. Source: Batten, 2008

Although the data captured are design-specific and cannot be directly transferred to a different design, they do form a valuable reference source when evaluating key performance criteria for a different HATT design. This type of work is invaluable to the evaluation of these devices as it is generally the case that much of the data associated with full scale prototypes are commercially sensitive and therefore unpublished.

2.3.4: Wake length

Another important feature of wind and tidal stream devices alike is the physics of the downstream wake following energy extraction. Work published by Vermeer et al, (2003) on the formation of wakes for a single wind turbine and farm effects reviews experimental and numerical wake formation in comprehensive detail. It is clear from this review that a considerable amount of work has been undertaken in the wind industry when compared with that of tidal energy production, ranging from near wake effects to the far stream wake. It is also the case that when a large number of HATTs are positioned in close proximity the width, length and flow dynamics of the wake become important both in terms of the power extraction of neighbouring devices and their combined effect on the seabed and water surface. To the author's knowledge no results have, to date, been published on wake formation of a full scale HATT during operation and therefore can at best be modelled. The study of an ensuing wake can be divided into three major areas. The first of these is in the near wake boundary very close to the blades of a single turbine. Here the formation of the vortices and surface attachment of the flow is of primary importance. The second is how the wake develops further downstream from a single HATT and how it may interact with the seabed and surface. The third is how the wake generated from a primary row of turbines interacts with devices that are adjacent and those that are downstream of the primary row. When considering the installation of large numbers of devices this latter interaction could have a significant effect on the total energy yield as shown by Bahaj and Myers, (2004). The first of these, near wake studies, are limited to the flow within the vicinity of the HATT blades and are subject to their design and operational characteristics such as blade pitch and angle and degree of twist. Modelling the near surface flow involves high mesh densities to predict turbulence levels from the mainstream flow to the laminar sub-layers. Fabrice et al, (2008) using an in-house developed code, studied the near wake vortices generated from each blade of a HATT and the resulting disturbance on the seabed and water surface. Figure 2.18 (a) shows the vortices leaving each turbine surface and passing downstream with the main flow field. Figure 2.18 (b) shows the resulting x-mean or longitudinal mean velocity profiles for different downstream locations across the central portion of the turbine wake (x-mean). The larger velocity deficit can be seen to occur in the near wake region which then decreases towards the main upstream velocity. The central

core of the wake at $Z/R = 0$ represents the rotational axis of the turbine. Along this line a reduction in the velocity deficit can be seen towards the near wake ($x/R=0.5$). Fabrice et al, (2008) suggest that this feature maybe over estimated due to the lack of a hub in the model and the resulting flow restriction.

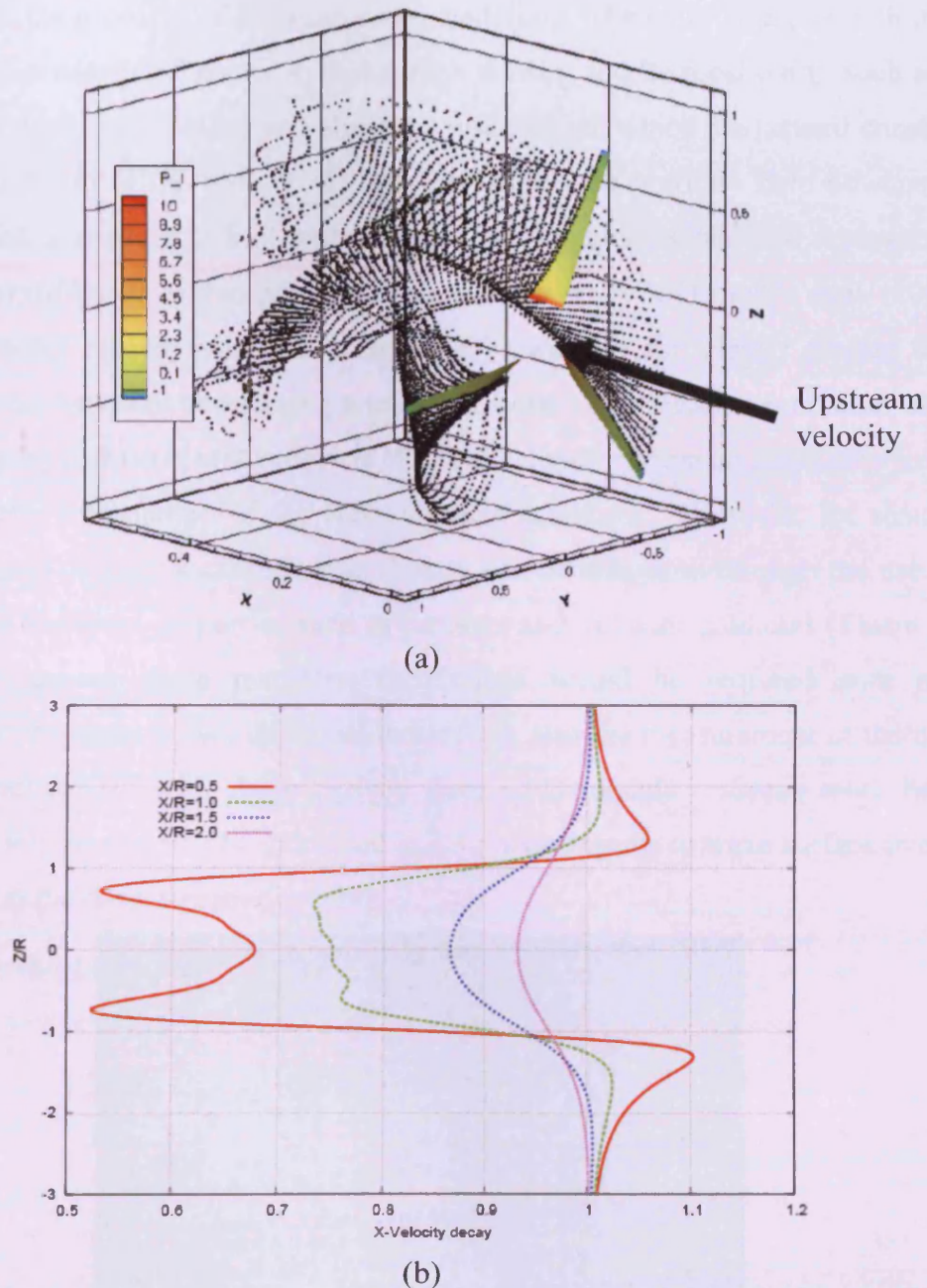


Figure 2.18: Predicted downstream vortex development (a) and downstream x-mean velocity profiles (m/s) (b) as presented by Fabrice et al, 2008

The computational model as applied to a tidal stream turbine however is still under development and awaiting correlation with measurements made in a re-circulating water flume. The general shape of the downstream wake however is a useful reference source for downstream wakes generated in this thesis. McCombes et al, (2008) have also investigated an approach to the problem of dynamic wake modelling. The main issue, as with the CFD models to be discussed in Chapter 4, is the mesh density and its focal point, such as in the region around the turbine blades and along the wake length which can extend considerable distance downstream of the turbine. Figure 2.19 shows the vorticity field downstream of the rotors which according to McCombes et al, (2008) is quickly smeared across the mesh due to the poor diffusion of transport properties. As stated by McCombes et al, (2008) this poses a dichotomy on where to cluster the cells in order to sufficiently capture the flow physics, specifically when considering a temporal flow. To overcome problems with poor transport property diffusion McCombes et al, (2008) suggested that an alternative lies in the vorticity-velocity formulation of the Navier-Stokes equations. However, for steady-state analysis the issue of high localised mesh density can be mitigated through the use of grid adaption using transport properties such as pressure and velocity gradients (Fluent, 2006). Ultimately to answer these questions correlations would be required with physical measurements of torque, power and axial thrust load, also the measurement of the near and far wake velocity field with those derived from CFD models. Some work has been undertaken in this area as will be discussed in 2.3.5 with regards to wake surface interaction and its length in the downstream direction.

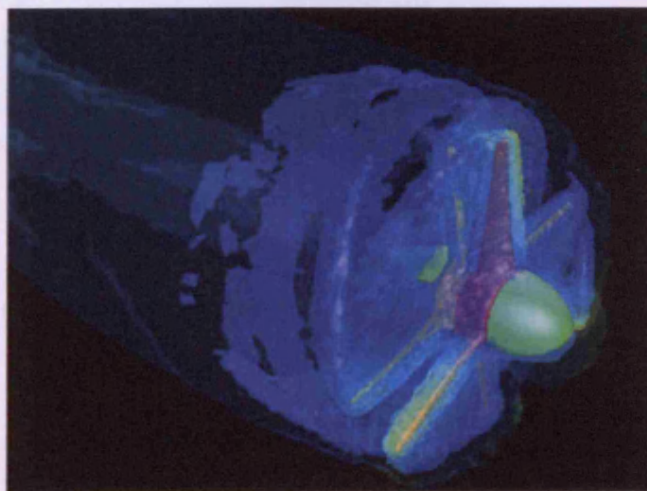


Figure 2.19: Poor diffusion of vorticity in the downstream wake of the rotor blades. Source: McCombes et al, 2008.

2.3.5: Surface interaction

Energy extraction using tidal stream technology is now at the prototype phase with full scale devices in operation. Although there are plans, as discussed, no full scale turbine arrays or farms are currently in operation even at the prototype phase. Although the marine application shares similarities with wind farm technology, fundamental differences from the water surface boundary, velocity profile, density and incompressibility of water limit the reciprocity of knowledge and data between the two operational environments. In comparison to tidal stream turbines, wind turbines only subtract energy from a very small proportion of the total kinetic flux from the earth's surface upwards. For tidal stream turbines the flexible upper surface boundary limits the total energy flux between it and the rigid seabed. The turbine therefore has the potential to occupy a large proportion of the water column and the total energy flux (Sun et al, 2008). Given the fact that a turbine could occupy a large portion of the water column, Sun et al, (2008) used CFD with an air to water surface model to study an energy extraction zone (porous medium) in 2D and 3D Volume Of Fluid (VOF) models, available in FLUENT™. Sun et al, (2008) used these models to elucidate changes in surface elevation introduced by the obstruction or porous medium located at a depth of 0.5 m from the extraction zone to the water surface. Figure 2.20 (a) and (b) show the theoretical free surface elevation and velocity magnitude with energy absorption. It is clear that the energy extraction causes the water surface level to rise upstream of the extraction zone with a sudden decrease immediately downstream, which is then followed by a rapid rise. This downstream surface level however remains below the level upstream, at least within the boundary of the model. The downstream surface feature resembles that of a hydraulic jump typically seen at the base of a water weir where relative to the waterbed, a stationary wave exists (Massey, 1989). This feature extends to around 4 to 5 time the height of the energy extraction zone downstream. Combined with vortex motion this feature could have a significant effect on devices positioned further downstream.

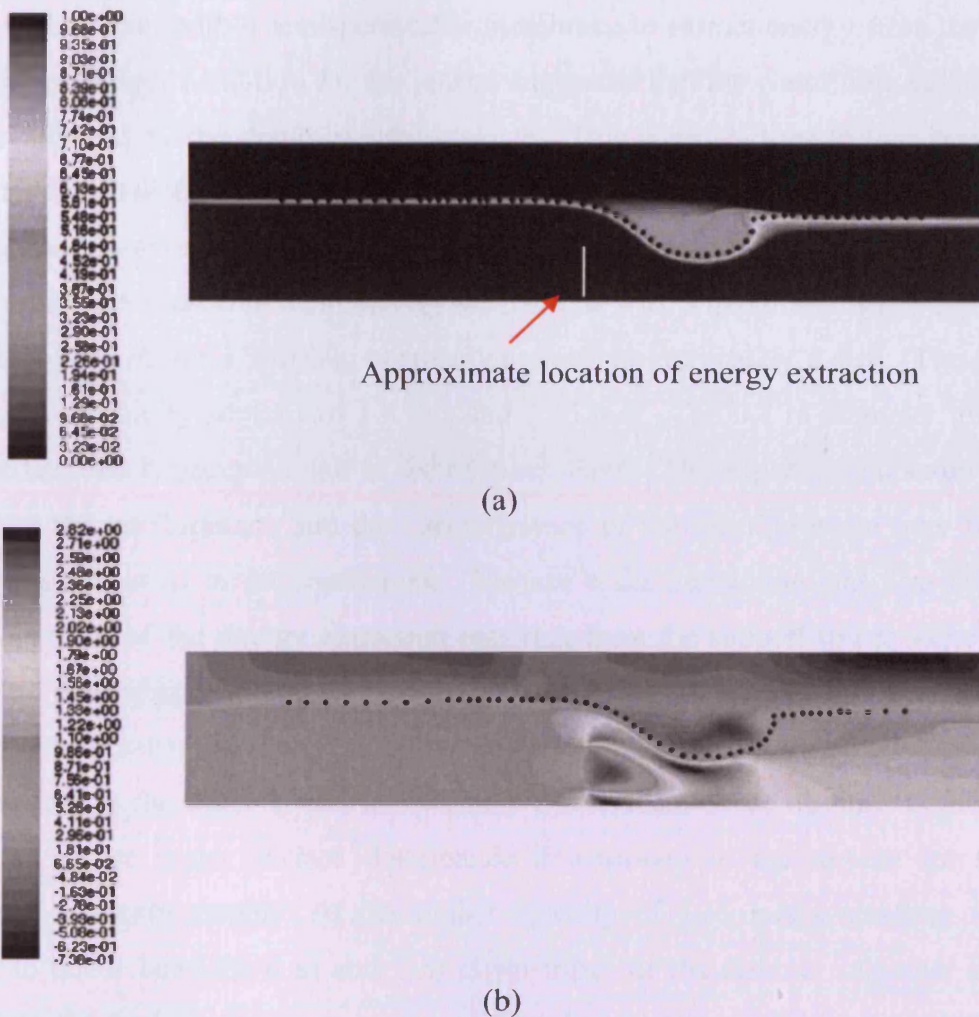


Figure 2.20: Up and downstream surface interaction with energy extraction using 2D VOF model (a) Normalised free surface elevation (b) Contours of velocity magnitude (m/s).

Source: Sun et al, 2008

Myers et al, (2008) studied the wake generated from porous discs placed at two different depths at two different flume locations. Due to the depth that the porous discs were placed at, interaction with the water surface was limited thereby mitigating the upstream and downstream effects discussed in Section 2.3.5. The work of Myers et al, (2008) provided an insight into the flow characteristics around the swept area of a turbine in a constrained flow. This is of particular interest in relation to the work carried out in this thesis, particularly as the distance between the device and the lower boundary is reduced. Using plug flow, Myers et al, (2008) showed that the rate of wake recovery was increased the closer the energy extracting disc was placed to the bed of the water flume. Contrary to the findings of Myers, et al, (2008) an earlier study by MacLeod et al, (2002) using a 3D

channel CFD model with a semi-permeable membrane to extract energy from the flow and the no-slip boundary condition for the seabed suggested that the centre line velocity deficit is barely affected by the depth of submergence. This contradictory feature however was not included in their final conclusions for the research. Energy extraction and wake effects have also been studied by Myers and Bahaj, (2007) using a 0.4 m diameter 1:30th scale marine turbine positioned in a circulating water flume with a maximum water depth of 0.84 m a width of 1.4 m and a working channel length of approximately 4.4 m. The tests were set using two velocity settings of 1.8 m/s and 2.35 m/s. The 0.4 m diameter turbine was positioned so that it occupied half of the channel depth. The experimental setup was used to measure the performance and the characteristics of the ensuing wake over a range of flow speeds and axial thrust coefficients. Surface wake interaction was also included up and downstream of the energy extraction resulting from the support tower alone and with the turbine extracting energy. As in the CFD study performed by Sun et al, (2007) the measurements showed increases in the water surface levels upstream of the turbine with a sharp decrease in the water height immediately downstream of the turbine. Figure 2.21 (a) and (b) show the water surface disturbance downstream of the turbine for the water velocities previously stated. At the higher velocity of 2.35 m/s a standing wave was reported to occur between 6 m and 7 m downstream of the turbine. Another interesting feature was the surface elevation at around 5 m downstream with a water velocity of 1.8 m/s. This feature was reported to occur as the wake from the energy extraction expanded and contacted the water surface, thereby retarding the main local axial velocity and causing a standing wave or hydraulic jump to occur. At greater depths this could impact the downstream performance of the HATT as there is no water surface to air interaction.

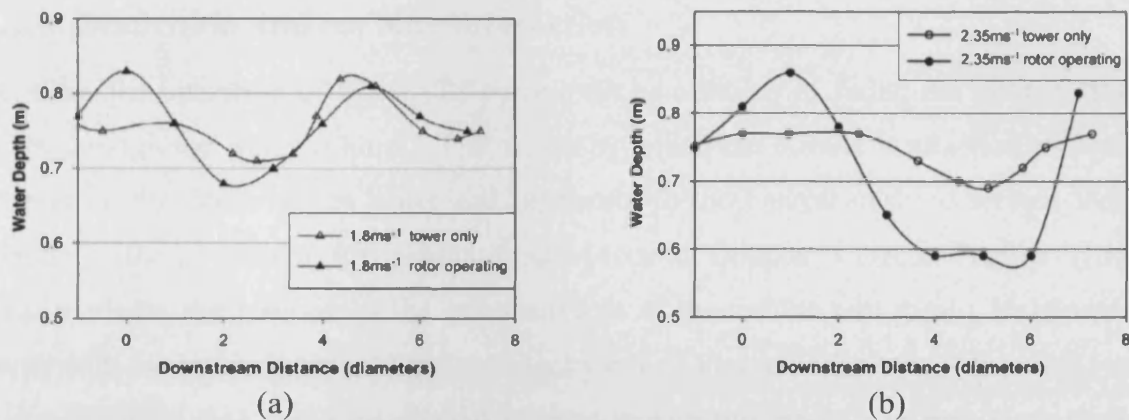


Figure 2.21: Measured water surface elevation for 1.8 m/s (a) and 2.35 m/s (b) flow velocity. Source: Myers and Bahaj, 2007

Therefore phenomena such as seabed proximity, wake interaction between marine devices, the water surface and its downstream velocity recovery rate is limited to data derived from laboratory testing and theoretical modelling (MacLeod et al, 2002). In an attempt to capture effects associated with wake phenomena most of the modelling and laboratory testing involved the use of porous meshed discs and small prototype turbines. As previously stated full scale prototype tidal stream devices have been placed in depths of around 40 m with HATT diameters approaching 20 m. Under such circumstances it is likely that some form of turbine interaction with the water surface will occur. It is hypothesised that with the introduction of arrays the combined wake effect of a say 100 devices could make a significant contribution to the instability of the water surface.

To mitigate surface interaction all the studies carried out in this thesis are either applied to a 35 m (site) or 50 m (reference) water depth giving Froude (Fr) numbers of 0.17 and 0.14 with a peak tidal velocity of 3.1 m/s. In both cases the turbine is located in relatively deep water with a tip to water surface distances of 20 m for both the site and reference domain, therefore surface interaction was assumed to be negligible.

Each study was also concerned only with the comparison between the wake developed from a single HATT within a high shear rate velocity profile near to the seabed with an ideal plug flow with minimal boundary interference. The only perceived interaction was therefore with the local bathymetry and the seabed mounting structure.

2.3.6: Stanchion and turbine interaction

To allow the operation of the HATT there must be a means of fixing the turbine at some depth through the water column. The means by which the turbine is attached will greatly depend on the depth of the water and proximity to the nearest onshore service location (Snodin, 2001). Given the results from Acoustic Doppler Current Profiler (ADCP) measurements, the position of the rotational axis of the turbine will ideally be placed at a depth with minimum shear and higher velocity band. Figure 2.22 shows 4 possible seabed fixing methods that could be applied to tidal stream turbines. The first three methods employ a gravity base, a mono-pile and piled jacket driven into the seabed. The fourth is floated and tethered to the seabed.

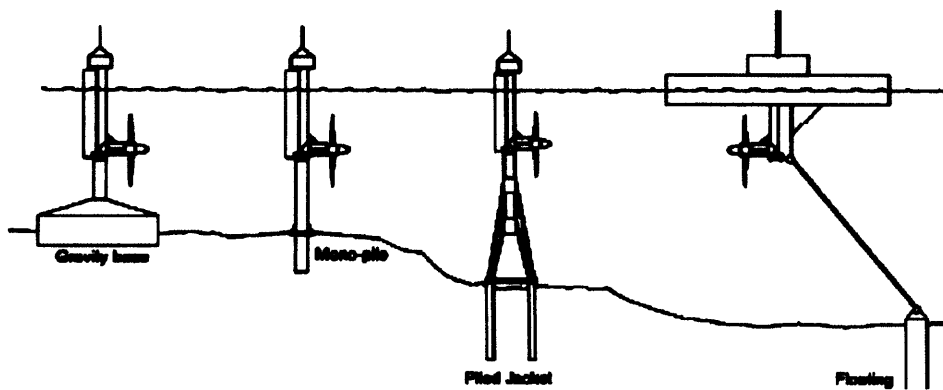


Figure 2.22: Support structures for marine current turbines. Source: Snodin, 2001

The first three seabed fixing methods are suited to depth between 30 m and 40 m. At depths greater than 50 m the application of a stanchion as a seabed fixing method becomes more difficult (Fraenkel, 2004). Another fixing method is via the last of those discussed, the buoyant tethered system. As suggested by Clarke et al, (2008) this system has the advantage of positioning the device higher in the water column without introducing excessive turning moments such as those imposed on a pile or stanchion fixed into the seabed. The tethered device could be attached to the seabed using sinks and floatation devices at the water surface. Alternatively ballast could be applied to the HATT assembly with neutral buoyancy allowing the assembly to float at a predefined depth. It has been suggested that using this type of methodology would have a number of potential advantages over the more conventional stanchion/pile design. One such advantage is the elimination of the torque moment transmitted to the support structure thereby reducing the height from the

seabed at which the device could potentially operate (Clarke et al, 2008). However, the method used to tether a floating HATT will need to limit the amount of yaw induced from reactive torque generated by the turbine blades during power extraction. In an attempt to overcome this problem Clarke et al, (2006) proposed the use of a contra-rotating turbine design where the reactive torque of the rear turbine corrects the yaw, thereby returning alignment and rectilinear flow. It also allows a simple and economic mooring system for deep water applications. A further advantage of the system was the reduction of stable vortex elements in the wake of the HATT. This type of feature will be seen later in Chapter 9 and may have implications when considering the spacing of an array of tethered HATTs. Some of the problems associated with tethered systems were also covered by Snodin, (2001) who stated that a number of major difficulties arise when dealing with forces induced by wave motion during storm surges, not only for the turbine assembly itself but also for the transmission of power to the shore via the power cables. Unlike for seabed fixed devices the power cables would have to be flexible to account for the induced movements.

When considering an array of HATTs the comparative costs between tethered and piled fixing methods were summarised in a 2001 study undertaken to investigate the installation of a 3 m to 5 m diameter HATT in 20 m water depth at fixed navigation marks. Capital costs of £400k and £600k for a tethered and fixed installation were given, respectively, (DTI, 2001). From information reported by Previsic, (2006) and summarised by Clarke et al, (2007), on the estimated breakdown of cost for a farm of pile-mounted tidal turbines, they showed that 33% of the estimated cost was in the structural steel elements alone and a further 16% for the turbine installation. Apart from the power conversion system at 35% the stanchion mounting system made up a considerable proportion of the overall cost, making an economic case for free floating systems that can be tethered to the seabed. However, it is likely that for the early development stages of the technology the use of pile driven stanchions will remain for depths between 20 m and 40 m. Black & Veatch, (2005) suggested that “UK technology development should be concentrated on devices that are suitable for sites of depth >40 m, with the highest focus on devices that are suitable for deep sites with high velocities”. As given in Table 2.2, 63 % of the total resource is at

depths > 40 m with 28 % of V_{msp} currents > 5.5m/s. However, the position of the device through the water column will still depend on the accompanying velocity profiles. As stated pile driven stanchions would not be suitable at these depths due to large turning moments as the turbine is positioned further up the water column. Companies such as Tidal Generation Ltd (TGL, n.d) are already considering designs that operate at greater depths. These devices would have to be either floated and tethered at some defined depth or fixed closer to the seabed using a modular frame. Given the depth of operation this latter option could potentially place the rotor in a high velocity shear rate band. However, given the high current velocities at greater depths a case could be made to study rotor performance and blade loading at these depths and shear rates. By taking a peak V_{msp} of 5.5 m/s and applying the $1/7^{th}$ power law at a greater depth from the seabed, say comparable with that of a turbine positioned at mid depth of a 40 m location. At the latter depth of 40 m the peak velocities are of the order 3.5 m/s. It can be shown that the velocity at the rotational centre of a 60 m (total depth) the velocity is still greater than that for the 40 m depth, e.g: At a depth of 60 m and a $V_{msp} = 5.5$ m/s the velocity at rotational depth of 40 m gives:

$$V_{deep} = 5.5 \left[\frac{40}{60} \right]^{1/7} = 4.7 \text{ m/s}$$

At a depth of 40 m and a $V_{msp} = 3.5$ m/s the velocity a rotational depth of 20 m gives:

$$V_{middepth} = 3.5 \left[\frac{20}{40} \right]^{1/7} = 3.2 \text{ m/s}$$

Figure 2.23 shows the velocity profiles at the 60 m and 40 m depths with the location of the rotational axis of a 20 m turbine positioned 20 m above the seabed. The 40 m depth scenario matches the approximate conditions of such devices as those discussed earlier in 2.2.3 such as the SeaGen and SeaFlow projects.

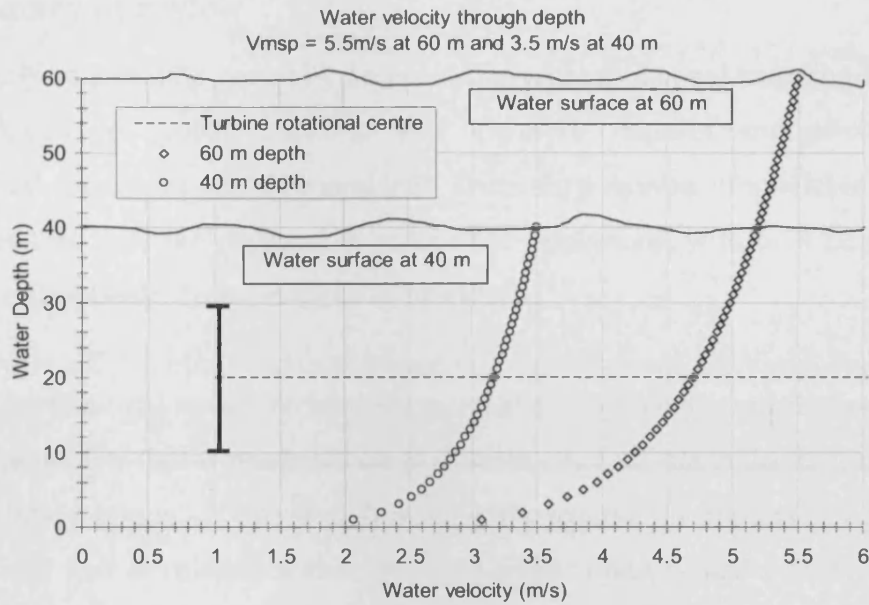


Figure 2.23: Velocity attenuation with depth using $1/7^{\text{th}}$ law

If operational parameters are understood at these depths, power extraction under high velocity shear within the lower 25 % of the velocity profile still has a significant contribution to make to the overall resource. A number of developers such as OpenHydro (see Figure 2.9 (d)) have proposed deep water designs that involve the use of modular frames consisting of a single or an array of turbines that could be mounted on the ocean floor. However, with velocity rates approaching 4.7 m/s at depths within the lower 25% of the velocity profile, issues associated with axial thrust loads are of greater importance. Due to the inaccessibility at depths greater than 50 m, maintenance procedures that address issues such as greater axial loading are further complicated. In the case of an array of devices the combined axial loads from the turbines and frame could be significant.

Although Black & Veatch, (2005) were referring to power extraction higher in the water column when they stated that “There appears to be little merit in focusing UK technology development on devices that are only suitable for sites of depth $<30\text{m}$ ” situations will arise that place seabed fixed designs within the lower 25% boundary.

2.4: Summary of review

If not the only source, it is generally accepted that anthropological warming is a factor that has contributed to global warming and therefore requires mitigation if extreme environmental conditions are to be avoided. There are a number of available and emerging technologies that have the potential to reduce CO₂ emissions, with tidal range and stream energy extraction being the main focus of this thesis.

It would seem that tidal stream technology can make a significant contribution to electricity generation in the UK that is predictable and without large offsets in demand and supply due to in phase tidal patterns. It was also shown that the technology applied to HATTs shares a great deal with that developed within the wind power industry and that due to the higher water density the diameter of tidal stream turbines can be made smaller. As a result of the accompanied higher axial loads this also requires the rotor design to be more robust than that of an equivalent wind turbine design. The number of blades included in a HATT design also shares similarities with that of HAWTs, in that the energy extraction is asymptotic with increasing blade number, whilst the associated costs increase. While there is no visual impact on the local vista from HATTs (above the water surface) their operation shares acoustic similarities with HAWTs which have the potential to affect marine life. Finally, given the large tidal stream resource at greater depths a case exists for the operation of HATTs within the lower 25% velocity profile. At depths > 50 m a better understanding of the power extraction and structural performance of the design is critical if maintenance schedules are to be minimised.

3: Literature review – modelling and ADCP measurement techniques

Along with measured data derived from flume and towing tank tests, as previously discussed, mathematical modelling methods can be used to study the near and far field hydrodynamics of a HATT. It is the purpose of this chapter to give a brief outline of the methodologies used in these procedures and as they are used within this thesis

3.1: Blade Element Momentum (BEM) Theory

A common methodology used in aerodynamic and hydrodynamic simulation of blade design and performance optimisation is the BEM theory. BEM uses a combination of momentum theory applied to an annular stream tube along with the lift and drag coefficients generated along the blade profile. The methodology has the advantage of being simple and easy to understand when compared to more sophisticated analytical methods such as CFD (Ingram, 2005). The BEM equations used in the methodology cannot be directly solved and therefore an iterative procedure is required, for example, starting with an initial guess and subsequent forward substitution of the variables is one methodology typically employed. With regard to wind turbines the subject is covered in great detail by Burton et al, (2001). For a performance based study using the BEM theory the power coefficient (C_p) can be estimated using an iterative approach to solve Equations 3.1 through to 3.5 at a number of (N) divisions along the radial length of the blade. The axial induction factor (a) and rotational induction factor (a') can be calculated from Equations 3.1 and 3.2, respectively.

$$a = \sigma' \frac{C_L \sin \beta + C_D \cos \beta}{4\psi \cos^2 \beta} (1 - a) \quad (3.1)$$

$$a' = \sigma' \frac{C_L \cos \beta - C_D \sin \beta}{4(\text{TSR})_r \psi \cos^2 \beta} (1 - a) \quad (3.2)$$

Where σ' in Equations 3.1 and 3.2 is the local solidity factor $\frac{Bc}{2\pi r}$ with B = number of blades and c the local chord length. $(\text{TSR})_r$ is the local tip speed ratio and ψ the tip loss factor.

With varying tangential velocity the relative flow angle (β) along the blade radius can be calculated using Equation 3.3.

$$\tan \beta = \frac{(\text{TSR})_r (1 + a')}{(1 - a)} \quad (3.3)$$

Finding the optimum blade pitch angle, using FluentTM, required a significant amount of time to re-mesh the individual models. Therefore, the BEM model was used to establish a first order approximation for the optimum blade pitch angle. To further simplify the BEM model, the drag coefficient (CD) and tip loss factor (ψ) were at all times set to 0 and 1, respectively, resulting in a reduced version of Equations 3.1. It was noted that this assumption would affect the resulting power extraction coefficient. However, the same procedure was used by Ingram (2005) with an alternative design. Equation 3.4 gives the axial induction factor (a) as used for the initial study.

$$a = \sigma' \frac{CL \sin \beta}{4 \cos^2 \beta} (1 - a) \quad (3.4)$$

Equation 3.2 gives the rotational induction factor (a') with CD and ψ included. As with Equation 3.4 the variables CD and ψ were neglected by equating them to 0 and 1, Equation 3.5.

$$a' = \sigma' \frac{CL \cos \beta}{4(\text{TSR})_r \cos^2 \beta} (1 - a) \quad (3.5)$$

Since the angle of incidence or attack (α) is the difference between the local blade pitch (γ) at radius (r) and the relative flow angle (β), CL can then be estimated from the lift and drag characteristics of the blade. Given this data the BEM theory can be used as a blade design tool or for the performance evaluation of a given design.

3.2: Computational Fluid Dynamics (CFD)

A powerful tool that can be used to numerically analyse the HATT's performance is through the use of discretisation methods such as CFD, where the theory surrounding

the methodology is very well established enabling, if required, the development of bespoke code. However, there are many commercially available codes that have undergone rigorous empirical testing and evaluation both academically and through industrial application. This has the advantage of saving time and the cost associated with the development of personalised software codes. For all the work presented within this thesis the CFD software package FLUENT™ was used. FLUENT™ uses the finite-volume method to solve the governing equations for a fluid flow field with predefined or user defined material properties for 2D and 3D domains. It also allows the combined use of various physical models such as those relating to turbulence, cell motion and free surface interaction (Fluent, 2006). A number of turbulence models are also available in FLUENT™ V 6.2.3 ranging between One-Equation Models (OEM) and Large-Eddy Simulation (LES) where the computational cost per iteration also increases along with the complexity of the viscous model used. When using the physical geometry of a HATT blade, the ability to apply cell motion is fundamental to the calculation of energy extracted from the moving fluid as the apparent flow angle (β) is related to the rotational velocity at a given radius (r). However, the use of a physical geometry can considerably increase computational time due to increased cell density toward the surface boundaries of the structure (Fluent, 2006). With the use of Reynolds Averaged Navier-Stokes (RANS) equations, turbulence models can be used to close the governing equations within FLUENT™ greatly reducing solution convergence time when compared to extreme methods such as DNS. FLUENT™ gives the option to use a range of viscous models that fall under the RANS category. These include the one equation Spalart-Allmaras model and two equation models such as the Standard k - ϵ , RNG k - ϵ , Realizable k - ϵ and Standard k - ω . Towards the more computationally expensive end of the RANS equations are the V2F and Reynolds-Stress models, above these are methods such as the Detached Eddy and Large-Eddy Simulation. As previously stated, due to the large number of cells used in the CFD models the RANS equations are computationally economic and therefore the following discussion will be limited to presenting these equations in general form and to outline their meaning along with a basic introduction to the governing equations. The Spalart-Allmaras model is not covered here, its inclusion in later correlations was a means for comparison with the RANS and RSM models and their use of near wall functions. As the Spalart-Allmaras model does not use this type of near wall treatment its ability to model turbine

performance would be limited by the mesh density near to the blades' surfaces. This however may prove to be an economic approach. Detailed and complete derivation of the governing equations discussed here can be found in the literature including Versteeg and Malalaseker, (1995).

3.2.1: RANS viscous models

The instantaneous flow can be used to extract the mean (U_i) flow properties via the use of ensemble averaging such that:

$$U_i(\bar{x}, t) = \lim_{N \rightarrow \infty} \frac{1}{N} \sum_{n=1}^{N_e} u_i^{(n)}(\bar{x}, t) \quad (3.6)$$

Where: N_e = Ensemble average of experiments.

$$u_i(\bar{x}, t) = \underbrace{U_i(\bar{x}, t)}_{\text{Mean}} + \underbrace{u_i'(\bar{x}, t)}_{\text{Fluctuation}} \quad (3.7)$$

The Reynolds-averaged momentum equations are shown below where the Reynolds stresses have to be evaluated through a model to close the set of equations (Fluent, 2005):

$$\rho \left(\frac{\partial U_i}{\partial t} + U_k \frac{\partial U_i}{\partial x_k} \right) = - \frac{\partial p}{\partial x_i} + \frac{\partial}{\partial x_j} \left(\mu \frac{\partial U_i}{\partial x_j} \right) + \frac{\partial R_{ij}}{\partial x_j} \quad (3.8)$$

Where:

$$R_{ij} = -\rho \overline{u_i' u_j'} \text{ also known as the Reynolds stresses.} \quad (3.9)$$

The RANS models can be closed using either the Eddy-Viscosity Models (EVM) or the Reynolds-Stress Model (RSM). The EVM approach uses the Boussinesq hypothesis where the Reynolds stresses are modelled using an eddy viscosity also known as the turbulent viscosity (μ_t), Equation 3.10. This hypothesis is reasonable for simple turbulent shear flows, boundary layers and cases involving mixing layers, round jets and channel flows (Fluent, 2005). Equations 3.11 to 3.16 are taken from the summary of the

FLUENT introductory notes which elucidate how μ_t is calculated with the use of the different turbulence models.

$$R_{ij} = -\rho \overline{u_i' u_j'} = \mu_t \left(\frac{\partial U_i}{\partial x_j} + \frac{\partial U_j}{\partial x_i} \right) - \frac{2}{3} \mu_t \frac{\partial U_k}{\partial x_k} \delta_{ij} - \frac{2}{3} \rho k \delta_{ij} \quad (3.10)$$

Based on dimensional analysis, μ_t can be obtained from velocity and length scales so that:

$$k = \text{turbulent kinetic energy (m}^2/\text{s}^2\text{):} \quad k \equiv \frac{1}{2} \overline{u_i' u_i'} \quad (3.11)$$

$$\varepsilon = \text{turbulence dissipation rate (m}^2/\text{s}^2\text{):} \quad \varepsilon \equiv \nu \overline{\frac{\partial u_i'}{\partial x_j} \left(\frac{\partial u_i'}{\partial x_j} + \frac{\partial u_j'}{\partial x_i} \right)} \quad (3.12)$$

$$\omega_s = \text{specific dissipation rate (1/s):} \quad \omega_s \sim \frac{\varepsilon}{k} \quad (3.13)$$

for:

$$\text{Spalart-Allmaras:} \quad \mu_t = C \tilde{\nu} \quad (3.14)$$

$$\text{Standard k-}\varepsilon\text{, RNG k-}\varepsilon\text{, Realizable k-}\varepsilon\text{:} \quad \mu_t = \rho C_\mu \frac{k^2}{\varepsilon} \quad (3.15)$$

$$\text{Standard k-}\omega\text{, SST k-}\omega\text{:} \quad \mu_t = \rho C_\mu \frac{\rho k}{\omega} \quad (3.16)$$

Each of these models solve transport equations for a modified turbulent viscosity in the Spalart-Allmaras case and for two equation models k and ε for the Standard k - ε , RNG k - ε and Realizable k - ε .

3.2.2: k- ε viscous model

As given by Equation 3.10 the turbulence viscosity, μ_t is assumed to be proportional to the product of a turbulent velocity and length scale. Where the velocity scale is taken to be $k^{1/2}$ and the length scale $k^{3/2}/\varepsilon$. The constant C_μ is empirically derived and is given a default value of 0.09 in FLUENTTM. For incompressible flows conservation equations 3.17 and 3.18 have to be solved for k and ε .

$$\frac{\partial k}{\partial t} + u_i \frac{\partial k}{\partial x_i} = \frac{\partial}{\partial x_i} \left(\frac{\mu_t}{\rho \sigma_k} \frac{\partial k}{\partial x_j} \right) + \frac{\mu_t}{\rho} \left(\frac{\partial u_i}{\partial x_j} + \frac{\partial u_j}{\partial x_i} \right) \frac{\partial u_i}{\partial x_j} - \varepsilon \quad (3.17)$$

Convection
Diffusion
Production

$$\frac{\partial \varepsilon}{\partial t} + u_i \frac{\partial \varepsilon}{\partial x_i} = \frac{\partial}{\partial x_i} \left(\frac{\mu_t}{\rho \sigma_\varepsilon} \frac{\partial \varepsilon}{\partial x_j} \right) + C_1 \frac{\varepsilon \mu_t}{k \rho} \left(\frac{\partial u_i}{\partial x_j} + \frac{\partial u_j}{\partial x_i} \right) \frac{\partial u_i}{\partial x_j} - C_2 \frac{\varepsilon^2}{k} \quad (3.18)$$

Convection
Diffusion
Generation

Where C_μ , C_1 , C_2 , σ_k and σ_ε are empirically determined constants that vary in value according to the approach used to determine them. From Jones and Launder, (1972), FLUENTTM expresses the constants as $C_\mu = 0.09$, $C_1 = 1.44$, $C_2 = 1.92$, $\sigma_k = 1.0$, and $\sigma_\varepsilon = 1.3$ for the standard k - ε model. Vorticity generation due to vortex stretching that is in turn connected with the energy cascade and viscous destruction of vorticity is represented by the Generation term in Equation 3.18. Due to its economy with regard to computational time and memory the k - ε model is a tried and tested turbulence model that is capable of modelling a wide variety of flow regimes without variation to the aforementioned constants. The k - ε model however is limited to the description of flows that can be effectively characterised by one Reynolds stress component and an isotropic description of the turbulence (Fluent, 2006). This can be a limiting feature when more complex flow patterns are involved such as separation, highly rotational flows and high pressure gradients. Some of the limitations inherent in the standard k - ε model are addressed in the Renormalization Group method (RNG k - ε) and Realizable k - ε (RKE) models. For the RNG k - ε viscous model the constants are derived using the Renormalization Group method which includes a number of sub-models that can account for variables such as; low-Re effects, turbulent Prandtl/Schmidt number and swirl modification (Fluent, 2005). These then give the RNG k - ε model the ability to better predict more complex shear flows, and flows with high strain rates and where separation may be experienced such as near the trailing edge of the turbine blade.

3.2.3: Reynolds Stress Model (RSM)

In all the previously discussed models the length and velocity scales are the same in all directions; implying that μ_t is isotropic. In circumstances where highly rotational flows are involved, such as the downstream vortices produced by each of the turbine blades, this assumption is inadequate. The RSM however is well suited to such a flow regime where the individual stress components are evaluated from 6 partial differential equations. Equation 3.19 gives the transport equation written in tensor notation for incompressible flows such as the flow of water around the relatively slowly rotating turbine blades. Equation 3.19 has been expressed with the turbulent diffusion and the pressure strain term.

$$\begin{aligned} \frac{\partial \overline{u'_i u'_j}}{\partial t} + u_k \frac{\partial \overline{u'_i u'_j}}{\partial x_k} &= \left[\overline{u'_i u'_k} \frac{\partial u_j}{\partial x_k} + \overline{u'_j u'_k} \frac{\partial u_i}{\partial x_k} \right] - \frac{\partial}{\partial x_k} \left(\frac{u_j P}{\rho} \delta_{ik} + \frac{u_i P}{\rho} \delta_{jk} \right) \\ + \frac{P}{\rho} \left(\frac{\partial u_i}{\partial x_j} + \frac{\partial u_j}{\partial x_i} \right) + \frac{\mu}{\rho} \frac{\partial^2 \overline{u'_i u'_j}}{\partial x_k^2} - \frac{\partial}{\partial x_k} \left(\overline{u'_i u'_j u'_k} \right) - 2 \frac{\mu}{\rho} \frac{\partial u_i}{\partial x_k} \frac{\partial u_j}{\partial x_k} \end{aligned} \quad (3.19)$$

Where: u_i is the component of mean velocity in x_i

u'_i is the component of fluctuating velocity in x_i

The second and third terms represent the decomposed turbulent diffusion by pressure and the pressure strain term, Equation 2.20

$$-\frac{\partial}{\partial x_k} \left(\frac{u_j P}{\rho} \delta_{ik} + \frac{u_i P}{\rho} \delta_{jk} \right) + \frac{P}{\rho} \left(\frac{\partial u_i}{\partial x_j} + \frac{\partial u_j}{\partial x_i} \right) = \frac{1}{\rho} \left(\overline{u_i \frac{\partial P}{\partial x_j}} + \overline{u_j \frac{\partial P}{\partial x_i}} \right) \quad (3.20)$$

Where P is the fluctuation of pressure about the mean value.

The terms in Equation 2.19 can be expressed such that;

$$C_{ij} = u_k \frac{\partial \overline{u'_i u'_j}}{\partial x_k} \text{ is the } \textit{convective} \text{ transport} \quad (2.21)$$

$$P_{ij} = - \left[\overline{u'_i u'_k} \frac{\partial u_j}{\partial x_k} + \overline{u'_j u'_k} \frac{\partial u_i}{\partial x_k} \right] \text{ is the stress production rate} \quad (3.22)$$

$$\Phi_{ij} = \frac{p}{\rho} \left(\frac{\partial u_i}{\partial x_j} + \frac{\partial u_j}{\partial x_i} \right) \text{ is a source/sink due to pressure/strain correlation} \quad (3.23)$$

$$D_{ij}^\mu = \frac{\mu}{\rho} \frac{\partial^2 \overline{u'_i u'_j}}{\partial x_k^2} \text{ is the viscous diffusion term} \quad (3.24)$$

$$D_{ijk}^t = \frac{\partial}{\partial x_k} \left(\overline{u'_i u'_j u'_k} + \frac{\overline{u_j p}}{\rho} \delta_{ik} + \frac{\overline{u_i p}}{\rho} \delta_{jk} \right) \text{ is the turbulent diffusion term} \quad (3.25)$$

$$\varepsilon_{ij} = 2 \frac{\mu}{\rho} \frac{\partial u_i}{\partial x_k} \frac{\partial u_j}{\partial x_k} \text{ is the dissipation term} \quad (3.26)$$

Conveniently Equation 2.19 can then be expressed as:

$$\frac{\partial \overline{u'_i u'_j}}{\partial t} + C_{ij} = p_{ij} + \Phi_{ij} + D_{ij}^\mu - D_{ijk}^t - \varepsilon_{ij} \quad (3.27)$$

FLUENTTM uses model approximations for unknown terms and an additional Equation for ε in the second-moment closure (Launder, 2005). The dissipation ε_{ij} is approximated in FLUENT by assuming that the small scale motions responsible for the dissipation of turbulence are isotropic, with large Reynolds numbers this assumption is reasonable (Fluent, 2006). A simple model for the dissipation term is given by:

$$2 \frac{\mu}{\rho} \frac{\partial u_i}{\partial x_k} \frac{\partial u_j}{\partial x_k} = \frac{2}{3} \varepsilon \delta_{ij} \quad (3.28)$$

Other approximations are applied to the turbulent diffusion term where the pressure contribution is also approximated, and finally the pressure-strain term. The pressure strain model used in FLUENTTM uses the return-to-isotropy term and the rapid-distortion term (Rodi, 1982) shown as the first and second terms on the right had side of Equation 3.29:

$$\Phi_{ij} = -C_3 \frac{\varepsilon}{k} \left(\overline{u'_i u'_j} - \frac{2}{3} \delta_{ij} k \right) - C_4 \left(p_{ij} - \frac{1}{3} \delta_{ij} p_{ij} \right) \quad (3.29)$$

Where: C_3 and C_4 are constants 1.8 and 0.6, respectively.

The RSM still requires some approximations to be made and that the model is time-averaged representing a mean of the transport of momentum performed by the turbulent/fluctuating part of the flow. However, the RSM is the most rigorous time-averaged model within FLUENTTM and if the associated computational cost can be accommodated, along with convergence difficulties from the close coupling between the momentum equations and the turbulent stresses, the RSM should be capable of capturing key performance characteristics associated with the operation of a HATT. These include the resulting downstream effects such as vortex rotation and dissipation and interaction between the turbine and support stanchion resulting from the upstream dam effect.

3.2.4: Near wall functions

The k - ϵ and RSM models are not valid in the near wall region due to low Reynolds numbers where laminar viscosity starts to play a significant role. These models are only suitable for high Reynolds numbers. Therefore to apply a reliable boundary condition 'near wall treatments' are required which model the velocity and turbulent parameters down to the blade surface (wall) and therefore do not require the grid density to be high in the near region. This methodology is more efficient than the high grid density used in the Spalart-Allmaras model especially with the solution complexity introduced by the k - ϵ and RSM approaches. According to Gupta and Lilley, (1985) the use of this approach assumes the presence of a near wall layer across which the shear stress is uniform, the existence of a local equilibrium between the production and dissipation of k and finally a linear variation with distance of the length scale of turbulence. Based on these assumptions a logarithmic velocity profile is generated near the surface as used in FLUENTTM and as originally proposed by Patankar and Spalding, (1970). FLUENTTM enables the use of three boundary conditions i.e. a Standard wall function, Non-Equilibrium wall functions and finally an Enhanced wall treatment. The type of function used greatly depends on the mesh density near to the blade surface. The function used greatly depends on the the local y^+ value (sometimes known as the local Reynolds number) which is give by:

$$y^+ = \frac{\rho u_r y_{nw}}{\mu} \quad (3.30)$$

Where: y_{nw} represents the distance from the wall and typical turbulence length scale

u_r represents the friction velocity and typical velocity turbulence velocity scale

The near blade boundary can be subdivided into a number of layers starting from the blade surface (Bradshaw, 1971). The first of these is the viscous sub-layer or laminar sub-layer. The middle area of Figure 3.1 is known as the buffer layer or the blending region. Above this layer is the so-called fully turbulent region or log-law region. Above this latter region is the outer layer. Figure 3.1 shows the three regions as presented by Fluent, (2005). Values for y^+ are given below in accordance with those presented by Hinze, (1987) for the 3 zone turbulence zones labelled A, B and C. Region A with a y^+ range ($0 < y^+ < 5$), region B where ($5 < y^+ < 30$) and finally C ($30 < y^+ < 400$). In FLUENT™ the law-of-the-wall for mean

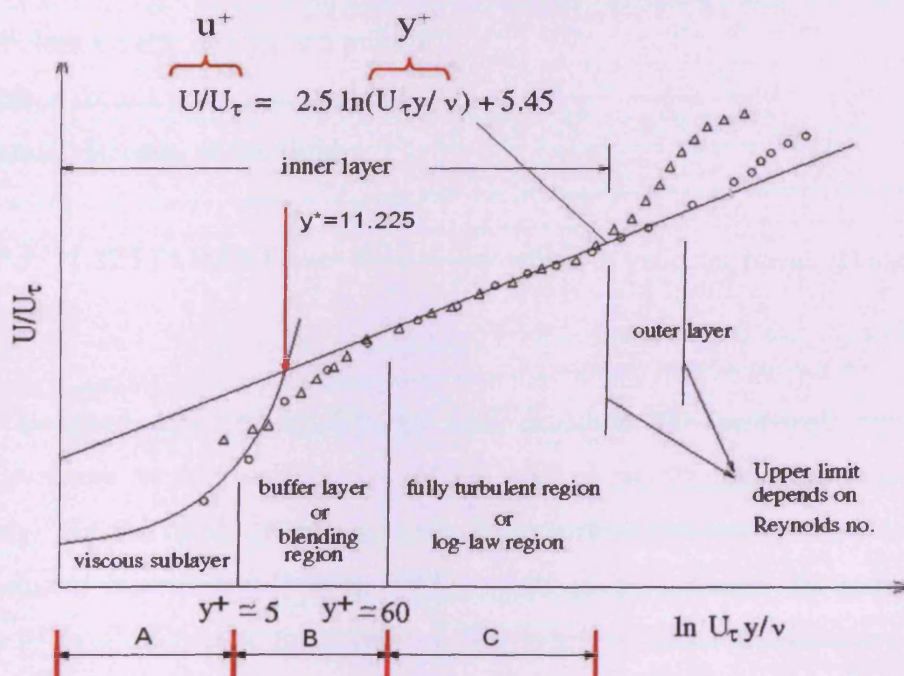


Figure 3.1: Near wall turbulence represented by the 'law of the wall'

Source: Fluent, 2005

velocity is based on the wall unit y^* rather than y^+ since these quantities are stated as being approximately equal in equilibrium turbulent boundary layers. The point at $y^*=11.225$ represents the point to which FLUENT™ extends the log-law layer to the

viscous sublayer thereby neglecting the buffer layer. When the mesh gives a $y^* < 11.225$ at the wall adjacent cell, FLUENT applies:

$$U^* = y^* \quad (3.31)$$

Which is a laminar stress-strain relationship where the mean velocity yields:

$$U^* = \frac{1}{k} \ln(Ey^*) \quad (3.32)$$

$$U^* \equiv \frac{U_p C_\mu^{1/4} k_p^{1/2}}{\frac{\tau_\omega}{\rho}} \quad (3.33)$$

and

$$y^* \equiv \frac{\rho C_\mu^{1/4} k_p^{1/2} y_p}{\mu} \quad (3.34)$$

Where:

k = von Kármán constant (0.4187)

E = empirical constant (9.793)

U_p = mean velocity of the fluid at a point P

k_p = turbulent kinetic energy at a point P

y_p = distance from a point P to the wall

μ = dynamic viscosity of the fluid

When $y^* > 11.225$ FLUENT uses the log-law which is valid for mean velocity between $30 < y^* < 300$.

For the standard and non-equilibrium wall functions the near-wall mesh can be relatively coarse as they use the law of the wall to supply turbulent flow boundary conditions. As the mesh density near the blade surface increases the latter Enhanced wall treatment is required (Fluent, 2006). This gives a means for monitoring the accuracy of the flow near to the surface of the blades and hence the accuracy associated with forces generated from lift and drag and the resulting power extraction and axial thrust loads for the whole HATT. The appropriate mesh density can be established by correlating measured and calculated performance characteristics using flume testing as previously discussed in Chapter 2. This is of key importance when considering the power extraction efficiency of the HATT when subjected to a profiled flow through the water column.

3.3: Acoustic Doppler Current Profiler (ADCP) measurements

If the velocity profile changes significantly through the water column it could have a detrimental affect on the ability of the HATT to extract energy from the flow. Moreover, if the velocity profile bounded by the turbine diameter is large a considerable amount of asymmetric loading could be applied to each blade as they rotate between higher and lower velocities at the top and bottom of the swept area. The vertical location of the HATT in the water column is therefore crucial to the efficient operation of the device. However, with the degree of variability between sites in the UK and the degree to which the technology would have to be expanded to enable the levels of energy extraction required to meet economic viability in shallow waters, extending the operation of the rotor into these high shear bands maybe necessary. Moreover, with the extension of the technology into depths > 50 m, where high velocity resources are available, a form of seabed fixing using modular frames may position all or part of the swept area of the turbine in the high velocity shear band. As a means to answer some of these questions ADCP can be used to study the velocity attenuation through the water column at a proposed HATT site. An ADCP operates by sending high frequency sound waves into the water, as the sound waves move down through the water column they impact particles moving with the flow of water, such as bubbles or grains of sand. The high frequency sound waves are then reflected back to the sensor. Depending on the direction of the moving water relative to the ADCP transmitter, the frequency of the returning sound is altered in exactly the same manner as given by the Doppler Effect. The corresponding depth can be calculated from the time it takes for the sound to travel back to the sensor. Since the ADCP is Vessel-mounted all instruments are powered via the vessel. A GPS navigation system is used to subtract the ship's own movements from the current data. The Woods Hole Oceanographic Institute (WHOI) give the following advantages and limitations associated with the use of ADCP, (WHOI, 2009):

3.3.1: ADCP advantages:

1. Velocity profile measurement historically required long strings of current meters; this is eliminated with the use of ADCP.
2. Small scale currents can be measured.
3. The absolute speed of the water and not just relative mass flow difference can be measured.
4. It has the capability to travel a water column up to 1000m long.

3.3.2: ADCP disadvantages:

1. Since high frequency signals yield more precision and low frequency signals travel farther through the water, a compromise must be made between the distance that the profiler should measure and the precision of the measurements.
2. If seabed-mounted, high frequency single repeats can rapidly deplete batteries.
3. In very clear water, such as the tropics, particle densities may not be sufficient to give a reliable return signal.
4. Erroneous data can be generated from bubbles in turbulent water and or schools of swimming marine life.
5. Regular maintenance is required to prevent marine life from attaching to the transducers.

3.4: Literature summary

The methodologies associated with the BEM theory and the more sophisticated CFD models are well suited to capture the hydrodynamics of the HATT blades under various flow conditions; in the case of the BEM as a first order approximation, while the CFD can be used to model the HATT's hydrodynamic performance. The main focus of the thesis is to use CFD to model energy extraction and axial thrust load with variation in the rotational angular velocity of the HATT while applying plug and profiled flow at the inlet boundary. ADCP is a reliable technology for the measurement of velocity profiles that are in turn fundamental to the characterisation of site specific energy fluxes and the dimensions and the optimum position of the HATT within the water column. Along with SWATH measurements to establish the local bathymetry these tools are essential to the future of tidal stream technology development. Moreover, as stated in Section 2.4, the characterisation of the local velocity profile is critical if the device is positioned within or partially within the lower 25 % of the water column. It is therefore the purpose of thesis to investigate the performance of a given HATT design under these conditions while subject to a realistic site condition. A number of experimental studies have already been undertaken in this area such as those on surface interaction, wake length, power extraction and axial thrust loads which form a useful base to correlate physical measurement and the CFD models. However, to the author's knowledge there are no data published from prototype or full scale HATTs positioned at such depths and profiled velocity flows.

4: Numerical study of turbine performance

As a first order approximation to optimise parameters such as blade pitch angle (θ) and Tip Speed Ratio (TSR), the BEM theory was used as a baseline for CFD analysis of the HATT design. In addition to the general assumptions made within the application of the BEM theory the drag force and tip losses were neglected. This helped to simplify the model and to limit its development time. The BEM model was not intended to be used as a comparative tool with either the CFD or measured data and therefore is not discussed beyond its initial evaluation of the prototype HATT's performance.

The Computational Fluid Dynamics (CFD) method was used via the use of the software package FLUENT™. The validation model for the flume is given in Table 4.1 along with its dimensions and boundary conditions. Following the validation procedure a reference flume CFD model was then developed to remove any flow concentration from the side, surface and seabed boundary walls. The reference flume CFD model was then scaled to dimensions suitable for effective power generation in open waters (Deep water, Table 4.1). Since a full scale HATT was not available for this research the remaining study was limited to the application of CFD. A site specific CFD model was then developed with an overall water depth derived from the measurement of a Bathymetric and ADCP surveys at a proposed site within the inner Bristol Channel off the coastline of Barry, South Wales, UK and four others off the coast of Anglesey. For the validation and reference modelling stage a plug flow was used at the inlet boundary and allowed to develop upstream of the turbine.

Table 4.1: Dimensions and boundary conditions for CFD models

CFD model	Dimensions			Boundaries						
	Length (m)	Width (m)	Depth (m)	Inlet (m/s)	Outlet (Pa)	Surface & sides	Seabed	Turbine Diameter (m)	Hub diameter from inlet (L_w/D)	Hub diameter to outlet (L_{out}/D)
Validation										
Flume	4	1.4	1.7	Plug	Pressure (atm)	Wall ($\mu = 0$)	Wall ($\mu = \text{no-slip}$)	0.5	4	4
Reference										
flume	25	2.5	2.5	Plug flow	Pressure (atm)	Wall ($\mu = 0$)	Wall ($\mu = \text{no-slip}$)	0.5	*	*
Deep water	500	50	50	Plug and profiled	Pressure (atm)	Wall ($\mu = 0$)	Wall ($\mu = \text{no-slip}$)	*	*	*
Site										
Severn	500	50	35	Plug and profiled	Pressure (atm)	Wall ($\mu = 0$)	Wall ($\mu = \text{no-slip}$)	*	*	*
Anglesey	500	50	35	Plug and profiled	Pressure (atm)	Wall ($\mu = 0$)	Wall ($\mu = \text{no-slip}$)	*	*	*
* Turbine scaling study										

The tidal velocity profile through the water column as measured using ADCP was then rescaled to what was to be considered as peak flow conditions for the thesis. The velocity profile was then added to the inlet-boundary of the reference deep water and site specific CFD models. Due to the large amount of shipping passing through the proposed HATT site a vessel depth restriction was included in the site CFD models. This limited the total height of the HATT to be below that of maximum vessel draft as given for the Severn Estuary (Auld, 2008). A means of fixing the HATT to the seabed was also investigated and its subsequent effect on turbine efficiency. A piled stanchion was used in the downstream position of the turbine it was also assumed that the HATT would rotate 180° around the vertical axis of the stanchion with the change in tide direction. Finally, a 5 turbine array was used to demonstrate the influence of axial thrust loads and turbine wake interaction.

4.1: 2D blade profile for BEM

The original HATT hydrofoil profile was selected by Egarr et al, (2003) at Cardiff University using the methods suggested by the National Advisory Committee for Aeronautics (NACA) for aerofoil sections and were optimised using the BEM theory. Using this methodology the shape of the profiles was plotted by calculating each ordinate perpendicular to the mean line, Figure 4.1. The final profile shape was a variant on the Wortmann FX 63-137. A comparison between the two profiles is shown in Figure 4.2

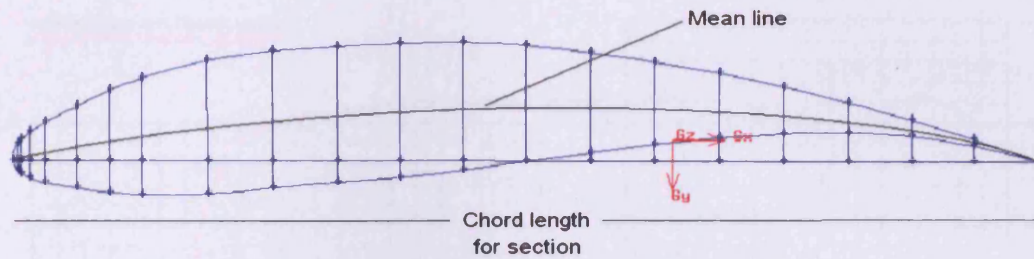


Figure 4.1: 2D cross section of 0.5m diameter laboratory turbine.

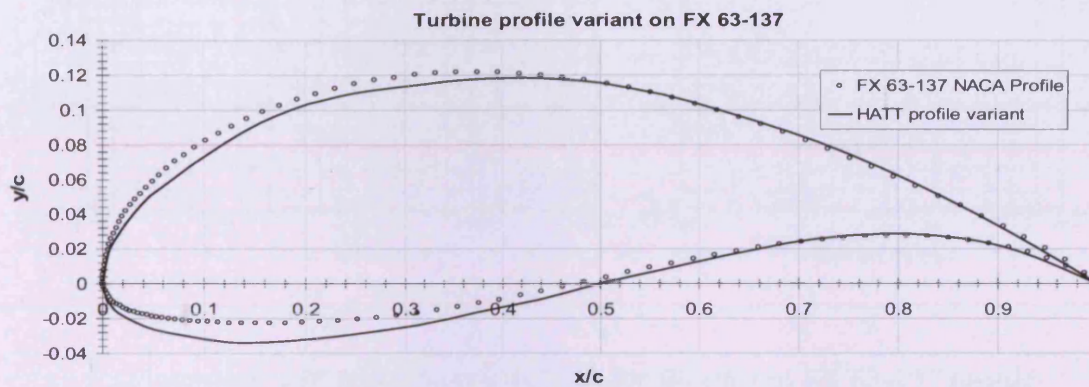


Figure 4.2: Comparison between FX 63-137 and prototype turbine profile

4.1.1: 2D lift and drag coefficients

During operation it is desirable for the blade profile to produce as much torque as possible, while maintaining the necessary structural integrity to withstand the high structural loading, specifically the axial thrust. For this reason the thickness of the profile cross-section was varied along the length of the blade with the thicker section at the blade root. To maintain a high torque the chord length was increased towards the root as the profile thickness increases. This is further achieved by applying a twist between the blade tip and the root to account for variations in tangential velocity along the length of the blade thereby maintaining an optimal attack angle to the resultant (apparent) water velocity. In an attempt to limit high bending moments the blade the attack angle was adjusted so that the lift forces decrease toward the tip.

Figure 4.3 (a) and (b) gives the lift and drag characteristics for the Wortmann FX 63-137 profile against attack angle α (Teoria Aeronáutica, 2009). To simplify the BEM modelling the coefficient of momentum (CM) is not included in the analysis.

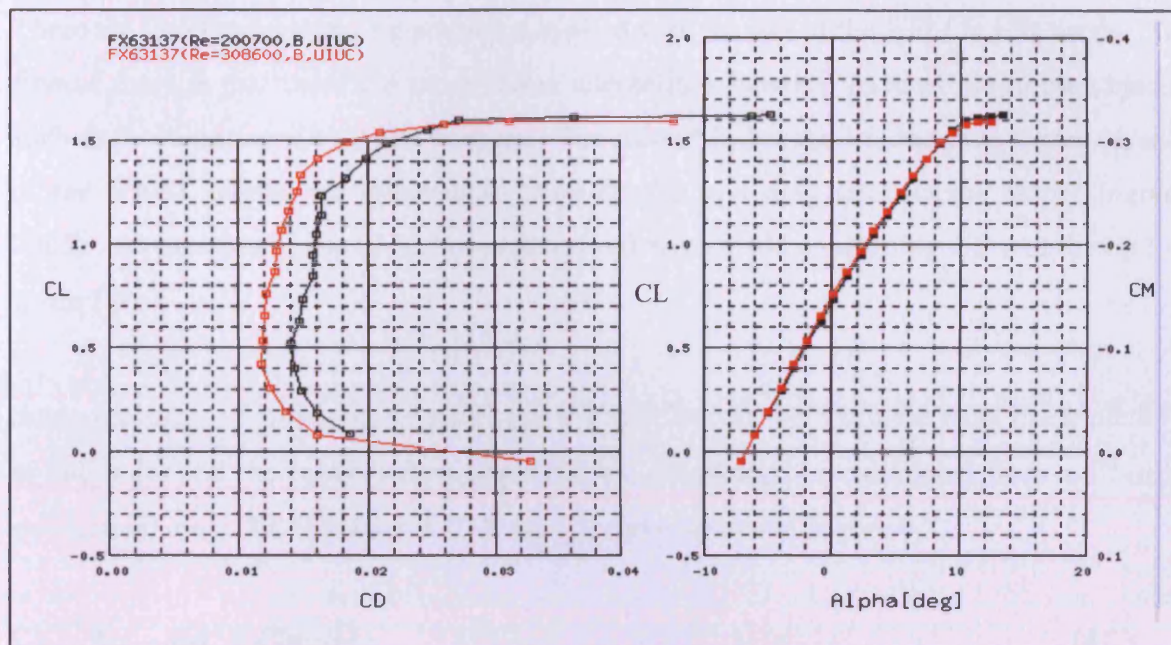


Figure 4.3: Lift and drag coefficients for Wortmann FX 63-137 profile
Source: Teoria Aeronáutica, 2009

4.1.2: Blade Element Momentum (BEM) theory and MatLab Code

BEM theory can be used to analyse the performance of a given design. Since the nature of the thesis was to use a prototype HATT, the BEM theory was used to evaluate the performance of the 0.5 m diameter prototype HATT. The BEM theory uses two methodologies to establish the operational performance of the rotating blades. By combining the lift (CL) and drag coefficients (CD) from Figure 4.3, and a momentum balance on a rotating stream tube (Ingram, 2005) the BEM theory was used in this study to give a first order approximation for the optimum blade pitch angle (θ) and associated Tip Speed Ratio (TSR). Texts, such as such as Leishman, (2006), discuss the BEM theory in great depth, therefore it will not be covered in detail here. However a brief outline of the theory will be covered for both completeness and to aid the description of the code. The code for the BEM theory was developed within Matrix Laboratory or MATLABTM 6.5. The BEM code is contained In Appendix 1.

There are two fundamental assumptions applied with the use of the BEM in this thesis. The first of these is that there are no dynamic interactions between each of the turbine blades, such as those imposed by wake vortices. The second is that the lift and drag forces on each of the HATT blades are determined from the lift and drag coefficients alone (Ingram, 2005). As previously stated further assumptions were made concerning CD and the tip loss factor (ψ).

Since the angle of incidence or attack (α) is the difference between the local blade pitch (γ) at radius (r) and the relative flow angle (β), CL could then be calculated from a 3rd order polynomial curve fit, Equation 4.1, of the CL curve shown in Figure 4.3.

$$CL = A\alpha^3 - B\alpha^2 + C\alpha + D \quad (4.1)$$

For the initial rotor design evaluation the code followed a performance procedure as suggested by Ingram, (2005). An initial guess was made for the axial induction factor (a), rotational induction factor (a') and the relative flow angle (β) at a predefined blade radius (r); in this case starting at the blade tip. At the same radius the local (TSR)_r and relative flow angle (β) can then be calculated.

An analytical solution cannot be found directly from the equations discussed in Section 3.1, instead an iterative approach is required for the solution of the above equations. Using CL from Equation 4.1 the axial and rotational induction factors (a) and (a') are then recalculated and the procedure continued until the convergence criteria is reached. The residuals for the axial and rotational induction factors were used to monitor the convergence at each segment radius along the blade using Equations 4.2 and 4.3.

$$\Delta a = \frac{|a_n - a_{n+1}|}{a_n} \quad (4.2)$$

$$\Delta a' = \frac{|a'_n - a'_{n+1}|}{a'_n} \quad (4.3)$$

A loop was used within MATLAB™ to continue the iterative process while $\Delta a > 1 \times 10^{-5}$ and $\Delta a' > 1 \times 10^{-5}$. A maximum number of $n = 1 \times 10^6$ iterations was used to ‘trap’ any non-convergence at each of the radial segments. Following convergence at each of the N segments the resulting power coefficient was then calculated for the whole blade. Ingram, (2005) showed that the total power generated by the rotor could be calculated by summing the power at each radius (r) using Equation 4.4.

$$P = \int_{r_0}^r \omega dT .dr \quad (4.4)$$

The power coefficient (C_p) can then be calculated via the quotient between the power available for the cross sectional area of the HATT and the power generated by the rotors, Equation 4.5.

$$C_p = \frac{\int_{r_0}^r \omega dT .dr}{\frac{1}{2} \rho A V^3} \quad (4.5)$$

Where, ω is the turbine angular velocity.

The torque on an element dT along the blade radius at each segment can be calculated from the corresponding tangential force multiplied by the radius (r), Equation 4.6.

$$dT = B \frac{1}{2} \rho V_{Ri}^2 (CL \cos \beta) c .r .dr \quad (4.6)$$

Where c is the blade chord length of the section.

By replacing the resulting incident flow velocity (V_{Ri}) and relative flow angle (β) with relationships for the axial and rotational induction factors, Equations 3.1 and 3.2, Equation 4.6 can be expressed as in Equation 4.7, (Ingram, 2005).

$$dT = \sigma' \pi \rho \frac{V^2 (1-a)^2}{\cos^2 \beta} (CL \cos \beta) r^2 \cdot dr \quad (4.7)$$

Using Equation 4.7 Ingram, (2005) showed that C_p can be expressed as an integral, Equation 4.8.

$$C_p = \frac{8}{TSR^2} \int_{TSR_0}^{TSR} TSR_r^3 a'(1-a) dTSR_r \quad (4.8)$$

The power at each radial segment (N_r) can then be summed via the trapezium rule, Equation 4.9.

$$\int_{TSR_0}^{TSR} (TSR)_r a'(1-a) d(TSR)_r = \frac{TSR_0 - TSR_r}{2N} \left[(Y_0 + Y_n) + 2 \left(\sum_{i=1}^{n-1} Y_i \right) \right] \quad (4.9)$$

Where, (Y_i) is the power ($TSR^3 a'(1-a)$) _{i} at each segment along the blade radius.

4.1.3: Input parameters for BEM MatLab code

At the input section of the BEM code the angular velocity (ω), upstream water velocity and the number of turbine blades (B) can be specified. An example data set is shown in Table 4.2, giving the blade twist (γ), chord length (c) and radius (r) for the prototype HATT divided into 11 segments along its radius for a blade set with a tip blade pitch of 6° .

Blade segment number (N)	Blade pitch / twist angle (γ) (Degrees)	Chord length (m)	Segment radius (r) (m)
0	83	0.0295	0.23725
1	83.75	0.03165	0.228
2	82.75	0.035	0.209
3	80.1	0.03903	0.19
4	78.38	0.03525	0.171
5	75.59	0.056	0.152
6	72.3	0.0635	0.1325
7	68.71	0.07	0.1135
8	63.13	0.0735	0.0935
9	57.99	0.0755	0.0755
10	50.11	0.075	0.0565

See Appendix 2 for the remaining blade tip pitch angles between 2° and 10° . Using the code with varying blade pitch angles an optimum blade pitch angle and corresponding TSR can be derived by performing an angular velocity sweep and plotting C_p to the base of angular velocity and blade tip pitch angle.

4.2: 3D CFD models of prototype HATT.

Prior work at the Cardiff School of Engineering involved the development of turbine blade profiles (Egarr et al, 2003). From this study an initial blade design was established through the use of BEM theory and CFD, Figure 4.2. The original assembly drawings for the turbine blades and hub assembly were created by Dr. D. A. Egarr between January and February 2003 using Solid Works. Blade and hub geometries were later created using Pro-Engineer by the Mechanical Engineering Centre (MEC) at Cardiff University. Three blade lengths were manufactured allowing 3 possible turbine diameters to be created: 0.3 m, 0.4 m and 0.5 m, each utilising identically scaled profiles. The turbine blades were designed to be clamped via a 15 mm diameter, 32 mm length pin between the hub and annulus plate. This allowed configurations of 1, 2, 3, 4 and 6 blades. The pin extends from the base of the blade 22 mm from the leading edge to pin centre.

4.2.1: Prototype reference CFD geometry preparation in Gambit.

The blade and hub geometries were imported into Gambit for meshing. Gambit is the pre-processor for FLUENTTM where geometry can either be created or imported from third party software (Fluent, 2006). Gambit also has a meshing facility and boundary definition suite allowing faces and volumes to be defined prior to exporting them to the analysis code FLUENTTM.

4.2.1.1: Geometry preparation and meshing for turbine volume

Using Gambit as the pre-processor, the scaled blade profiles were split up into 6 upstream facing and 6 downstream faces, Figure 4.4, with the tip of the blade made up of 3 faces, 2 at the leading edge and 2 with edges converging at the trailing edge. Each face was stitched to form the blade volume which also included the blade/hub assembly pin. The faces on

the hub were also stitched to form a second volume. The turbine blade volume was then aligned with the Y axis and the rotational centre of the hub with the Z axis. By moving the blade pin along the Y axis the outer radius of the rotor was adjusted to 0.25 m with the blade positioned so that the upstream flow face was along the positive Z axis. The blade pitch was adjusted by rotating the turbine clockwise around the Y axis giving a positive pitch angle, Figure 4.4, (a). Before the blade was attached to the hub a copy of the blade volume was made and repeated at 120° intervals around the z axis, thereby forming a three bladed HATT. At this stage however the blades volumes were not connected to the hub volume. The length of the original connecting pin was extended before copying the blade so that they extended further into the hub volume, Figure 4.4, (b). This procedure allowed each blade to be subtracted and merged into the hub forming a single turbine volume consisting of three blades labelled B1, B2 and B3 in a clockwise direction around the Z axis and the hub volume itself.

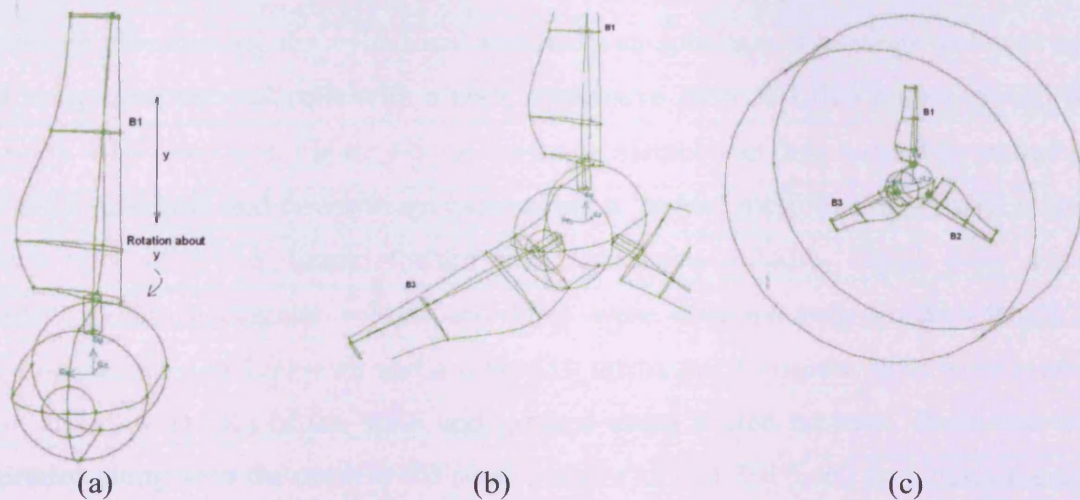


Figure 4.4: (a) Unconnected B1 and hub, (b) Blade B1 copied at 120° to B2 and 240° to B3, (c) blades B1, B2 and B3 connected to hub

To simulate rotation the HATT volume was then subtracted from a cylindrical volume and removed so that the cylindrical volume remained but with a cavity matching the original turbine assembly, Figure 4.4, (c). For each model created for this thesis a relative distance, in this case 0.165 m, was left between the blade tips and the edge of the MRF to limit poor solution and numerical diffusion near the non-conformal interface (Fluent, 2006). This then formed the premise for the Moving Reference Frame (MRF) to be defined later within FLUENT™. The MRF volume was then subtracted from a rectangular channel

representing a portion of the main flow field. The depth and width of the channel were chosen to limit flow concentration effects between the turbine and the boundary walls except for the flume model, where the boundary conditions were specified to match the flume. A channel depth and width of 5 turbine diameters was chosen as an initial guess based on studies by Egarr et al, (2003). The subtracted cylindrical MRF volume however was retained; this introduced a non-conformal interface between the rectangular and MRF volumes so that when meshed the cells at the surface of each volume did not share the same nodes. In such a case it is recommended that the cell size along each coincident surface be the same to limit diffusion problem across the interface (Fluent, 2006). To comply with this requirement all of the CFD models developed in this thesis used the same cell spacing along both the MRF and channel MRF edges that make up the non-conformal interface.

4.2.1.2: Geometry preparation and meshing for all rectangular channels

The rectangle surrounding the cylindrical volume was split into 8 separate volumes and meshed using quadrilateral cells with a node successive ratio of 1.016 biased toward the edges of the MRF interface, Figure 4.5. A meshed channel was then created by extruding each of the 8 upstream and downstream faces along a 'guide' mesh line again with a node successive ratio of 1.016, biased toward the rectangular volume, Figure 4.6. Faces downstream of the rectangular volume and MRF were extruded with a z-axis length to turbine diameter ratio of $L/D = 40$ and a $L/D = 10$ upstream. Two new faces were created upstream and downstream of the MRF and meshed using a tiled scheme. Each face was then extruded along with the mesh in the same manner as that discussed previously thereby creating two cylindrical volumes. Each cell created during extrusion share a common node along the faces and edges of the neighbouring volumes, Figure 4.6.

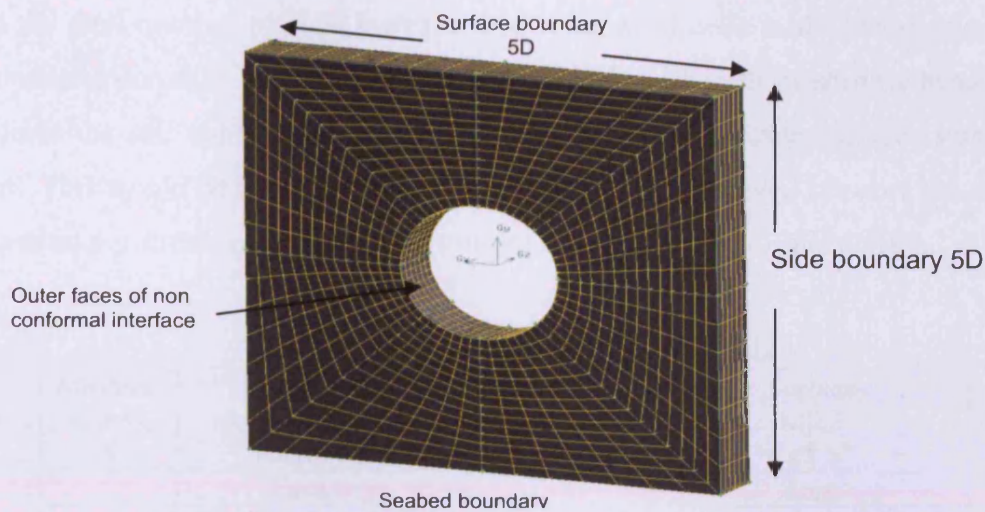


Figure 4.5: Central rectangular channel with MRF removed

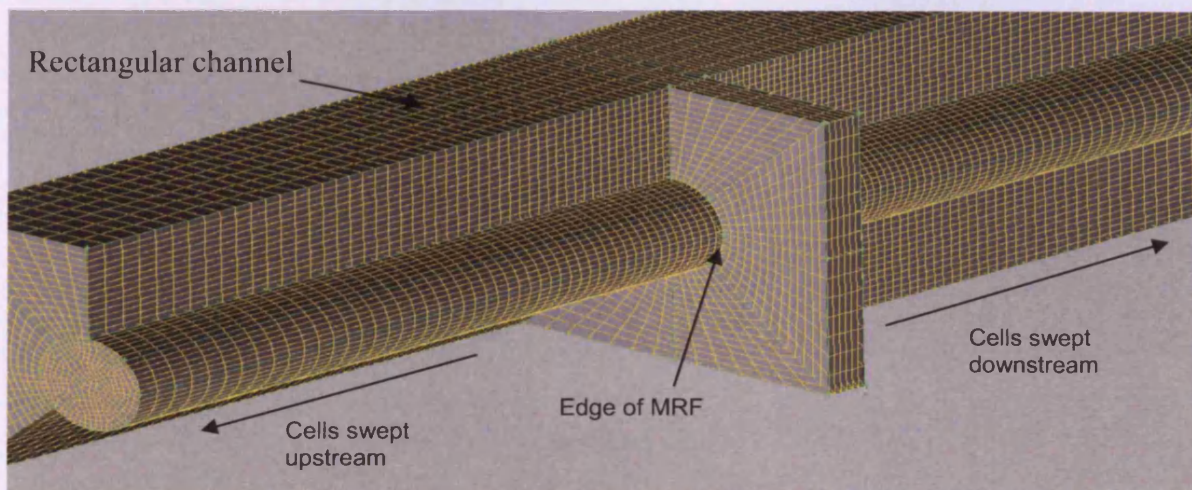


Figure 4.6: Volume creation and meshing of channel volume

4.2.1.3: Meshing schemes for reference, site and flume MRF volumes

The number of cells in the MRF and rectangular channel volumes greatly depends on the converged solution and its dependency on mesh density, in all the CFD models the primary calculation is the energy extraction. To determine the appropriate mesh density, various meshing schemes were developed. Table 4.3 gives the meshing schemes used to mesh the 0.5 m HATT while using the reference model dimensions, i.e. where the width and depth of the channel is 5 times the turbine diameter. The upstream and downstream edge lengths for each surface on the turbine blades were varied in accordance with the defined cell spacing along the edge lengths e.g (30-60-30-80) in Table 4.3. As the edge lengths in the MRF are

reduced the total number of cells increase. The number of cells in the rectangular volume was maintained constant. Figure 4.7: shows the blade mesh with meshing scheme number 4. To limit the cell count no inflation of the cells from the blade surfaces was initially included. This would be included if a poor correlation was achieved between the numerical and measured performance characteristics of the HATT, such as torque and C_p .

Table 4.3: Cell count for all CFD models

Meshing scheme N°	Upstream and downstream edge length scale	Rectangular channel Cell N°	Turbine MRF Cell N°
	Face key	Zone	Zone
	Tip-middle-root-hub	2	3
1	30-60-30-80	89533	278327
2	30-30-30-60	89533	512373
3	20-30-20-60	89533	730903
4	20-30-20-50	89533	969332
5	20-20-20-30	89533	1239038
6	20-20-20-30	89533	1393921
7	15-20-20-30	89533	1750803

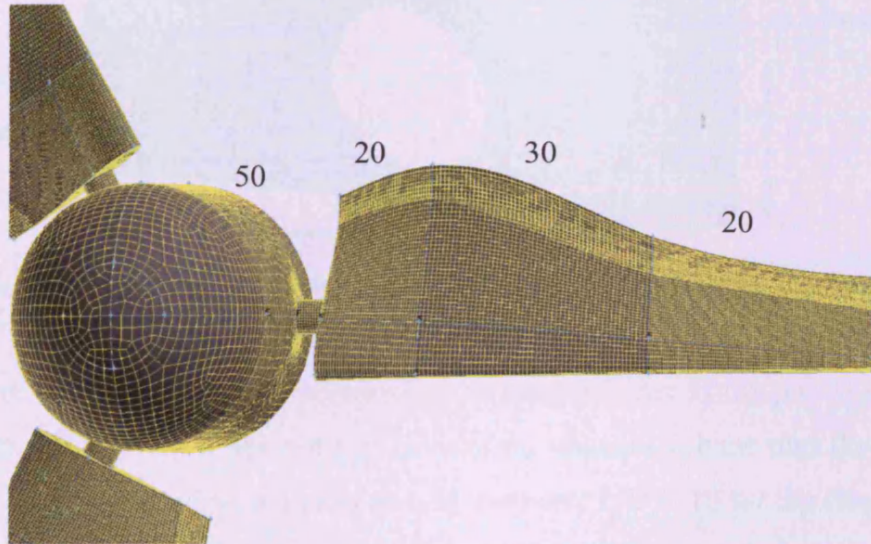


Figure 4.7: Mesh pattern for meshing scheme 4, column 1, Table 4.3

4.2.1.4: Geometry preparation and meshing of site turbine volume

The meshing procedure of the turbine for the site model was the same as for the reference flume, deep water and flume models, as shown in Table 4.3. The resulting MRF volume dimensions were maintained and subtracted from the rectangular site channel volume.

4.2.1.5: Geometry preparation and meshing of site rectangular volume

The dimensions of the rectangular channel volume surrounding the site MRF volume were reduced through the depth. However, the width of the channel is maintained the same. The depth of the site channel was adjusted to 35 m, Figure 4.8. This depth was used to fit into the 30 m to 40 m depth band where current full scale prototypes are being developed (Black and Veatch, 2005).

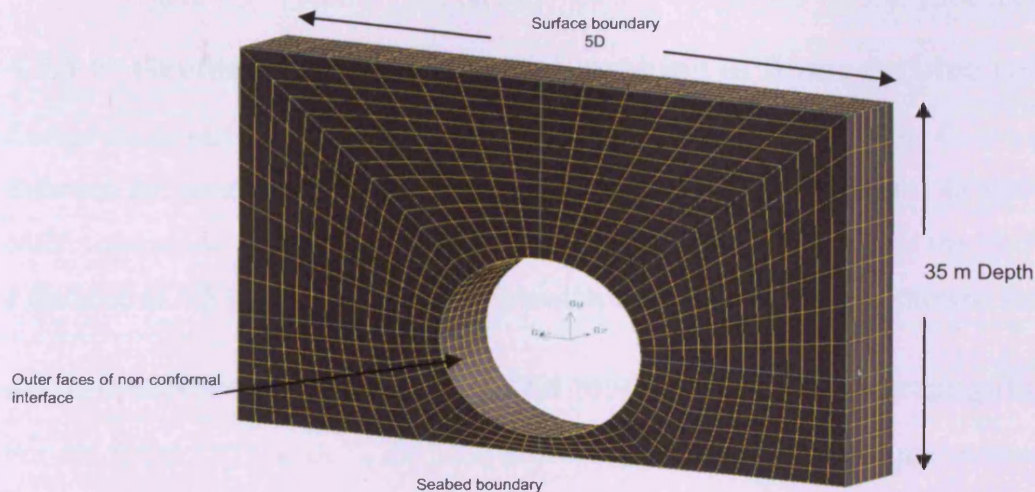


Figure 4.8: Central rectangular channel with MRF removed (Site model)

The length of the channel was also created in the same manner as the previously discussed CFD models. Each of the 8 downstream faces of the channel volume plus the circular face of the MRF were extruded with a ratio of $L/D = 40$ and $L/D = 10$ for the downstream and upstream channel lengths. Again, the channel volumes were created along with the mesh, again following a guide line with a node successive ratio of 1.016, biased toward the rectangular volume. Meshed volumes were then created by extruding each of the 8 upstream and MRF faces along a 'guide' mesh line with a node successive ratio of 1.016, biased toward the rectangular volume, Figure 4.9. These meshing procedures are therefore

generic to all the CFD models developed in this thesis. Further discussions on meshing will only cover variances to this when necessary.

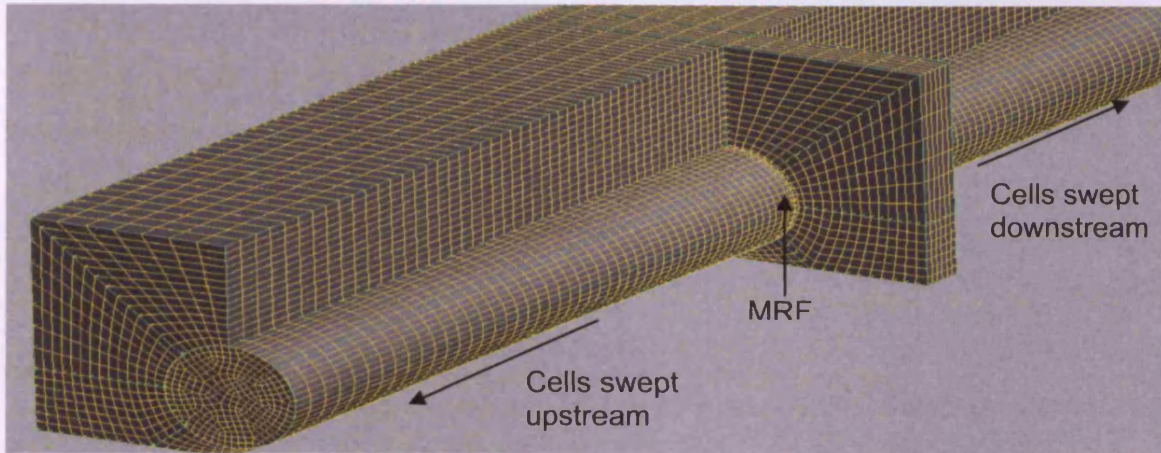


Figure 4.9: Volume creation and meshing of channel volume (Site model)

4.2.1.6: Geometry preparation and meshing of flume turbine volume

Except for its physical dimensions the cylindrical volume for the flume CFD model followed the same procedure as for the reference and site CFD models. In addition to the MRF volume the circular support tube was also placed directly behind the MRF volume at a distance of 1.5 stanchion diameters to match that of the physical prototype setup.

4.2.1.7: Geometry preparation and meshing of flume rectangular volume

For the flume CFD model a different procedure was used to create the rectangular volume due to the complexity added from the support tube. For the flume CFD model the rectangular volume was created by positioning vertices at 2 m upstream and downstream of the HATT forming the inlet and outlet boundaries of the flume. The final volume was then created by joining faces created from a wireframe linking up the vertices. For the CFD model to replicate the physical conditions during the flume tests, it would be required to include the interaction between the water surface and air. The 'deformable' boundary would allow the free surface to deform as the pressure upstream and downstream of the turbine increase and decrease, respectively. An example of this is represented by the partial blockage shown in Figures 2.20 (a) and (b). FluentTM has the capability to model such an interface via the use of a Volume of Fluid (VOF) model. However, it was not possible to use a VOF model due to the large number of cells already used to model both the blades

hydrodynamic performance and to resolve the resulting downstream wake. If the VOF boundary were applied, the number of cells required to give a sufficient resolution across the interface would have exceeded the PC's memory. Without a free surface in the CFD model, the height of 0.85 m between the rotational axis and the rigid surface boundary would result in flow concentration and an increase in velocity around the turbine. The confined flow over estimates the power extracted by the turbine as the open channel assumption no longer holds. To give an initial estimate to the required water depth above the turbine's rotational axis, the surface boundary depth was increased to closely match that of the reference CFD models. Due to the increased cell density from the vertical support stanchion the resulting depth was limited to 1.7 m, Figure 4.10. To check the validity of this assumption to account for blockage effects, non-dimensional performance curves for both the 0.85 m and 1.7 m flume depths were plotted against the reference CFD model curves and those obtained from the flume tests. The non-dimensional curves are compared and discussed later in Chapter 8, Section 8.2.5.

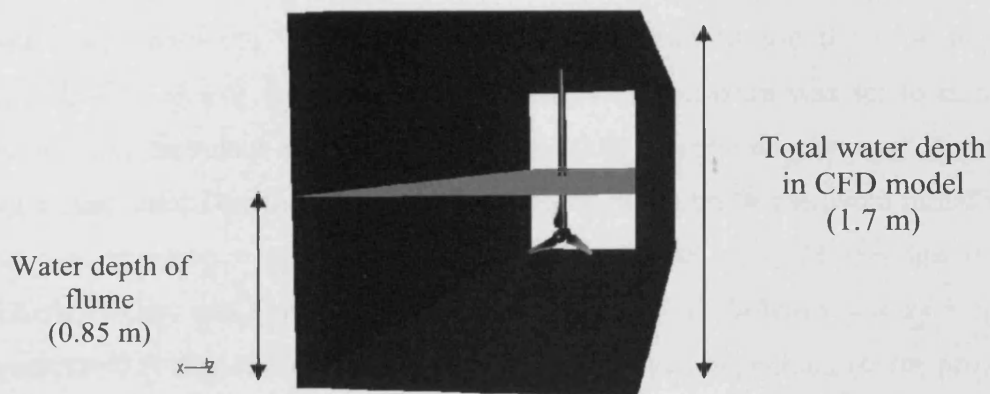


Figure 4.10: Geometry of flume CFD model

The face on the support stanchion was meshed with a quadrilateral scheme and an interval spacing of 6 which gave an appropriate mesh density to resolve the near wall boundary. The turbine blades and hub were meshed using the same procedure as for the reference and site CFD models. The rectangular channel of the flume was meshed with a tetrahedral scheme and an interval size of 100.

4.3: Boundary conditions applied to reference, site and flume models

Following the application of boundary and volume types within Gambit, the meshed models were exported to a FLUENT™ mesh file. Each of the mesh files was read into Fluent where further boundary and material data were added using both the Graphical and Transcript User Interfaces (GUI) and (TUI).

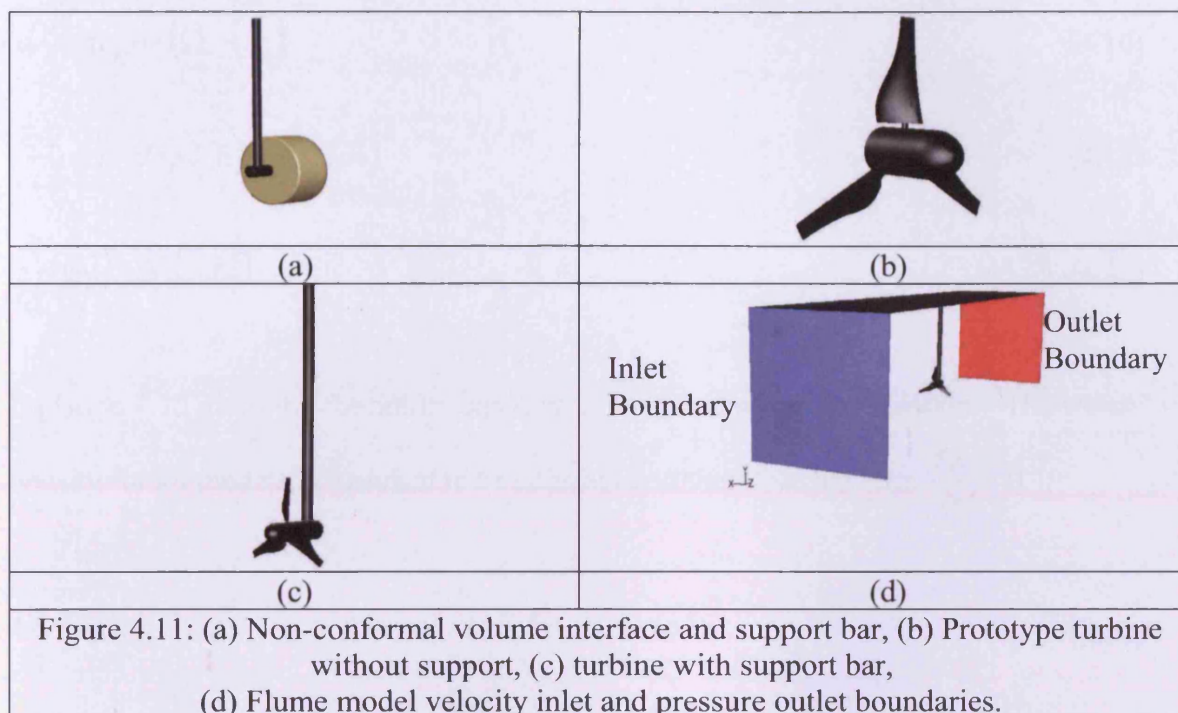
4.3.1: Quasi-static approach to HATT modelling

Temporal variables such as tidal velocity, throughout a tidal cycle, and angular position of the HATT blades were modelled using a quasi-static methodology, whereby the same domain was used but with variation to either the inlet boundary conditions or by pre-processing the rotational position of the turbine prior to exporting to FLUENT™. In this way a performance picture of the turbine was built up from the solution of each steady-state model. Therefore, the Fluent Time Solver was defined as steady using a Pressure Based formulation. The Absolute Velocity formulation was used with the Green-Gauss Cell Based Gradient option. For Solution Control flow, turbulence and Reynolds Stress equations were used with the Pressure-Velocity coupling set to use the semi-implicit methodology (SIMPLE). For the discretisation method the pressure was set to standard with the momentum, turbulent kinetic energy, turbulent dissipation rate and Reynolds stresses using a first order Upwind scheme. The under-relaxation factors were initially set to default so that Pressure = 0.3, Density = 1, Body Forces = 1, Momentum = 0.7, Turbulent Kinetic Energy and Turbulent dissipation rate = 0.8, Turbulent viscosity = 1, and Reynolds stresses = 0.5. However, these defaults were changed depending on the progress of each solution.

To assess the progress of each steady-state solution a number of monitoring points were created downstream of the turbine along the Z axis and given labels relative to their position, for example P50 = 50 m, P100 = 100 m etc. These were then read into the Define Surface Monitor where a report of velocity magnitude was applied to each monitoring point using an area-weighted average methodology. The labels for P50, P100 etc are then labelled V50, V100 etc. Each solution was initialised from the velocity-inlet with the reference frame relative to the cell zone.

4.3.2: Application of Moving Reference Frame (MRF)

As previously discussed a MRF model was used to simulate the rotation of the turbine. The MRF approach allowed the cells contained within the MRF to be modelled in an accelerating reference frame rotating the fluid entering the volume around its axis of rotation with the addition of its Z-axis component. The cells contained in the rectangular channel are modelled in a non-accelerating coordinate system separated by the non-conformal interface. Thus, during meshing the cells close to each surface do not share common nodes and therefore the mesh grid is also non-conformal. Under steady-state conditions there is no relative motion between the nodes attached to the MRF boundary and the channel surfaces therefore the non-conformal boundary between the turbine cylindrical and rectangular channel volumes does not require any temporal calculations and thus only a single surface layer is actually required between each volume. This gives the advantage of allowing cells adjacent to the surface to share common nodes. However, the non-conformal interface was retained in all models to allow the possibility of future temporal studies and to rotate the MRF within Gambit. In this way the position of the blades can be easily changed without having to remesh the turbine and MRF volume. To allow the diffusion of flow variables across the non-conformal mesh the cells attached to the outer surfaces of the MRF cylindrical volume and the surfaces remaining from the MRF channel subtraction were coupled using the Grid Interface commands within Fluent. Each of the aforementioned surfaces were previously defined within Gambit. All 3 surfaces associated with the MRF cylindrical volume were defined as 'turb_inter' while the remaining channel surfaces were defined as 'sea_inter'. Within Fluent these boundary definitions were coupled and defined as 'inter'. Figure 4.11 (a) shows the turbine interface (turb_inter) which forms the outer boundary of the MRF volume. Figures 4.11, (b), (c) and (d) show the prototype turbine, the turbine attached to the support tube and the velocity-inlet and pressure-outlet boundaries.



4.3.3: Momentum and continuity equations in MRF model

By introducing rotation to the mesh via the MRF additional acceleration terms were applied to the momentum equations. As the fluid enters the MRF through the non-conformal interface a rotational component is added with a magnitude equal to $\bar{\Omega}$ (rad/s) as specified via the FLUENT™ Graphical User Interface (GUI) and Terminal User Interface (TUI) interface or via a batch file. $\bar{\Omega}$ is the angular velocity of the MRF which in turn is translated to the turbine face cells, which is defined as ω (rad/s). For all the HATT models the velocity inlet was sufficiently far away from the MRF to use the absolute velocity formulation as shown in Equation 4.10 (Fluent, 2006). Where, \bar{u}_r is the relative velocity and \bar{r} is the position vector in the rotating frame. The additional rotation terms in the left hand side of the momentum equation, in absolute form, is given by Equation 4.11. Equation 4.12 is the left hand side of the momentum equation for the inertial channel volume.

However, it should be noted that since a steady-state methodology is used the temporal

component $\frac{\partial}{\partial t}(\rho\bar{u})$ in Equations 4.11 to 4.12 is 0.

$$\bar{\mathbf{u}} = \bar{\mathbf{u}}_r + (\bar{\boldsymbol{\Omega}} \times \bar{\mathbf{r}}) \quad (4.10)$$

$$\frac{\partial}{\partial t}(\rho\bar{\mathbf{u}}) + \nabla \cdot (\rho\bar{\mathbf{u}}_r\bar{\mathbf{u}}) + \rho(\bar{\boldsymbol{\Omega}} \times \bar{\mathbf{u}}) \quad (4.11)$$

$$\frac{\partial}{\partial t}(\rho\bar{\mathbf{u}}) + \nabla \cdot (\rho\bar{\mathbf{u}}\bar{\mathbf{u}}) \quad (4.12)$$

Equation 4.13 gives the continuity equation using the absolute formulation. The water density for all models is assumed to be constant and therefore the term $\frac{\partial \rho}{\partial t} = 0$.

$$\frac{\partial \rho}{\partial t} + \nabla \cdot (\rho\bar{\mathbf{u}}) = 0 \quad (4.13)$$

4.3.4: Power and wake sensitivity to MRF grid resolution

Sufficient grid resolution was required near the turbine and hub walls due to the rotational component, which can introduce very thin boundary layers (Fluent, 2006). To investigate solution sensitivity to grid size a series of models were run using the meshing schemes shown in Table 4.3. With increasing mesh density at the surface of each turbine blade changes in power extraction were monitored. The power extracted by the turbine for the fixed flume velocity (1 m/s) was used as a measure of the grid dependency.

4.3.5: Power and wake length sensitivity to MRF length

To investigate any effects on power extraction and wake length the length of the MRF was varied between 1.2 and 8 hub diameters downstream of the turbine along (δz_{DS}), Figure 4.12 where (δz_{DS}) is the distance between the rear face of the turbine hub and the downstream grid interface. The distance between the upstream hub tip and grid interface (δz_{US}) was maintained at 1.5 hub diameters in each case.

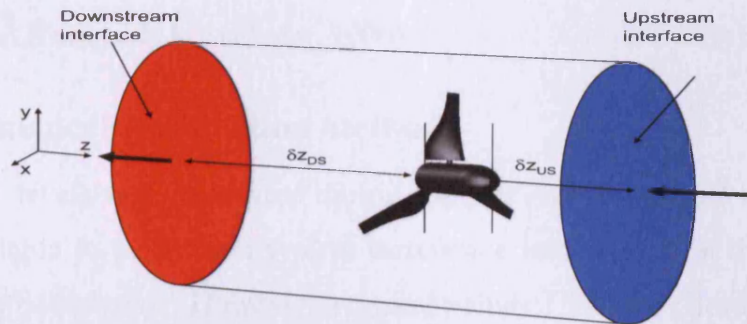


Figure 4.12: Power sensitivity to MRF lengths δZ_{DS} & δZ_{US}

4.3.6: Suitability of viscous model

Fluent gives the option to use both Reynolds averaging and filtering to avoid the direct simulation of small-scale turbulent fluctuations via the use of Reynolds averaging or Large Eddy Simulation (LES). In order to calculate each unknown related to these models a sufficient number of equations are required to achieve closure of the governing equations. From a convergence time and memory standpoint, the use of time averaged or ensemble averaged versions of the exact Navier-Stokes (N-S) governing equations was desirable due to the number of cells within the CFD models and the number of solutions required to generate a reasonably detailed turbine performance curves, such as torque, power and axial thrust. For all the models developed in this thesis this figure was approximately 1.3 million cells in total with approximately 1 million cells within the MRF turbine volume.

A practical solution between model size and accuracy was achieved via the application of the Reynolds Averaged Navier-Stokes (RANS) equations to relate the Reynolds Stresses to the mean velocity gradients also known as the Boussinesq approximation. With the use of models the RANS equations remove small and high frequency turbulent fluctuations thereby reducing the computational demands both in terms of memory and time. Due to its capability to model anisotropic flow all initial studies into mesh density and boundary flow concentration used the RSM model. A further study was later used to compare the results of other viscous models and measured data obtained from the flume tests. This included

the following viscous models: Spalart_Allmaras, Standard k-e, Renormalization-group (RNG) k-ε, and Realizable k-ε (Fluent, 2006).

4.3.7: Turbulence specification method

No turbulence levels were measured during the site ADCP transect surveys therefore no data was available to calculate a typical turbulence intensity (I) at the velocity-inlet and pressure-outlet boundaries. However, a typical value of 5 % for (I) was derived from LDA measurements of the flume channel (Owen, 2009). Therefore, as a base condition a uniform value of 5 % turbulence intensity was applied at the inlet and outlet boundaries. For the flume model the ‘turbulence specification method’ was used to enter a uniform constant turbulence value (Fluent, 2006). Using this methodology the turbulence intensity (I) and hydraulic diameter (D_H) method was used to define turbulence at the inlet boundary. I is the ratio of the root-mean-square of the velocity fluctuations (u') to the mean inlet flow velocity (u_a), Equation 4.14. $D_H = L$ was used to define the characteristic turbulence length scale (ℓ), Equation 4.17, where L is a characteristic length. The factor 0.07 is based on the maximum value of the mixing length for a fully developed turbulent pipe flow (Fluent, 2006).

$$I \equiv \frac{u'}{u_a} \quad (4.14)$$

Where:

$$u' \equiv \sqrt{\frac{1}{3}(u_x'^2 + u_y'^2 + u_z'^2)} \quad (4.15)$$

$$u_a \equiv \sqrt{u_{a,x}^2 + u_{a,y}^2 + u_{a,z}^2} \quad (4.16)$$

$$\ell = 0.07L \quad (4.17)$$

As previously stated no account was taken of a free water surface and as such the flow can be considered to be a fully enclosed pipe flow. Therefore, as a first order approximation

the empirical correlation derived for pipe flows was used to compare the turbulence intensity of the assumed fully developed upstream flow, Equation 4.18.

$$I = 0.16(\text{Re}_L)^{-\frac{1}{8}} \quad (4.18)$$

Where:

$$\text{Re}_L = \frac{\rho_w u b_T}{\mu} \quad (4.19)$$

For all the flume tests mains water was used therefore for the flume CFD model the water density was 1000 (kg/m³). For the water viscosity a constant default value of 0.00103 (kg/ms) at 20°C was also used as stored in the Fluent database and checked via Massey, (1989). Using these values I was calculated using the chord tip length at a flow velocity of 1 m/s.

Therefore:

(I) using tip chord length (0.0016 m) so that $L = b_T$:

$$I_{b_T} = 0.16 \left(\frac{1000 \times 1 \times (0.0016)}{0.00103} \right)^{-\frac{1}{8}} \times 100$$

$$I_{b_T} = 6.3 \%$$

Using the turbine diameter for the characteristic length ($L = b_D$)

$$I_{b_D} = 3.4 \%$$

As a guide a turbulence intensity of 1% or less is generally considered to be low and turbulence intensities greater than 10% are considered high (Fluent, 2006). The 5% value of I measured at the test flume was around the average of I_{b_T} and I_{b_D} and therefore seems a

reasonable approximation. As previously stated, no measurements were made during the ADCP measurements and therefore the 5 % value of I was extended to all CFD models developed for this thesis.

4.4: Determination of turbine power

As used extensively in the wind industry for over 30 years, the power characteristics of a HAWT can be estimated by representing the turbine as an actuator disk with an ideal frictionless efficiency (White, 1999). The ideal frictionless efficiency therefore results from the theoretical maximum power extraction which is typically stated in terms of the maximum power coefficient (C_p) as derived by A. Betz, (Betz, 1966). Using this methodology a theoretical limit ($C_{p,max}$) of $16/27$ or 0.593 is possible.

4.4.1: Forces on turbine blades

The power coefficient C_p used to relate the measured and calculated power extracted by the prototype HATT to the available power flux across the turbine swept area is given by Equation 4.20 (White, 1999). The methodology used for a HAWT can be applied to a HATT but with the density of air substituted for water. The density of sea water is regionally dependent and is influenced by both temperature and salinity with dissolved salts having the greatest regional influence (Encyclopaedia Britannica, 1965). For all the CFD models relating to an oceanic application a water density of 1025 kg/m^3 was used. However, for the flume studies a fresh water density of 1000 kg/m^3 was used to calculate all performance characteristics for both the measured and calculated CFD data.

$$C_p = \frac{P}{\frac{1}{2}\rho AV^3} \quad (4.20)$$

A real turbine is not frictionless, as assumed by the derivation of the Betz limit thus the force acting on the turbine is made up of the shear force on the turbine blades and the force due to the static pressure, hence

$$F = F_s + F_p \quad (4.21)$$

To calculate the force on a discretised turbine blade that has been divided into finite faces, the forces in the x , y and z directions must be considered. The force due to the static

pressure is given by the product of the static pressure and the area vector of the face, hence, in the x-component

$$F_{Px} = P \cdot A_x \quad (4.22)$$

Similar expressions apply for the y and z components.

The torque is required only for the components of the forces in which the plane of the turbine lies. Hence, if the turbine axis is in the z-direction, then only the forces in the x and y directions are required and for simplicity, the axis of rotation of the turbine was located at (0,0,0) of the global coordinate system. The total torque acting on the turbine then is the summation of the torque acting on each face which is given by the cross-product of distance and force vectors, i.e.

$$T = \sum_{n=1}^{n=N} [r_x x F_y - r_y x F_x] \quad (4.23)$$

The power extracted by the turbine is then given by:

$$P = T \cdot \omega \quad (4.24)$$

4.4.2 User Defined Function (UDF) for torque, power and axial thrust load calculations for all CFD models

To enable the calculation of torque, power and axial thrust a bespoke User Defined Function (UDF) was written in C++ and compiled in FLUENT™ 6.3.2. The UDF reports the power, torque, angular velocity, available energy, turbine efficiency and force components in the x, y and z directions. The UDF uses a combination of C++ code and predefined macros created by FLUENT™. The code was split up into two main sections: the first contains parameters that have to be defined by the user and the second is where the calculation routine is performed by FLUENT™. A copy of the UDF is given in Appendix 3.

4.4.3: Manual input of user defined variables for all models

To compile the UDF, Fluent was run via a Visual Studio.net command prompt. The UDF was then loaded into FLUENT™ via the User Defined command where the UDF library is

also created. The `#DEFINE T1_WALLS (number)` command was used to define the number of walls that make up the surface of the turbine. For all models the wall names were created in Gambit before exporting to Fluent. For all the models that follow in the thesis the number of turbine walls created remain the same. The turbine was split up into 3 parts each given the Wall boundary condition as defined by FLUENT™. Each turbine blade along with its connecting pin constitutes a single wall and the hub the final wall component. The label or ID for each wall was given by Fluent through the Define Boundary command and copied to the Fluent utility with the command `(T1wall_ids[T1_WALLS] = {ID1, ID2, ID3, ID3, ...IDn})`. The upstream tide velocity component (`DEFINE U_FS`), the turbine diameter (`DEFINE T1_DIAMETER`) and the domain name given to the MRF containing the turbine walls (`DEFINE T1_DOMAIN`) complete the user input to the UDF. The remaining data necessary to run the UDF were read from input to FLUENT™ via the Graphical User Interface (GUI) and Terminal User Interface (TUI) commands.

4.4.4: Code read input variables to CFD models

To calculate the torque from the forces exerted by each cell on the surface of each turbine blade, a matrix of the corresponding face areas (`F_A[ND_ND]`) and face centroid (`F_CEN[ND_ND]`) were created as static real variables. Variables were also defined for the rotational centre of the turbine defined by (`T1_CENTRE_{x,y,z}`) and the total torque (`T1_TORQUE`) created from lift forces. The extracted power (`T1_POWER`) was calculated from the product of angular velocity and the torque. The power coefficient (`Cp`) was then calculated from the available power over the swept area (`T1_MAX_POWER`). The angular velocity (`T1_OMEGA`) as input via Fluent's GUI was read and set using a macro (`T1_OMEGA = THREAD_VAR(T1ct).fluid.omega`). The coordinates for the turbine rotational axis were also set to the fluid origin using a macro (`THREAD_VAR(name).fluid.origin[x]`). For all the models it was important that the x, and y coordinates were at the fluid origin, however it is irrelevant where the rotational axis is positioned along the z axis. It should be noted that in the case of multiple turbines the coordinates to the centre of rotation for each turbine must be defined. A material property macro (`MATERIAL_PROP(THREAD_MATERIAL(T1ct),PROP_rho)`) allowed the

density of sea or fresh water (fluid_rho) to be read from the FLUENT™ material definitions, as input through the GUI, in much the same way as the angular velocity component. The hydrodynamic pressure and shear x, y and z component forces are stored in matrix form (T1_TP_FORCE[ND_ND] and T1_TS_FORCE[ND_ND]), respectively. Finally, the total pressure and shear x, y and z component forces are stored in their respective matrices (T1_TP_FORCE_T[ND_ND] and T1_TS_FORCE_T[ND_ND]).

4.4.5: Execution of On-Demand UDF

The UDF is run by the user following solution convergence. This is defined with the use of DEFINE_ON_DEMAND (name) in the code. This is located at the start of the calculation procedure. Once the UDF was activated through the GUI within FLUENT™ the mesh domain was read (DOMAIN*DOMAIN = GET_DOMAIN(1)). The torque and force vectors were initialised and reset to zero (T1_torque = 0.0 and NV_S(T1_Force,=,0)). A thread pointer then seeks the pointer to zone (T1_DOMAIN) along with the pointer to face thread data type on the turbine surface in this case labelled as (TURBINE 1). The resultant of the pressure and shear forces was subsequently calculated and stored in a matrix (T1_Force[ND_ND]) for the x, y and z components. The procedure was repeated for all the cells on the surface of each defined wall, in this case blade 1, blade 2, blade 3 and the hub. A for loop (i=0;i<T1_WALLS;i++) was used to calculate the pressure and shear forces on each cell face at a distance Δr from the rotational origin, Figure 4.13. The shear force components for the turbine were stored using: N3V_V(T1_ts_force,=,F_STORAGE_R_N3V(f,T1ft,SV_WALL_SHEAR)). The static pressure force components were calculated and stored using equations 4.25, 4.26 and 4.27:

$$T1_tp_force[0] = f_A[0]*F_P(f,T1ft) \quad (4.25)$$

$$T1_tp_force[1] = f_A[1]*F_P(f,T1ft) \quad (4.26)$$

$$T1_tp_force[2] = f_A[2]*F_P(f,T1ft) \quad (4.27)$$

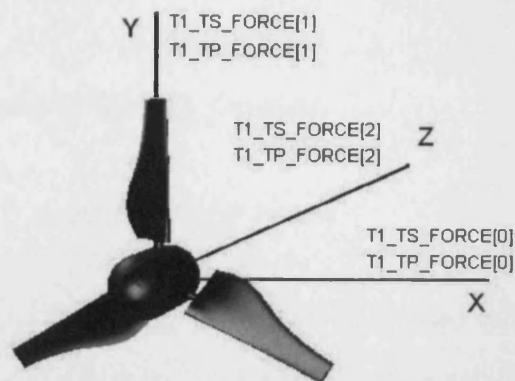


Figure 4.13: UDF blade force components

The resultant x, y and z force components for each blade and hub were then calculated from

$$T1_Force[0] += T1_tp_force[0] - T1_ts_force[0] \quad (4.28)$$

$$T1_Force[1] += T1_tp_force[1] - T1_ts_force[1] \quad (4.29)$$

$$T1_Force[2] += T1_tp_force[2] - T1_ts_force[2] \quad (4.30)$$

The torque generated by the turbine via energy extraction from the upstream water velocity was then obtained from:

$$T1_torque += (T1_tp_force[0]-T1_ts_force[0])*(f_cen[1]-T1_centre_y) - \\ (T1_tp_force[1]-T1_ts_force[1])*(f_cen[0]-T1_centre_x) \quad (4.31)$$

The maximum power available upstream of the turbine is given by Froude's momentum theory and was calculated in the UDF using Equation 4.32

$$T1_Max_Power=0.5*fluid_rho*(T1_Diameter/2.0)*(T1_Diameter/2.0))*pi*.... \\ U_fs*U_fs*U_fs) \quad (4.32)$$

Finally, the power extracted by the turbine along with its efficiency were calculated from Equations 4.33 and 4.34

$$T1_POWER = fabs(T1_torque)*fabs(T1_Omega) \quad (4.33)$$

$$EFFICIENCY = 100.0*T1_Power/T1_Max_Power \quad (4.34)$$

Following solution convergence for each angular velocity the data were used to build quasi-static torque, power and axial thrust curves for the prototype design.

4.4.6: Generation of torque, power and axial thrust curves

Angular velocity (ω) sweeps were run for a range of blade pitch angles, resulting in a series of torque and power curves, where pitch angle (θ) was defined as the angle between the chord of the blade and the normal to the rotational axis of the turbine hub. To limit the number of runs required to determine the optimum pitch angle (θ_p), coarse ω sweeps were run with changes in θ from 0° to 12° at increments of 3° . The torque (T) was calculated at every converged solution by integrating and resolving forces at each cell face via the On-Demand UDF. The power curves were calculated from the product of $T\omega$ (W) from which the peak power P_p (W) was established. The power available (P_a) for the swept area was calculated followed by the power coefficient (C_p).

4.5: Scaling for estuarine and oceanic application

Following the correlations between the measured and CFD flume data, further CFD studies were undertaken on the scaling of the turbine to match the power requirements necessary for economic power extraction from open estuarine and oceanic sources. A range of turbine diameters were studied, with an aim to test design specific non-dimensional relationships with changes in plug and profiled upstream velocity. Changes in the blade pitch angle was also included. Although the 0.5 m diameter HATT could in practise be used for irrigation or for low power energy generation in fast flowing rivers its output is far too small to be considered for any practical estuarine or oceanic electricity generation applications. In order to study the turbine's performance in large channels and open waters

the dimensions of the turbine were increased from the prototype model. In Chapter 2 a number of operational turbines were discussed such as the SeaGen, Lanstrom and OpenHydro designs. These designs have diameters between 10 m and 20 m depending on the depth of the water at the specific location. In Chapter 8 of this thesis a suitable size of the studied HATT will be discussed for a location within the inner Bristol Channel UK and Anglesey Skerries. The sizing of the HATT design will, in part, be guided and restricted by local shipping requirements. However, larger and smaller diameters will be studied in the scaling study to note and clarify any anomalies associated diameter variation.

Scaling the 0.5 m diameter prototype turbine to larger proportions may significantly change its operating parameters. Using the reference CFD model, these effects can be studied to give a qualitative insight to any changes in the turbine's operating conditions. The possibility that key performance parameters for the HATT may change as physical dimensions are increased or decreased is the main focus of the study. Parameters such as optimum blade pitch, angular velocity at peak power, torque and Reynolds number are fundamental to the design. To investigate possible changes, 5 CFD models were developed with increasing turbine diameter ranging between 0.5 m and 30 m. The boundary conditions were also scaled to maintain the same as the reference, deep water CFD model. The inlet velocity was defined as a plug flow with an inlet velocity of 3.08 m/s and a profiled flow was measured during the Severn Estuary surveys.

4.5.1: Non-dimensional analysis of CFD and measured flume data

To investigate its effect on torque, power and axial thrust load, the 0.5 m diameter HATT was scaled to larger diameters, using CFD. The aim was to firstly assess changes to its performance characteristics under ideal conditions. A plug flow was used for the upstream velocity, and the boundary conditions were matched to that of the reference CFD model. Non-dimensional parameters were then used to quantify the turbine performance as the turbine diameter was increased. An additional study was included to investigate the effect of a reduction in the upstream flow velocity at a fixed turbine diameter. Once the optimised performance was established for the turbine, a velocity profile was added to investigate power attenuation at depth. To determine the available energy in the upstream

flow, and hence the power, torque and axial thrust coefficients, the average velocity across the turbine swept area was established. The average of the Severn Estuary velocity profile, bounded by the turbine diameter, was calculated through its depth. The depth averaged velocity was then compared with the average velocity calculated from the volumetric flow rate across the turbine's swept area. The total volumetric flow rate (Q) was calculated by summing the products of $A_i \cdot u_i$; where A_i is the area at $(h_i + z)$ and u_i is the local velocity. The equation, used to discretise the turbine's swept area and to calculate (Q) is given by equation 4.35.

$$\sum_{H-r}^{H+r} Q_i = \underbrace{2r \sin \left[\cos^{-1} \left(\frac{r - ((h_i + z) + D_{H+r})}{r} \right) \right] z}_{A_i} \cdot \underbrace{u_f (D_{H+r} + (h_i + z))}_{u_i} \quad (4.35)$$

Where: (h_i) is the local radius along the swept area radius (r) , while (z) is the incremental step size.

The performance characteristics for the turbine were non-dimensionalised using Froude's Momentum Theory for an actuator disk, which discussed further in literature such as Chaney and Eggers, (2001) and Hansen, (2001). The performance data, measured during the flume tests, were also non-dimensionalised using the same non-dimensional groups. The combined non-dimensional CFD and measured flume data were then compared at the optimum blade pitch angle. The non-dimensional groups used for both the CFD and flume data include the power coefficient (C_p). C_p is the ratio between the energy extracted by the turbine to the total energy available over the turbine's swept area.

$$C_p = \frac{2P_a}{\rho A V^3} \quad (4.36)$$

The torque coefficient C_{Torq} was calculated by taking the ratio between the torque generated via the hydrodynamic lift and the maximum theoretical torque.

$$C_{\text{Torq}} = \frac{2T}{\rho A r V^2} \quad (4.37)$$

The thrust coefficient (C_T) is the ratio between the axial thrust along the rotational axis of the turbine, generated via the hydrodynamic drag on the rotor blades and hub, and the axial thrust load over the swept area of the turbine.

$$C_T = \frac{2F_T}{\rho A V^2} \quad (4.38)$$

As proposed by Osborne Reynolds, the Reynolds number is the ratio between the viscous and inertial forces and can be used to characterise the turbulence of the main flow field.

$$\text{Re} = \frac{\rho V d}{\mu} \quad (4.39)$$

The ratio between the tangential velocity at the tip of the blade and the upstream velocity of the tidal flow is given by the tip speed ratio (TSR).

$$\text{TSR} = \frac{\omega r}{V} \quad (4.40)$$

If the performance curves of the non-dimensional groups C_p , C_{Torq} and C_T all collapse onto the same curve, for the conditions previously discussed, it is proposed that the scaling is independent of the Re number. An independence from the Re number allows the performance characteristics of larger devices to be predicted from the performance of smaller devices, such as the prototype HATT. Flow concentration effects between the turbine and boundary were then assessed by comparing the flume CFD model power curve with the power curves from the scaled reference CFD models.

4.5.2: Scaling of a HATT

It was proposed by (Egarr et al, 2003) that key operational parameters of a scaled turbine could be calculated from a single CFD analysis if the process proved to be independent of the Re number. To investigate if the peak power and performance curves for a HATT with different diameters could be predicted with the use of non-dimensional parameters, CFD models were developed with HATT diameters of 0.5 m, 6 m, 10 m, 15 m, 20 m and 30 m. The 0.5 m diameter flume data was also used to verify the models.

4.5.3: Peak power calculation using scaling

The prediction of the peak power extraction with increasing diameter was also studied following CFD analysis and the establishment of the peak power coefficient (C_p). The power extracted can be expressed as a function of the available power and the efficiency of the turbine. The upstream tidal velocity can be calculated from Equation 4.40.

Substituting (4.40) into (4.36) and rearranging with A expressed as a function of the turbine diameter gives:

$$P = C_p \frac{\rho \pi D^5 \omega^3}{64(\text{TSR})^3} \quad (4.41)$$

Either the angular velocity or the diameter can be eliminated from (4.41) by substituting (4.40) as required. Equation 4.42 is expressed in terms of angular velocity.

$$P = C_p \frac{\pi \rho (\text{TSR})^2 V^5}{2\omega^2} \quad (4.42)$$

Equation 4.42 is semi-empirical as the TSR and C_p of the turbine must be known. However, once this data is available, the power extracted can be predicted for any turbine diameter in any tidal flow.

The semi-empirical relationship relies on data obtained from CFD models and or experimental measurements to estimate the power generated by the HATT, from which the variance in C_p can be calculated. Once C_p is known for a predefined design over an angular velocity range it is possible to use the non-dimensionalised curves to predict the power for a range of HATTs with varying diameters and/or upstream water velocity. Moreover, by substituting ω/TSR for V/D in Equation 4.42 the peak power (P_p) can be expressed as:

$$P_p = C_p \frac{\rho \pi D^5}{64} \left(\frac{2V}{D} \right)^3 \quad (4.43)$$

Grouping known terms and substituting values gives:

$$P_p = kD^2 V^3 \quad (4.44)$$

Equation 4.44 can therefore be used to calculate P_p subject to variation in diameter and upstream water velocity and is a convenient way to represent the design specific power extraction in graphical form.

4.6: Optimisation of a deep water 10m diameter turbine reference CFD model with plug flow

Pertaining to the deep water conditions outlined by Black and Veatch, (2005), a 50 m water depth was selected for the CFD model. The deep water reference model consists of a single 3 bladed 10 m diameter HATT located in a MRF with its axis of rotation 25 m below the water surface boundary, Figure 4.14. The MRF allowed the angular velocity (ω) of the turbine to be varied for each given tide velocity by applying the rotational component $\bar{\Omega}$ to the MRF volume. The MRF volume was subtracted from the 50 m x 50 m x 500 m rectangular channel where upstream and downstream boundary conditions were applied using the same L/D ratios as described for each of the models.

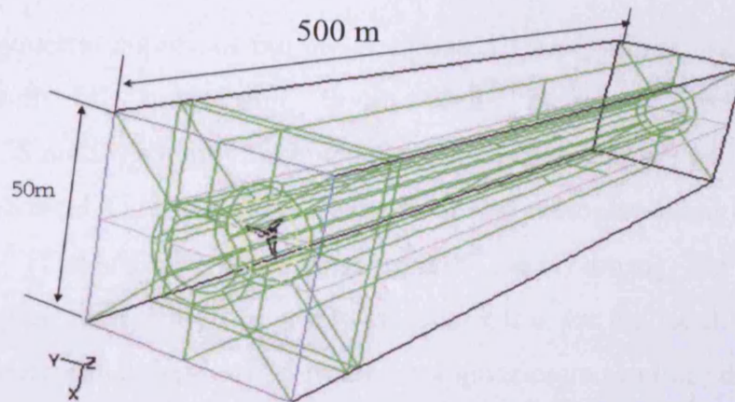


Figure 4.14: Dimensions of deep water reference CFD model

Since the ADCP measurements discussed in Chapter 9 did not include turbulence intensity an estimate for the scaled turbines was based on the turbulence intensity and hydraulic Diameter method as used in the previous CFD models. To maintain consistency with the flume model a turbulence intensity of 5% was also applied at both the velocity-inlet and pressure-outlet. The characteristic length for the flume model ($L = b_T$) was also applied to the reference model. The velocity-inlet and pressure-outlet were positioned 10 diameters upstream and 30 diameters downstream of the turbine, respectively. To simulate an open water scenario zero friction was applied to the sides and surface boundaries of the channel, however for the seabed the no-slip formulation was assumed. As in the previous models, the water depth was assumed to be such that there was no interaction between water surface and the turbine. For plug flow conditions, the velocity profile was allowed to develop upstream of the turbine with a peak value of 3.08 m/s (6 knots). The latter velocity was chosen to define peak conditions for the turbine as 3.08m/s is approaching the higher end of the economic potential for UK sites (Black and Veatch, 2005).

At each converged steady-state solution, the previously discussed on demand User Defined Function (UDF) was used to extract the torque (T) and axial thrust force (F_T). The user defined variables for turbine diameter, water velocity and wall IDs were altered to match the dimensions, tidal flow and turbine face IDs for each blade and hub.

4.7: 10 m diameter site turbine reference CFD model with plug flow

The SWATH bathymetric survey of the pre-designated 1 km² survey site approximately 3 nautical miles south of Stout Point, South Wales in water depths varying from approximately 18-35 mCD (where CD represents the chart datum which is calculated from the Lowest Astronomical Tide, LAT) was used to define the operational conditions for the site CFD model. The ADCP site measurements made during the spring ebb tide represented the highest tidal velocities and lowest slack tide for the location. The site CFD domain was modelled with a depth of 35 m which approximated to the tidal height HSW+3 hrs, Figure 4.15. During this time period the peak tidal velocity was approximately 1.8 m/s and occurred 1 m below the water surface. To enable the use of these data with that of the reference and site CFD models, the velocity magnitude of the profile was scaled to a peak of 3.06 m/s, since these models were previously used to study peak conditions. However, the rate of the velocity attenuation through the water column was maintained the same. The characteristic length for the reference model ($L = b_T$) was also applied to the site model. The velocity-inlet and pressure-outlet were also positioned 10 diameters upstream and 30 diameters downstream of the turbine, respectively. To simulate an open water scenario, zero friction was applied to the sides and surface boundaries of the channel. For the seabed the no-slip formulation was assumed. No interaction between surface waves and tidal current was considered. For plug flow conditions, the velocity profile was allowed to develop upstream of the turbine with a peak value of 3.08 m/s (6 knots).

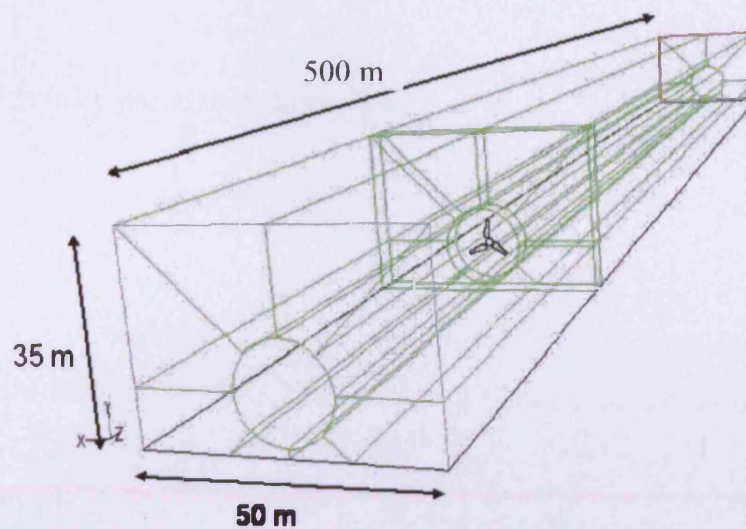


Figure 4.15: Dimensions of 35 m depth site CFD model

4.8: Power attenuation in 35 m depth reference CFD model (Severn data)

To study power attenuation effects through the water column in the 35 m depth CFD site model a profiled flow field was derived from averaged ADCP data and applied to the velocity inlet boundary of the CFD model using a UDF written in C++ and compiled in FLUENT 6.3.2. The UDF labelled, `inlet_parab`, uses a polynomial curve fit to distribute the water velocity to each cell face through the Y axis or depth of the CFD model. By creating a loop the coordinates of all the faces belonging to the identified thread are assigned a velocity component perpendicular to the inlet face, according to depth. A series of floating variables are also created such as `FLOAT x[3],y` which relates to the face centroid coordinates and `FACE_t f` which is the face identifier. The velocity perpendicular to the velocity inlet V_z is then calculated from a polynomial curve fit, Equation 4.45. A further set of floating variables are required to account for the constants derived from the curve fit, with the number of variables depending on the order of the polynomial required to accurately represent the measured velocity data. The `inlet_parab` UDF is given below:

```

#include "udf.h"

DEFINE_PROFILE(inlet_parab,thread,equation)
{
float x[3],y;
face_t f;
float Vz;
float C1 = ##;
float C2 = ##;
float C3 = ##;
float C3 = ##;
float Const = ##;

begin_f_loop(f,thread)
{
F_CENTROID(x,f,thread); /*get the face centroid coordinates*/
y=x[1];

Vz = -(C1*y*y*y*y)-(C2*y*y*y)+(C3*y*y)+(C3*y)+ Const;          (4.45)

F_PROFILE(f,thread,equation)=Vz;
}
end_f_loop(f,thread)
}

```

To study how the velocity profile affects the power attenuation through the water column a series of CFD models were developed with the turbine's rotational axis positioned at a number of depths as given in Table 4.4. Due to the fact that the velocity of the water is reducing through the water column, the angular velocity of the HATT had to be altered to maintain optimal performance. An initial guess at the optimal angular velocity can be made through the use of the relationship between the Tip Speed Ratio (TSR) and the ratio between the product of the angular velocity (ω) and blade tip radius (r) to the upstream water velocity (V). Since the turbine diameter is also bounded by a profiled flow which introduces a shear rate through the depth, the magnitude of the mean velocity will therefore depend on the rate of change of velocity with depth, a further reduction in performance and operational parameters such as TSR through a full rotation will result in changes to blade axial loading and power extraction.

Table 4.4: Rotational axis depth for 10 m turbine in 35 m depth

CFD domain depth 35 m
9
11
13
15
17
19
21
23
25

4.9: Power attenuation in 50 m depth reference CFD model (Severn data)

To study power attenuation effects through the water column in the 50 m depth reference model, a profiled velocity-inlet was derived from normalised and rescaled ADCP data measured on site within the inner Bristol Channel, UK. The profile was scaled from the 35 m depth site model as discussed and applied to the velocity profile UDF. As in the site case, a series of CFD models were developed with the rotational axis of the turbine positioned at various depths through the 50 m depth, Table 4.5. As in the reference CFD model the width of the domain is 50 m with an overall downstream channel length of 300 m and 100 m upstream. Again, zero shear stress is applied to the sides and surface boundaries of the domain with the No-slip boundary applied to the seabed.

Table 4.5: Rotational axis depth for 10 m turbine in 50 depth .

CFD domain depth 50 m
12.9
15.7
18.6
21.3
23.3
27.1
30.0
32.9
35.7

4.10: Velocity profile survey at 3 locations within the Anglesey Skerries

In addition to the Severn Estuary data, ADCP surveys were performed within the Anglesey Skerries by the School of Earth, Ocean and Planetary Sciences, Cardiff University, to give a perspective on the data obtained from the Severn Estuary location. The velocity profiles were measured during a neap tide cycle while anchored at 4 identified sites shown in Figure 4.16, using the same procedure as previously discussed in 3.10. To give an idea of the velocity profile variability across each site, measurements were taken along a predetermined transect line, Figure 4.16. Velocity profiles were measured during the flood and ebb of a neap tidal cycle along the transect line as shown. By comparing these curves with those obtained from the Severn Estuary survey a more informed conclusion could be made on power attenuation through the water column.

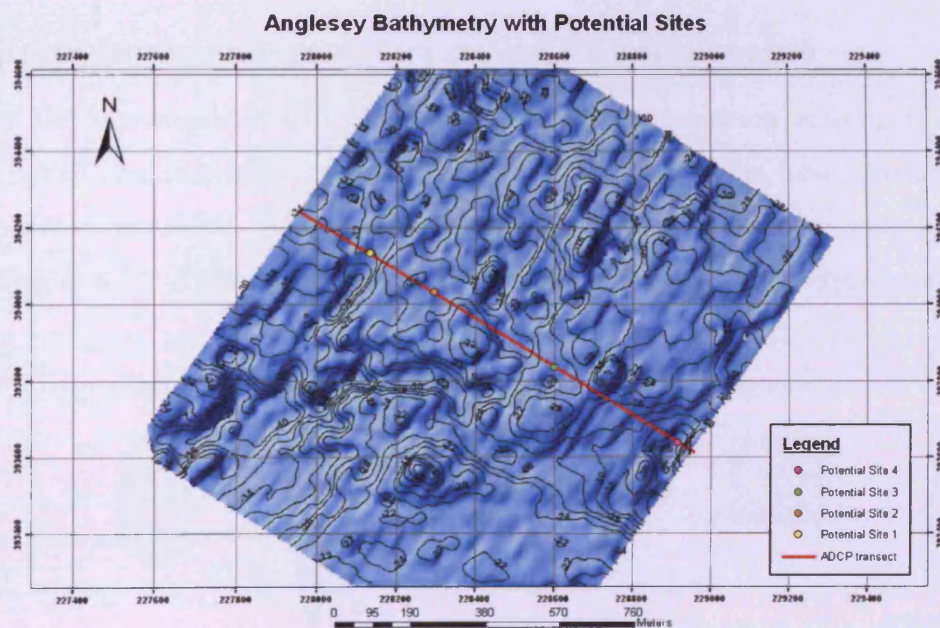


Figure 4.16: Proposed HATT sites along transect line within the Anglesey Skerries.

4.11: Turbine stanchion loading

Prior to an investigation into power attenuation from turbine and stanchion interaction the drag characteristics of five different stanchion geometries were studied with the stanchion positioned downstream of the turbine. The intention of this study was to isolate the axial loading of the stanchion from that of the turbine. Five basic geometric shapes were chosen

for a 20 m depth domain. The cross sections include a diamond, square, profiled, elliptical and circular stanchion. The dimensions for the CFD model in this case were based on the site model with a depth of 35 m and a width of 50 m. The upstream and downstream dimensions were maintained the same as both the reference and site CFD models. The viscous models and associated parameters were set to match that of the reference CFD model. The rotational axis of the turbine was set at 10 m above the seabed. The section of stanchion above the turbine was extended to the surface boundary.

Although a factor in the performance of the HATT, differences in stanchion width were not included and the stanchion was assumed to be rigid and therefore maintained alignment between the HATT hub rotation axis and the upstream flow path.

4.12: Effect of stanchion geometry on HATT performance

To further the investigation into the effects of power attenuation relating to the 10 m diameter HATT a study was undertaken on the interaction of the turbine with a vertical seabed mounted stanchion. Five basic geometric shapes were used to study axial thrust loading, Figure 4.17, followed by the dam effect of the chosen geometry upstream of the stanchion.

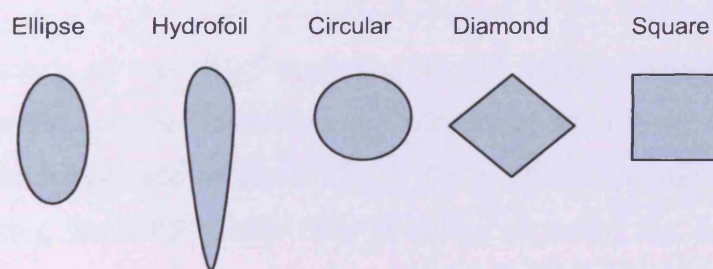


Figure 4.17: Stanchion geometries for axial thrust load study

In each case the turbine blade centre was positioned 2 m in front of the stanchion, Figure 4.18 with the same upstream and downstream position as in the site and reference CFD models.

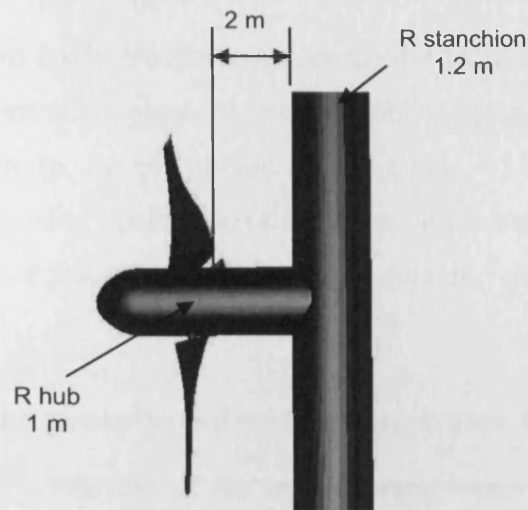


Figure 4.18: Distance between turbine blades and stanchion

The space between the turbine swept area and the boundary walls was also maintained along with the same boundary definitions such as no-slip for the seabed and zero strain rates at edge and surface boundaries. As in the other models a set of angular velocity sweeps were run to establish the optimum angular velocity for each case.

4.13: Effect of blade position on turbine performance with and without stanchion

With the introduction of a profiled upstream velocity profile distribution, oscillations in power generation and axial thrust loading will become an issue as the turbine blades rotate. To investigate the magnitude of these effects the rotational position of each blade was changed by rotating the MRF within Gambit before exporting the model to FLUENT™ thus allowing a steady-state solution to be performed for each rotational position. The study was then extended to include the stanchion and velocity profile.

As discussed in Chapter 2, a typical velocity profile can be estimated from the $1/7^{\text{th}}$ power law. The $1/7^{\text{th}}$ power law was used as a base profile condition to compare oscillatory power and axial thrust results obtained when using a profiled velocity inlet derived from site ADCP data.

5: Recirculation water flume and ADCP measurements

It was imperative to study the performance of the existing 0.5 m diameter prototype HATT within a controlled physical environment if optimal design functionality at a planned location were to be studied using CFD. Torque and angular velocity measurements were made via the use of a re-circulating water flume at the University of Liverpool, School of Engineering, producing data for the validation of a numerical model.

5.1: Validation of prototype design using water flume

Figure 5.1 shows a schematic of the re-circulating water flume at The University of Liverpool. An axial flow impeller is driven by a 75 kW motor capable of pumping a water capacity of approximately 80000 litres. Following pumping via the impeller the water passes through a long circular diffuser from which it travels into a rectangular cross-section. To ensure flow uniformity, honeycomb and contraction guide vanes are used prior to the water entering the working section. The working section was set to be an open channel, allowing the prototype turbine to be lowered and installed from above. At the downstream end of the working section flap 1 was adjusted to separate the top most layer of the water from the main flow. The separated water is then slowed down by passing it through a divergent section that contained gauzes which allow enough time for air to escape from the flow.

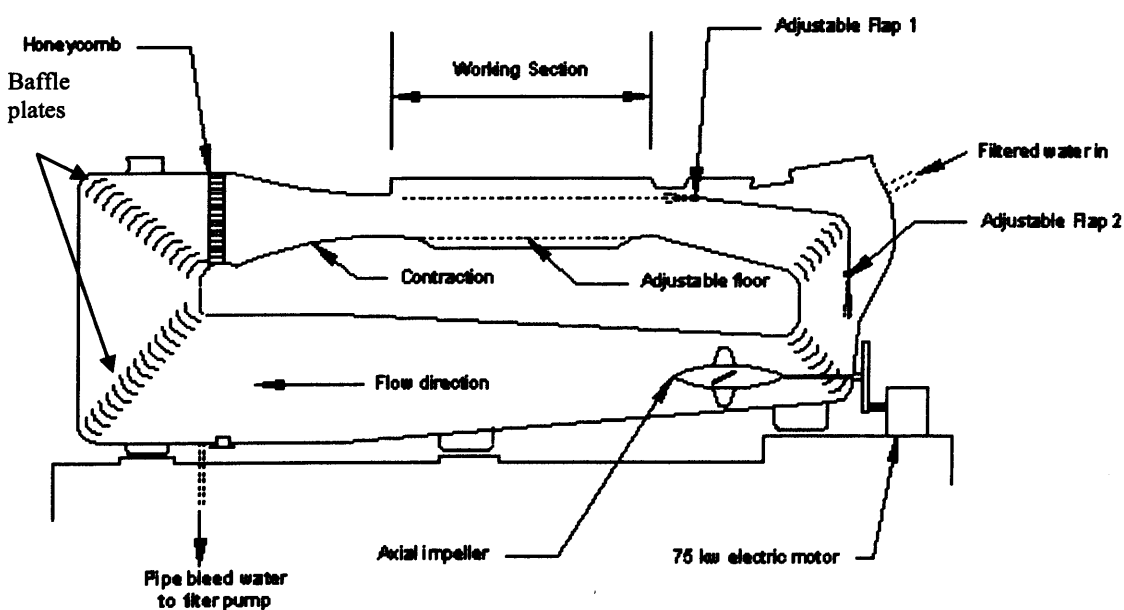


Figure 5.1: Schematic of re-circulating water flume at The University of Liverpool

The separated flow is then reintroduced to the main flow by adjusting flap 2. Following passage through another set of guide vanes the flow is re-circulated around the flume by the impeller. To account for, and adjust for surface velocity deficits from air drag a jet system is provided at the beginning of the working section to bleed off water in a plane jet at free surface level through a 1 mm wide slot which in turn spanned the whole width of the working section. Therefore the water surface velocity deficit due to air drag can be removed by varying the jet velocity. The boundary layers for the flume floor and side walls were of the order of 16 mm normal to the surface (Owen, 2009).

The dimensions and flow specifications of the working section are given below:

Width = 1.4 m

Length = 4 m

Range of depth = 0.15 m to 0.85 m

Range of velocity = 0.03 to 6.3 m/s

5.1.1: Servomotor and control system

A system was devised to enable the testing of the prototype HATT design by which the torque generated via the hydrodynamic lift was opposed by an AC servomotor. A BALDOR brushless AC servomotor, Figure 5.2, manufactured by BALDOR Electronics CO. was selected and combined with a control system which in turn was programmed via a laptop computer. Table 5.1, gives the turbine's specifications.



Figure 5.2: BALDOR AC servomotor

CAT	BSM80N-375AF	
SPEC	S2P131W035G1	
MFG	W0705217037	
TORQ	CONT.	3.52 Nm
STALL		
CURR	CONT.	5.35 A (RMS)
STALL		
POWER	1.28 kW	
RATED SPEED	3000 RPM	
RATED	BUS	300 VOLTS
VOLTAGE		
PEAK CURRENT	19.3 A (RMS)	
MAX SPEED	7000 RPM	
CLASS	F	
	25°C AMB	

Figure 5.3 shows a schematic summary of the recommended wiring for the servomotor control system. The optional regen resistor or dynamic brake was used to apply an opposing load to that developed by hydrodynamic forces from the turbine. Figure 5.4 shows the final assembly situated within its protective control container. The motor power, feedback and serial communication cables were sealed and protected from water ingress at the container outlet with rubber seals.

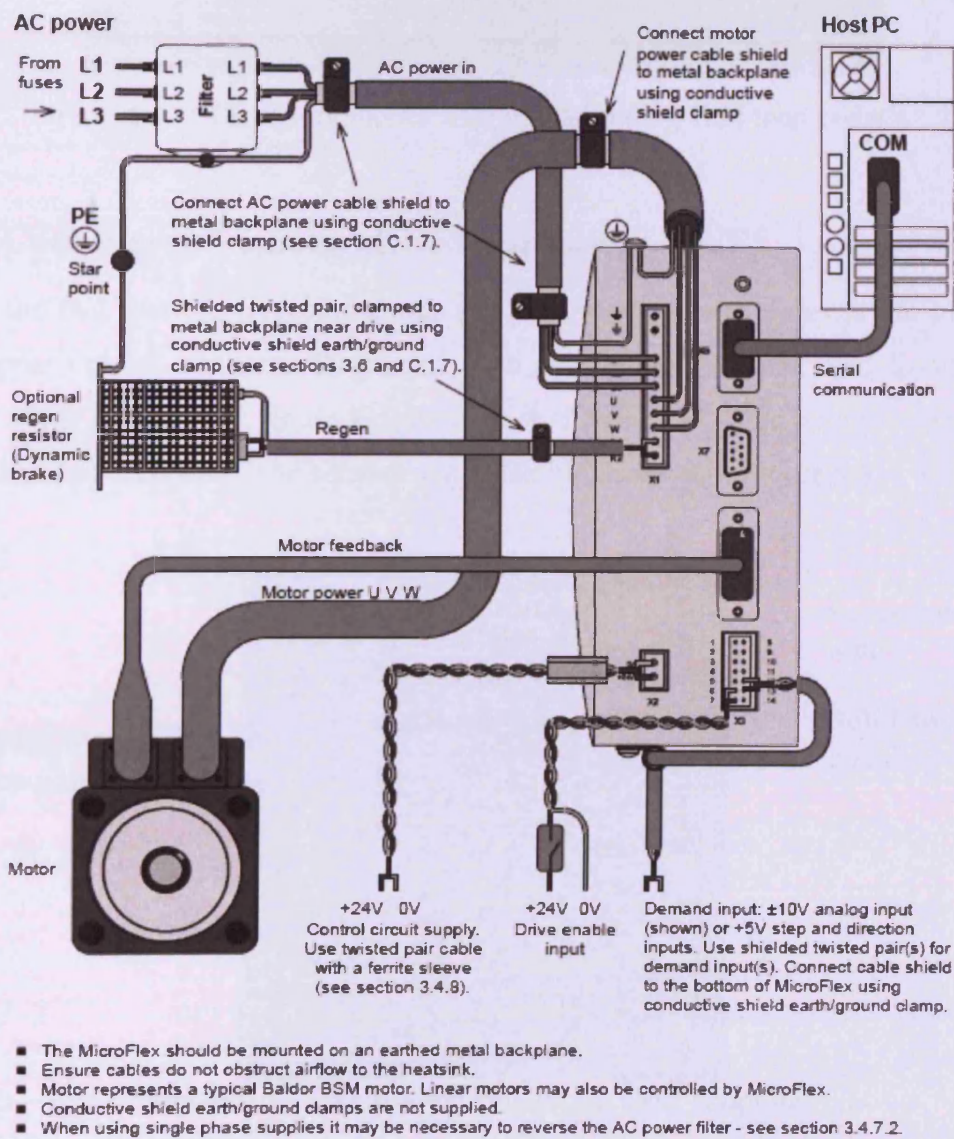


Figure 5.3: Schematic of connection summary - recommended wiring for servomotor and control system. Source: Baldor Motion Products, 2005.

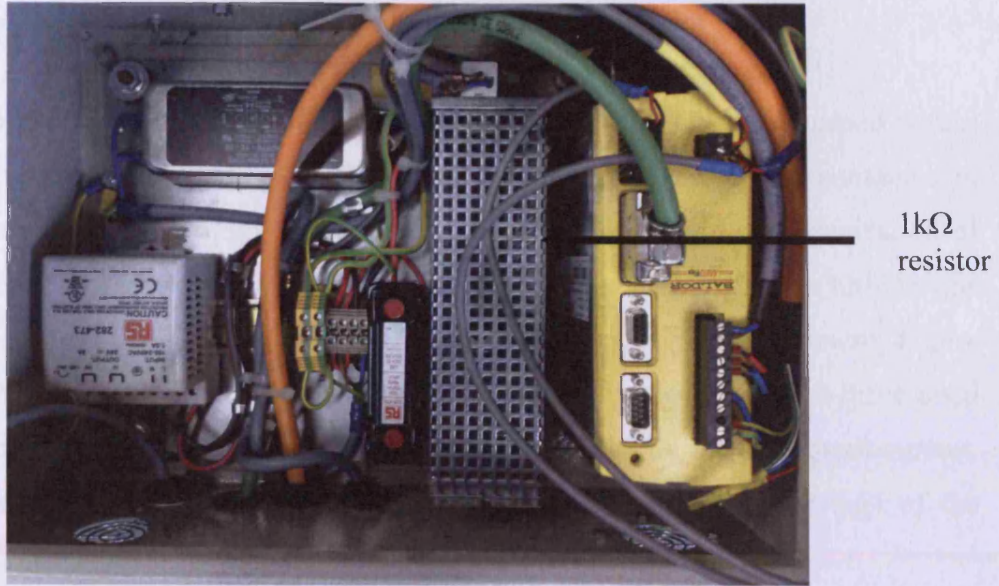


Figure 5.4: Final servomotor assembly showing 1kΩ load resistor

5.1.2: Coupling servomotor drive to prototype HATT

Due to the fact that the servomotor was not waterproof, it was necessary to locate the servomotor out of contact with water. Two configurations were used to attach the turbine to the servomotor; firstly a rigid drive shaft was used fitted with universal joints at either end of the shaft. The second was a flexible drive shaft Figure 5.5.



Figure 5.5: Flexible and solid drive shaft couplings

5.1.3: Programming and servomotor control for flume tests

The servomotor torque was controlled using software package MintMT housed within WorkBench v5 (Baldor, 2005). By using the motion-specific keywords contained in MintMT, control over the motor's speed, torque, interpolation and synchronization of multiple axes was obtained. For the flume tests the torque supplied to the turbine was controlled via the TORQUEREF command embedded in an incremental macro, Figure 5.6. Values between $\pm 100\%$ gave the torque demand as a percentage of the drive rated current. It was however possible to specify values up to $\pm 200\%$, the drive peak current. The rotational direction of the prototype HATT was controlled via the sign of the TORQUEREF value.

```

dim i
cancel
capturemode.0=25
capturemode.1=22
captureperiod=800000
capture=1
driveenable=1
Percent of angular velocity (%) → for i = 5 to 75 step 5
torqueref=i
Sample period (ms) → wait=10000
?"Speed = "; speedmeasured * 6.28 / 6; "rad/s"
?"Torque = "; currentmeas.0 * 0.906; "Nm"
next
driveenable=0
capture=0

```

Figure 5.6: Torque macro for servomotor flume tests

Within the written torque macro the FOR loop was used with limits, incremental steps and the WAIT command between increments. The WAIT command was used to allow the rotational speed of the turbine to stabilise once the next value of torque was applied. However, while running the TORQUEREF command the turbine could be stopped with ABORT, CANCEL, STOP, RESET, RESETALL or by an error condition.

To run the controller in TORQUEREF mode, the axis control mode was set to CURRENT and the axis enabled with its mode set to zero. Then for example with TORQUEREF = 50, 50% of the motor rated current is applied. By setting

TORQUEREF = 0 the turbine was allowed to freewheel as no current is applied, such as in the case of the initial setting. It should be noted however that Setting TORQUEREF = 0 did not change the axis mode. This can only be achieved through the mode specification method such as current, velocity and position.

The torque generated by the servomotor was proportional to the drive rated current, in this case 6 A (max). The current limit throughout the tests was set to 70% of the current limit giving a peak of ~4.2 A. The relationship between current and torque for the servomotor is linear with a proportionality constant of 0.906 (Nm/A) (Baldor, 2005). Taking the product of the peak current and torque proportionality constant, a peak torque of ~3.8 Nm was obtained.

The corresponding rotational speed of the motor was measured as a percentage (speed%) of the rated rotational speed for the motor which was 1000 rpm for the setup discussed in this thesis.

Therefore the angular velocity of the turbine for each load case was calculated using:

$$\omega = \frac{\text{speed}(\%)}{100} \times \frac{1000}{60} \times 2\pi = \text{speed} \times \frac{\pi}{3} \quad (5.1)$$

5.1.4: Setting optimum blade pitch angle on prototype HATT

Figure 5.7 shows the assembled 0.5 m diameter prototype HATT with the stanchion attachment point and nylon nose cone. Figure 5.7 also elucidates key geometric features such as the blade tip and root along with the blade to hub connection pin. The three turbine blades were fixed to the hub by tightening screws to the rear of the hub.

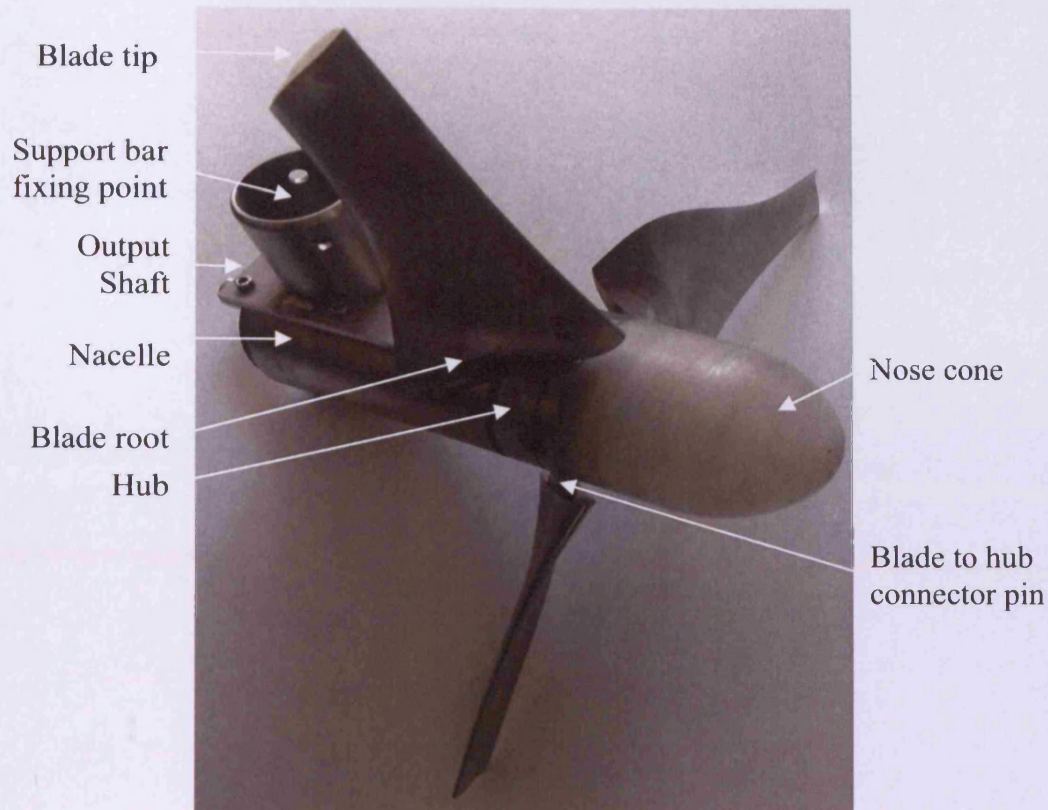


Figure 5.7: 0.5 m diameter prototype HATT

The optimum pitch angle, as calculated from the BEM and confirmed by CFD, was set using precision machined blocks and a marking table, Figure 5.8. The optimum angled block was aligned with the chord at the tip of the blade and the hub assembly slackened via the hub retaining screws.

The hub assembly screws were then retightened following the blade pitch adjustment of the remaining two blades. Prior to attaching the turbine assembly to the cylindrical supporting bar the nylon nose cone was re-attached to the front of the turbine hub assembly. In all cases the blades and hub were assembled prior to attaching the blade hub assembly, the nacelle and the cylindrical supporting bar.

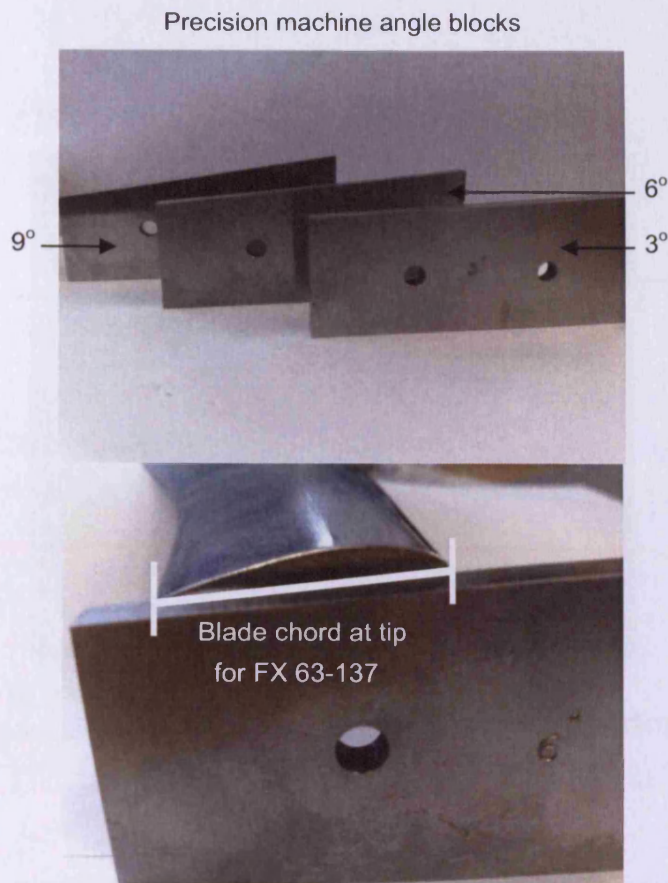


Figure 5.8: Angled precision blocks with 6° block aligned with blade tip on surface table

5.1.5: Prototype HATT and re-circulating water flume placement

The turbine blade and hub assembly were then attached to a cylindrical supporting stanchion which in turn was attached to a rectangular cross beam spanning the 1.4 m width of the flume working section. The prototype turbine was then positioned midway through the depth and width of the channel, Figure 5.9. The water depth of the flume was set at 0.85 m making the rotational axis depth of the prototype HATT 0.425 m below the surface and above the channel floor. Figure 5.9 also shows the servomotor setup using the solid drive coupling. The solid driveshaft can be seen leaving the water surface and passing behind the main supporting frame before being attached to the servomotor (not shown).

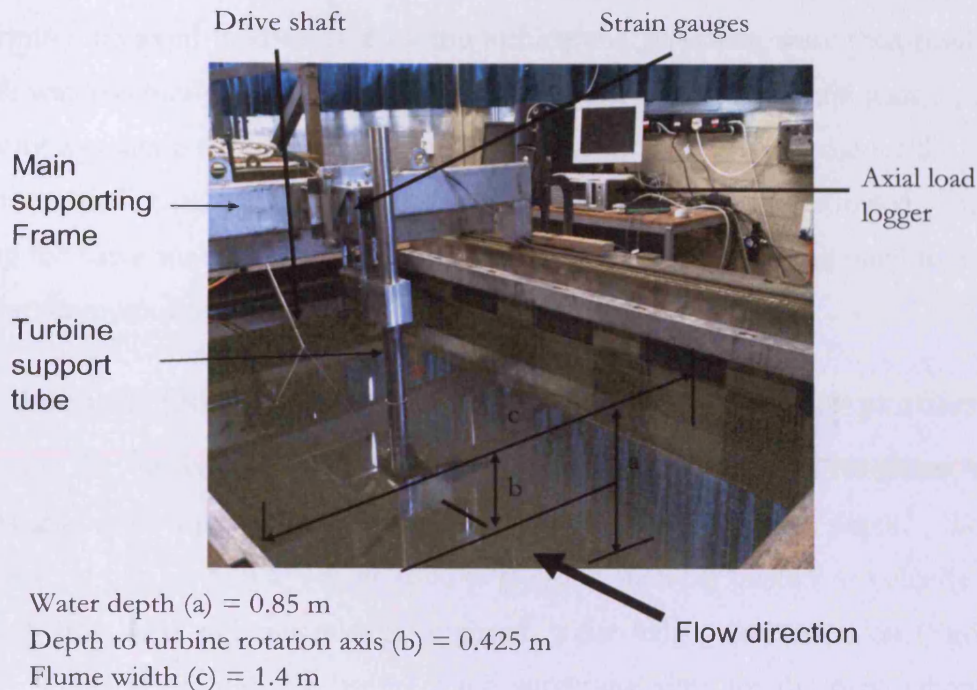


Figure 5.9: Turbine positioned in circulating water flume at the University of Liverpool

The assembly holding the support bar to the cross beam also housed strain gauges which were used to determine the axial load exerted by the turbine throughout each angular velocity sweep. The strain gauges were zeroed with the flume water velocity set to zero while a test file was created on the strain logger. The water velocity within the flume was then slowly increased to 1 m/s. With a zero load applied to the servomotor, the HATT was allowed to freewheel at the start of each test procedure.

5.1.6: Verification of optimal blade pitch angle using water flume

To verify the optimal blade pitch angle derived from BEM and CFD, blade pitch angles were selected either side of the calculated optimum angle. The prototype turbine blades were again adjusted using angled machined spacers and a marking table. As with the optimal blade pitch angle, the edge of the angled spacer was aligned with the chord of the blade tip profile. The securing screws at the hub were slackened so as to enable each blade to rotate about the centre of the connecting pin. This procedure was then repeated for the remaining two blades. Once the blade pitch angle for each blade was set the retaining screws for the hub assembly were tightened and the blade pitch re-

checked. The prototype turbine was then returned to the flume and attached to the supporting stanchion as previously shown in Figure 5.9. The strain gauges used to determine the axial load exerted by the turbine and stanchion were then reset with the flume water velocity set to zero. Following the zeroing of the strain gauges, the water velocity was again slowly increased to 1 m/s. As in the previous case for the calculated optimum blade pitch angle the servomotor and the turbine were allowed to freewheel. Using the same macro, as discussed in Section 5.1.3, a load was applied to the turbine via the servomotor and the TORQUERE macro.

5.2: Acoustic Doppler Current Profiler (ADCP) velocity profiles

Although they serve as a useful tool in the initial identification of resources, admiralty charts give little insight on how the velocity field changes with depth. To fill this information gap an ADCP can be used to measure such parameters as velocity variation through the water column and, if required, wave height and direction (Strong et al, 2000). This is particularly useful when surveying sites for the deployment of tidal stream devices as local velocity profiles can have a significant impact on the estimated energy extraction for the site in question. Depending on the orientation of interest an ADCP can be configured to measure water velocity in the horizontal plane, such as between two shore lines or harbour walls or vertically through the water column. An ADCP can be seabed (looking up) or surface (looking down) mounted. The surface ADCP can be fixed to a buoy or anchored vessel, alternatively it could be operated while attached to a moving vessel. For the work carried out in this thesis an ADCP was attached to the side of a vessel since only the velocity profile through the water column is of primary importance. However, by performing a series of surveys along a transect line, a picture of the horizontal flow field can also be developed for the Severn and Anglesey site locations. The sites were represented by site number and their corresponding latitude, longitude, easting and northing, Table 5.2.

Table 5.2: Coordinates for proposed HATT sites

Severn Estuary Survey				
Site number	Latitude	Longitude	Easting	Northing
1	51.3307933	-3.3953339	365598	5688058
Anglesey Surveys				
1	53.41578397	-4.58693103	228172	394114
2	53.41499957	-4.58442065	228336	394020
3	53.4138023	-4.57981925	228637	393876
4	53.41205332	-4.57494865	228953	393670

5.3: ADCP data for profiled flow analysis at Severn Estuary and Anglesey locations

A hull-mounted Acoustic Doppler Current Profiler (ADCP) was used to estimate the horizontal and vertical velocity as a function of depth by using the Doppler Effect to measure the radial relative velocity between the instrument and that scattered in the ocean. As a minimal requirement for measuring the three velocity components the study used three acoustic beams in different directions. The ADCP transmitted a 'ping' from each transducer element approximately once per second. The returning echoes of each 'ping', sensed by the instrument, were taken over an extended period, with echoes from shallow depths arriving sooner than ones from greater distances. Velocity profiles were then developed by range-gating the echo signal at successively greater depth ranges; these were then broken down and grouped into segments called depth bins.

The ADCP transducers (east, north and up directions) generate sound pulses at a given frequency (in this case 1000 kHz) along a narrow beam of sound, in which the energy was concentrated in a cone approximately 2° degrees wide. As the sound propagates through the water column, it is reflected in all directions by particulate matter, specifically sediment, biological matter and bubbles, but a certain amount of the reflected energy travels back along the transducer axis toward the transducer where the processing electronics measure the backscattered frequency, and thus the Doppler shift. The Doppler shift states that if a source of sound is moving relative to the receiver, the frequency of the sound at the receiver is shifted from the transmit frequency given by:

$$F_D = 2F_s(V/C) \quad (5.2)$$

Where V is the relative velocity of particles between source and receiver, C is the speed of sound; F_D is the change in the received frequency at the receiver (i.e. the Doppler shift) and F_s is the frequency of the transmitted sound. The frequency increases if the distance between the transducer and the reflecting object is decreasing but decreases if the distance is increasing. The Doppler shift measured by a single transducer thus quantifies the mean velocity of the water along the axis of the acoustic beam (Kostaschuk, 2005). The current velocities were then depth averaged to a single profile 50 m upstream of the HATT at the location given by Table 5.2.

5.4: Severn Estuary and Anglesey site SWATH Measurements

The SWATH plus survey system was utilised to collect high resolution (0.1 m accuracy) depth data by running approximately eight transects at each of the locations, spaced at 130 m, across the survey sites in an alternating northerly to southerly direction. The SWATH system measured the depth and sonar reflectivity of the seabed below and to the side of the sonar transducers. Depths were measured in a line extending outwards from a transducer and each line producing a profile. As the survey vessel moved forwards, the profiles combined to form a swath of depths across the survey areas. By measuring the motion and location of the transducers using ancillary devices, the depth information was correctly located with respect to the Earth's surface. Figure 5.10 shows the ADCP fixed to the CodaOctopus Guiding Light.



Figure 5.10: ADCP and bathymetric survey aboard the CodaOctopus Guiding Light

6: HATT and velocity profile characterisation using water flume and ADCP survey

Using a similar methodology to that proposed by Myers and Bahaj, (2005) and Bahaj et al, (2007), a re-circulating water flume based at the University of Liverpool was used to test the hydrodynamic performance of the 3 bladed 0.5 m diameter prototype HATT. A mechanical load was applied to the turbine using the servomotor and control system discussed in Section 5.1.1 at a fixed water velocity of 1 m/s. The results of these tests will be discussed and compared with those presented in literature and those obtained from CFD. To establish the operational characteristics of a scaled HATT the results of the ADCP and SWATH surveys are considered in preparation for later discussions on its application to CFD.

6.1: Re-circulating flume test results

The flume water velocity was set to 1 m/s from zero velocity to match the conditions in the CFD reference model. With the use of a pitot tube, the flume velocity was measured at the beginning and end of each test, and was estimated to be better than 5 % over the water depth. Figure 6.1 shows the turbine during testing and the wake generated downstream of the support tube. Using the precision angled blocks shown in, Figure 5.8, the turbine was set up with the optimum pitch angle of 6° . A series of angular velocity sweeps were then performed.



Figure 6.1: Turbine during testing at 1 m/s showing wake from support bar

With no load applied to the turbine the rotational velocity is at a maximum and therefore freewheeling. Under these conditions the control circuit was activated and the

load applied via torque macro 3, as discussed in Section 5.1.3. A single point was taken for the axial load at freewheeling no other data points were collected for this study. As the load is applied through the macro, the torque applied by the servomotor starts to decrease the angular velocity of the turbine. Appendix 4 contains the data for all the flume tests carried out using both the solid and flexible drive couplings.

In its raw form the angular velocity of the servomotor at each load increment was saved as a percentage of the maximum velocity of the servomotor (1000 rpm). A sample time of 5 sec and 10 sec was used to record the angular velocity of the servomotor for the solid and flexible drive couplings, respectively. The sampling frequency for the 5s and 10s sampling intervals were both 1.2 Hz. The total test duration in Figure 6.2 was approximately 110 sec producing 11 data sets. From Figure 6.2 it is clear that there is scatter in the angular velocity data across each sample period. The angular velocity reduces as the load current is increased to the servomotor. This is demonstrated by the downward trend from left to right in Figure 6.2 as the turbine slows from freewheeling at the start of the test ($t = 0$). Figure 6.3 gives the measured servomotor current for the sample period. Here however there is considerably less scatter in the data, indicating a stable load current. The current is increased and held for each sample period.

Figure 6.4 gives the average angular velocity (%) and average load current (A) for each sample period. The confidence intervals were calculated to 2 standard deviations, as discussed by Kirkup, (1994). It is evident from the error bands shown in Figure 6.4 that there is a larger degree of error in the angular velocity data when compared to that of the load current. It was postulated that the high degree of scatter in the angular velocity was introduced via the interaction of the turbine blades and support stanchion. To overcome this potential issue it was necessary to locate the turbine further upstream of the stanchion. However, given the time frame allotted for the flume tests, the alteration to the nacelle and drive seals was not possible.

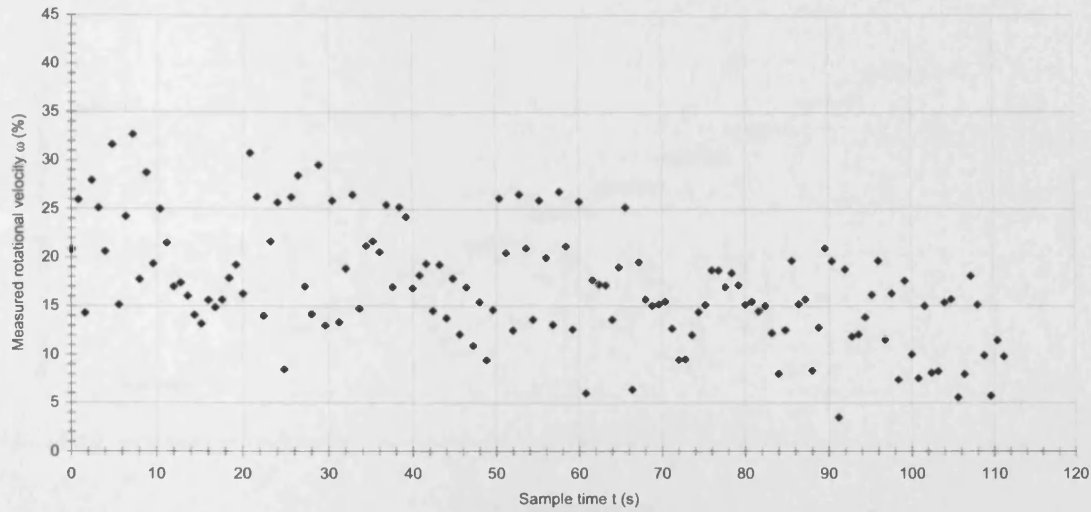


Figure 6.2: Angular velocity as a percentage of maximum servomotor velocity (1000 rpm) at each sample period over the test duration (flexible drive coupling)

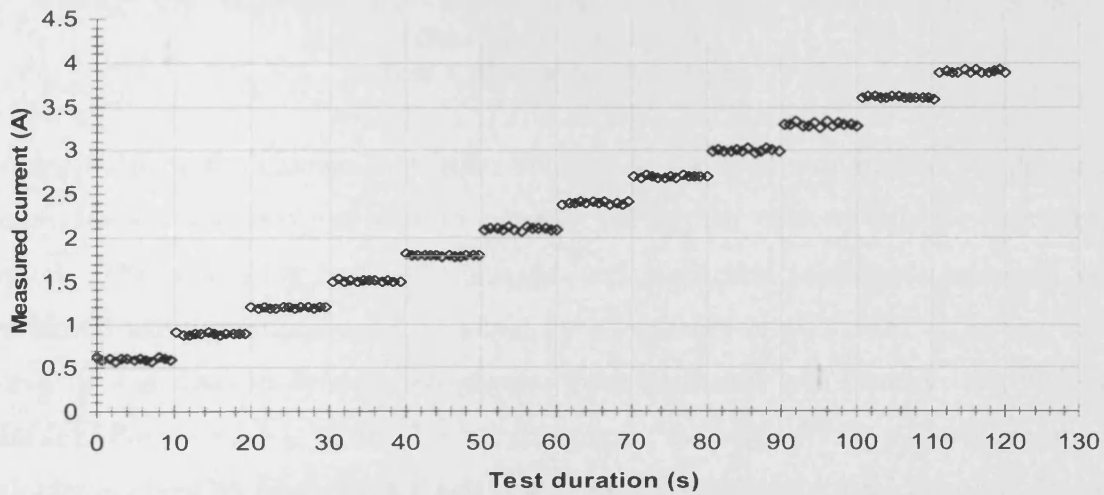


Figure 6.3: Measured servomotor current (A) at each sample period over the test duration (flexible drive coupling): Test 1; Flow velocity = 1 m/s

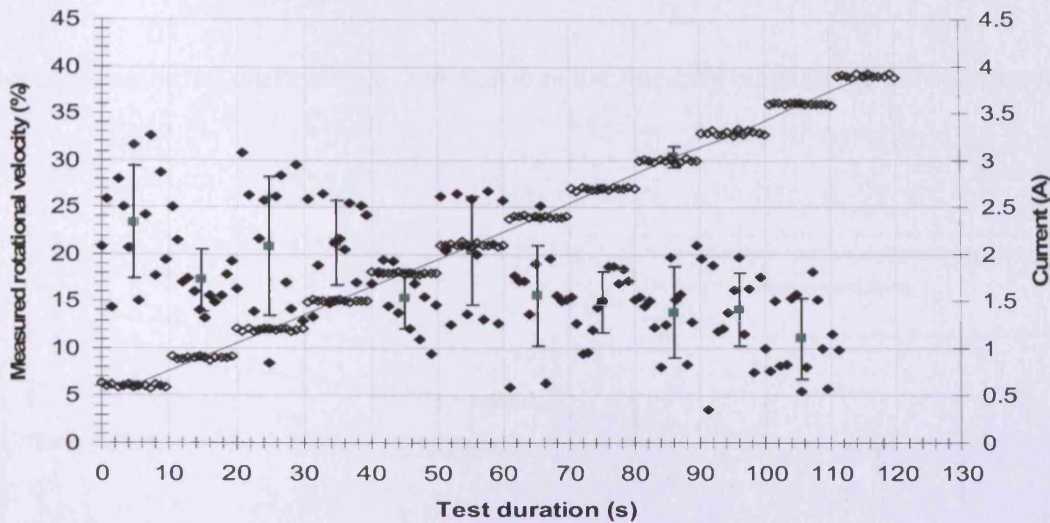


Figure 6.4: Combined angular velocity (%) and servomotor current (A) showing average and confidence intervals (2 standard deviations) for each sample period (flexible drive coupling).
Test 1; flow velocity = 1 m/s

To approximate the change in angular velocity as the load was applied via the servomotor, linear regression was used to curve fit the angular velocity data for each sample period. The regression curve fit constants and associated confidence intervals, were calculated using methodologies as given by Kleinbaum et al, (1988). The regression curve fit was used to average the angular velocity scatter and thereby ‘smooth’ each data set. For data set 1, of the flexible drive tests, the curve fit for the average angular velocity is given by Equation 6.1 and is also shown in Figure 6.5 for the same data set. The same procedure was applied to of the 6 data sets. The error in the intercept and slope in equation 6.1 were calculated to 2 sigma with (n-2) degrees of freedom.

$$\omega = (-0.1012 \pm 0.0211) t + (23.945 \pm 3.58) \quad (6.1)$$

$$\omega = \omega\% \times \frac{\pi}{3} \quad (6.2)$$

To allow comparisons between the flume tests and CFD flume model Equations 6.2 and 6.3 were used to calculate the average angular velocity (rad/s) and torque (Nm) for each data set. Linear regression was again used to curve fit the average angular velocity (%) data as in Equation 6.1.

$$T = 0.9061 \quad (6.3)$$

Where I = measured current (A). The 0.906 is the linearity constant of the servomotor.

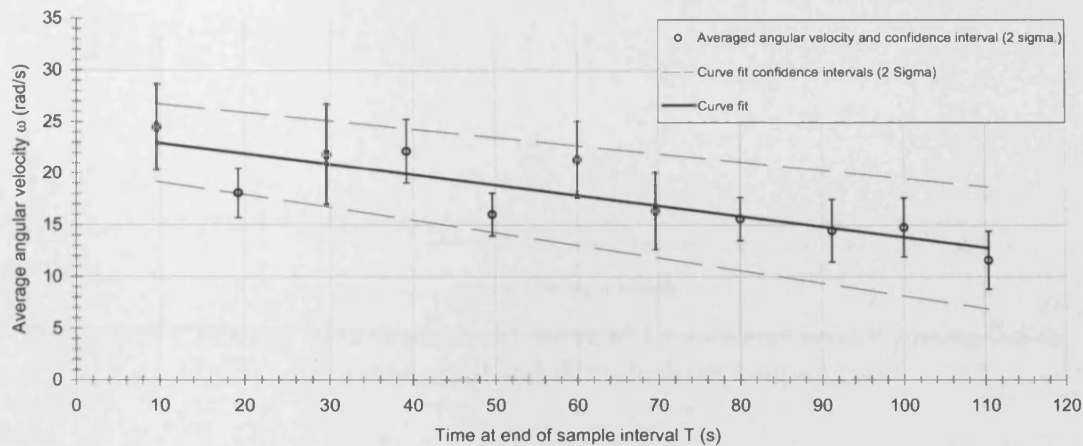


Figure 6.5: Average angular velocity (%) data with confidence intervals of 2 Sigma. Linear curve fit with confidence intervals of 2 Sigma. (Combined solid and flexible data).

The solid and flexible drive tests were then combined to generate torque and power curves for each of the 6 tests, Figures 6.6 and 6.7. As the angular velocity of the turbine decreases the torque generated by the hydrodynamic lift forces start to increase towards a maximum torque of 3.5 Nm at an angular velocity of approximately 10 rad/s. The flume tests give a maximum average power of 39.8 ± 4.85 W at an angular velocity of 14.3 ± 1.3 rad/s and a TSR of 3.57 ± 0.325 .

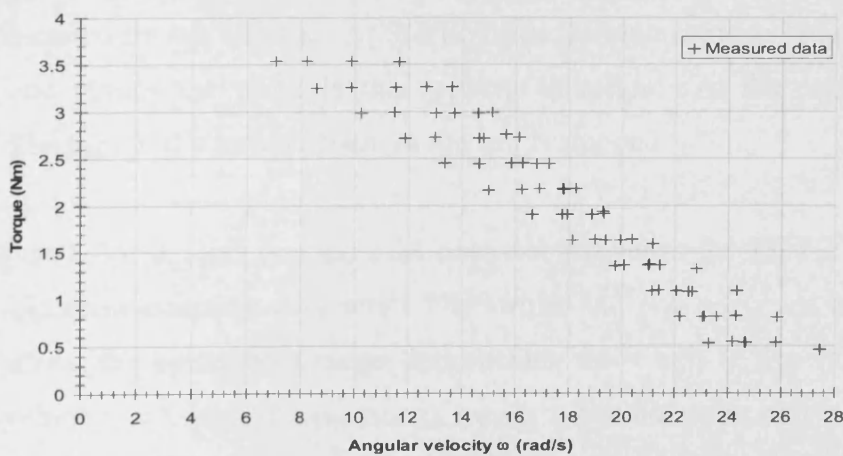


Figure 6.6: CFD and measured turbine torque at 1 m/s water velocity using 0.5 m HATT: combined solid and flexible drive coupling data

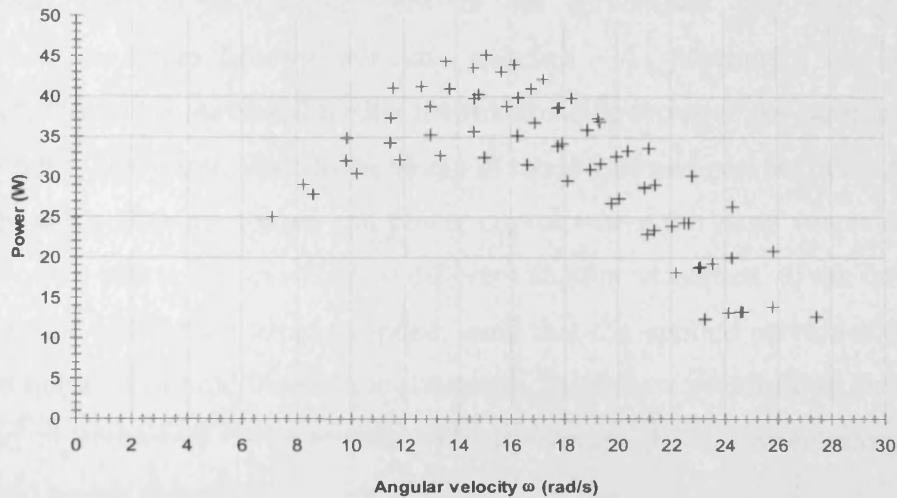


Figure 6.7: CFD and measured power curve at 1 m/s water velocity using 0.5 m HATT: combined solid and flexible drive coupling data

Once stabilised the servomotor's torque represents the corresponding balanced hydrodynamic turbine torque and frictional losses. In this way the torque curves generated for each test are linear in form as they directly match the output of the motor. The angular velocity of the turbine reduces as the load is increased. The torque required to oppose that generated by the servomotor is proportional to a percentage of the maximum rated servomotor current (1%). As the turbine slows from the freewheeling state, at around 24 rad/s, the hydrodynamic forces generated from the lift characteristics of the turbine profile start to increase. The servomotor torque is gradually increased until it matches the maximum torque generated by the turbine for the 1 m/s water velocity. Below an angular velocity of 13.5 rad/s and a torque of 3.5 Nm the rotational direction of the turbine alters as the servomotor torque overcomes the hydrodynamic torque generated by the turbine. At this point the turbine starts to oppose the direction of flow and pumps the water in the opposite direction. At the point at which the rotation direction of the turbine changes the test is stopped.

From Figure 6.8 it is clear that the TSR does not fall below 3.1 for the combined solid and flexible drive coupling data sets. The torque and power curves theoretically rise and fall across the operational range, approaching the x axis at freewheeling and zero angular velocity, whereas the measured results given thus far only cover the upper portion of the range between peak and a minimum torque at freewheeling. During the tests it was found that following maximum torque the angular velocity rapidly

approached zero as the torque between the servomotor and that generated by hydrodynamics forces become perfectly matched. As previously mentioned, if the servomotor torque is increased further the rotational direction of the turbine changes and starts to pump the water. Due to the shape of the torque and power curves there are two locations along both the torque and power curves where the same values of torque and corresponding power can exist at two different angular velocities. If the turbine were to be physically held and a torque applied, such that the applied servomotor load is less than that required to hold the turbine stationary, just below peak torque, then the turbine will start to accelerate to an angular velocity toward the freewheel side of the peak torque and power curves.

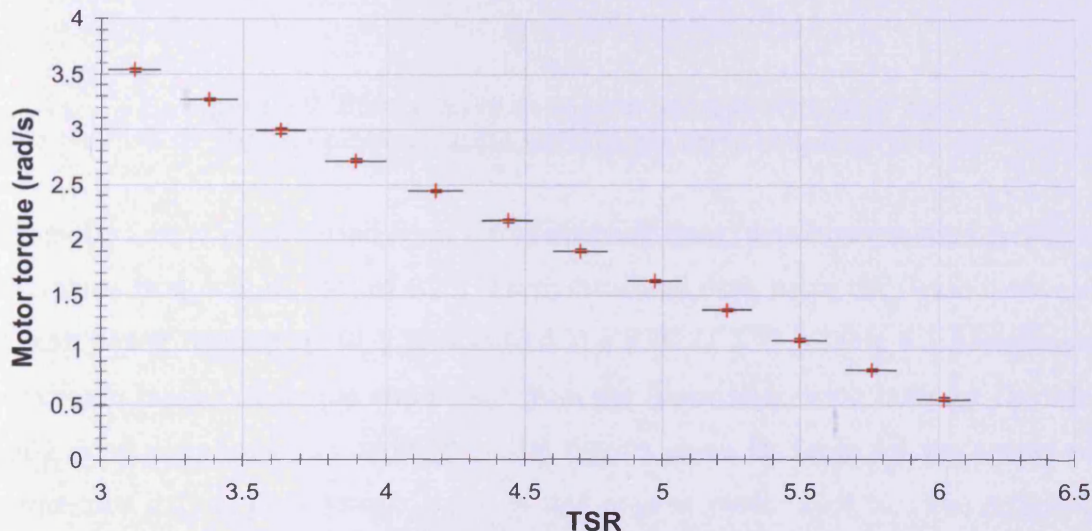


Figure 6.8: Averaged servomotor torque vs TSR: Test 1; combined solid and flexible drive coupling data.

The torque curves for each of the 6 data sets, Appendix 4, show some variance in the point at which the rotational direction of the turbine switches. For each flume test the average maximum torque generated from the servomotor, before switching the rotational direction, was 2.81 ± 0.41 Nm at a TSR of 2.7 ± 0.78 . The power generated was calculated from the product of the averaged torque and average of the curve fitted angular velocity data $T\omega$ (W). Figure 6.9 shows the power curve for the full data along with the error in both the power and TSR.

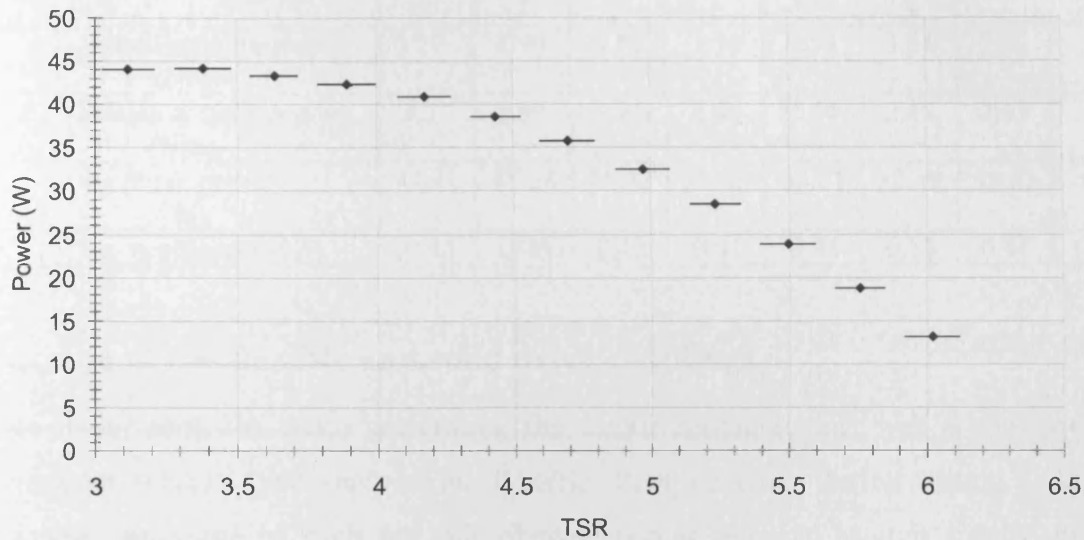


Figure 6.9: Power curve vs angular velocity with error bars:
Test 1; combined solid and flexible drive coupling data.

Since the torque is increased from a freewheeling state, the corresponding power curve also starts from a high TSR of 6.25. From measured data, using the flexible drive shaft, a peak power reading of 44.4 W occurred at a TSR of 3.25. Table 6.1 summarises the maximum measured torque and power from the flume tests using both the flexible and solid drive couplings. In addition to the figures given in Table 6.1 the spread of the torque raw data at peak torque was 8 % and at peak power 25.4 %. The difference in maximum and minimum peak power extraction was 27.6 %. The standard deviations in Table 6.1 also elucidate the error imposed by the large angular velocity fluctuations on the power calculations when compared to the torque. Since the torque is calculated from the servomotor proportionality constant 0.906 (Nm/A) and the stable current load its standard deviation for the complete test set is ± 0.22 Nm and ± 0.41 Nm at maximum torque and during maximum power, respectively. However, since the power was calculated from the product ($T\omega$) the error in the angular velocity impacts its standard deviation, for the study this was ± 4.85 W. The results given in Table 6.1 will be discussed later in Chapter 7 in combination with the CFD derived performance characteristics.

Table 6.1: Summarised results for flume tests using both flexible and solid drive shafts

	Flexible drive shaft			Solid drive shaft			Av.	Standard deviation
	Test 1	Test 2	Test 3	Test 1	Test 2	Test 3		
T_m (Maximum torque) (Nm)	3.27	2.99	3.53	3.54	3.54	3.54	3.36	0.22
T_{mp} (Torque at max. power) (Nm)	3.27	2.99	3.26	2.45	2.44	2.45	2.81	0.41
P_p (Peak power) (W)	44.41	45.18	41.32	39.88	35.71	32.69	39.82	4.85
Power coefficient (C_p)	0.45	0.46	0.42	0.41	0.36	0.33	0.41	0.05

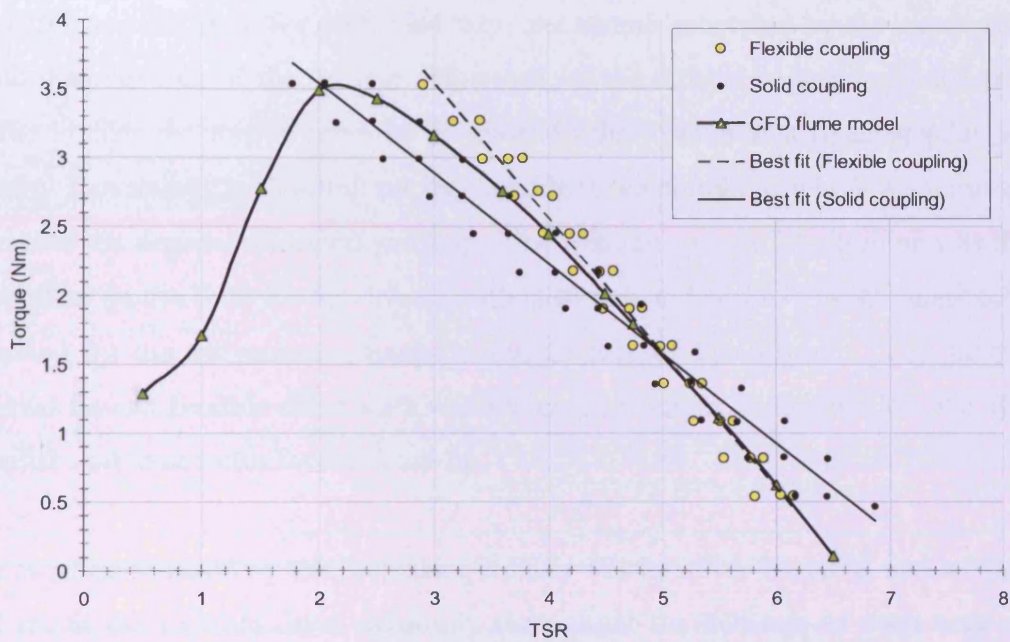
6.2: Use of the flexible and solid drive couplings

One major problem when performing the torque measurements was a considerable degree of torsion ‘wrap-up’ of the flexible drive coupling during testing. At the freewheeling stage of each test this phenomenon is minimal as it is limited to the opposing torque generated from friction within the flexible coupling and servomotor. However, as the percentage of load current is increased, the opposing torque generated by the servomotor increases, which in turn reduces the angular velocity of the turbine. With the reduction of angular velocity the hydrodynamic efficiency and hence opposing torque increases. Since the load between the servomotor and the turbine is transferred through a central cable the outer casing of the flexible drive coupling has to oppose the applied loading. However, due to the inherent flexibility of the outer casing it starts to coil. As the turbine angular velocity decreases further its hydrodynamic torque starts to approach maximum, at this point the amount of torsion wrap-up of the drive coupling is severe. The whole flexible drive coiled back on itself causing the cable at the core of the drive coupling to bend through large angles, which in turn increases frictional loading due to increased contact with the outer case and bending stresses in the core drive cable. Maximum coiling of the drive cable occurred toward the servomotor end of the drive coupling assembly which with repeated testing resulted in the failure of the core wound drive cable.

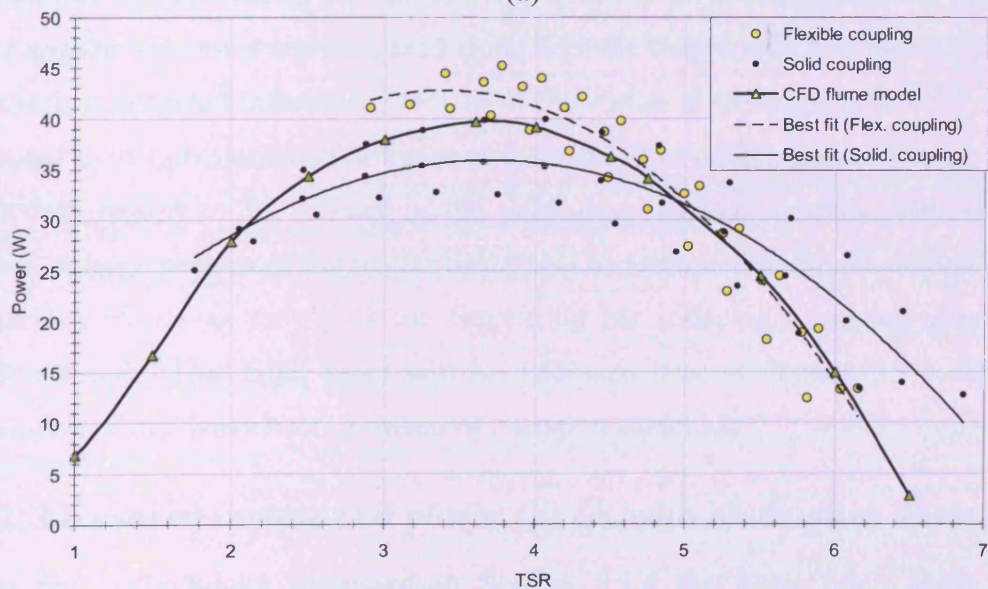
6.2.1: Drive coupling effects on torque and power curves

Due to the fact that the drive shaft rotates within the outer case of the flexible coupling a higher frictional loading is experienced than when compared with the solid drive arrangement. For the solid drive shaft arrangement the freewheeling angular velocity is approximately 4 rad/s higher than that developed by the flexible drive, indicating higher

frictional loading through the drive assembly with zero load applied by the servomotor Figure 6.10 (a) and (b). This is further translated to the lower angular velocity end of the power curve, following the point at which the turbine reaches maximum hydrodynamic performance (i.e. peak power extraction) the turbine torque drops off sharply, causing the turbine to stall and rotate in an opposite direction as the servomotor starts to drive the turbine.



(a)



(b)

Figure 6.10: Variation in torque (a) and power (b) measurement when using solid and flexible drive couplings also CFD flume model data.

Therefore, if the internal friction of the flexible drive coupling is greater than that produced by the universal drive joints of the solid drive, stall will occur at a higher angular velocity. Both methods however give a similar value for the TSR at peak power ranging between 3.49 (13.95 rad/s) and 3.63 (14.5 rad/s) for the flexible and solid drives, respectively, Figure 6.10 (a) and (b). As the torque from the servomotor is increased the angular velocity of the turbine gradually decreases, once its angular velocity has stabilised, for each load step, the torque generated by the servomotor once again matches that of the turbine. However, as the turbine angular velocity decreases, so the greater the torque required to maintain the turbine at a fixed angular velocity, thereby increasing the loading on the flexible drive coupling, which as a consequence increases the degree of torsion wrap-up. The rotation speed of the turbine was therefore dependent on the time for the drive coupling to flex and coil to a point where the torque supplied by the servomotor approximates to that of the turbine. The sample time interval for the flexible drive tests was increased from 5s to 10s to allow the system to stabilise and to account for the wrap-up.

The twisting induced by the increasing torsion was however unstable, and would uncoil and recoil the flexible drive randomly throughout the duration of each time interval. The number of coils along the length of the flexible drive shaft remained constant at lower angular velocities and increased along with the torque, which in turn increased the previously mentioned instability. Not all of the scatter in the angular velocity could be attributed to this phenomenon however as the solid drive coupling also showed a similar trend with regard to the scatter in the percentage angular velocity with increasing torque. A large portion of the scatter could also be attributed to the interaction between the turbine blades as they pass the supporting bar inducing a pulsing effect in the rotation speed. This latter point will be discussed later in Section 7.3.1 aided by a description of the dam effect upstream of a support stanchion.

6.2.2: Measured torque and power curves with blade pitch variation

Using the methodology discussed in Section 5.1.4 the blade pitch angle for the prototype turbine was changed to 3° and 9° with the flume water velocity maintained at 1 m/s. Since the torque and power curves generated for both the 3° and 9° pitch angles used the flexible coupling exclusively all data derived for the 6° pitch case with the solid drive coupling are not included with pitch angle variation. Here again, linear

regression was used to smooth the large fluctuations in the angular velocity. The power is calculated as before using the measured current and the linear relationship between current and torque (0.906 Nm/A). As in the 6° tests, 4 torque curves were generated for each blade pitch. To give insight to the general trend a linear curve was added to each combined 3° and 9° data sets, Figure 6.11. It is clear from this figure that there is very little difference between the torque curves across the angular velocity sweep. What is interesting is that the best curve fit for the optimum 6° pitch angle is now shown to produce a lower torque than that at 3° and 9°, with 3° now showing a torque at peak power of 3 ± 0.48 Nm and 2.8 ± 0.41 Nm at 6°. Given the close numerical torque values at all three angles and with the associated errors in each of these readings it is statistically possible for these results to overlap.

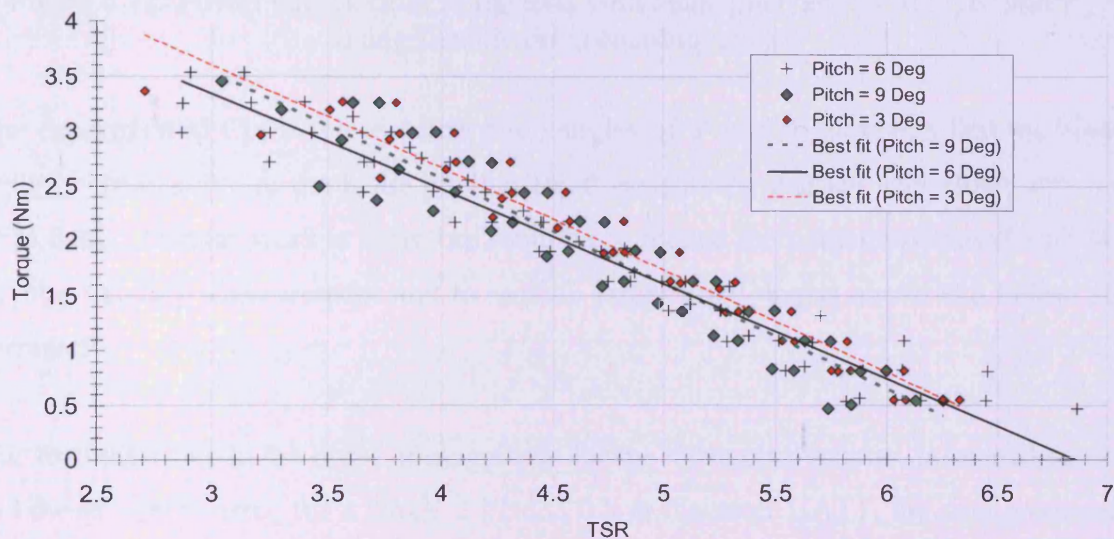


Figure 6.11: Torque curves from flume tests with blade pitch angles of 3°, 6° and 9° using flexible drive coupling only.

In a similar manner the power curves in Figure 6.12 show similar trends. The average power generated for a blade pitch angle of 6° was 39.82 ± 4.85 W (Table 6.1) and 43.5 ± 5.6 W for a blade pitch of 3°. Again, the peak power values are numerically similar with error bands that suggest that statistically these values overlap. The power curve for 9° is between these curves and therefore the same observation can be made.

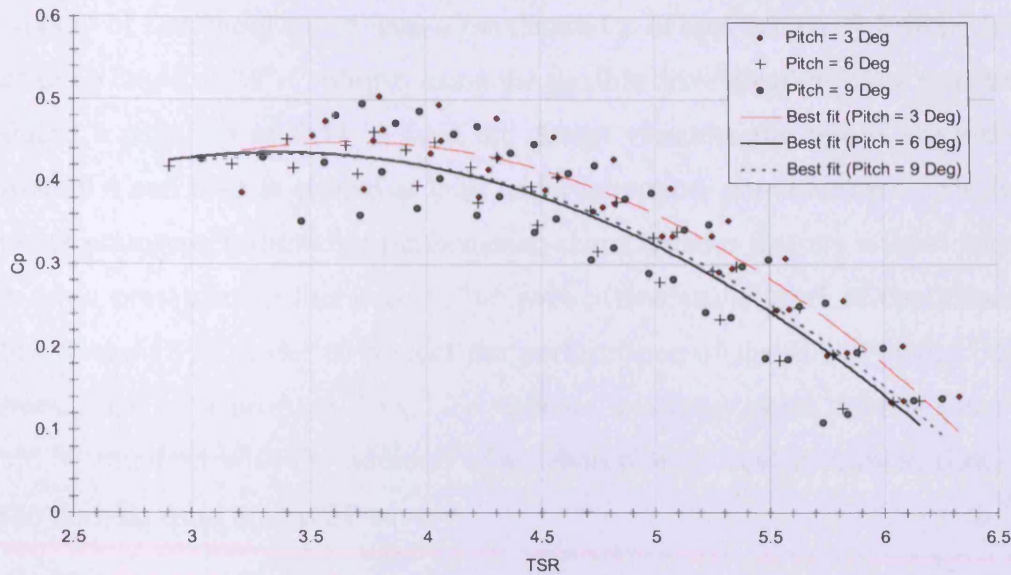


Figure 6.12: Power curves from flume tests with blade pitch angles of 3° , 6° and 9° , using flexible drive coupling only

The experimental C_p , between blade pitch angles of 3° and 9° , suggests that the blade design is insensitive to the blade pitch angle, this will be discussed later along with the CFD data. Further work is therefore required to reduce the scatter associated with the angular velocity measurement and to include larger pitch angles above and below the current 6° .

Due to similarities in the order of magnitude for the turbine's diameter, measured power and thrust coefficients, for a single 3 bladed 0.8 m diameter HATT, the data presented by Bahaj et al, (2006) were used as a comparative reference to the data obtained from the University of Liverpool flume tests. However, it should be acknowledged that the experimental arrangements were very different, and that the Liverpool data was not corrected for the blockage ratio. Taking these factors into account, the performance characteristics of the HATT, discussed in this thesis, and that of the reference, show similar trends in peak performance and overall operational range. Although, these data sets can not be compared directly, they do give some confidence to the general trends of power extraction.

With the use of a 2.4 m x 1.2 m cavitation tunnel and a 60 m towing tank, a 0.8 m HATTs performance was measured with varying pitch and yaw angles, for various immersion depths. Using the 0° yaw angle data (Figure 2.17) for comparisons with the

University of Liverpool flume data, a maximum C_p of approximately 0.46 occurred at a blade pitch angle of 20° . Whilst, using the flexible drive coupling, data from this work produced a peak C_p of 0.44. Given the design variables the results show that a C_p between 0.4 and 0.45 is typical at least under laboratory conditions and that the 0.5 m diameter prototype turbine has performance characteristics that are at least comparable with those presented in literature. This gave a reasonable level of confidence in the ability of the CFD model to predict the performance of the HATT under other flow regimes, such as a profiled flow. To validate this latter point, further flume testing would be required with the addition of an appropriately scaled profiled flow, such as can be derived from an ADCP survey.

6.3: ADCP and SWATH surveys

The hydrographic and hydrodynamic high resolution SWATH bathymetric survey and vessel-mounted ADCP surveys, that were briefly discussed in Sections 5.2 and 5.3, produced excellent data to investigate the feasibility of installing a HATT in the inner Bristol Channel and Anglesey. The bathymetric survey provided accurate and detailed topography of the site, thus allowing the identification of a potential location to site a HATT. The ADCP transect surveys produced detailed current velocities through the water column and the overall flow regime. Flow velocities were measured in order to assess whether the currents possess the necessary strength to power the HATT.

From the Severn Estuary surveys, the maximum peak spring ebb tide velocity was found to be 1.8 m/s towards the water surface. The tidal velocity for economic energy extraction is typically quoted to be between 2 m/s and 3 m/s at mean spring tide (Black and Veatch, 2005). For the site in question if the HATT were to be located well below the surface it would never see the peak value of 1.8 m/s. It is unlikely then that this location would be suitable for energy extraction. The study has shown that local velocity profiles may vary considerably from that typically calculated using the $1/7^{\text{th}}$ power law. In shallower waters where the turbine diameter occupies a larger percentage of the water column this will have a significant effect on power extraction or, as in this case, when its position is limited by shipping requirements and placed closer to the seabed. When preparing data for the velocity profile through the water column for the EPRI North American Tidal In Stream Power Feasibility Demonstration Project the $1/7^{\text{th}}$ and $1/10^{\text{th}}$ power laws were used along with data from the JOULE 1996 Report

(Hagerman² et al, 2006), Figure 6.13. It is interesting to note the increase in the rate of decay at an elevation depth of approximately 0.5 and the relatively poor correlation with the power law curves. The JOULE 1996 velocity profile shows similarities with both the Severn Estuary and Anglesey data in that the rate of decay increases toward the seabed at a higher rate than estimated by both the 1/7th and 1/10th power law.

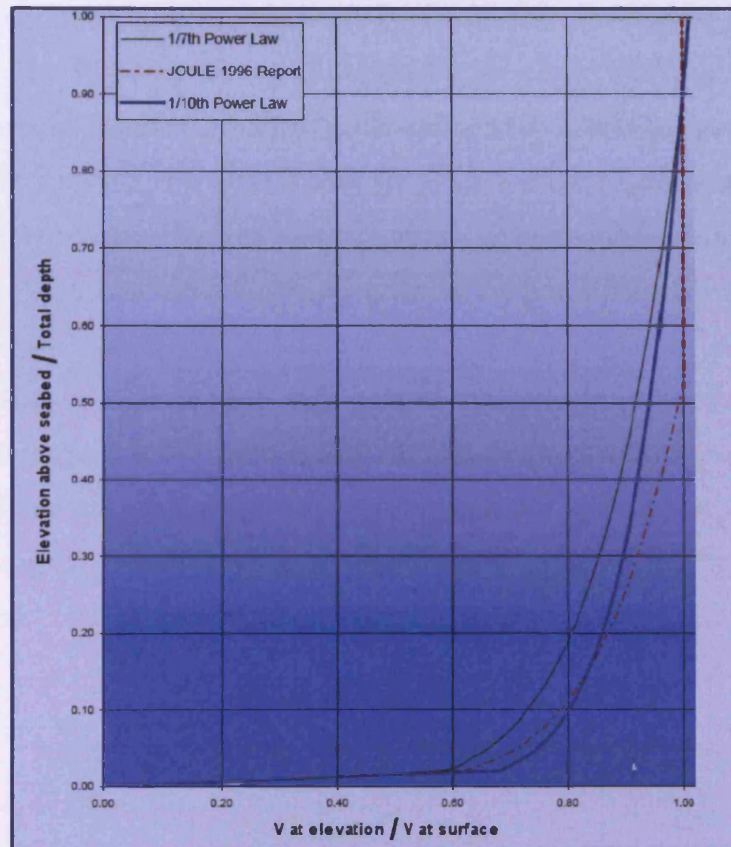


Figure 6.13: Alternative velocity profiles normalised with depth and velocity. Source: Hagerman., et al., 2006. EPRI Methodology for estimating tidal current energy resources and power production by tidal in-stream energy conversion (TISEC) devices.

6.3.1: ADCP measurements in Severn Estuary

Each transect line took approximately 30 minutes to complete and provided mean velocity data for the entire water column. Depending on the water depth between 19 and 26 data points were taken through the water column at 5 second intervals along the transect line. Low water occurred at 07:36 (1.12 m) and high water was at 13:56 (12.59 m) giving a tidal range of 11.47 m. In order to remove velocity spikes present in the data due to varying bathymetry outside the proposed site the acquired velocity data for each transect was subsequently filtered by removing the velocity profile data to the

north of the relatively flat region to the south of the area (below 5 688 256 m), Figure 6.14 (a). This region is identified in the figure between the two bold lines.

Following analysis of the SWATH and ADCP data the relatively deep flat seabed of the location was deemed suitable in bathymetric terms to site the HATT since it allowed the turbine to be positioned higher in the water column without infringing the local shipping requirements. The turbine location is shown by the circle in Figure 6.14 and by the vertical stanchion in Figure 6.15. The water surface represents the depth +3 hours post slack tide during a spring ebb tide (HWS+3). Once the HATT position was established the ADCP data was further filtered to only include velocity profiles directly upstream of the turbine. The data sets were then used to model the performance of the HATT.

Once the data had been filtered to only include the velocity profiles between the bold lines shown in Figure 6.14 the velocity vs. depth profile was used to investigate shipping requirements. Adequate distance between the blade tip at Top Dead Centre (TDC) and maximum vessel draft likely to be experienced within the site location had to be maintained.

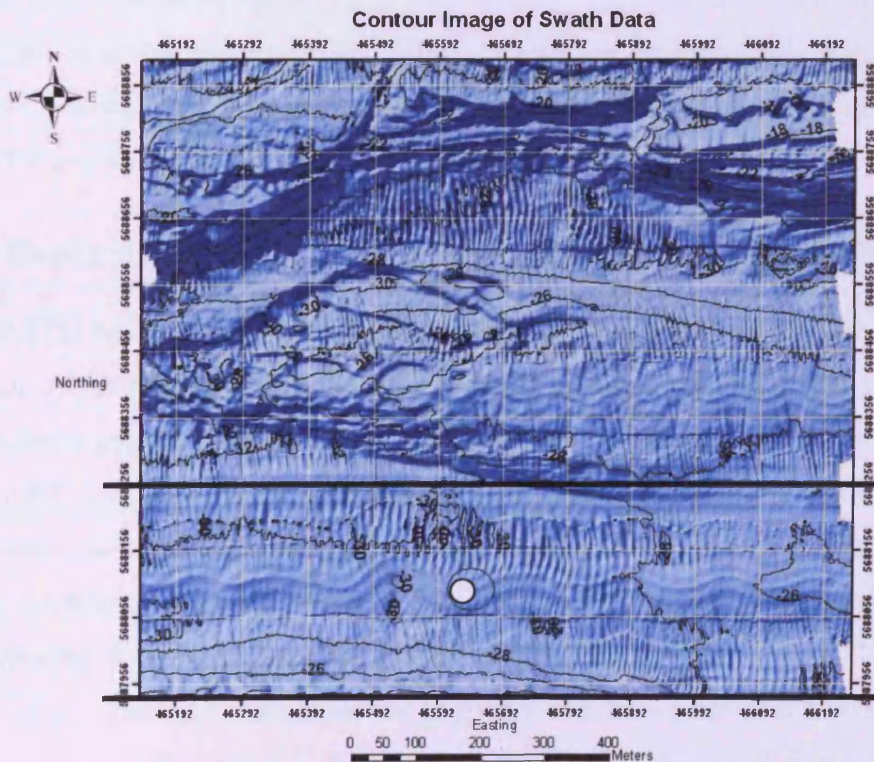
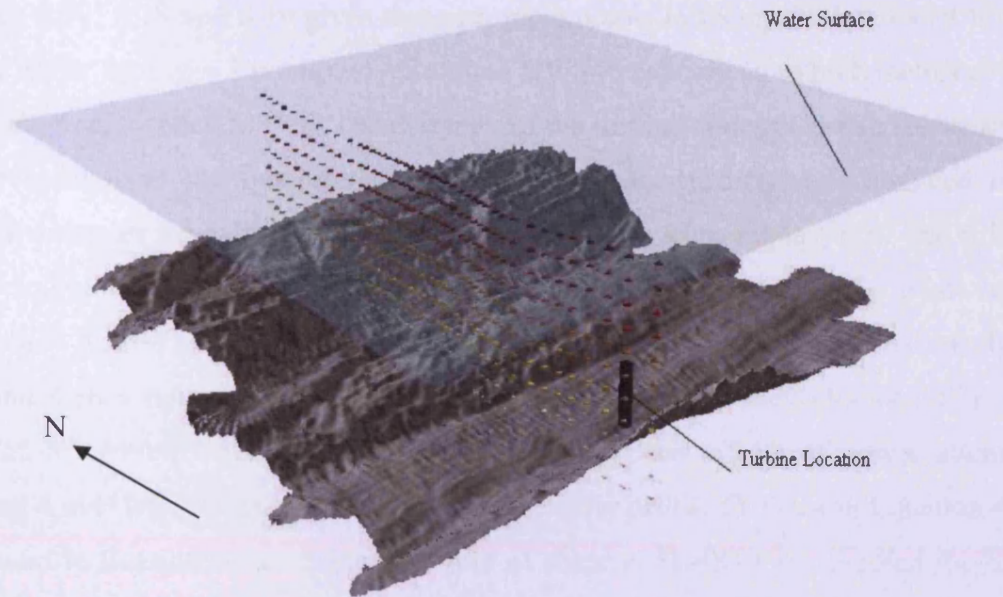


Figure 6.14: SWATH of surveyed area and turbine location (Easting vs Northing)



(b)

Figure 6.15. 3D SWATH of survey area showing turbine location, velocity vectors and water surface (Severn Estuary).

Below the 30 m contour, Figure 6.14 the seabed drops into an ancient river bed, possibly from the last ice age, then rises again from 30 m to 20 m. Immediately south of this position is a bank with depths of 18, 19 and 15 m. In these circumstances it was expected that vessels of a draft up to 14.5 m may deem it a safe route on their approach to the pilot boarding points (Auld, 2008). Therefore, for this study a maximum vessel draft of 15 m was assumed in the vicinity of the turbine giving ~ 7 m between TDC of the HATT and the vessel draft.

6.3.2: Depth averaged ADCP velocity profiles at proposed Severn site

The SWATH bathymetric survey of the pre-designated 1 km² survey site approximately 3 nautical miles south of Stout Point, The Severn Estuary, South Wales in water depths varying from approximately 18-35 mCD was used to define the conditions for the site CFD model. The ADCP site measurements made during the spring ebb tide represented the highest tidal velocities and lowest slack tide for the location. Figure 6.16 gives the velocity profile through the water column directly upstream of the turbine for a tidal cycle ranging from slack tide to a flood and a High Water Spring (HWS) ebb. A number of the transects were removed to give a clearer picture of the velocity profile as the tide starts to ebb towards peak velocity, in this case transects 2, 3, 5 and 7.

Figures 6.17, 6.18 and 6.19 gives three example points in the cycle detailed at HWS+2 (High Water Spring + 2 hours), HWS+3 and HWS+6 referenced to both metres of water and metres referenced to CD. The diameter of the turbine at depth is also shown in each figure to indicate the magnitude of the current velocity difference bounded by the turbine diameter through the water column. It is clear from Figures 6.17 and 6.18 that the velocity difference across the turbine diameter increases as the tidal velocity increases. At HWS+2 the velocity difference across the diameter is approximately 0.45 m/s and a maximum of 0.58 m/s at HWS+3. At HWS+6 the velocity difference is reduced to around 0.1 m/s, Figure 6.19. To study the effects of power attenuation transect 4 at HWS+3 was used to generate a velocity profile (V_z) using Equation 4.1 (as discussed in Section 4.8). Since the rate of shear at HWS+3 represented the highest level of velocity differential across the HATT diameter

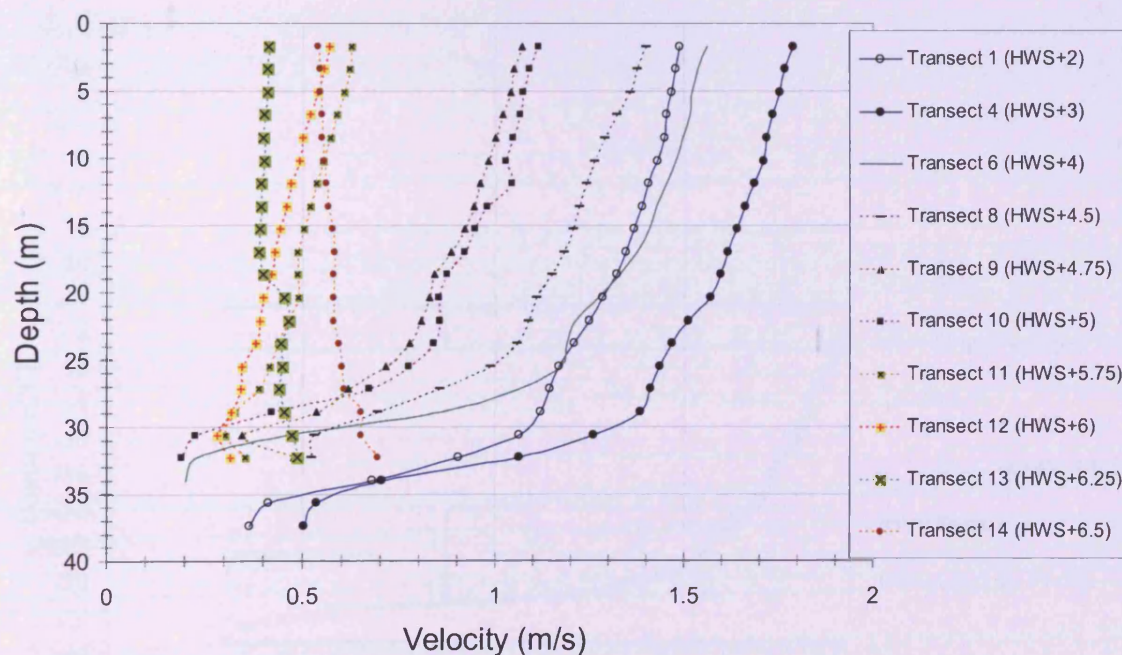


Figure 6.16: Filtered depth averaged ADCP Velocity profiles (Severn Estuary)

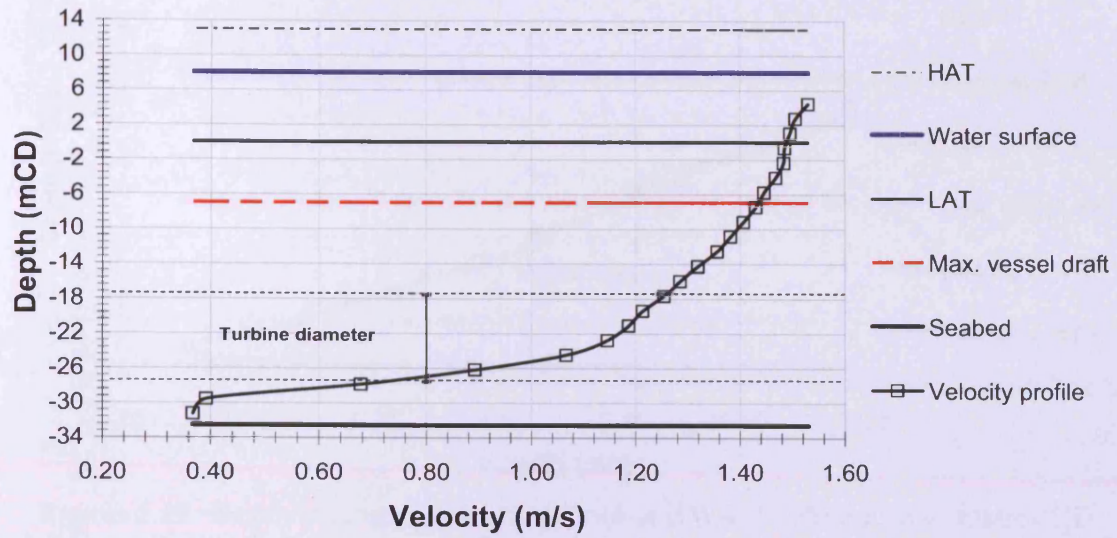


Figure 6.17: Depth averaged velocity profile at HWS+2 reference to metres CD (Severn Estuary)

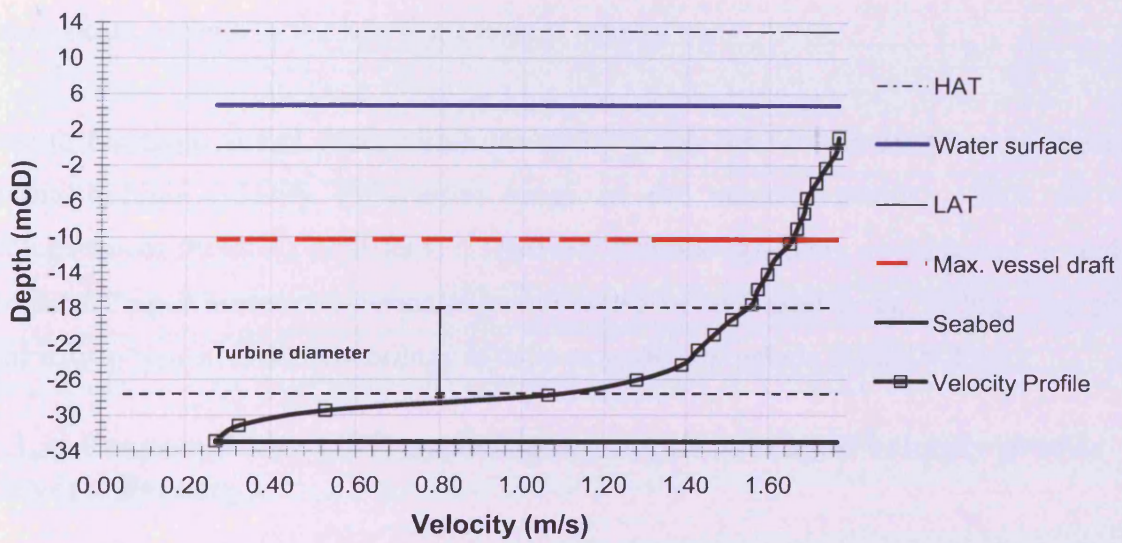


Figure 6.18: Depth averaged velocity profile at HWS+3 referenced to metres CD (Severn Estuary)

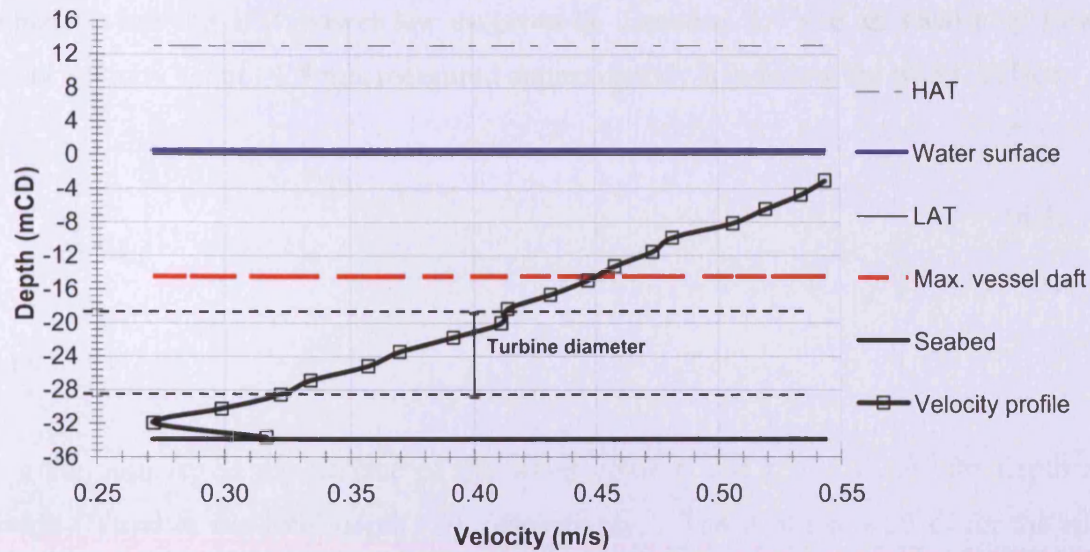


Figure 6.19: Depth averaged velocity profile at HWS+6 referenced to metres CD (Severn Estuary)

it was taken to be worst case scenario for the measurements taken. Moreover, whilst the positioning of the HATT, due to shipping restrictions, may not fall within parameters recommended by Bryden et al, (1998) it is likely to represent a more realistic situation if large arrays of HATTS are to be considered for locations such as the Severn and many other locations such as the Mersey, Channel Islands, etc.

Due to the large vessel draft within the vicinity, the HATT was therefore positioned within a high velocity differential range of the velocity profile. This set of circumstances therefore represents a relatively extreme operating environment to study the HATT's performance in terms of power extraction and axial thrust loading. But one that maybe typical if the technology is to be extended to include depths > 40 m.

6.3.3: Proposed Site CFD model using depth averaged velocity profile (Severn Estuary)

The site CFD domain was modelled with a depth of 35 m which approximated to the tidal height HSW+3 hrs. During this time period the peak tidal velocity was approximately 1.8 m/s and occurred approximately 1 m below the water surface. Figure 6.20 gives the ADCP averaged and filtered velocity profile data upstream of the turbine along with the curve fit as entered into the velocity-inlet boundary of the CFD model using the methodology discussed in 3.11. Also included in this figure for

comparison are the $1/7^{\text{th}}$ power law as given by Equation 6.4 and an ideal plug flow with its velocity set at ~ 1.8 m/s measured approximately 2 m below the water surface.

$$V_z = V_0 \left(\frac{z_i}{z_D} \right)^n \quad (6.4)$$

Where $n = 1/7$

V_0 is the velocity at the surface of the water column and z_i and z_D are the depth at position (i) and at the total depth (D), respectively. The depth was 35 m for the site model and 50 m for the reference ‘deep water’ CFD model. Due to the shipping restrictions, as previously discussed, the position of the turbine is given relative to the depth of its rotational axis which is 25 m below the surface at HWS + 3hrs.

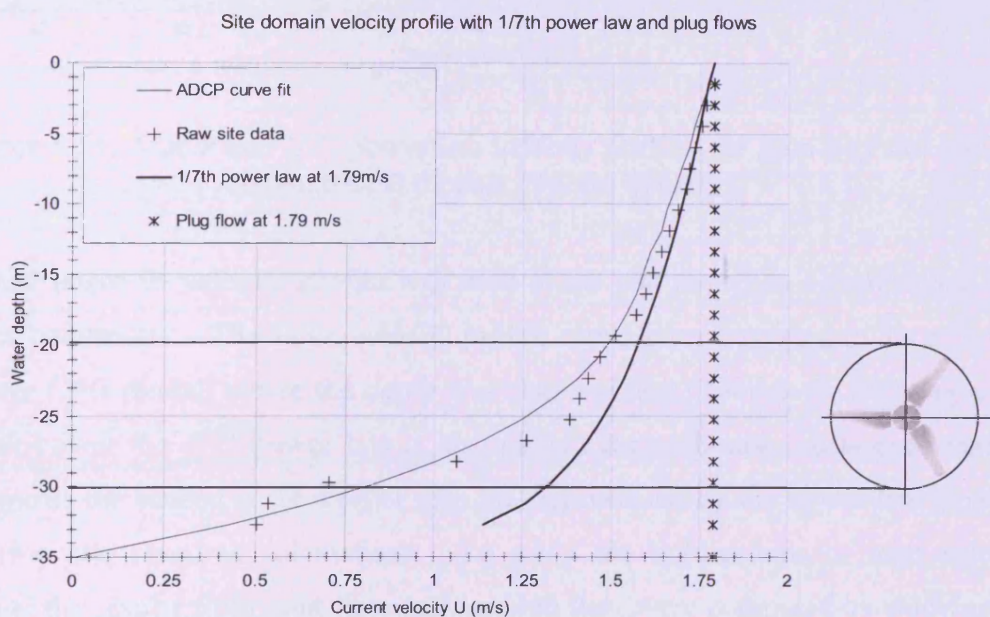


Figure 6.20: Site CFD model upstream velocity profile with $1/7^{\text{th}}$ power law and plug flow (Severn Estuary)

To enable the use of these data with that of the site and reference CFD models the velocity magnitude of the profile was scaled to a peak of 3.08 m/s, since these models were previously used to study performance under these conditions. This allows a direct comparison with all the models at a rated flow of 3.08 m/s, Figure 6.21. Also illustrated

are the relative positions of the HATT for both the reference and site CFD models between a depth of 20 m and 30 m. For maximum power extraction the optimum position for the turbine is towards the water surface. However, as previously stated this is prohibitive due to restrictions imposed by local shipping requirements.

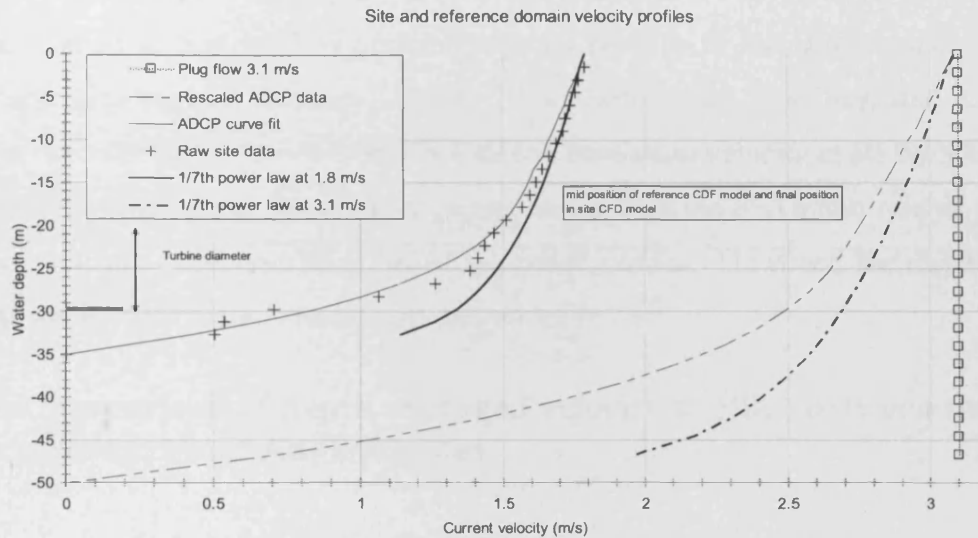


Figure 6.21: ADCP and $1/7^{\text{th}}$ power law velocity profiles for proposed site and reference CFD models (Severn Estuary)

The ADCP curve fit velocity profile was used in the site model as a comparison with plug flow conditions. The same velocity profile was further extended to the reference deep water CFD model, where the depth was also rescaled. Moreover, for comparison with peak power the $1/7^{\text{th}}$ power law is also plotted for each case. It is clear that the shear towards the seabed is far steeper than that represented by the power law typically used during site resource calculations. To study the implications of high velocity differential the results from plug flow and profiled flow were compared by studying the performance of the HATT under both conditions.

With a plug flow of 3.086 m/s the site CFD model gave peak power extraction of the same order as that calculated from the reference CFD domain under the same flow condition. However, with the introduction of the scaled profiled velocity flow, derived from the ADCP site data, the energy density at 25 m below the water surface is considerably reduced and therefore so is the torque and power extracted by the HATT. Under plug flow conditions the peak power extraction was circa 466 kW and with the

introduction of the scaled velocity profiled the peak power extraction was reduced by 30.5 % to 142 kW since the upstream mean velocity was now approximately 2.1 m/s. There is however one assumption that is problematic since it affects the shape of the velocity profile through the water column. As previously mentioned when the velocity profile is scaled up the rate of change in velocity through the depth was unchanged, whereas with a higher velocity the profile shape may also change. The shape change can be likened to that used to describe velocity profiles in the laminar and turbulent boundary layer regions (Massey, 1989). This phenomenon was illustrated in Figure 6.16, as the velocity increases from slack tide to maximum velocity at HSW+3 hrs. The high velocity differential moves to a greater depth with the maximum rate of velocity decrease starting at around 26 m below the water surface. However, the magnitude of this change in reality needs further investigation.

6.3.4: Comparison of depth averaged velocity profiles between the Severn Estuary and Anglesey sites

To ascertain whether or not the steep velocity attenuation reported in this study is typical of other locations, further ADCP measurements and numerical modelling are required with higher local tidal flows. Another potential site is off the coast of North Wales within the Anglesey Skerries. Bathymetric and ADCP surveys were carried out at 4 locations within this region, Figure 6.22. Due to the depth similarities between the Severn Estuary site and site 2 of the Anglesey data the velocity profile for the latter location was selected for all subsequent modelling.

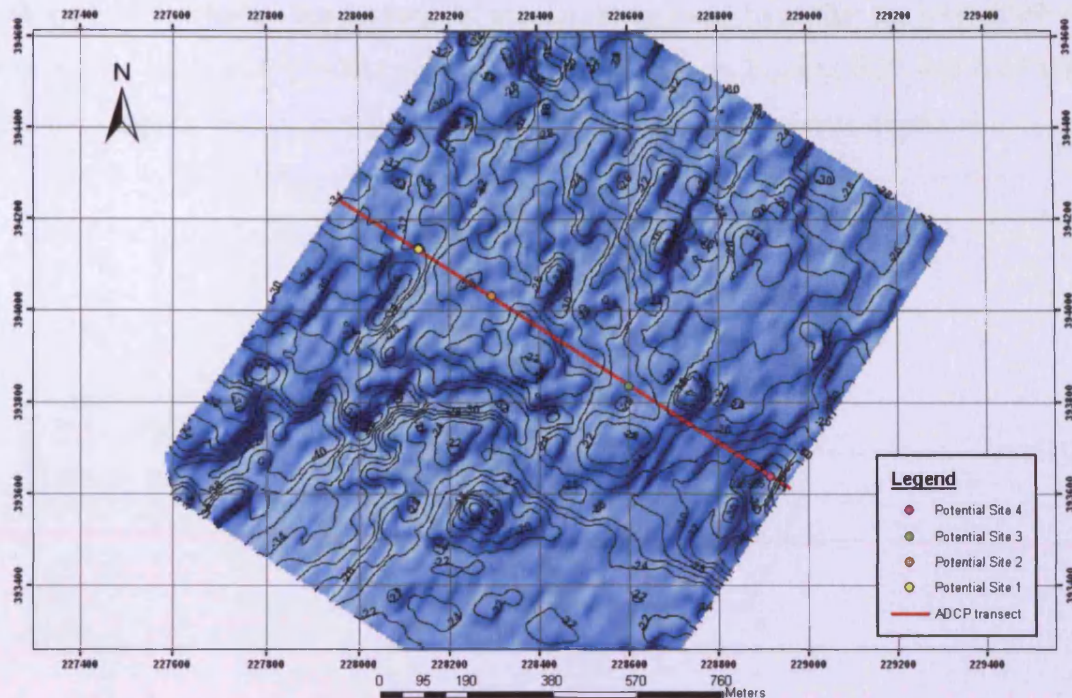


Figure 6.22: Bathymetry showing proposed HATT sites along transect line within the Anglesey Skerries

The data collected from the Severn estuary site was taken during a Spring tide whilst the data from the Anglesey site was taken during a neap tide. According to the Sustainable Development Commission, “there is approximately eight times more tidal stream power during spring tides than at neaps” (Carbon Trust, 2005). Hence this implies that the peak velocity for the Anglesey site, for a spring tide, would be twice that at neap tide (i.e. up to 4 m/s). This assumes that the velocity profile during a spring tide is the same as the profile found from the data collected during a neap tide. This is only an approximation but gives an indication of the power generated during a spring tide. Ideally further data would need to be collected from the Anglesey site during a spring tide to verify this. Figures 6.23 and 6.24 compare scaled velocity profiles from the Severn Estuary and Anglesey site 2 data with the $1/5^{\text{th}}$, $1/7^{\text{th}}$ and $1/10^{\text{th}}$ power laws. For the sake of continuity the scaled maximum velocity of 3.08 m/s was used for all the curves will be discussed later in Section 8.1. Both figures elucidate that both the Severn Estuary and Anglesey site 2 velocity profiles can be characterised up to depths of around 50 % using the $1/7^{\text{th}}$ power law. As discussed the distance between the lower diameter of the HATT and the seabed should not be greater than 25 % of the total water depth. For The Severn Estuary data this would occur at approximately 26 m below the

surface and 19 m below the surface for the Anglesey data, given that the total depth was 26 m at that point in the tidal cycle. It can be seen from Figures 6.23 and 6.24 that a sudden change in the velocity profile does start at these approximate depths.

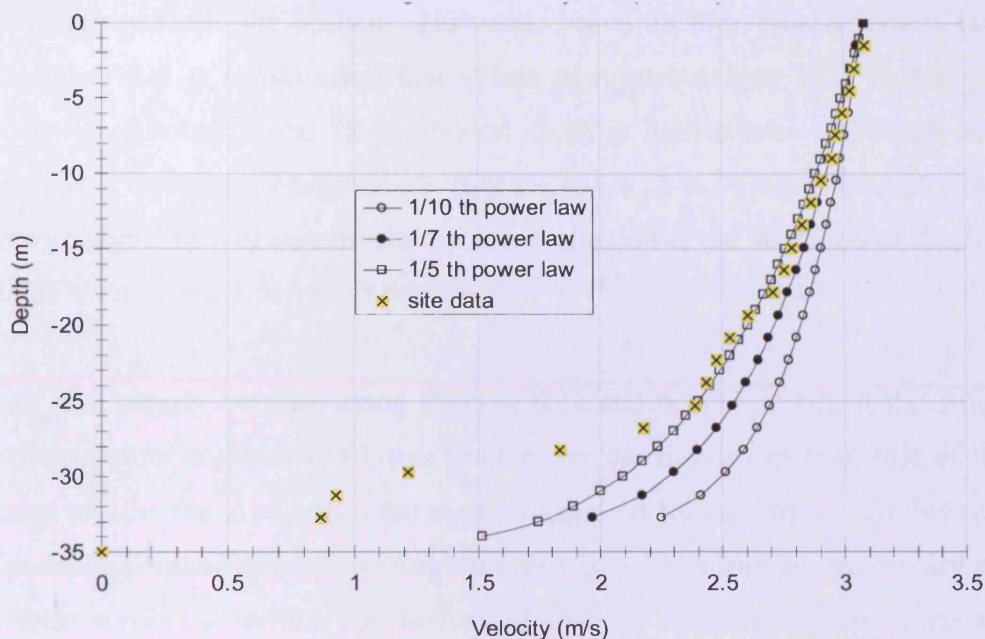


Figure 6.23: Comparison between rescaled Severn Estuary data and 1/5th, 1/7th and 1/10th power laws (HWS+3)

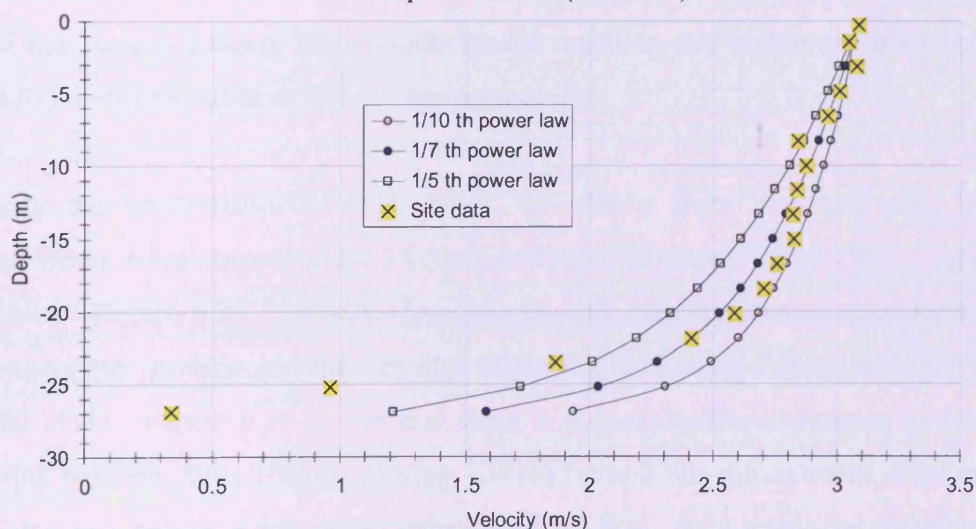


Figure 6.24: Comparison between rescaled Anglesey site 2 data and 1/5th, 1/7th and 1/10th power laws: Site 2, Anglesey data (LWN+3)

For the Severn Estuary data the power law constant $n = 1/5^{\text{th}}$ shows better correlation with the data to a greater depth below the 19 m limit. In this case up to a depth of around 25 m; this coincides with the rotational axis of the HATT. For the Anglesey data both the $1/10^{\text{th}}$ and $1/7^{\text{th}}$ power laws correlate well with the profile data down to a

depth of around 24 m. If the velocity profile below the 25 % of the overall depth is to be considered due to circumstances such as those imposed by shipping, as in the case of the Severn Estuary site, a higher order power could be used to estimate the velocity attenuation towards the seabed. However, based on the velocity data obtained from both these sites it would seem that values of n approaching $1/5^{\text{th}}$ do not capture the velocity profile below the 25 % of total depth in both cases. Although scaled, it is clear, based on these measurements, that the lower 25 % velocity boundary is relatively unpredictable and will require site by site evaluation if the operation of the HATT is to be reliable even across an array of devices.

It can also clearly be seen using Figures 6.23 and 6.24, that whilst the Anglesey site profile provides a much shallower gradient in the first 20 m than that of the Severn estuary profile, the gradient in the region suggested for the turbine, i.e. between 20 and 30 m depth, is much greater for Anglesey site than that of the Severn estuary site. Hence the shear across the turbine will be much higher for Anglesey site, with the potential to cause greater 'wear and tear', damage and maintenance costs over the life of the turbine. However, the average velocity 'seen' by the turbine in the Anglesey site is nearly twice that of the Severn estuary site, which would result in the maximum potential power output to be ~8 times that of the Severn estuary site.

To study the implications of high shear, the results from idealised plug flow and profiled flows were compared by looking at the performance of the HATT under both conditions. Figure 6.25 and 6.26 show the current velocity located at a depth of 3 m below the water surface and the velocity difference across the turbine diameter through the tidal cycle. Figure 6.25 shows that there is a considerable difference in the current velocities between sites 1 to 4. During LWN+3 site 2 has a maximum velocity of 2.2 m/s with site 3 having a minimum velocity of 1.7 m/s. As a result the potential power extractions are 171.4 kW and 79.1 kW, respectively. For sites 1 and 4 the potential power extractions are 160 kW and 93 kW, respectively at LWN+3. Taking a single velocity measurement of 2.2 m/s at site 2, for example, and multiplying this by 4 for the four sites, will give a potential power extraction of 685.6 kW (assuming a C_p of 0.4). By taking the variance across the 4 sites into account, the total potential power extraction is reduced by 26.6 % to 503.5 kW. Figure 6.26 shows the velocity differential across the turbine diameter for each of the 4 Anglesey sites with the turbine

positioned with its rotational axis 25 m below the water surface. At peak power extraction sites 1 and 2 show the largest velocity difference across the diameter at 0.75 and 0.65, respectively, indicating that all 4 sites are subject to a considerable increase in velocity shear with increase in current velocity. This phenomenon correlates with the velocity shear measured at the Severn site indicating that it may be very well be a typical feature at large number of potential sites.

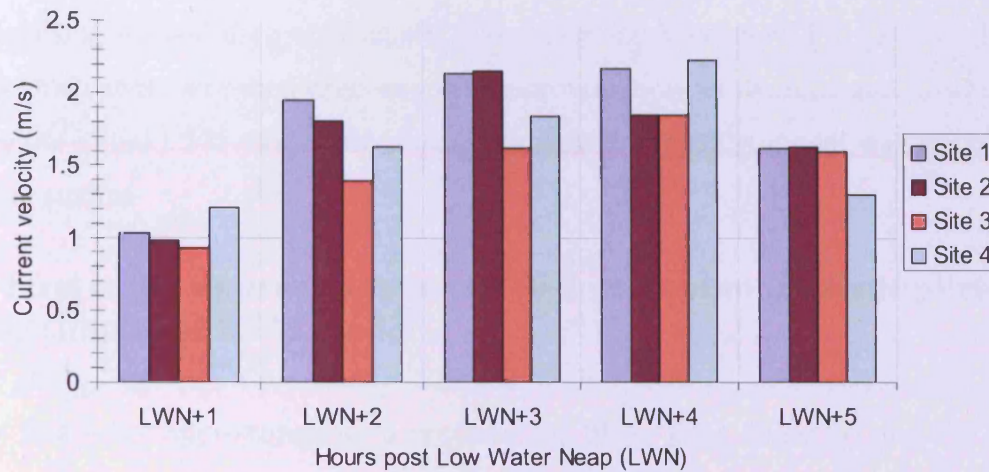


Figure 6.25: Peak velocity 3 m below water surface through tidal cycle (All Anglesey sites)

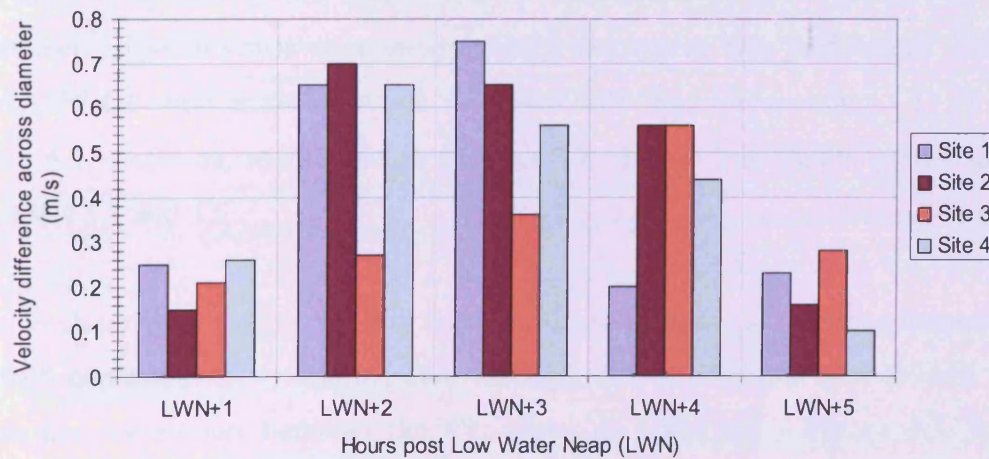


Figure 6.26: Velocity difference across turbine diameter (All Anglesey sites)

7: CFD modelling

This chapter is concerned with the development of reference and flume CFD models to calculate the load, torque and power extraction efficiency of a 0.5 m diameter laboratory prototype turbine when subjected to a plug flow. An initial BEM study is also briefly discussed. The BEM study was used to establish an initial estimate for the blade pitch angle, using lift and drag coefficients derived for the Wortmann FX 63-137. The resulting blade pitch angle was then used as a first approximation for the reference CFD model setup. Once the initial CFD model setup was established, the BEM model was no longer used in further studies.

7.1 First order approximation for TSR and optimum blade pitch angle using simplified BEM model

As a first order approximation to optimise the blade pitch angle (θ) and Tip Speed Ratio (TSR) the BEM theory was utilised as discussed in Section 4.1.2. An initial guess was made for θ by varying it between 2° and 10° normal to the rotational axis of the prototype HATT. An upstream flow velocity of 1 m/s and a HATT diameter of 0.5 m were maintained constant while an angular velocity (ω) sweep was performed. The Wortmann FX 63-137 CL with angle of attack was used with the corresponding CD set to zero, see Figure 4.3. Also as, mentioned in Section 3.1, the tip loss factor ψ was set to zero in Equations 3.1 and 3.2.

CL at each profile or segment (Ns) was calculated from the 3rd order polynomial, Equation 4.1 with constants: $A = -0.0002$, $B = -0.0013$, $C = 0.1095$ and $D = 0.7458$. Figure 7.1 shows the correlation between the CL curve as taken from Figure 4.3, lift and drag coefficients for Wortmann FX 63-137, and Equation 4.1 derived from the curve fit. Although the methodology used for the BEM theory was an ideal frictionless scenario (see Section 3.1) it simplified the development and use of the code.

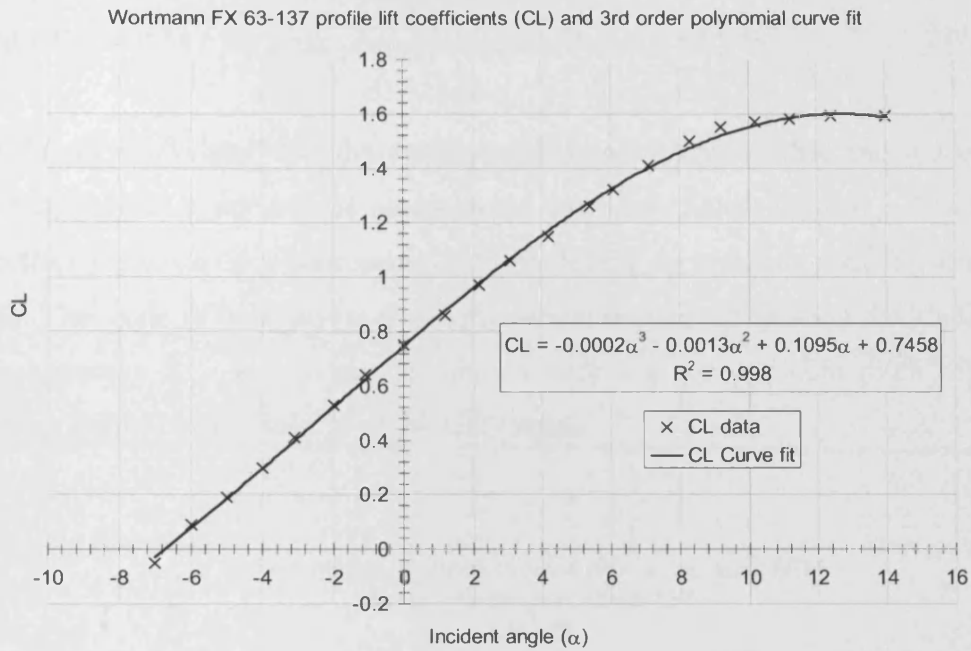


Figure 7.1: Correlation between CL curve Figure 4.3 and curve fit Equation 4.1

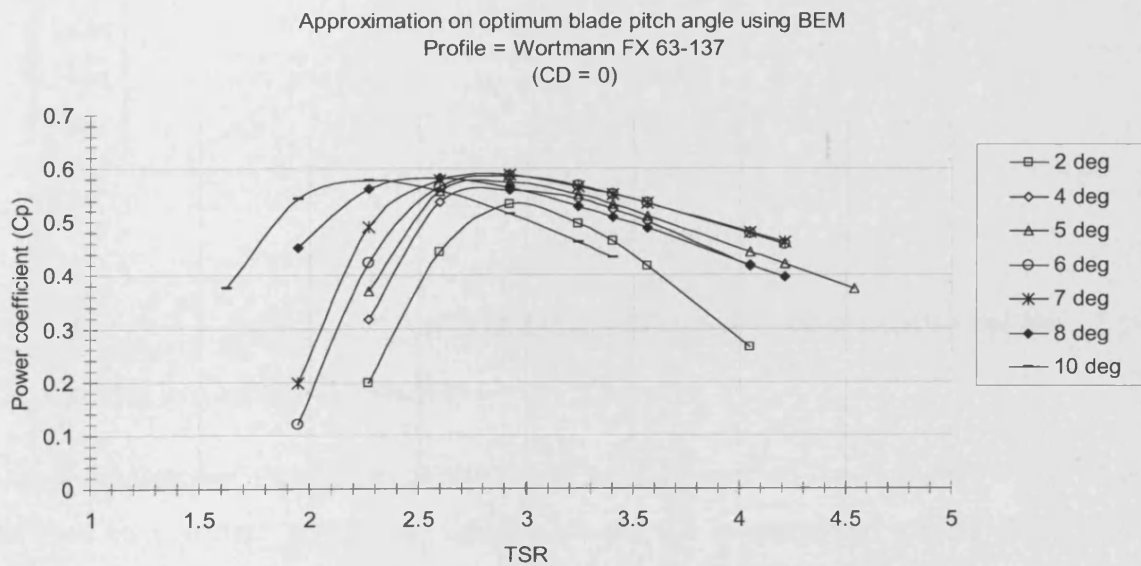


Figure 7.2: Power coefficient (Cp) with blade pitch variation using BEM to the base of Tip Speed Ratio (TSR)

The peak Cp of 0.587 is approaching the theoretical maximum value of 0.593. The peak Cp occurred at a blade pitch of 7 deg and a TSR of 2.9. This is more clearly seen in Figure

7.3 with C_p plotted to the base of blade pitch angle (θ). With an upstream water velocity of 1 m/s and a C_p of 0.587 the peak power extracted (P_p) was 57.9 W.

Whilst it is acknowledged that the optimum blade pitch angle, TSR and indeed the C_p value are subject to a number of assumptions they nonetheless formed a baseline from which to start the more time consuming CFD modelling by reducing meshing and solution iterations. The angle of twist and cord length at each segment (N_s) along the blade radius is given in Appendix 2. It will also be shown later that the optimum pitch angle of 7° , derived from BE|M, was within 1° of the CFD result.

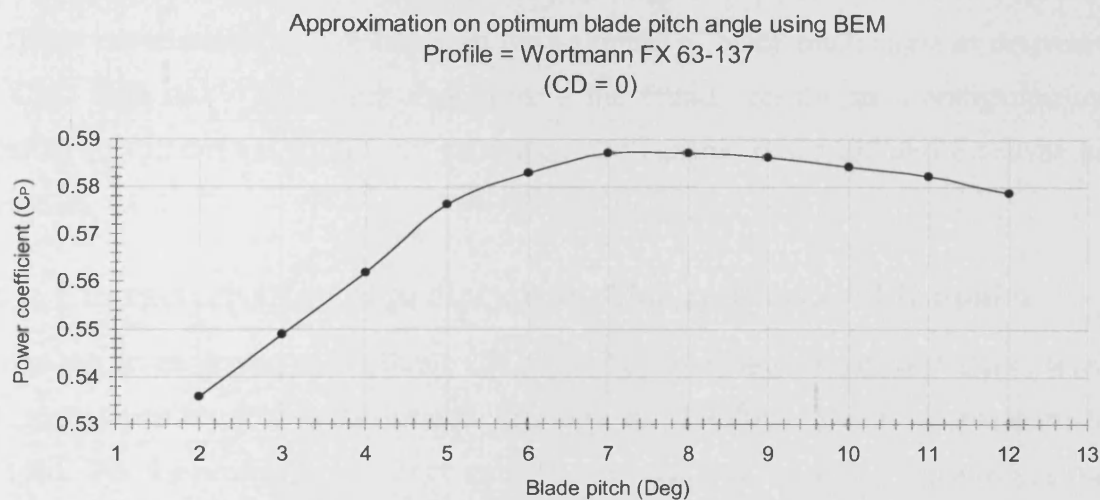


Figure 7.3: Peak power coefficient (C_p) with blade pitch angle (θ) variation

7.2: Validation of CFD models

Using the boundary constraints of the flume working section the flume CFD model was then used to correlate power extraction with the 0.5 m prototype turbine flume power measurements. The reference flume model was used to limit convergence sensitivity to mesh density and variation in MRF length along the axial flow direction. Given the validated turbine performance the turbine was then scaled to larger diameters so that its performance could be assessed under plug and profiled tidal flows. A quasi-static approach was used to calculate the power extracted over the operational range of the turbine for both the reference and flume models.

For correlation with the CFD flume model, the experimental equipment and procedure described in Chapter 4 were used to determine the torque and power curves for the 0.5 m turbine. The power extraction efficiency was determined using a re-circulating water flume at the Department of Engineering, University of Liverpool. The results of these experiments were then correlated with the flume CFD models. This procedure was used to establish the optimal viscous model to effectively capture the hydrodynamic physics of the rotors while maintaining a reasonable computational economy both in terms of memory and convergence time. The blade pitch angle for the flume tests was set using the procedure as outlined in Section 5.1.4 and the optimal pitch angle was as calculated from the reference and flume CFD models. Two further blade pitch angles of 3° and 9° were also included in the flume experiments to correlate with the optimum 6° blade pitch angle as derived from the CFD analysis. This work then formed the foundation for an investigation on the rescaling of the turbine to dimensions typical for economic oceanic and estuarine power extraction.

7.2.1: Characterisation of prototype turbine reference CFD model

Prior to the development of the flume CFD model an investigation into boundary placement and grid dependency was performed to study the resulting effects as parameters are changed. For the prototype reference model no account was taken of a supporting structure as this was added later. The TSR of 2.9 and blade pitch angle of 7° generated from the BEM study were applied as a starting point in the CFD analysis. The torque and power characteristics were then extracted using the on-demand UDF.

The first parameter to be studied was the number of cells in both the rectangular channel and in the turbine MRF. As shown in Table 4.3 the number of cells in the rectangular channel or main flow field was maintained constant at 89533 cells. The number of cells in the MRF was increased from approximately 278 thousand to 1.75 million cells. The cell count was controlled by the number initially generated while meshing the faces of each turbine blade and hub. During peak power extraction, the optimum blade pitch angle would result in a high proportion of the torque being generated within the last 1/3 of the blade

length. A finer mesh density was therefore generated towards the blade tip. The upstream and downstream faces were meshed with increasing mesh densities as shown in Table 4.3 and Figure 4.7.

The turbine blade cell density was replicated across each of the blades and was meshed using a mapped scheme with quadrilateral cells. By increasing the cell count on each of the upstream and downstream faces a series of meshes were made in accordance with the edge length scales shown in Table 4.3. The cell count on each face labelled tip, middle, root and hub were increased using the length scales as given. For example, by using the length scale sequence of 40-60-40-80 and an external MRF edge length scale of 800 a total of 278327 cells were subsequently generated within the MRF volume. With the length scale of 15-20-20-40 a cell count of 1750803 was obtained. Given the complex shape of the blades and geometry between the blades and the hub, the MRF cylindrical volume was finally meshed with a tetrahedral hybrid scheme. Figure 7.4 shows the MRF and non-conformal interface between the tetrahedral and quadrilateral (channel) meshes.

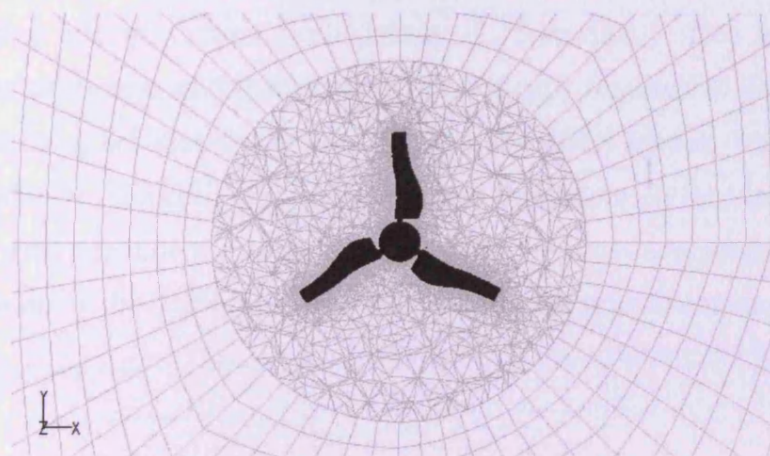


Figure 7.4: Tetrahedral MRF and quadrilateral channel mesh with non-conformal interface

The growth rate from each surface was set to the default value of 1.2. The outer boundary lines of the MRF were meshed with an edge length of 800 allowing the cell growth to be controlled between each turbine surface and the outer boundary of the MRF. The rectangular channel was meshed with quadrilateral cells with the non-conformal face at the MRF meshed with a paved scheme. Following mesh completion each model was exported to FLUENT™. For the reference flume model the velocity inlet and pressure outlet

boundaries were maintained as in the flume model. All parameter used for the viscous models were also maintained. Due to the large number of runs required to generate enough detail to calculate torque and power curves by varying the angular velocity, higher mesh densities were considered too computationally expensive. It was found that using the RSM viscosity model and the cell density scheme 7, approximately 10 hours were required for convergence and thus the computational time to calculate a single data point. Moreover, using mesh scheme 7 the model memory requirement was within 2% of the workstation maximum RAM of 2G Byte, any increase in mesh density beyond this value exceeded available memory. In comparison, cell meshing scheme 4 took approximately 5 hrs to converge and only required 75 % of the available RAM.

Using scheme 4 and a blade pitch angle of 7° a peak power of 39 W was obtained, Figure 7.5. For the 3 hour reduction in convergence time the difference in the peak power calculation is small $\sim 1\%$. This gives a reduction of 5 days from 13 days to 8 days for a power curve with 39 data points. The power obtained at mesh scheme 4 was within 99% of that obtained at the maximum mesh density (1.75 million). Due to the asymptotic change in power extraction and the large number of runs required to generate a detailed power curve, meshing scheme 4 was used for all subsequent models with minimal effect from grid dependency. The computation time is also dependent on the viscous model used; however as the grid dependency study was based on the most computationally expensive viscous model, namely the RSM, this represents the longest time to convergence.

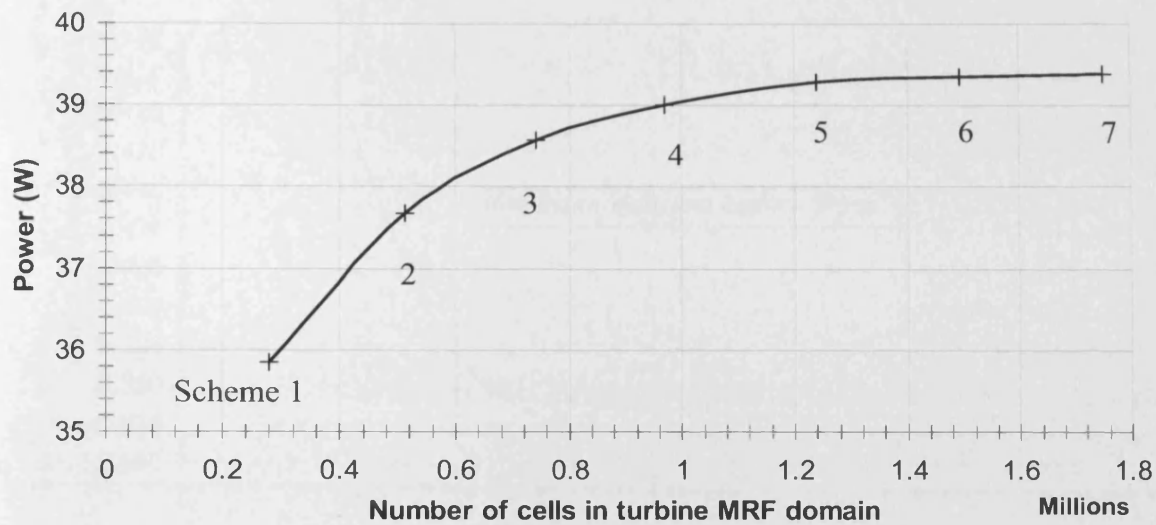


Figure 7.5: Cell count grid dependency peak power checks for reference domain prototype model.

Peak power ~ 39 W; Number of cells in rectangular channel = 89533; Blade pitch = 7°

Prior to comparing the results from the physical flume test with its equivalent CFD model a reference CFD model was used to characterise the performance of the turbine under ideal conditions i.e. free from boundary constraints and support structure. As the distance between the turbine rotational centre and boundary walls is varied any effects associated with flow concentration are exposed. The width and height of the channel directly affects the water velocity passing between the channel walls and the edge of the turbine's swept area. As the width increases the output of the turbine subsequently reduces as the flow is no longer concentrated. Figure 7.6 shows the prototype turbine efficiency against the ratio between a maximum channel width and depth of $15D$ and specific width and depth xD . For the prototype reference model a maximum width and depth of $15D$ was used to limit the domain cell count, this gave a maximum width and depth of 7.5 m. From the study, flow concentration has a reduced effect on power extraction at around 0.33 or 2.5 m width and depth. To limit any affect of flow concentration between the turbine and the boundary walls, while also limiting the cell count, a channel width and depth of 2.5 m was therefore used for the prototype reference model. The 0.33 ratio between D and the channel width and depth was therefore applied to all reference models.

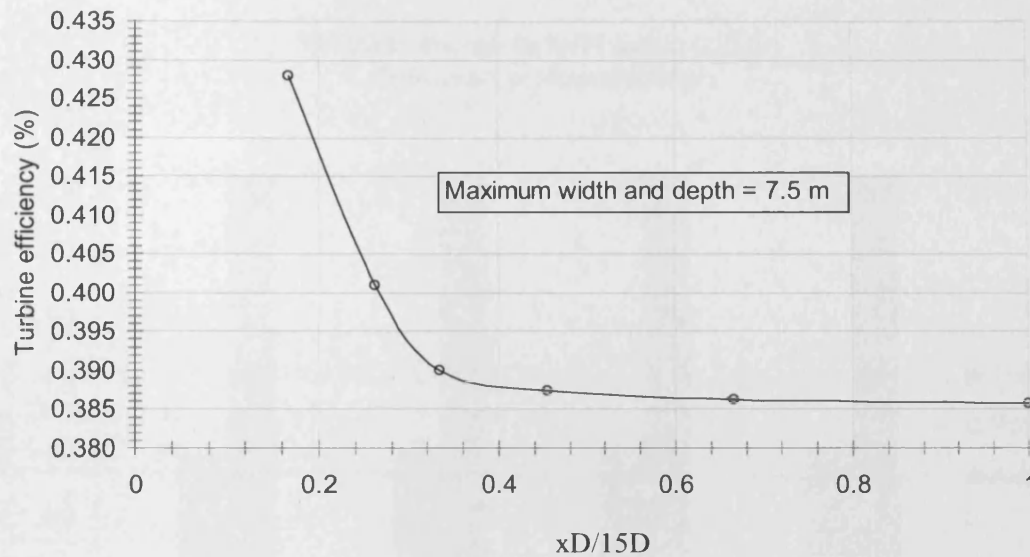


Figure 7.6: Limitation of blockage effects from boundary walls with increasing domain width and depth
(cell increase range: 0.97E6 at 2.5m & 1.3E6 at 7.5m)

7.2.2: Effect of MRF on torque, power and axial thrust load

Using the methodology discussed in Section 4.3.5 the length along the ZDS axis of the MRF volume was increased to account for any changes in turbine performance. Figure 7.7 gives the torque, power and axial thrust for 4 MRF lengths for the prototype reference model. It is clear that by varying the length of the MRF there is little effect on the torque, power or the axial thrust calculations and therefore does not require a constant length for comparison between models. However, for the sake of clarity the length of the MRF was maintained at 0.6D. Therefore, for the 0.5 m prototype turbine the MRF length $\delta ZDS = 0.3$ m, which is the base point given in Figure 7.7. However, wake recovery rates were noted to be influenced by the length of the MRF.

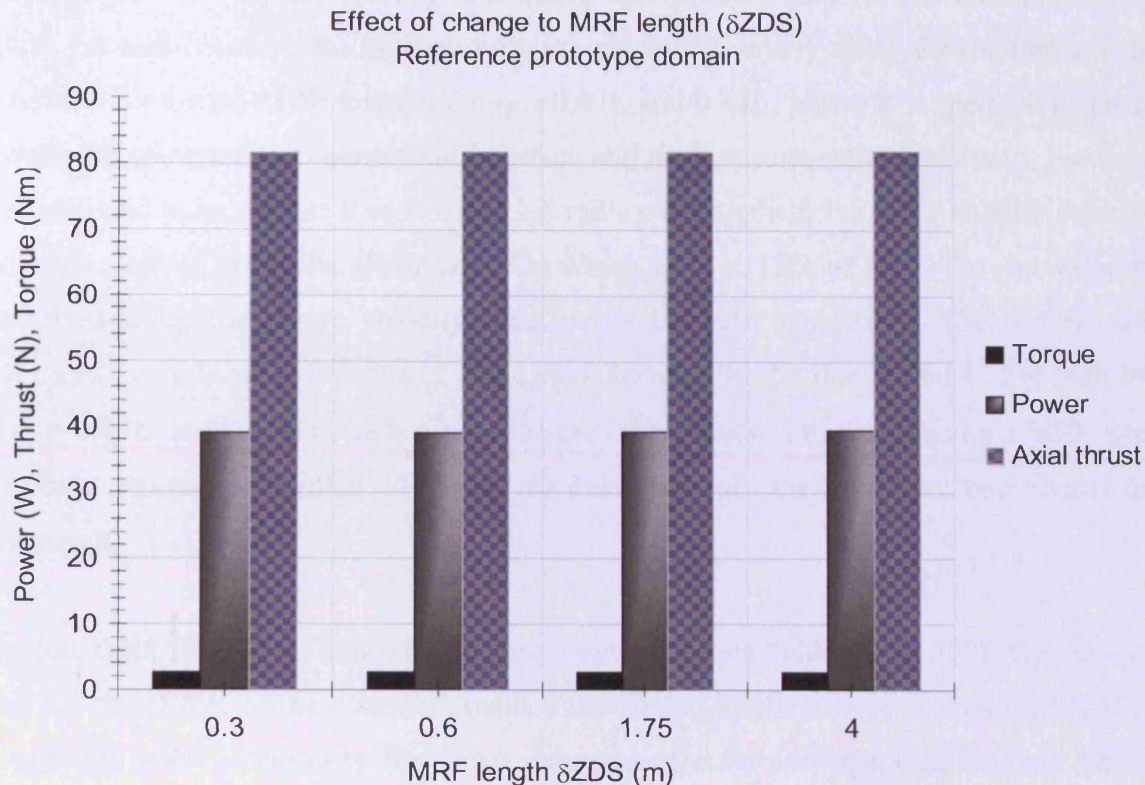


Figure 7.7: Effect of MRF length on 0.5 m diameter HATT using reference domain

7.2.3: Effect of MRF on wake velocity recovery rates

Although the length of the MRF has no effect on the torque, power and axial thrust load results it does have an affect on the wake velocity recovery rate. The magnitude and nature of the velocity field entering the channel upstream of the turbine is dictated by the conditions set at the velocity-inlet boundary. In defining the fluid momentum entering the channel the magnitude of the mass of water was specified as entering normal to the boundary along the positive Z axis. As the MRF is 5 m up stream of the velocity-inlet, there are no sheared faces between the inlet boundary and the upstream face of the MRF allowing the Absolute reference frame specification to be used (Fluent, 2005). Downstream of the velocity-inlet the water contacts the upstream interface of the MRF, which is again normal to the flow. Via the introduction of Ω to the governing momentum equations a rotational component is applied to the flow field within the MRF (Section 4.3.3, Equation 4.10). At the downstream MRF non-conformal interface the flow is once again

influenced by the channel velocity and hence the recovery rate for the channel length. Figures 7.8 and 7.9 show the normalised wake velocity recovery along the rotation axis of the turbine for a total MRF length of $Z_{DS} = 0.07L$ and $0.47L$, where L is the total distance between the upstream non-conformal interface and the pressure-outlet boundary. For each case rotational velocities of 0 rad/s and 11.6 rad/s were applied, the latter angular velocity being that derived from the BEM peak C_p which gave a TSR of 2.9. The curves were normalised using the 1 m/s velocity specified at the inlet boundary. The downstream position of the turbine is maintained at the same location as the flume model. For both the $\delta ZDS = 0.07L$ and $0.47L$ models a baseline condition was run by introducing a MRF with no turbine geometry included. Figure 7.10 then combines the data from both charts for comparison.

It is clear from Figure 7.8 that with no turbine geometry included in the MRF the velocity along the centre line of the overall domain is unaffected by the rotation component applied through the MRF. Naturally the wake recovery of a turbine operating at peak power extraction would be expected to be greater than that of the blockage effects introduced by a stationary turbine, again this is shown in Figure 7.8. These conditions are again repeated for the $\delta ZDS = 0.47L$ case, Figure 7.9. However, the wake recovery for the stationary turbine compared to one operating at peak velocity is different. For the $\delta ZDS = 0.07L$ stationary case the wake velocity at 0.1 and 0.2 of overall domain length are 0.8 and 0.9, respectively. However, for the stationary $\delta ZDS = 0.47L$ case, Figure 7.9, at the same downstream locations, the wake velocity recoveries are now 0.67 and 0.79. Indeed a reduced recovery is apparent for the $\delta ZDS = 0.47L$ case up to approximately 0.6 of the overall domain length. More noticeable is the downstream location of the non-conformal interface at around 0.44 where a small sudden rise in recovery is apparent. In Figure 7.8, the downstream non-conformal interface of the $\delta ZDS = 0.07L$ case occurs at 0.05 but with no sign of a sudden change in recovery rates. Due to the fact that zero in Figures 7.8, 7.9 and 7.10 represents the rear of the turbine a value of $\delta ZDS = 0.03L$ is subtracted from the x axis.

The same reduction in wake recovery can be seen while the turbine is operating at peak power extraction with an angular velocity of 11.6 rad/s. For the $\delta Z_{DS} = 0.07L$ case at 11.6 rad/s, with turbine, the recovery at 0.1 and 0.2 downstream locations are 0.58 and 0.74, Figure 7.8. Again, at the same downstream locations for the $\delta Z_{DS} = 0.47L$ case the normalised velocity recoveries are 0.55 and 0.64, respectively. Further downstream at approximately 0.7 the wake recovery in both instances starts to converge. With peak power extraction no sharp increase in wake recovery is noted in both the $\delta Z_{DS} = 0.07L$ and $0.47L$ cases at their respective downstream non-conformal interfaces.

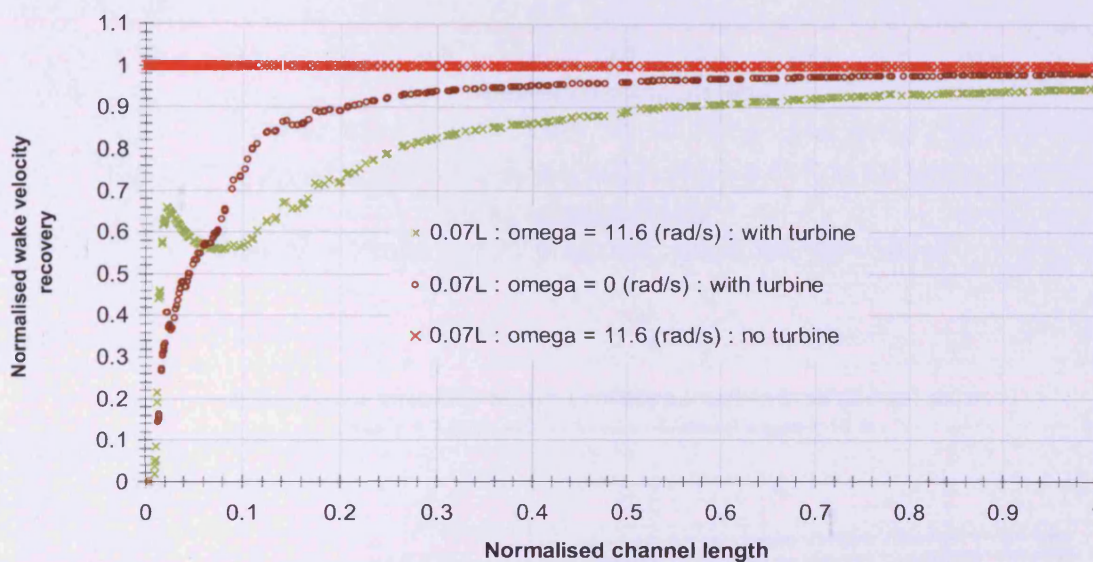


Figure 7.8: Axial wake velocity recovery with a 0.07L MRF length Z_{DS} along the rotational axis.

(Peak $V = 1$ m/s; $\omega = 11.6$ rad/s; Channel length = 10 m)

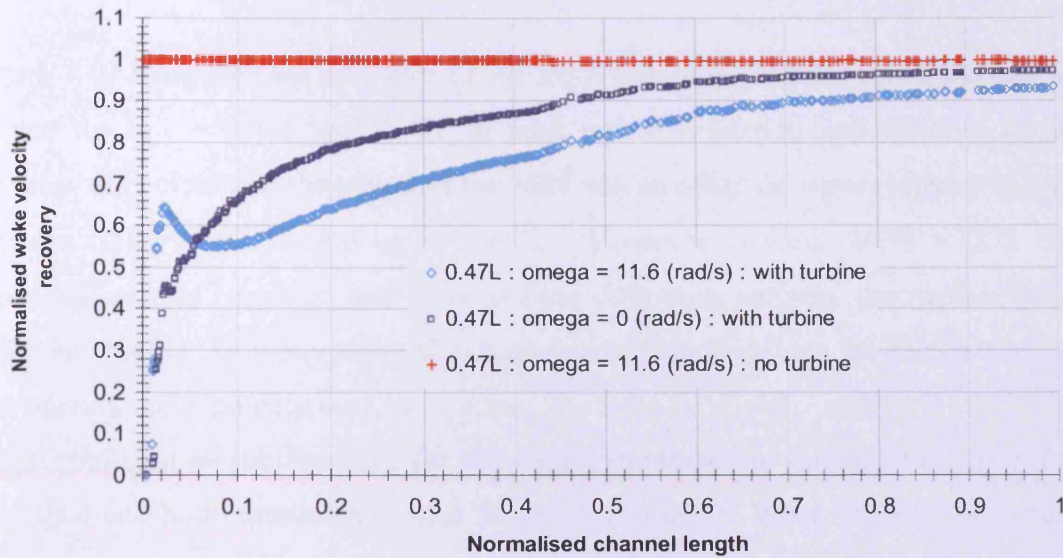


Figure 7.9: Axial wake velocity recovery with a 0.47L MRF length Z_{DS} along rotational axis
(Peak $V = 1$ m/s; $\omega = 11.6$ rad/s; Channel length = 10 m)

Axial wake velocity along prototype turbine rotational axis
Peak $V = 1$ m/s : $\omega = 11.6$ rad/s : Channel length = 10 m

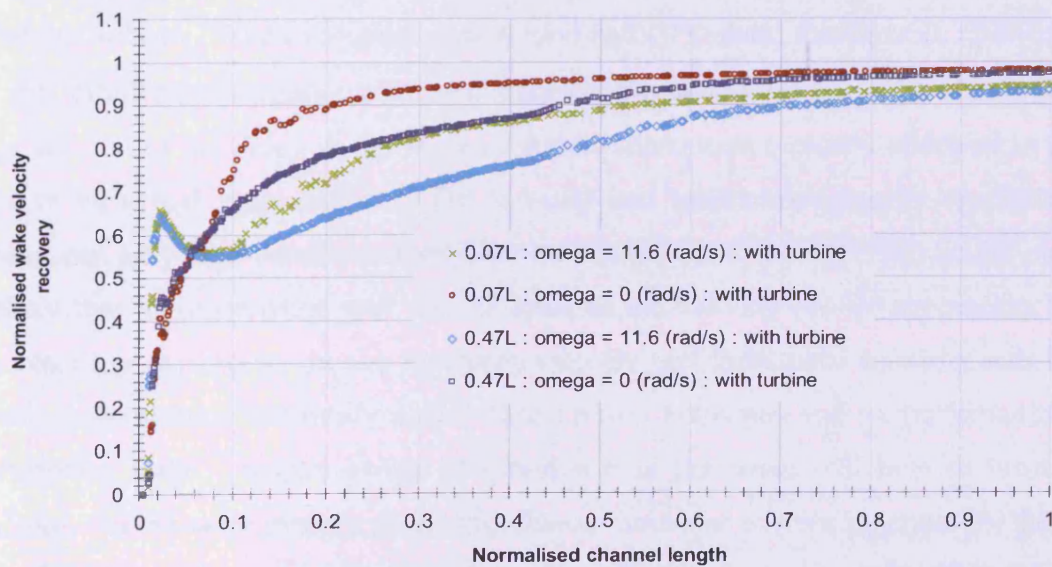


Figure 7.10: Comparison of axial wake velocity recovery with MRF length at 0.07L and 0.47L Z_{DS} along rotational axis
(Peak $V = 1$ m/s; $\omega = 11.6$ rad/s; Channel length = 10 m)

Figure 7.10 compares the recovery of the axial velocity along the rotational centre of the turbine for $Z_{DS} = 0.07L$ and $0.47L$ at peak power extraction and while in a stationary position. It is clear that the length of the MRF has an effect on wake recovery in both cases between $\delta Z_{DS} = 0.07L$ and up to $0.65L$. However, beyond $\delta Z_{DS} = 0.7L$ the wake velocities start to converge and there is little difference between the models with $Z_{DS} = 0.07L$ and $0.47L$. Without physical measurements, which include the design characteristics and operational parameters of the turbine, the near field wake recovery relative to MRF length could not be substantiated for this thesis, and therefore should be a subject for future investigation, both numerically and via measurement. What is clear however is the increase of poor diffusion beyond the MRF. This is due to the sudden decrease in mesh density in the main channel volume, which is indicated by the slightly increased scatter in each of the velocity recovery curves.

Due to time and equipment constraints during the period of testing, the CFD wake results presented in this thesis were not validated against experimental data. For this reason the data should be taken as a first order approximation of the flow downstream of the scaled prototype turbine. When comparing measured and CFD data, Rados et al, (2009) showed that the turbulence dissipation term in $k-\epsilon$ solvers has to be modified. The $k-\epsilon$ modification takes account of the delay in the velocity deficit attenuation typically observed in the near wake of an actual wind turbine. The velocity and turbulence intensity upstream of the turbine, can vary significantly between the horizontal, vertical and perpendicular planes. It is likely that the turbulence will also increase as the velocity profile approaches the bed. The resulting asymmetry in the upstream velocity and turbulence intensity will have an impact on the turbine's hydrodynamics during power extraction and on the formation of the downstream wake. Higher levels of turbulence in the wake will help to break up its structure. In the same manner as the turbulence, there also exists a potential for the wake's Reynolds stresses to be asymmetric (Myers et al, 2008). Rados et al (2009) stated that the turbulence length scales in the near wake are smaller than those further downstream. It is likely that closer correlations between measured and simulated data would be obtained if

the turbulence length scales vary downstream. The local length scales would then share a correlation with the local turbulence dissipation and kinetic energy formulation.

7.2.4: Effect of inlet turbulence intensity on peak power extraction

For the HATT optimisation study a turbulence intensity of 5 % was used, as measured using LDA along the centre of the water flume at the University of Liverpool. Taking the peak value of 39 W the turbulence intensity was varied between 2 % and 20 %, Figure 7.11.

The 18% increase in turbulence intensity between 2 % and 20 % reduces the peak power for the reference prototype model by 0.6% with a peak power reduction of 0.1% between 2 % and 10 %. By varying the length scale, Section 3.4.7, the turbulence intensity was calculated using both the turbine diameter of 0.5 m and blade tip chord length of 0.0016 m. Using these values the respective turbulence intensity was 3.1 % and 6.4 %. The difference in power extraction between the two turbulence intensities was 0.014 %. Therefore given the low sensitivity to length scale ℓ the 5% turbulence intensity measured during the flume testing was used in all subsequent CFD models.

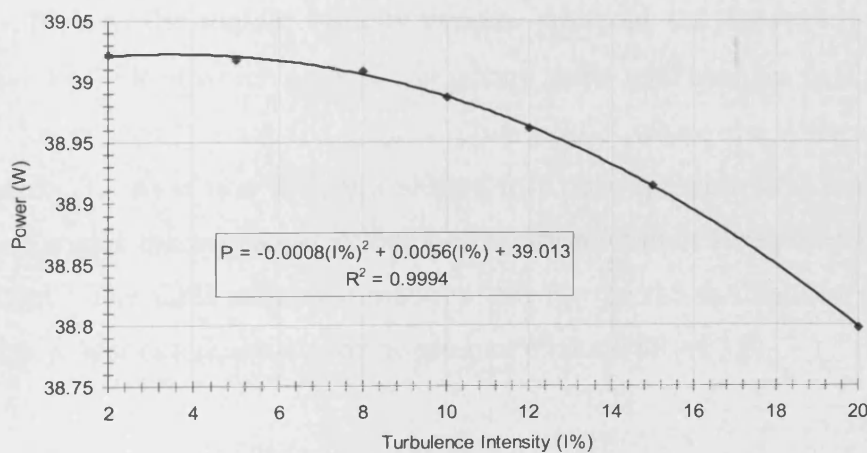


Figure 7.11: Peak power reduction with increasing turbulence intensity (I%) for flume model (V = 1 m/s)

7.3: Optimisation of flume model

Using the methodology as discussed in Section 4.4.2 the on-demand UDF was used to

extract the torque (T) and axial thrust force (F_T) at each converged steady-state solution. The total torque was calculated using:

$$P = \sum_{n=1}^{n=N} [r_x \times F_y - r_y \times F_x] \cdot \omega \quad 7.1$$

The maximum energy available (P_a) upstream of the turbine was calculated using Equation 4.36 with $C_p = 1$. For the turbine swept area an available power of 98.2 W was calculated with a maximum theoretical power extraction of 58.2 W as given by the Betz limit. From the baseline operational conditions calculated from the BEM code of 7° pitch angle and 2.9 TSR the maximum power developed by the turbine (P_p) was 57.9 W. Using the CFD model the power was calculated to be 39.1 W using the RSM model at an angular velocity of 13.6 rad/s. C_p was calculated to be approximately 0.59 and 0.39 from the BEM code and reference CFD model, respectively. To verify the optimum pitch of 7° , angular velocity (ω) sweeps were run over a range of blade pitch angles from which a series of power curves were developed. To limit the number of runs required to verify the optimum pitch angle (θ_p), coarse ω sweeps were run. Figure 7.12, shows the power curves obtained at each pitch angle (θ) over the angular velocity sweeps. Although the power curves are coarse it is evident that the TSR at which peak power occurs shifts with changes in θ as with the BEM results. This is clearly seen for a blade pitch of 12° where the TSR at peak power is approximately 3. At 6° the TSR has shifted to a new optimum of 3.6, indicating that at larger pitch angles the rotational velocity of the turbine must decrease to obtain optimum power output. The CFD reference model result for the 0.5 m diameter prototype HATT gives a peak power extraction at a blade pitch of 6° at a TSR of 3.6.

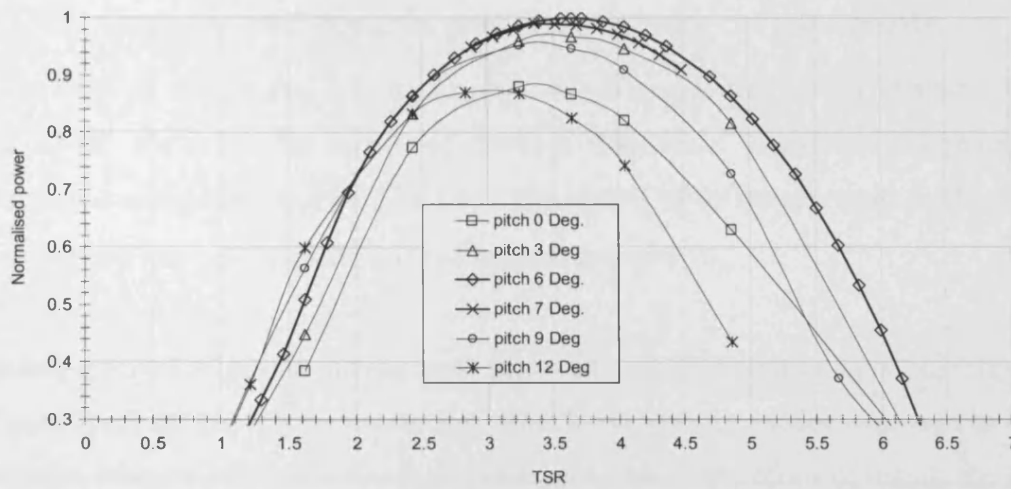


Figure 7.12: Normalised power optimisation with blade pitch variation
 (water velocity = 1 m/s plug flow)
 Peak power = 39.7 W

This is further seen in Figure 7.13 which shows C_p to the base of pitch angle (θ). It is clear from the C_p curve that the optimum blade pitch angle has shifted by only -1° relative to that calculated using the BEM theory. To increase the resolution around peak power extraction two further points were added at 5.5° and 6.5° , again the addition of these two points show that 6° is at the point of peak power extraction. The TSR at peak C_p was 3.6 at an angular velocity of 14.4 rad/s. Given the simplicity and assumptions used in the BEM theory (i.e. $C_D = 0$ and $\Psi = 1$) the small shift in θ has provided a very good first order approximation.

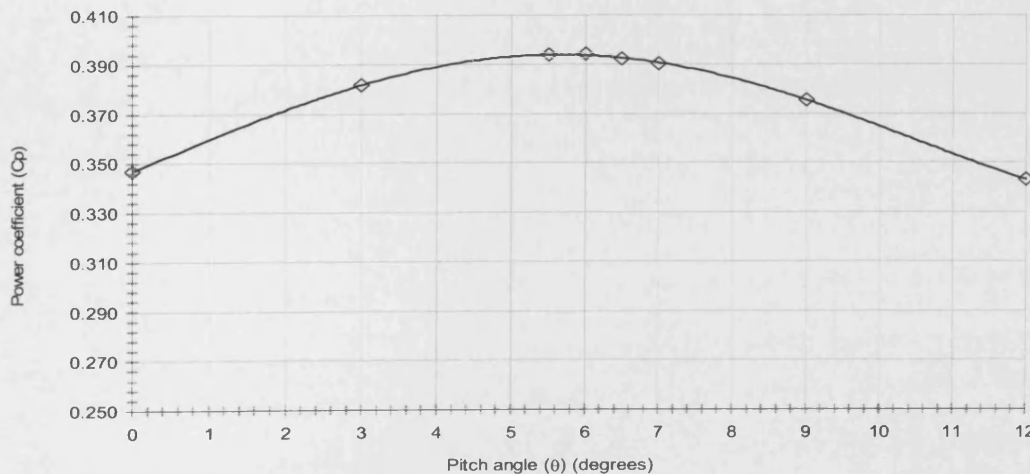


Figure 7.13: Power coefficient variance with blade pitch angle

7.3.1: CFD flume model torque, power and wake deficit results

A CFD model of the flume was used to generate torque and power characteristics for correlation with the measured flume test results as discussed. The torque and power curves were extracted using the on-demand UDF. The results of this study were used to generate graphs of torque and power to the base of angular velocity (ω).

In addition, a series of power curves were included each represented by a different viscous model used to close the RANS equations. The RSM viscous model was used to establish the optimum blade pitch angle for the prototype turbine, therefore by using the different viscous models available within FLUENT™ it was also possible to validate the use of the RSM model when anisotropic turbulence and swirl are present (Fluent, 2005).

All of the viscous models use the Reynolds averaging methodology and all except the RSM assume that the turbulence characteristics of the flow field are isotropic. The results from each of the viscous models were then summarized to give the key turbine performance parameters for each of the viscous models. As with the flume data the power (C_p) and thrust (C_T) coefficients were non-dimensionalised using Froude's Momentum Theory (Carlton, J., 2007), Table 7.1:

$$C_p = \frac{T \omega}{\frac{1}{2} \rho a V^3} \quad (7.2)$$

$$C_T = \frac{F_T}{\frac{1}{2} \rho a V^2} \quad (7.3)$$

$$TSR = \frac{\omega r}{v} \quad (7.4)$$

Table 7.1: Summary of results for CFD flume model using different viscous models

	Spalart-Allmaras	Realizable k - ϵ	RNG k - ϵ	Standard k - ϵ	RSM	Experimental Data set Av	Experimental Data set Stdev
T_m (Nm)	2.93	3.39	3.22	2.95	3.49	3.36	0.22
T_{mp} (Nm)	2.39	2.74	2.70	2.49	2.75	2.81	0.41
P_m (W)	34.39	39.41	39.67	36.52	40.4	39.82	4.85
C_p	0.350	0.401	0.397	0.365	0.404	0.41	0.05
$F_{T_{mp}}$ (N)	81.71	83.11	81.50	80.46	82.65	*	*
$C_{T_{mp}}$	0.832	0.847	0.830	0.819	0.842	*	*
$F_{T_{fw}}$ (N)	94.60	94.79	96.79	96.37	94.46	98.2	*
$C_{T_{fw}}$	0.964	0.966	0.986	0.982	0.962	0.98	*

The correlation between key turbine performance parameters for the flume tests and CFD flume model can be assessed by comparing Tables 6.1 and 7.1. In general, all the models showed good agreement with the measured data. The average maximum measured torque during the flume tests equated to 3.36 ± 0.22 Nm. From the CFD model using different viscous models good correlations were realised with the use of the Realizable k- ϵ , RNG k- ϵ and RSM with a maximum torque of 3.39 Nm, 3.22 Nm and 3.49 Nm, respectively.

The average torque at maximum power for the flume tests, including the flexible and solid drive shafts, was 2.81 ± 0.41 Nm. With the inclusion of each viscous model the respective average power from the flume CFD model was calculated to be 39.82 ± 4.85 W. From CFD the Spalart-Allmaras and Standard k- ϵ models gave the weakest correlation at 2.39 Nm and 2.49 Nm, respectively. Again, in the same order as for the maximum torque the corresponding maximum powers for the Realizable k- ϵ , RNG k- ϵ and RSM models correlate well with values of 39.41 W, 39.67 W and 40.4 W, respectively. As before the Spalart-Allmaras and Standard k- ϵ viscous models show slightly lower power extraction at 34.39 W and 36.52 W. Again, due to the interrelation of the parameters the viscous model pattern extends into the power coefficient as calculated from measured flume data and the reference CFD model. The average power coefficient for the flume tests equated to 0.41 ± 0.05 and an average of 0.38 ± 0.024 from the CFD viscous models used in the study. In general, even though there are differences in their formulation, all the viscous models

correlated well with the measured flume data and in general follow the torque characteristics of a typical horizontal axis turbine (Orme and Masters, 2004).

The power characteristics of the turbine were calculated in the same way as for the flume test data by taking the product of the torque and its corresponding angular velocity. Again, the results are plotted with different viscous models as given by Figures 7.14, 7.15 and 7.16. In terms of the power curves all the viscous models show good correlation with the RSM model with the exception of the Standard $k-\epsilon$ and Spalart-Allmaras models where differences in the shape of the torque and power curves are apparent over the complete angular velocity sweep. Starting from the freewheeling state, all of the viscous models, except for the Spalart-Allmaras, correlate well, down to an angular velocity of approximately 18 rad/s, below this value the Standard $k-\epsilon$ model starts to diverge with a maximum divergence coinciding with the point of maximum torque where it then converges with the peak torque as given by the Spalart-Allmaras model.

Both the RNG $k-\epsilon$ and Realizable $k-\epsilon$ models track the RSM curve very closely up to 12 rad/s and 8 rad/s, respectively. The largest difference between these two models and the RSM model is demonstrated by the RNG $k-\epsilon$ model around maximum torque. As the turbine slows, however, the RNG $k-\epsilon$ model starts to converge with the RSM and Realizable $k-\epsilon$ at approximately 6 rad/s. As the torque curves approach zero angular velocity the torque reduces to the stationary torque of the turbine for the given flow conditions, for the RSM viscous model this is approximately 1.2 Nm. The standard $k-\epsilon$ model gives a maximum power of approximately 35.8 W with a small shift in the angular velocity at which maximum power occurs (3 rad/s).

There is very little difference in the axial thrust load predicted by each of the viscous models. The largest difference in the axial thrust load is again between the RSM and the Standard $k-\epsilon$ and Spalart-Allmaras models. The Spalart-Allmaras model however does not use a near wall function and therefore the near surface grid resolution is insufficient to resolve the flow near to the blade surface. This occurs around the point of peak torque at an angular velocity of approximately 9 rad/s, Figure 7.14. Beyond this point the axial load

converges again. Interestingly, as the angular velocity approaches the freewheeling velocity, the axial thrust load, then start to diverge with the RSM model showing a lower

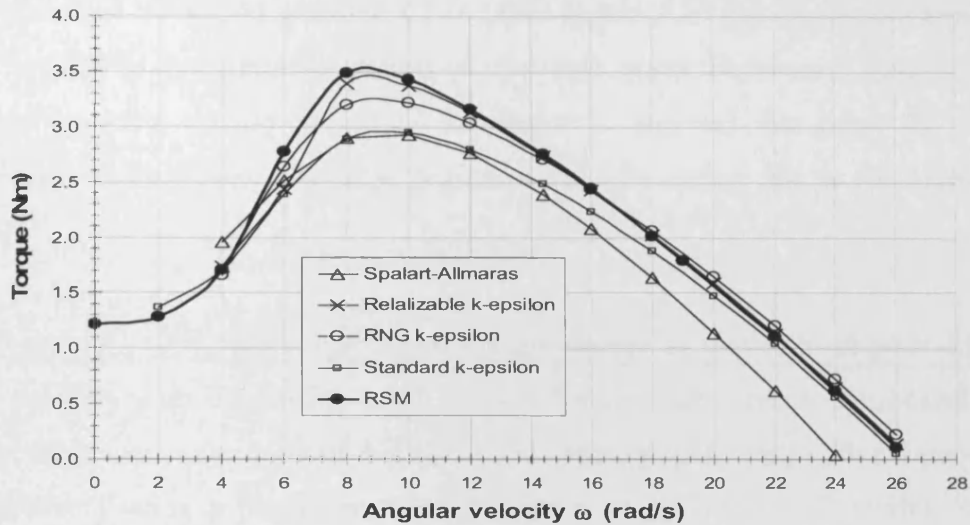


Figure 7.14: Flume CFD model using different viscous models at 1 m/s (0.5m diameter prototype turbine with blade pitch = 6°)

peak axial thrust load than that given by the other viscous models, Figure 7.16. The coefficient of axial thrust load C_T was calculated using Equation 7.3 at peak power extraction, and freewheeling. At peak power and freewheeling C_T was calculated using the RSM.

$$C_{T(\text{mp})} = 0.84(\text{RSM})$$

$$C_{T(\text{fw})} = 0.96(\text{RSM})$$

The axial thrust load measurements for the flume tests were limited to freewheeling due to the attached solid drive coupling limiting the deflection of the turbine support tube. While using the flexible coupling fluctuations were introduced as the shaft coiled and uncoiled during loading. As a result a value for C_T at peak power could not be obtained and compared to the CFD data. The experimental work, using strain gauges, gave an axial thrust force on the turbine of approximately 96.2 N, which gave a C_T at freewheeling of around 0.98 which compares well with the C_T value of 0.962 calculated using RSM viscous model (O'Doherty et al, 2009).

The velocity deficit downstream of the turbine was not measured during the flume tests and was therefore not compared with the CFD data. Figure 7.17 (a) shows that there is very little difference in the velocity deficit in the near wake between 0 and 12.5 of the normalised working section length of the flume. Beyond this point the RSM and Realizable k- ϵ model show a greater degree of velocity deficit due to the higher energy extraction.

The averaged cell node results also show a slight degree of scatter from poor diffusion of the axial velocity with decreasing mesh density towards the pressure-out boundary. The general trend however for each of the viscous models compare well with a velocity deficit curve calculated using a porous medium situated in a 3D VOF CFD model, Sun, et al, 2007.

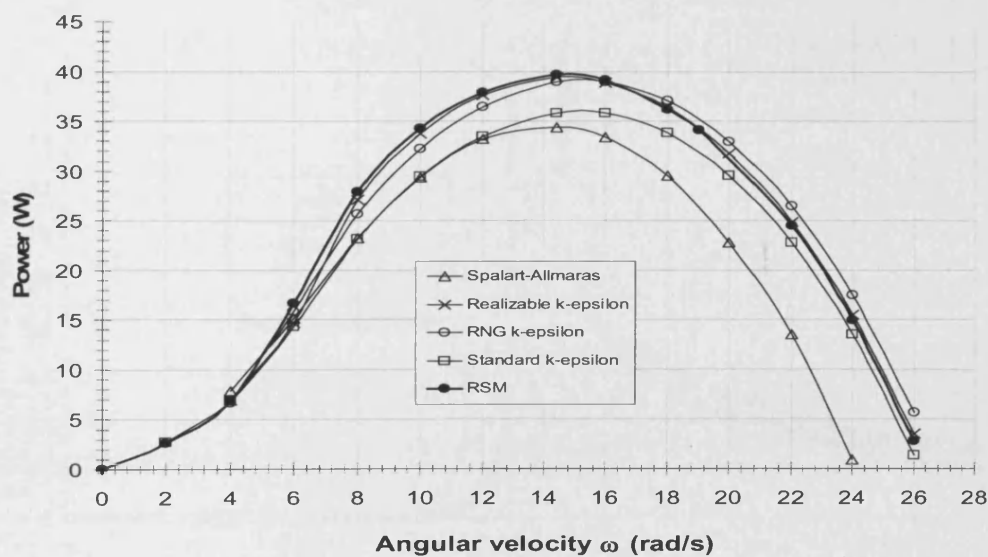


Figure 7.15: Flume CFD model using different viscous models at 1 m/s to calculate power vs angular velocity (rad/s) (0.5 m diameter prototype turbine with blade pitch = 6°)

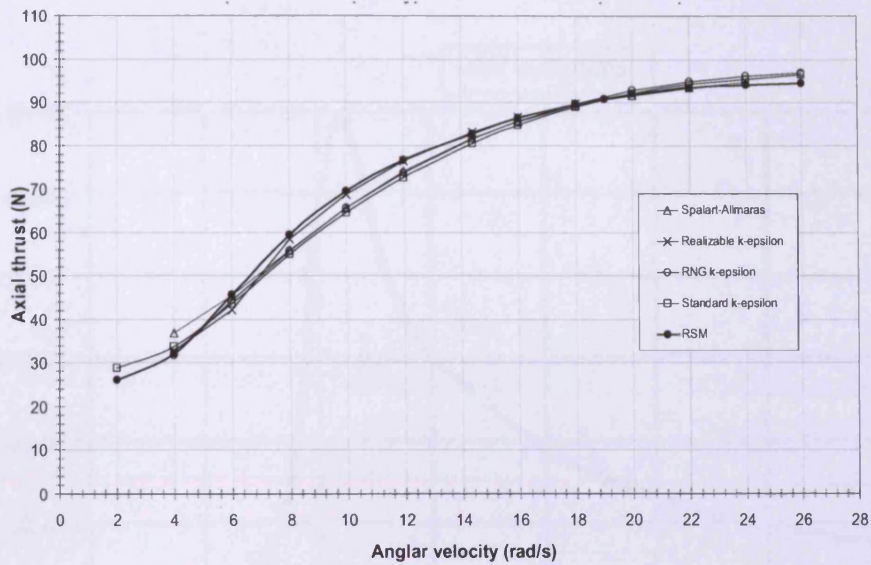


Figure 7.16: Flume CFD model using different viscous models at 1 m/s to calculate axial thrust (N) vs angular velocity (rad/s) (0.5 m diameter prototype turbine with blade pitch = 6°)

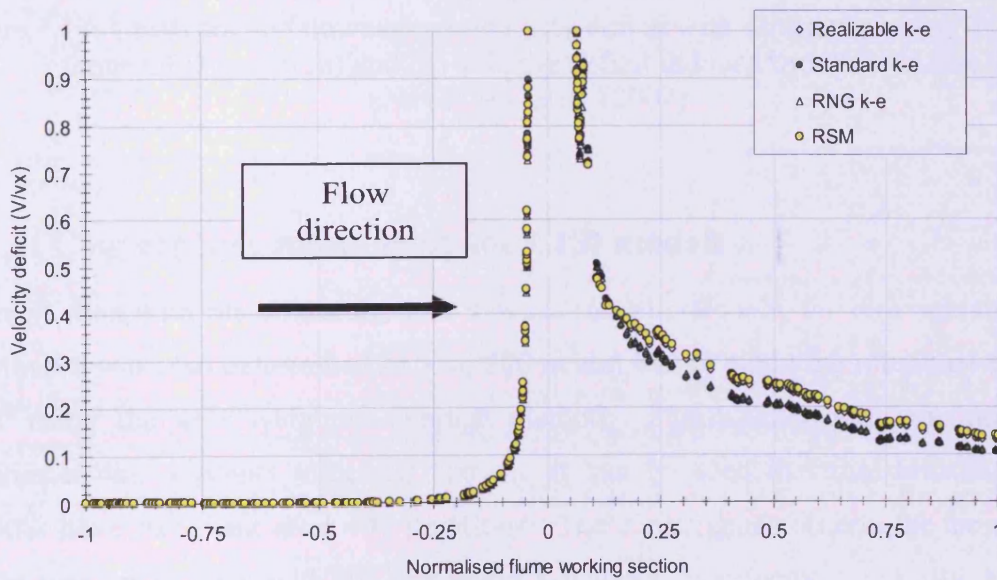
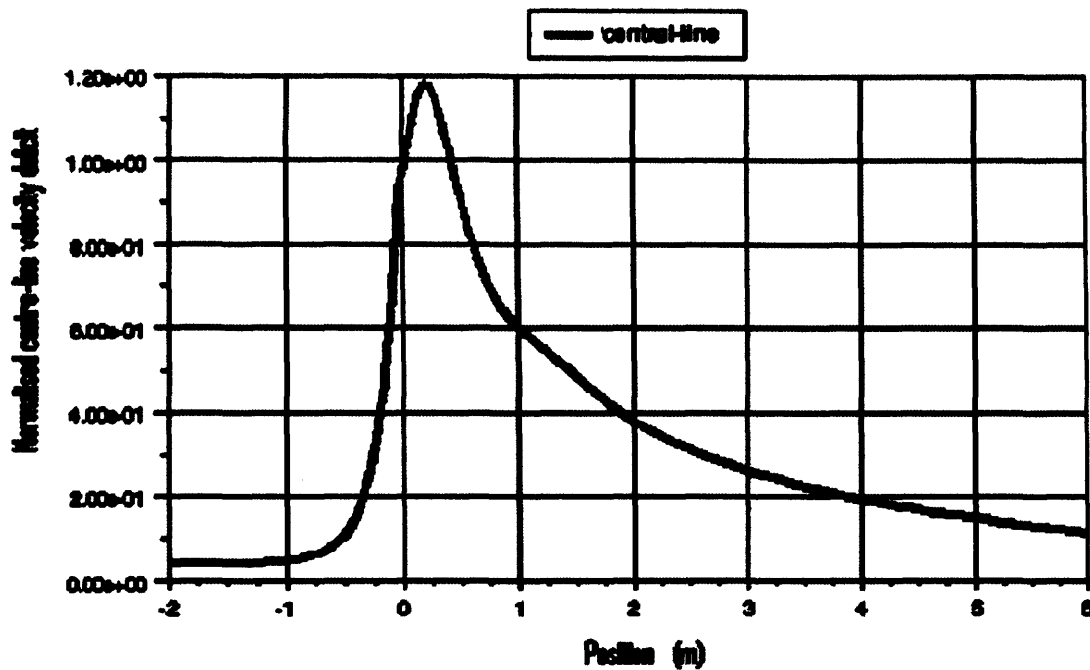


Figure 7.17 (a)



(b)

Figure 7.17: Upstream and downstream velocity deficit with different viscous models for flume CFD model (a) and (b) velocity deficit induced by a porous disc.
source: Sun et al, (2007)

7.3.1.1: Convergence monitoring for CFD models

In combination with the continuity and viscous model residuals, the downstream velocity convergence was also determined at 5 m, 200 m and 400 m along the rotational axis of the HATT using the area weighted average method. Figure 7.18 gives the downstream velocities at the 3 points indicated above. It can be seen that the downstream axial velocities have stabilized after 400 iterations. The convergence criteria for the continuity residual was set to $1E-4$ with the remaining x-velocity, y-velocity, z-velocity, k, epsilon, uu-stress, vv-stress, ww-stress, uv-stress, vw-stress and uw-stress set to $1E-3$. However, to achieve these criteria the under-relaxation factors for the continuity equation, were reduced by 2 units at around 400 iterations and a further 2 intervals at 500 iterations. It can be seen from Figure 7.18 that no further changes in the downstream velocity occur with changes in the under-relaxation factors. This procedure was also applied to the momentum, turbulence dissipation (k) and turbulence energy (ϵ) parameters: The y^* value along each of the blade

surfaces ranged between 300 and 500 for all of the models, with value of 500 towards the tip of the blade.

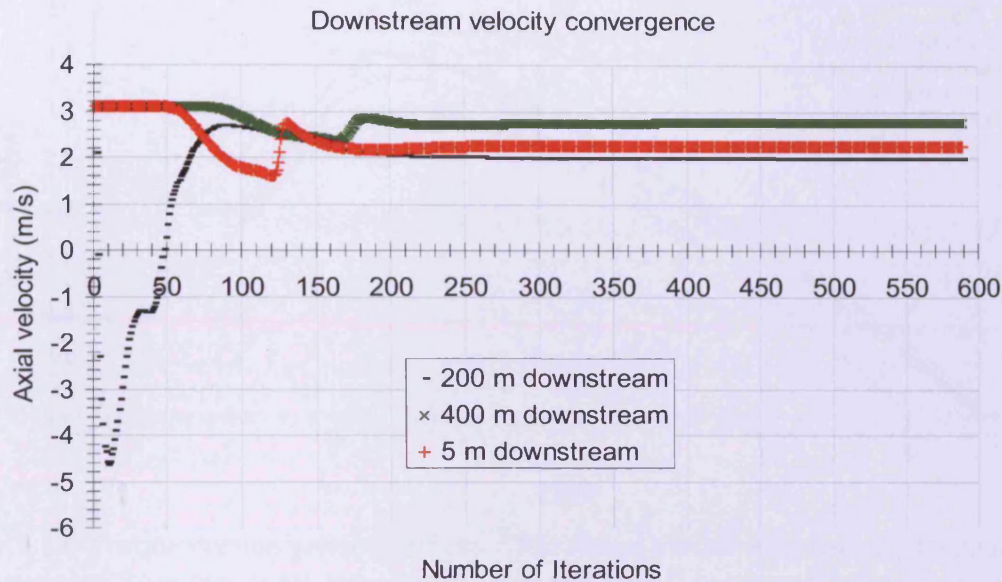


Figure 7.18: Downstream axial velocity convergence monitoring

7.4: Comparison of flume CFD model and measured flume results

Figures 7.19 and 7.20 combine the torque and power data from the measured flume and CFD flume model. The measured torque and power plots are a combination of data from both the flexible and solid drive couplings. In general all the viscous models correlate with the measured data, in particular the RNG $k-\epsilon$, Realizable $k-\epsilon$ and RSM match the torque and power curves well in both shape and with regard to the average peak torque and power calculated from the flume tests. Although the most computationally expensive the RSM model will be utilised for all other models in the thesis in part due to the close correlation with the measured data and recommendations made by FLUENTTM when swirling flows are involved (Fluent, 2005). Since the default settings on the discretisation method for the RSM viscous model allowed a good correlation with the measured flume data no attempt was made to include a further study using a second order discretisation for the momentum, turbulent kinetic energy, turbulent dissipation rate or the Reynolds stresses. It was envisaged that adding a higher order discretisation scheme would add unnecessary

computation time to the calculation of the power curves with little improvement to those already obtained with the first order discretisation scheme.

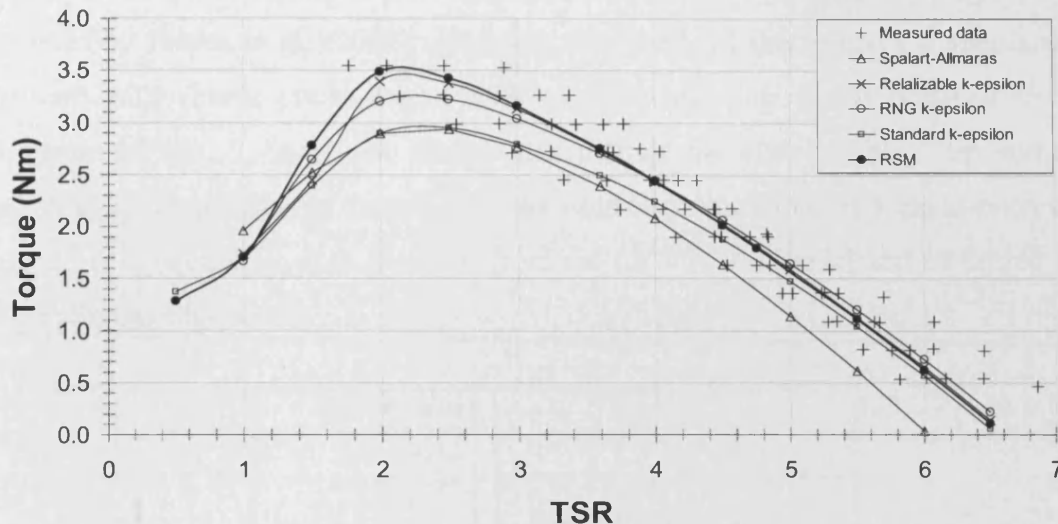


Figure 7.19: Torque curves generated from CFD flume model with various viscous models and measured from the flume tests while using both the flexible and solid drive couplings (0.5m diameter prototype turbine with blade pitch = 6°)

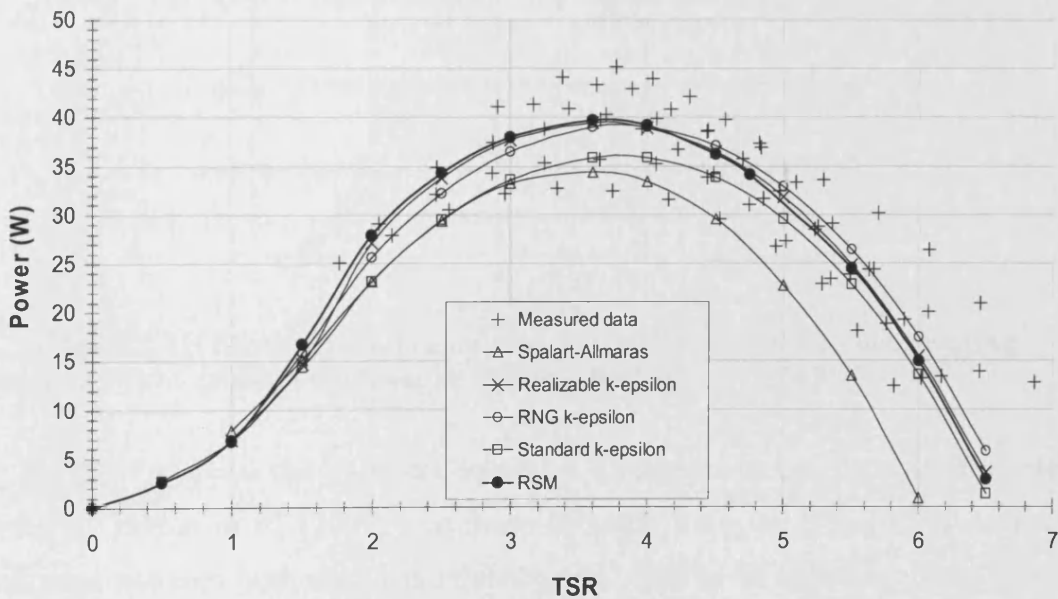


Figure 7.20: Power curves generated from CFD flume model with various viscous models and measured from the flume tests while using both the flexible and solid drive couplings (0.5m diameter prototype turbine with blade pitch = 6°)

Although there are fundamental differences in blade design and test conditions, data sets produce by Batten et al, (2007) make a useful comparison for the results of both the CFD

flume model and measured flume data produced for this thesis. Figure 7.21 gives the results of the study relating to the performance characteristics of the model via measurement using a cavitation tunnel and those data obtained from BEM theory. The data as presented by Batten et al, (2007) compares the results of theoretical C_p simulations at various hub pitch (blade pitch) angles with experimental data points obtained from the cavitation tunnel test. Again, the results also include the effect of blade tip immersion depths, although as previously stated, only the optimum conditions at a blade pitch of 20° are directly compared with data obtained from the CFD flume model and measured flume data for optimum conditions.

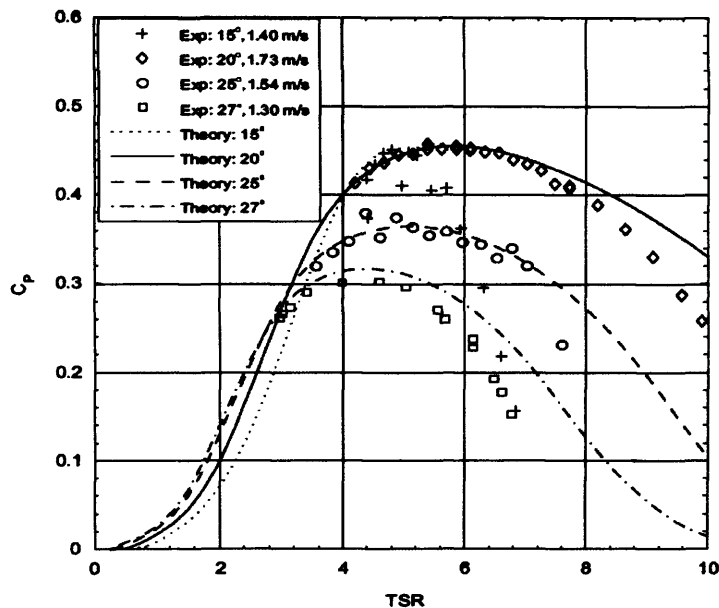


Figure 7.21: Measured and calculated power coefficient (C_p) with varying blade pitch angle. Source: Batten et al, (2007)

Using the RSM to close the transport equations a comparison can be made between data presented by Batten et al, (2007) and those obtained from the flume CFD model. The general trend between both data sets is very good. It is to be expected that a shift in the TSR would occur due to fundamental differences in blade design and diameter and that higher power extraction is obtained with blade optimisation. It is interesting to note that the general trend of the curves match that of the BEM model discussed at the start of this chapter to generate an initial guess for the optimum blade pitch angle. The theoretical curves in Figure 7.21 start with a sharp rise in power then a slower decay with increasing

angular velocity, which is repeated with each blade pitch variation. The RSM, RNG and Realizable k - ϵ models on the other hand indicate that the power drops off more sharply with increasing angular velocity, Figure 7.20. The one equation Spalart-Allmaras model shows a much sharper decay in the power following peak power extraction than all the other models. This earlier decay is also present in the measured data represented in Figure 7.21 where all three measured power curves show an increased in the rate of decay of power extraction with increasing TSR when compared with the theoretical power curves. The general shape in the measured data however shows a closer correlation with that of the RSM, RNG and Realizable k - ϵ viscous models given in Figure 7.20. From the mechanically loaded run the power curve generated by Orme and Masters, (2004) also shows a similar rate of decay above peak power extraction, Figure 2.12. This then increases confidence in the use of the RSM viscous model outside the flume validation measurements performed for this thesis. Also the averaging methodology applied to smooth the scatter introduced via the measured angular velocity during the flume measurements.

7.4.1: Effect of stanchion dam on power measurements

There is another phenomenon that could contribute to the fluctuation in the measured flume data which involves the interaction between the blades and the supporting stanchion. The resulting variation in power and axial thrust as the blade passes the stanchion is a result of the slower moving water upstream of the stanchion. The true dynamics of this interaction were not studied during the experiments and therefore can not be characterised quantitatively in this discussion, there is however literature from the wind industry that discusses this phenomenon with regards to acoustic emissions, blade loading and cyclic power generation or ‘flickering’. Murtagh et al, (2005) and Zahle and Johansen, (2007) discuss some aspects of these interactions through the use of mathematical modelling. Although there are fundamental differences between the two operating media i.e. air and water density, the main causation for pulsing in the blades and tower motion is from turbulence intensities, flow shearing between the top and bottom of the rotation cycle and vortex shedding between the turbine blades and stanchion or tower.

It is hypothesised that in addition to the flexing of the flexible drive coupling, the scatter experienced in the angular velocity data could also be attributed to blade and stanchion interaction. Although not studied in the flume model, the cyclic loading induced by a stanchion is studied later for a scaled 10 m HATT. For upwind blade turbines the distance between the rotors and the stanchion are typically high (Zahle and Johansen, 2007). Hau, (2006) suggests that for air, the distance between the tower and the rotor should be around 1 tower diameter upstream of the tower. Figure 7.22 shows the so-called tower dam effect or reduction in the upstream velocity ahead the tower for a wind turbine. When x/D approaches 1 the relative free stream velocity is around 0.9 of the upstream velocity. Figure 7.23, shows the dam velocity upstream of the stanchion in the flume model. At 1 stanchion diameter the relative velocity recovery was approximately 0.82 indicating a slightly reduced upstream velocity from dam effects when compared with the wind tower example. This further reduction could be attributed to the incompressibility of the water extending the dam effect further upstream.

The diameter of the stanchion in the flume tests was 0.05 m and the upstream location of the turbine centre was 0.1 m upstream of the front edge of the stanchion, this gives a Z_{us}/D ratio of 2 which gives a relative upstream velocity of 0.92 from the stanchion dam. Figure 7.23 also elucidates that the relative upstream distance (Z_{us}/D) should be between 4 and 5 if the dam effect is to be minimised or removed from the measurements when operating in water.

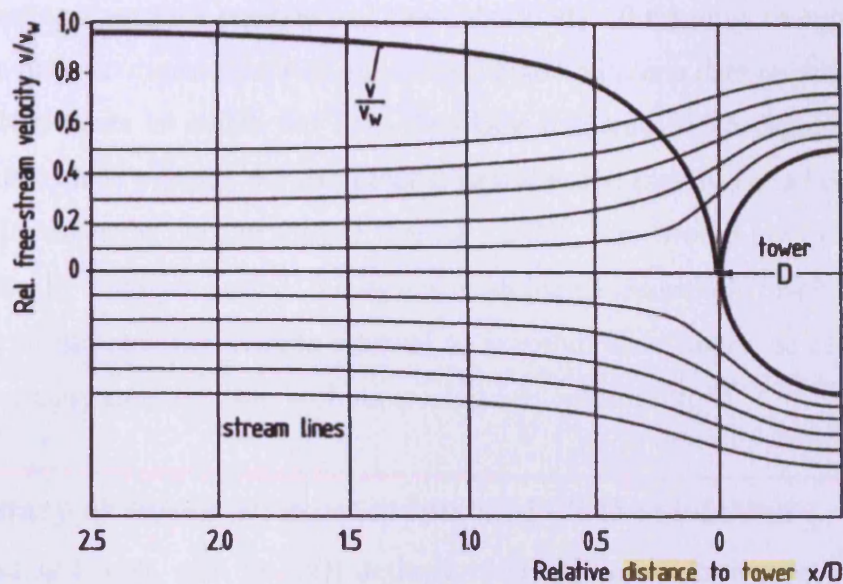


Figure 7.22: Normalised velocity profile of upstream tower dam effect. Source: Hau, 2006

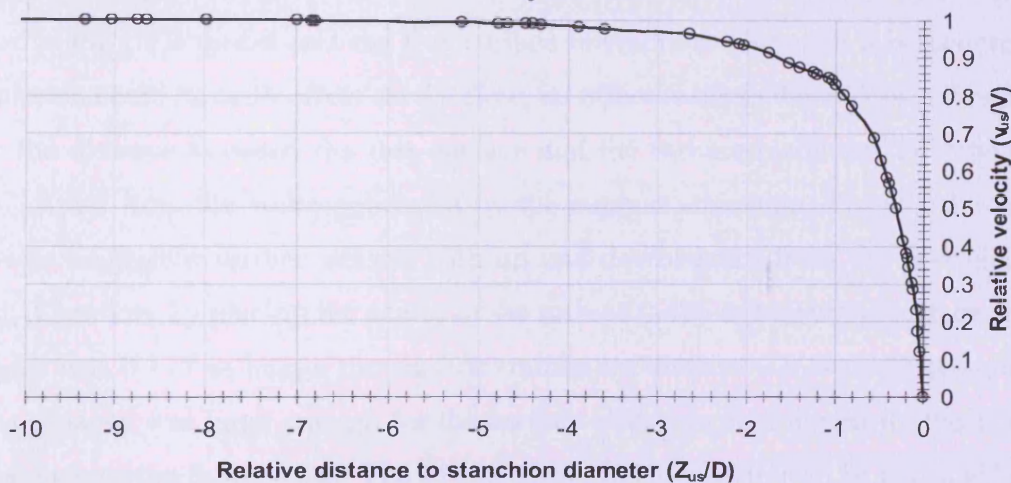


Figure 7.23: Normalised relative distance (Z_{us}) upstream of stanchion dam (circular cross section)

$V = 1 \text{ m/s}$

To further quantify the impact of the cyclic loading a higher sampling frequency would need to be applied to the load macro. The highest sampling rate would be required at freewheeling where the angular velocity for the 0.5 m diameter prototype HATT is approximately 26.5 rad/s which equates to a rotational frequency of 4.2 Hz using $\omega = 2\pi f$. Since the turbine has 3 blades the passage frequency is then 3 times the rotational frequency, 12.6 Hz. For the 10s sample interval used during the flexible drive coupling

tests the sampling frequency equated to 12 samples every 10 s giving a sampling frequency of 1.2 Hz. In order to capture the passing of each blade with one data point this would have to increase 10.6 times to match the 12.6 Hz blade frequency. To capture the dynamics before and after blade passage the sampling frequency will then have to be increased to at least 50 or 100 times the current sample rate of 1.2 Hz. This would give 10 thousand data points over the 10 s sample period. However, with increased sample resolution it will also be necessary to increase the sample interval to accommodate improved resolution on the time to reach steady state rotation with increasing servomotor torque

7.5: Summary of flume measurements and CFD validation

The recirculating flume, with its well defined velocity profile, known level of turbulence intensity and size of the boundary layer in the working section provided a test facility that could be easily replicated in the CFD model of the working section. The only parameter not included in the CFD model was the free surface interaction. Although it is recognised that this omission could have an effect on the flow, its effect is depth dependent and reduces the greater the distance between the free surface and the turbine blade tip (O'Doherty et al, 2009). Apart from the wake generated by the support stanchion, Figure 6.1 shows that there were negligible surface effects both up and downstream from the operation of the turbine. Therefore by placing the centre of the turbine 0.425 m below the surface, the tip of the blades was 0.175 m below the surface (minimum distance). It was therefore assumed that this distance was large enough for the surface effects to be minimal for the 1 m/s flow used for each of the flume tests. The results show this assumption to be reasonable for the conditions described, however, if the inlet velocity were to be increased the blockage effects of the turbine may cause substantial up and downstream surface interaction as indicated by Meyers and Bahaj, (2007). On inspection of the experimental results it is clear that the measurement of the torque provided an accurate data set with an average of 3.36 Nm and a standard deviation over the tests of 0.22 Nm. The same level of accuracy could not be said of the measurement of the angular velocity where there is a definite scatter. The accuracy of the torque is due to the fact that this is a measure of the applied torque from the servomotor. The scatter found with the angular velocity however was much larger and therefore requires further investigation into the servomotor control and data acquisition.

What is interesting is the fact that when a best line fit is applied to the angular velocity data and then used to calculate the power, the data can be seen to provide a good comparison, i.e. a maximum power of 39.8 W against a predicted (RSM) value of 40.4 W. Whilst the validation of the CFD models are reasonable there is evidence that in order to reduce the scatter in the experimental data, particularly the angular velocity, the blades should be set clear of the stanchion. Mitigation of the experimental errors may also be produced by integrating the servomotor with the blade hub, so providing a direct drive from the turbine shaft into the motor.

Examining the CFD data shown in Table 7.1 it is clear that the Realizable k- ϵ model and the RSM are the most reliable for this work, providing very close global results which are comparable to the experimental data. The RSM has been primarily used for this work due to its capability to reasonably model anisotropic turbulence and flow separation from the turbine blades. There is however a discrepancy between the experimental and CFD data in terms of the power produced as a result of the scatter in the measured angular velocity. Figure 6.12 shows that whilst there is only a small difference between 3° and 9°, the maximum power occurs at 6°. The experimental data, using the averaged values of torque and angular velocity results in the maximum power being derived at 3°. The differences in the maximum values are, however, also showing only small differences which are in agreement with the CFD data. This provides an interesting point which is that this turbine is reasonably insensitive to the blade angle over this range, as also suggested by the 0.5 m prototype reference CFD model.

8: Scaling from 0.5 m diameter prototype turbine

To establish the operational parameters of the prototype HATT under estuarine and or oceanic conditions, it was necessary to scale the 0.5 m diameter prototype turbine to dimensions proportional to those summarised by the DTI report on the Economic viability of a simple tidal stream energy capture device, (DTI, 2007) and UK resource estimates from Black and Veatch, (2005). From the aforementioned citations, with water depths up to 40 m, a HATT diameter of between 10 m and 20 m is typically quoted. However, for many sites there are restrictions from local water depths and shipping, as in the Severn Estuary. This Chapter discusses the scaling of the HATT to a suitable dimension using CFD and preliminary data obtained from flume tests on the 0.5 m diameter prototype turbine.

8.1: Geometric scaling of prototype turbine

There are essentially two scenarios when considering the size of a HATT above and beyond rated power requirements. Although this subject area was covered in studies little over a decade ago by researchers such as Bryden et al, (1998) the link between depth and the nature of the local velocity profile is still site and design dependent. The only constant link is through the use of the $1/7^{\text{th}}$ or $1/10^{\text{th}}$ power law for predicting a typical velocity profile. Table 8.1 shows the influence of water depth on maximum permitted HATT diameter for a range of water depths. It is suggested that where shipping restrictions exist, the tip of the rotor needs to be 1.5 m below LAT for the lowest negative storm surge, 2.5 m for the trough of a 5 m wave and a further 5 m to minimise the potential for damage from local shipping lanes. Therefore, the tip of the HATT at top dead centre should be around 9 m below LAT. The bottom of the HATT should not be within 25 % of the water depth at LAT from the seabed. At the proposed site the water depth at LAT is around 34 m, this would give an undesirable depth band of 8.5 m between the HATT lower diameter and the seabed. However, due to the large vessel draft of approximately 14 m (Auld, 2008) near the proposed site, the lower depth restriction could not be realised as this would place the tip of the HATT diameter at LAT. The 25 % restriction on the distance between the lower diameter and the seabed may not be practical at locations where large cargo vessels are

common place, such as within the Severn Estuary. The Severn Estuary, however, remains an important part of tidal stream resource with its ability to make a valuable contribution to mitigate problems associated with power variability from out of phase tidal cycles. It has been shown that with the installation of tidal stream devices located in the Severn Estuary along with further installations in the Clyde, Tees, Humber, Menai Straits and the Mersey a more or less regular National grid supply could be established (Hardisty, 2007). With no local shipping restrictions the rotational axis of the turbine could potentially be positioned at mid water depth.

Table 8.1: HATT diameter with water depth. Source: Bryden, et al., 1998

Water depth (m)	Rotor diameter (with local shipping restriction) (m)	Rotor diameter (without local shipping restriction) (m)
< 20 m	-	10 m
20 – 25 m	5 m	20 m
25 – 40 m	10 m	20 m
> 40 m	20 m	20 m

Using the relationship between water depth and rotor diameter for a water depth between 25 m and 40 m with local shipping restrictions, the recommended rotor diameter is 10 m and 20 m with no restrictions. To establish the operational performance characteristics of the prototype HATT, used for this thesis, a series of scaled CFD models were developed with the domain boundary conditions proportional to that developed for the prototype reference model. For example, the 5D spacing between the turbine and the boundary walls, and from Table 4.3 meshing scheme 4 with its associated grid density.

In phase II of their UK Tidal Stream Energy Resource Assessment, written for the Carbon Trust, Black and Veatch stated that at depths between 30 m and 40 m the Mean Spring Peak velocity (V_{msp}) is between 2 m/s and 4.5 m/s for the UK (Black and Veatch, 2004). Moreover, in the Variability of UK Marine Resources report the rated tidal velocity was taken to be 70% of the Mean Spring Current peak speed (Carbon Trust, 2005). Therefore, to keep the study in line with typical UK resource estimates the velocity at the proposed site was scaled from the local peak of 1.87 m/s to 70% of the maximum V_{msp} of 4.5 m/s as proposed. This gave a peak velocity of 3.17 m/s, which was rounded to 6 knots or 3.08 m/s

as the use of knots is a typical nautical unit. This velocity was also used in Section 6.3.4 to scale the Anglesey velocity profiles.

The 3.08 m/s plug flow was applied at the velocity inlet boundary with the turbulence intensity (I%) and hydraulic diameter D_H as specified in the turbulence specification method, discussed in Section 4.3.7. The turbulence intensity (I%) was set to 5% and the hydraulic diameter set to the chord length at the blade tip with increasing diameter. The blade tip pitch angle was set to 6° as calculated from the prototype reference model.

8.2: Non-dimensional analysis of CFD and flume data

Using the methodologies discussed in Chapter 4, the power, torque and axial thrust load were non-dimensionalised for both the CFD and measured flume data. Using a fixed pitch angle (θ) of 6° , with increasing turbine diameter and upstream water velocity, the results gained from the non-dimensional study allowed the turbine's performance characteristic to be studied. The non-dimensionalised CFD and flume data were then used to give a quantitative estimate to the CFD model's ability to capture changes in key turbine performance characteristics.

To explain any changes in the HATT performance with the transition from the prototype turbine diameter to larger diameters, a series of CFD models were developed ranging from 10 m to a maximum diameter of 30 m. The 0.5 m prototype turbine was also added to the data set later in the study. The performance characteristics of the larger diameter turbines were then compared with the prototype turbine. The quasi-static approach using a MRF model was again used. Through the use of the UDF, angular velocity sweeps, for each turbine diameter, were run producing a set of torque, power and axial thrust curves. The CFD torque, power and axial thrust data were then non-dimensionalised producing key performance curves of torque (C_{Torq}), power (C_p) and axial thrust (C_T) coefficients against tip speed ratio (TSR).

8.2.1: Comparison of non-dimensional study for reference CFD models with increasing turbine diameter and upstream water velocity (Plug)

If the upstream tidal velocity is assumed to be constant and the turbine diameter increased, then the angular velocity must be reduced to maintain the optimum TSR. If the TSR and the torque are maintained, the efficiency of the turbine should be unaffected by changes in diameter and upstream water velocity. The operational range of the TSR should also be the same for each case. However, to check for any changes in efficiency, C_p curves were plotted to the base of TSR for each increase in turbine diameter and upstream water velocity.

Figure 8.1 shows C_p vs TSR for the CFD reference model with increasing turbine diameter and water velocity. What is clear from Figure 8.1, as the turbine diameter is increased from 10 m to 30 m, is that C_p collapses to a single curve over the operational range of the turbine. It is also clear, from Figure 8.1, that the maximum C_p of 0.4 is unaffected when either the diameter of the turbine or the upstream water velocity is increased. Again, it is also evident that the C_p curves, while subject to changes in the upstream water velocities, collapses onto a single curve. Figure 8.2 shows the same coincidence in the curves, when the TSR is plotted against C_{Torq} , again, for the same increase in turbine diameter and water velocity. As with Figure 8.1 C_{Torq} follows the same trend and collapses onto a single curve. When plotted against TSR the axial thrust coefficient (C_T) curves, Figure 8.3, also collapse onto a single C_T curve.

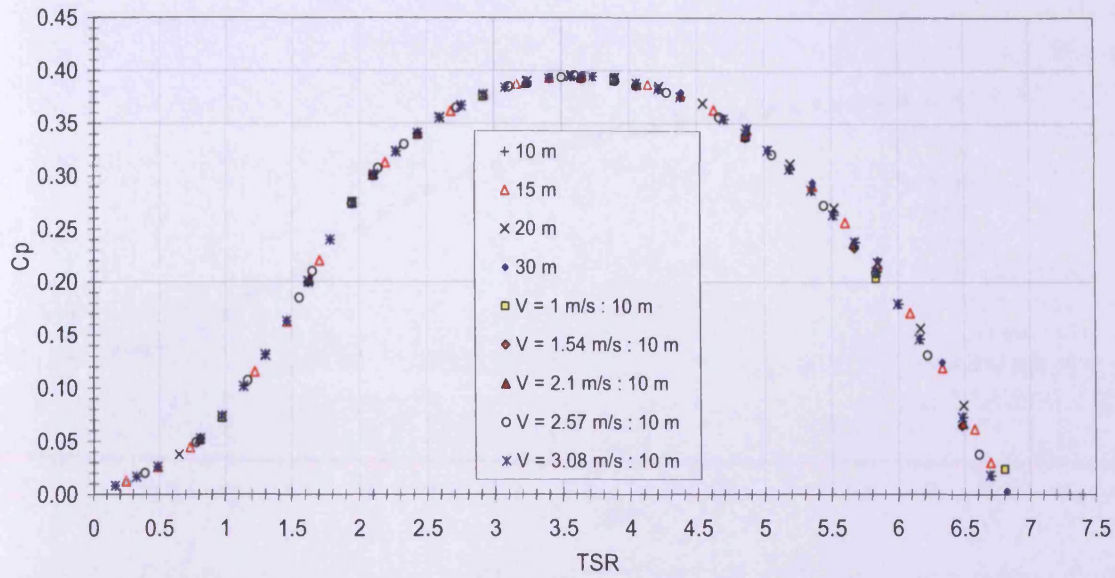


Figure 8.1: Combined power coefficient (C_p) vs TSR with increasing turbine diameter and upstream water velocity (plug flow = 3.08 m/s for diameters 10 m to 30 m)

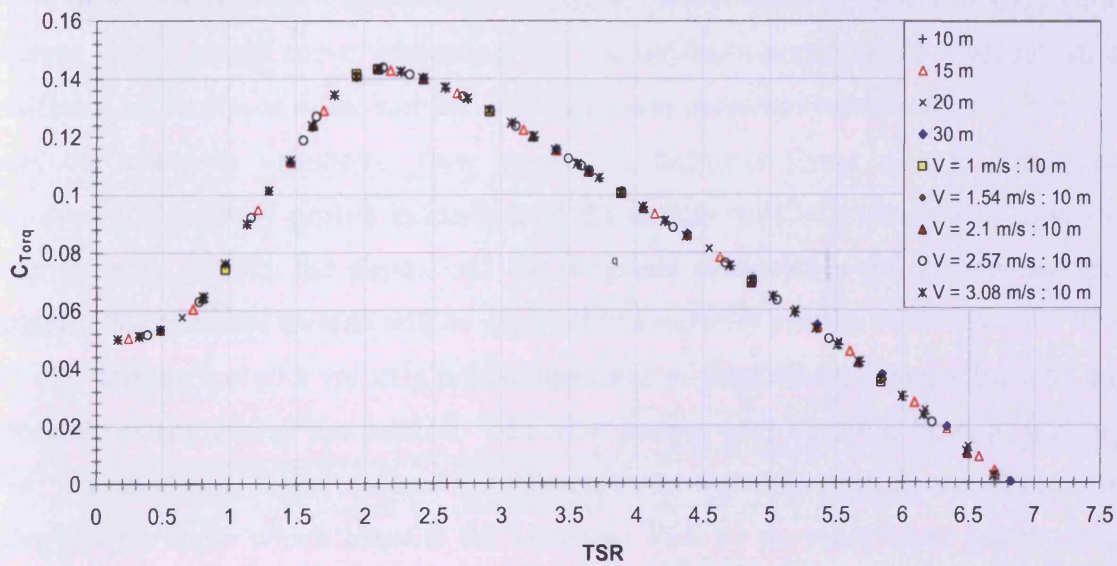


Figure 8.2: Combined torque coefficient (C_{Torq}) vs TSR with increasing turbine diameter and upstream water velocity (plug flow = 3.08 m/s for diameters 10 m to 30 m)

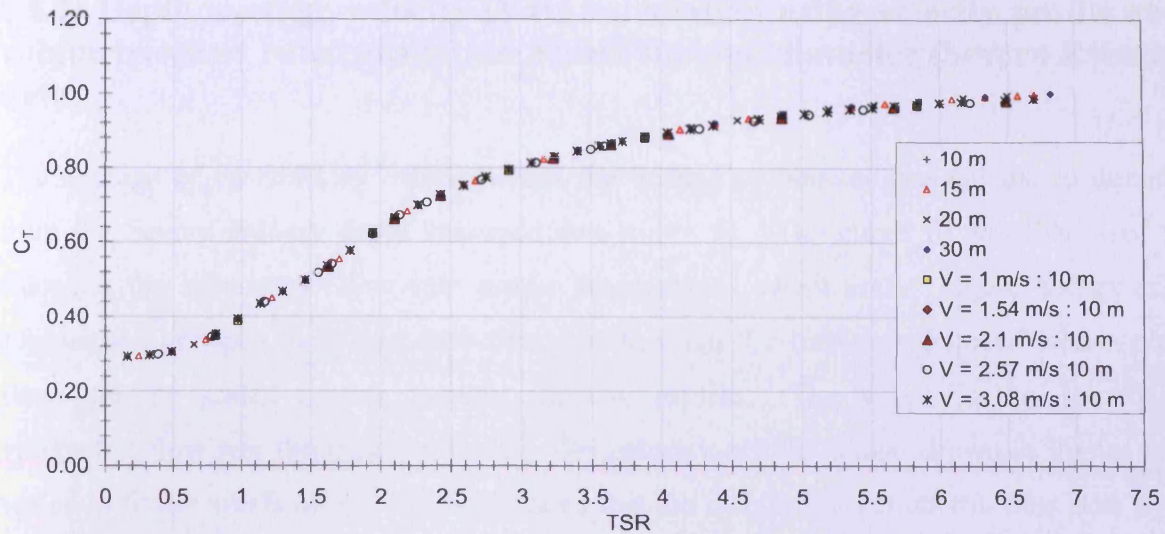


Figure 8.3: Combined axial thrust coefficient (C_T) vs TSR with increasing turbine diameter and upstream water velocity (plug flow = 3.08 m/s for diameters 10 m to 30 m)

While using a plug flow, Figures 8.1, 8.2 and 8.3 show that the combined CFD data sets collapse onto a single curve, indicating that the turbine's performance characteristics are unaffected by increases in the turbine's diameter and upstream water velocity. With a plug flow, the upstream volumetric flow across the turbine's swept area is homogeneous. However, if a velocity profile is introduced the turbine will be exposed to a reduction in water velocity through the depth. At the proposed sites within the Severn Estuary and Anglesey Skerries, the turbine will be exposed to a velocity profile, as discussed in Chapter 6. The introduction of a velocity profile upstream of the turbine, changes the total energy across the swept area of the turbine. The total energy with a profile flow, as with a plug flow, is proportional to the cube of the velocity. For a profile flow, however, the velocity changes with depth which impacts the optimum TSR as the rotor blade rotates between TDC and BDC. To investigate the magnitude of the average velocity, the volumetric flow rate across the turbine's swept area was calculated. The turbine's swept area was discretised through its depth and multiplied by the velocity at that depth, as given by the Severn Estuary data, see Equation 4.35. The horizontal velocity distribution, across the swept area was assumed to be constant. The resulting averaged velocity was then used to calculate the available energy upstream of the turbine. For comparison the swept depth average of the velocity profile was also calculated.

8.2.2: Depth average velocity (V_{av}) calculation using velocity profile and volumetric flow rate calculation across turbine diameter (Severn Estuary data)

The average of the velocity profile across the turbine's diameter was calculated directly from the Severn Estuary depth averaged data curve fit. The curve fit was then used to calculate the volumetric flow rate across the turbine's swept area. Figure 8.4 gives a comparison between the volumetric flow rate through the turbine calculated with a plug flow and the scaled Severn Estuary velocity profile. The x-axis is the discretised volumetric flow rate through the depth. The velocity profile is also shown in Figure 8.4, scaled to fit the x-axis ($1E-2$). It can be seen that the discretised volumetric flow rate, with a plug flow, is symmetrical either side of the rotational axis of the turbine at a depth of 25 m. The depth average velocity of the profile across the turbine area was 2.2 m/s, producing a volumetric flow rate of $173 \text{ m}^3/\text{s}$. Using the volumetric flow rate method, a total of $164 \text{ m}^3/\text{s}$ was calculated with an average velocity of 2.07 m/s. With a velocity profile, the peak volumetric flow rate can also be seen to shift towards the TDC of the turbine. For the Severn Estuary data, 56% of the overall flow rate occurs above the rotational axis.

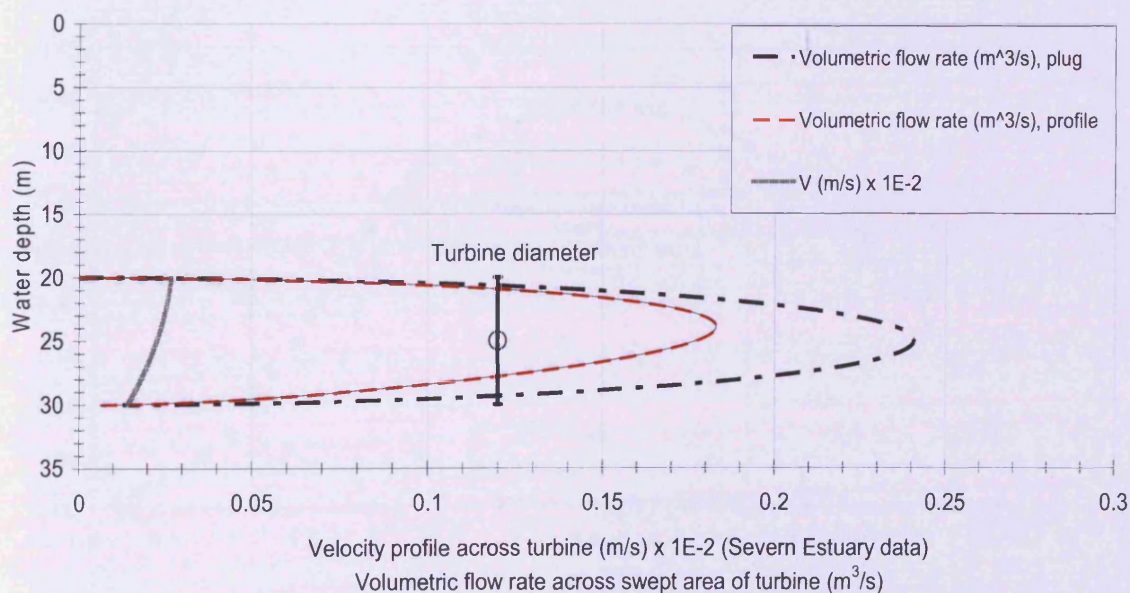


Figure 8.4: Comparison between profiled and plug volumetric flow rate across turbine area

8.2.3: Non-dimensionalised turbine performance characteristics using the average of the upstream velocity profile (Severn Estuary data)

Figures 8.5, 8.6 and 8.7 show the collapsed curves for C_p , C_{Torq} and C_T for the 10 m diameter turbine with varying upstream water velocity (plug), depth average velocity and the average velocity calculated from the volumetric flow rate. Figure 8.5 shows that the peak C_p , while applying the depth average, was reduced to 0.34 from 0.4. A similar reduction in the peak C_T is also evident from Figure 8.6. At a TSR of 2.1, C_T is reduced from 0.144 to 0.12. However, using the average velocity of 2.07 m/s, derived from the volumetric flow rate calculations, it can be seen that the C_p , C_{Torq} and C_T curves once again fall onto the single curve. It is clear, from each of the latter figures, that the velocity profile has very little effect on the key performance characteristics of the turbine if the average of the volumetric flow is used (2.07 m/s). What is apparent, however, is the effect of the cubic proportionality between the flow velocity and C_p and the square proportionality of both C_{Torq} and C_T . These proportionalities result in each of these curves having a high sensitivity to the value of the upstream water velocity, which ultimately affects the calculation for the available energy in the flow.

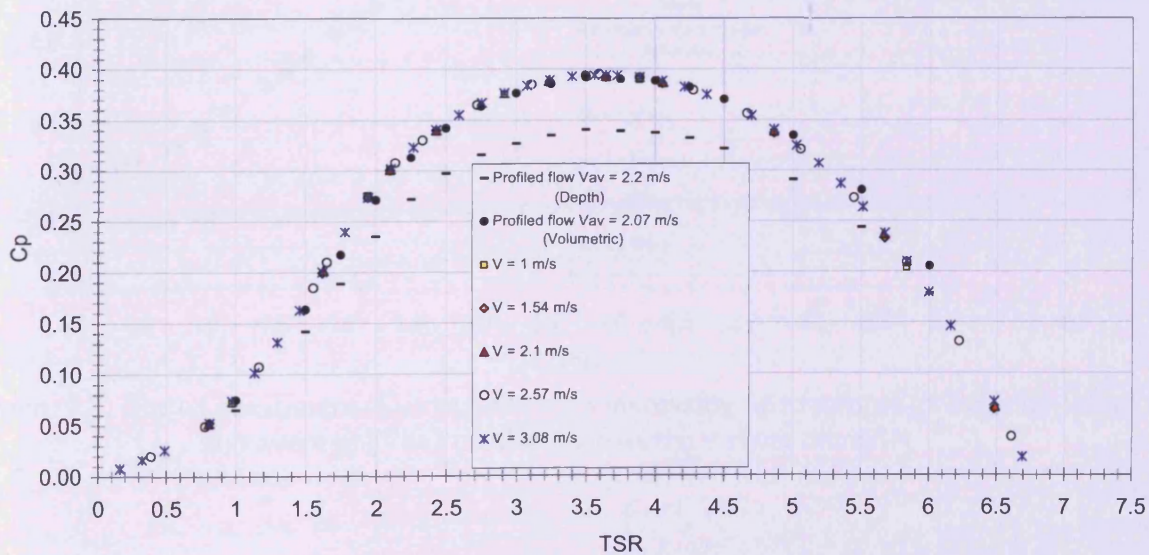


Figure 8.5: Power coefficient (C_p) vs TSR with increasing upstream water velocity (plug) and average (V_{av}) profiled flow across the turbine diameter

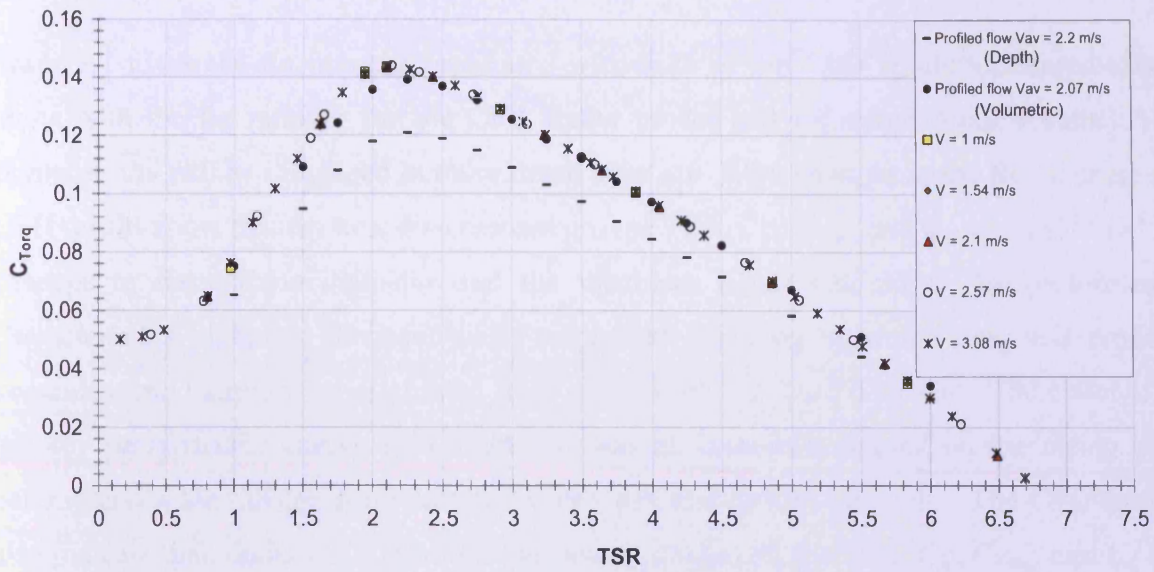


Figure 8.6: Torque (C_{Torq}) coefficient (C_{Torq}) vs TSR with increasing upstream water velocity (plug) and average (V_{av}) profiled across the turbine diameter

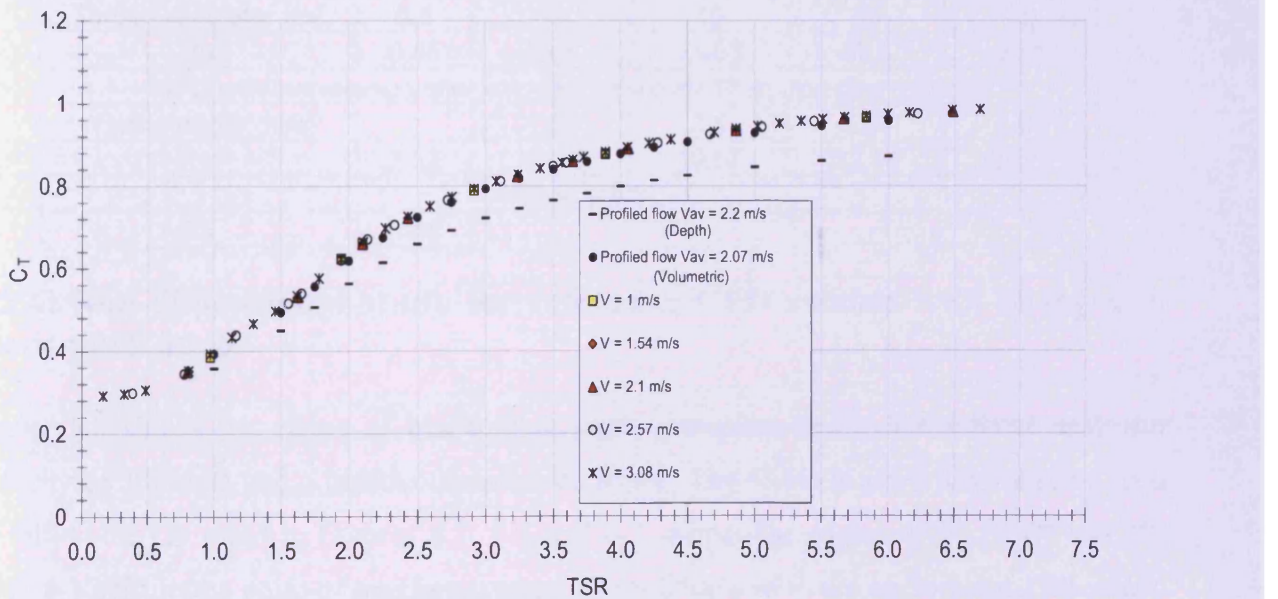


Figure 8.7: Thrust coefficient (C_T) vs TSR with increasing upstream water velocity (plug) and average (V_{av}) profiled across the turbine diameter

Table 8.1 gives the Re number associated with each of the CFD results discussed above along with the Re number for the CFD flume model and measured flume results. The flume results will be discussed in more detail later on. With changes in the Re number, the CFD results show that the non-dimensional groups TSR, C_p , C_{Torq} and C_T are unaffected by changes to the turbine diameter and the upstream water velocity. The performance characteristics of scaled devices, while subject to changing upstream plug and profiled velocities, can therefore be calculated from non-dimensionalised data sets. The collapse of the key performance curves to a single set has an important impact on the sizing of a commercial scale turbine from smaller prototypes and or CFD models. The CFD results also indicate that, under the conditions previously discussed, the TSR, C_p , C_{Torq} , and C_T are independent of the Re numbers given in Table 8.2.

Table 8.2: Reynolds number (millions) for CFD and flume tests

CFD with increasing turbine diameter					
Turbine diameter (m)	0.5	10	15	20	30
Re	0.45	28.7	43.05	57.4	86.1
CFD with increasing water velocity (based on 10 m diameter turbine)					
Water velocity (m/s)	1	1.54	2.1	2.57	3.08
Re	9.32	14.35	19.57	23.95	28.70
Flume tests					
Re	0.45				

8.2.4: Non-dimensional study for reference CFD models with changes in blade pitch angle

Figure 8.8 shows the effect of blade pitch angle variation on C_p for a fixed upstream velocity of 3.08 m/s and a turbine diameter of 10 m. The 6° blade pitch angle can be seen to follow the C_p trend in Figures 8.1, 8.4 and 8.7, whilst for angles of 0°, 3°, 9° and 12° there is a shift in the point of maximum energy extraction and in the operational TSR range. This clearly shows that the non-dimensional group C_p can only be used for a turbine design defined by a blade pitch angle. Variation in C_{Torq} and C_T can also be seen with changes to the blade pitch angle, Figures 8.9 and 8.10. Figure 8.9 clearly shows an increase in peak C_{Torq} with blade pitch angles of 9° and 12° while operating at lower TSRs than those at 6°, 3° and 0°. The pitch angles of 9° and 12° also give a higher start-up torque, allowing the turbine to operate in slower moving water. Figure 8.10 shows the axial thrust coefficient

(C_T) with the same blade pitch variation as in Figures 8.8 and 8.9. Again, it is clear that changes to the blade pitch angle affects C_T , specifically as the torque starts to increase at a TSR of approximately 1.6, Figure 8.9. With blade pitch angles of 9° and 12° C_T is reduced from that obtained at the optimum blade pitch angle of 6° . At angles of 0° and 3° C_T is increased and exceeds unity at approximately peak power extraction ($C_p = 0.4$). Due to the blockage adjustments made on the reference CFD model, C_T exceeded unity for blade pitch angles of 0° and 3° . The width and height of the CFD domain was increased to minimise blockage effects while operating at peak power extraction (Chapter 4). However, as the blade pitch angle is reduced, a larger proportion of the rotor's upstream face is exposed to the flow, which increases the hydrodynamic drag in the axial flow direction. The increased drag slows the flow upstream of the turbine, causing the downstream wake to expand further around the turbine than with pitch angles of 6° , 9° and 12° (see Figures 8.27, 8.28 and 8.29, later in Chapter). The expanded wake thereby increases flow concentration between the turbine swept area and boundary walls of the CFD model. It is recommended that adjustments for blockage effects should be based on TSRs greater than that obtained at peak power extraction. A blade pitch angle should also be chosen that induces the highest axial thrust load for the highest velocity chosen for the study. Using this methodology a suitable ratio between domain width and height to turbine diameter will be obtained.

Some advantages and disadvantages of blade pitch variation will be discussed later on in this Chapter. However, it can be seen, that altering the blade pitch angles changes the performance characteristics of the turbine, requiring a new set new non-dimensionalised curves.

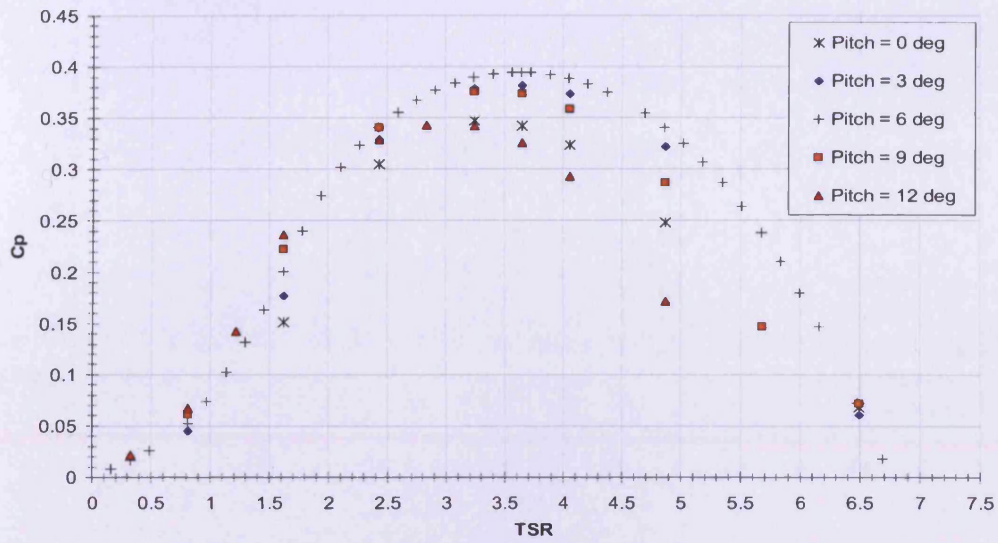


Figure 8.8: Effect of blade pitch angle on C_p with changes in blade pitch angle (plug flow $V = 3.08$ m/s)

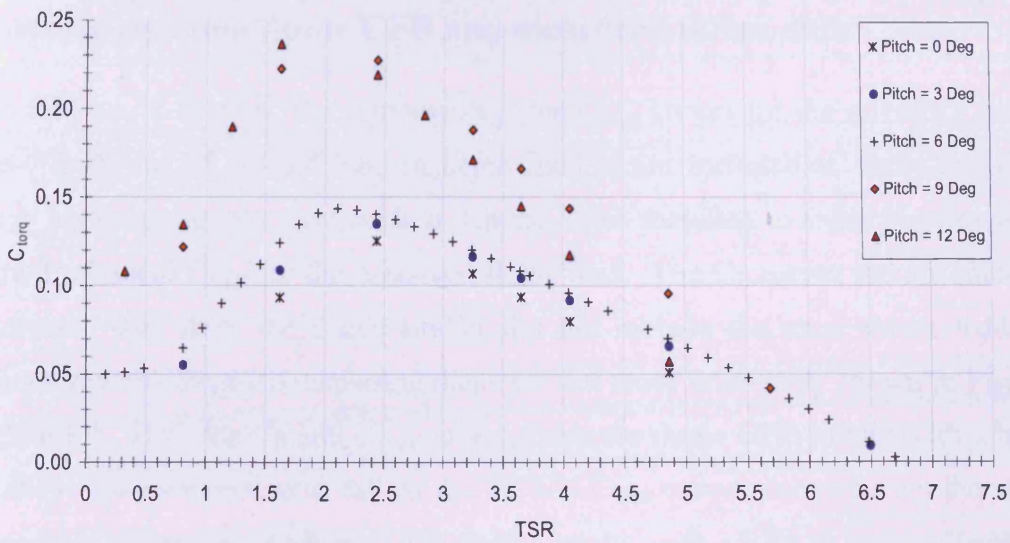


Figure 8.9: Effect of blade pitch angle on C_{Torq} with changes in blade pitch angle (plug flow $V = 3.08$ m/s)

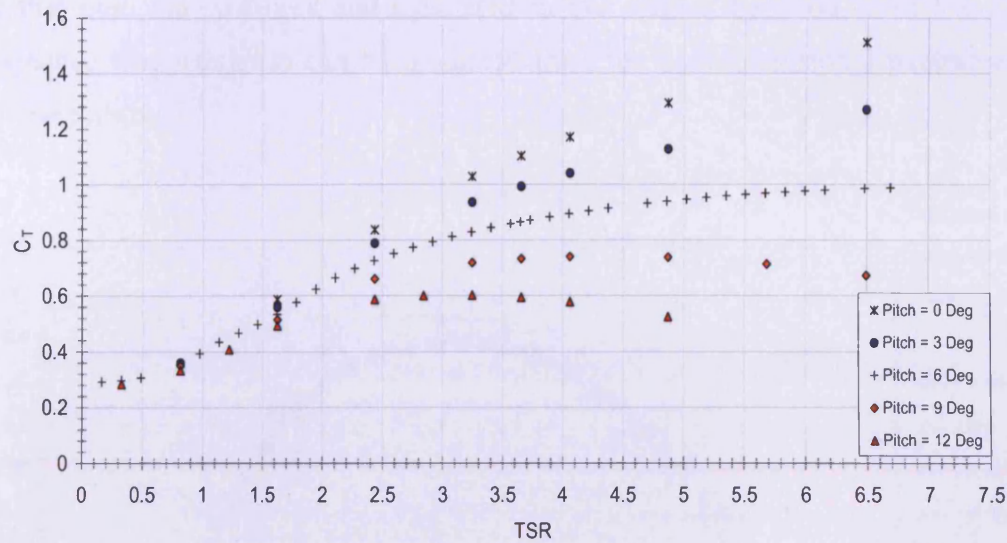


Figure 8.10: Effect of blade pitch angle on C_T with changes in blade pitch angle (plug flow $V = 3.08$ m/s)

8.2.5: Comparison of Non-dimensionalised turbine performance characteristics using flume CFD and measured flume data

Figures 8.11 and 8.12 show the combined C_p and C_{Torq} curves for the reference and flume models. Both the 1.7 m and 0.85 m depth models are included to show the effect of blockage between the two rigid surface depths. Also included in these Figures 8.11 and 8.12 are the C_p and C_{Torq} for the measured flume data. The C_T curves are not included, as the measured data from the flume studies did not include the axial thrust load. The reference CFD models, with increasing diameter, are those previously shown in Figures 8.5 through to 8.7. Both the C_p and C_{Torq} curves, from the flume CFD model with a height of 1.7 m above the rotational axis, fall on the C_p and C_{Torq} curves derived from the reference CFD models. However, the flume CFD model results, with a 0.85 m surface height, show that the blockage between the turbine and the surface boundary increases the flow rate between the turbine's outer diameter and the boundary walls. The aforementioned boundary blockage removes the open flow assumption producing an over estimate of the turbine's C_{Torq} and C_p . Given the noted assumptions made for the surface boundary in the flume CFD model and the scatter in the measured data, Figures 8.11 and 8.12 indicate that both C_p and C_{Torq} , (measured and simulated) show a reasonable correlation with the assumption that they all collapse on to a single curve. The correlation is reasonable in the

sense that both the measured and simulated curves follow the trend so that the turbine's performance characteristics can be predicted from the non-dimensional parameters of the prototype turbine.

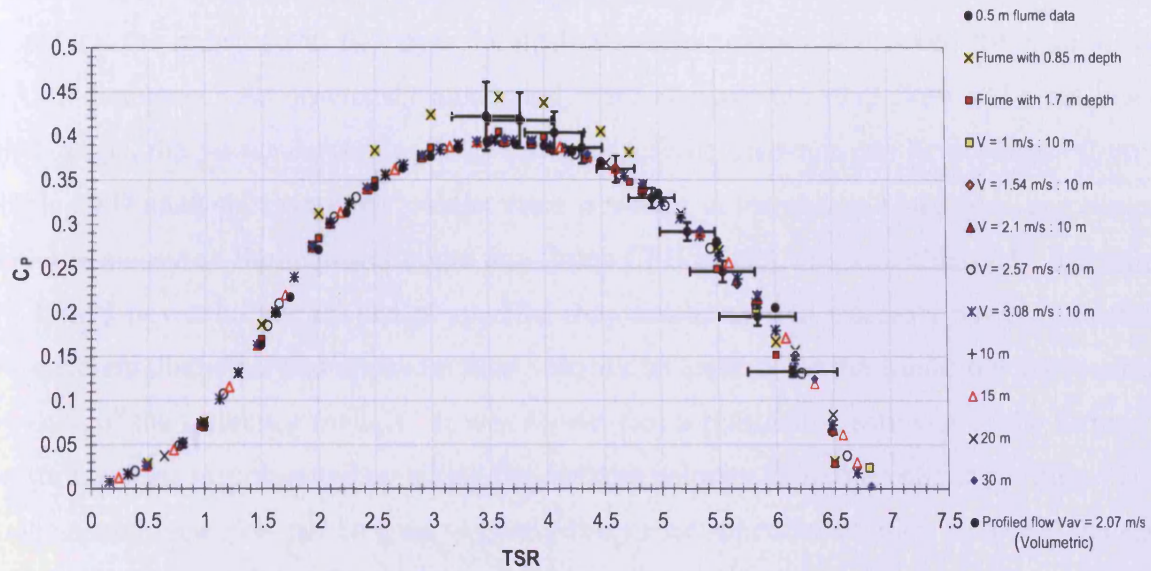


Figure 8.11: Combined C_p curves for reference CFD and flume models. Also non-dimensionalised data from flume model and volumetric velocity profile average

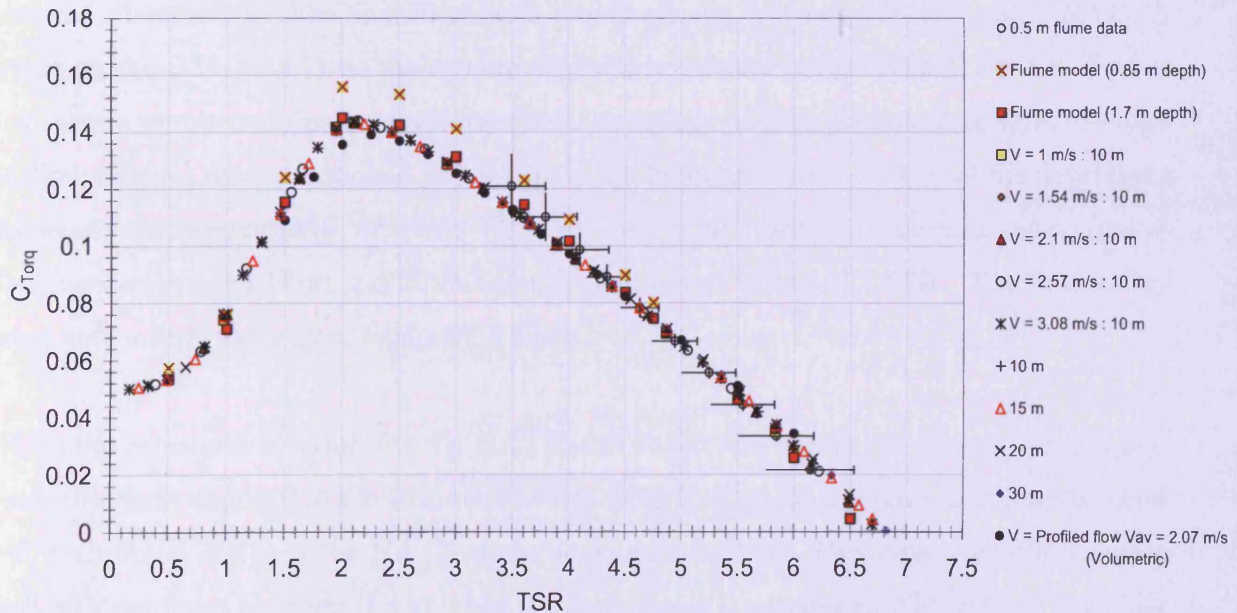


Figure 8.12: Combined C_{Torq} curves for reference CFD and flume models. Also non-dimensionalised data from flume model and volumetric velocity profile average

8.3: Performance charts for prototype HATT design

Figure 8.13 shows the peak power curve of the HATT design between diameters of 10 m and 20. Also shown is a curve fit for the peak power extraction using the peak tidal velocity of 3.08 m/s. A curve fit, as calculated from the 10 m diameter reference model, elucidates the reduction in power as the upstream tidal velocity is reduced for each of the HATT diameters. As previously mentioned, with an upstream plug flow and a set blade pitch angle, the power curves for different sized turbine diameter can be predicted from a single CFD analysis. Moreover, whilst there is scatter in the data, a reasonable correlation with the measured flume power curve and flume CFD model was also obtained. Although the HATT power curves are design specific, they can be used to elucidate power extraction for different diameters and upstream flow velocity, at least under the conditions represented by each of the reference models. It was shown that a reasonable estimate of the turbine's performance can be obtained by taking the average velocity from the volumetric flow. This fundamental approach can be used to give a first order approximation on matching the size and operational range for the HATT design.

From literature the typical size and power rating for current tidal stream designs ranges between diameters of 6 m and 20 m with power ratings between 250 kW and 2 MW. A report by the DTI, (2007) on the economic viability of tidal stream energy capture devices discusses a number of device developers and the ratings of their proposed designs. Several of these devices were mentioned previously in the literature review. Most of the developers discussed are developing or have installed full scale prototype devices with typical dimensions between 18 m and 20 m and a typical power rating of 1 MW. The devices are rated with a tidal velocity of typically 2.5 m/s.

Given the proposed location for the HATT; see Table 5.2, within the Severn Estuary and the restrictions imposed at the site, such as that from local shipping lanes, both the diameter and operational depth of the HATT are to some extent fixed. This type of restriction may well be a common problem if and when the technology is expanded. Using Equation 4.44, Figures 8.14 and 8.15 give a graphical representation of the peak performance

characteristics in terms of power (W) and angular velocity (rad/s) of the HATT with different diameters and upstream tidal velocity.

Figure 8.15 shows the maximum power curves with the operational range power curves, as shown in Figure 8.13, removed. To cover a larger operational range, a peak flow velocity of 5.14 m/s was used to represent spring peak tidal velocities typically measured at the Pentland Skerries, UK, (Carbon Trust, Variability of UK resources, 2005). A minimum velocity of 1.54 m/s was chosen to be just above the recommended minimum cut in flow velocity of 1 m/s (Black and Veatch, 2005).

For clarity Figure 8.15, focuses on lower current velocities between 1.54 m/s and 3.086 m/s for the same diameters range. Using Figure 8.15, it can be shown that to produce a rated power of 1 MW with the existing HATT design, a diameter of 15 m would be required at a tidal velocity of 3.08 m/s (at the turbine depth). At a mean spring peak velocity of 2.57 m/s, typically discussed in literature, would require a diameter of approximately 18 m. However, with the shipping restrictions imposed near the site, diameters of 20 m and 15 m would exceed the limited depth clearance between the maximum vessel hull depth for the location (14 m below the water surface) and the tip of the turbine while at the top of its rotation cycle. Given these restrictions it was decided to limit the diameter of the HATT to 10 m as this gave the hull clearance required. Moreover, due to the rapid decay in the velocity profile toward the seabed, to be discussed, the HATT rotation axis was raised to an optimum height, given the restrictions discussed above, of 5 m above the seabed.

The local spring tide velocity of 1.87 m/s as measured during the ADCP site survey gave a maximum power output, assuming plug flow, of approximately 144 kW, which is well below the 1 MW rating specified in literature. The HATT is also to be located in a water depth of approximately 35 m, during a spring ebb tide, and is seabed mounted with the use of a monopile or stanchion. Due to the 3rd power law for power extraction this limited the rated power output of the turbine to approximately 466 kW with the maximum scaled upstream tidal velocity of 3.08 m/s. At the quoted UK mean spring tide velocity of 2.57 m/s the power would drop to 270 kW, Figure 8.15. Apart from the local current velocities,

it is clear that the local shipping restrictions have a significant effect. To match the 1 MW rated output that frequently occurs in literature, the number of turbines would have to be doubled with a local velocity of 3.08 m/s, again assuming plug flow conditions. The introduction of a velocity profile through the water column has a significant effect on power attenuation through the water depth, as discussed. Power attenuation will be discussed in greater detail in Chapter 9. Given the constraints discussed above and peak rated power output of the HATT given by Figure 8.15 the output of the HATT was limited to around 500 kW with a peak mean spring peak velocity of 3.08 m/s.

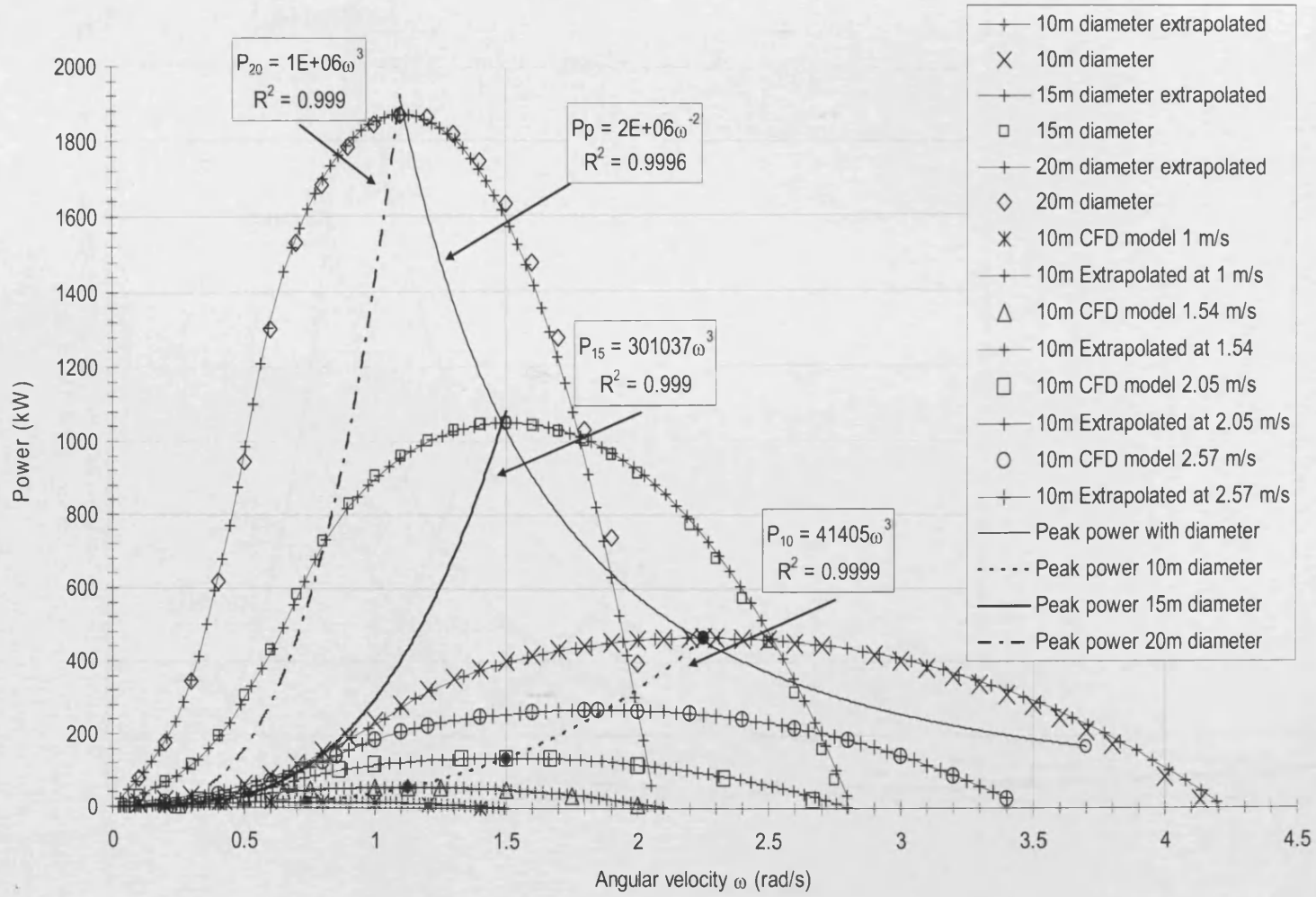


Figure 8.13: Extrapolated power curves from 6 m diameter HATT and calculated using scaled CFD

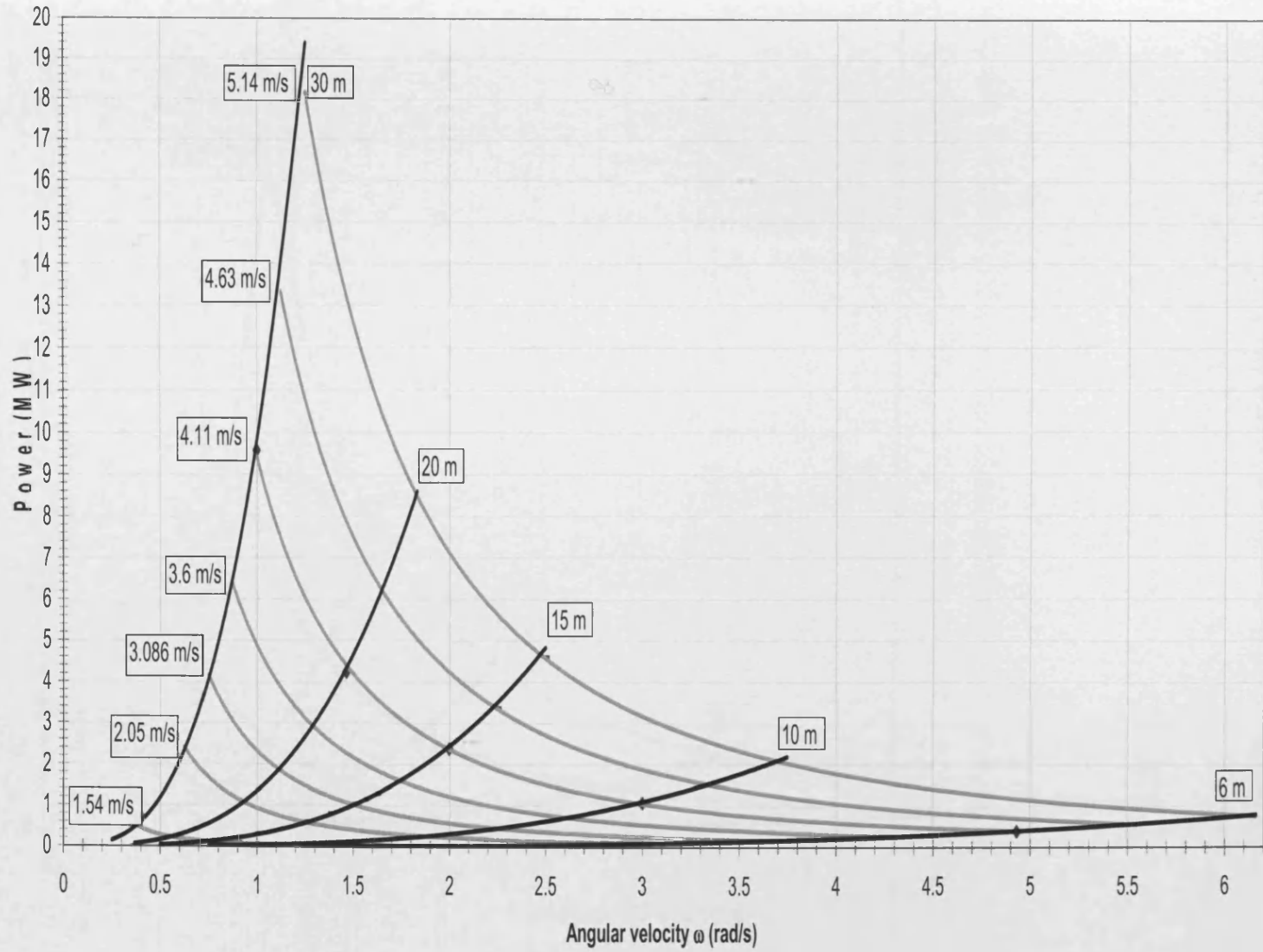


Figure 8.14: Design specific Peak power curves with increasing diameter and tidal velocity

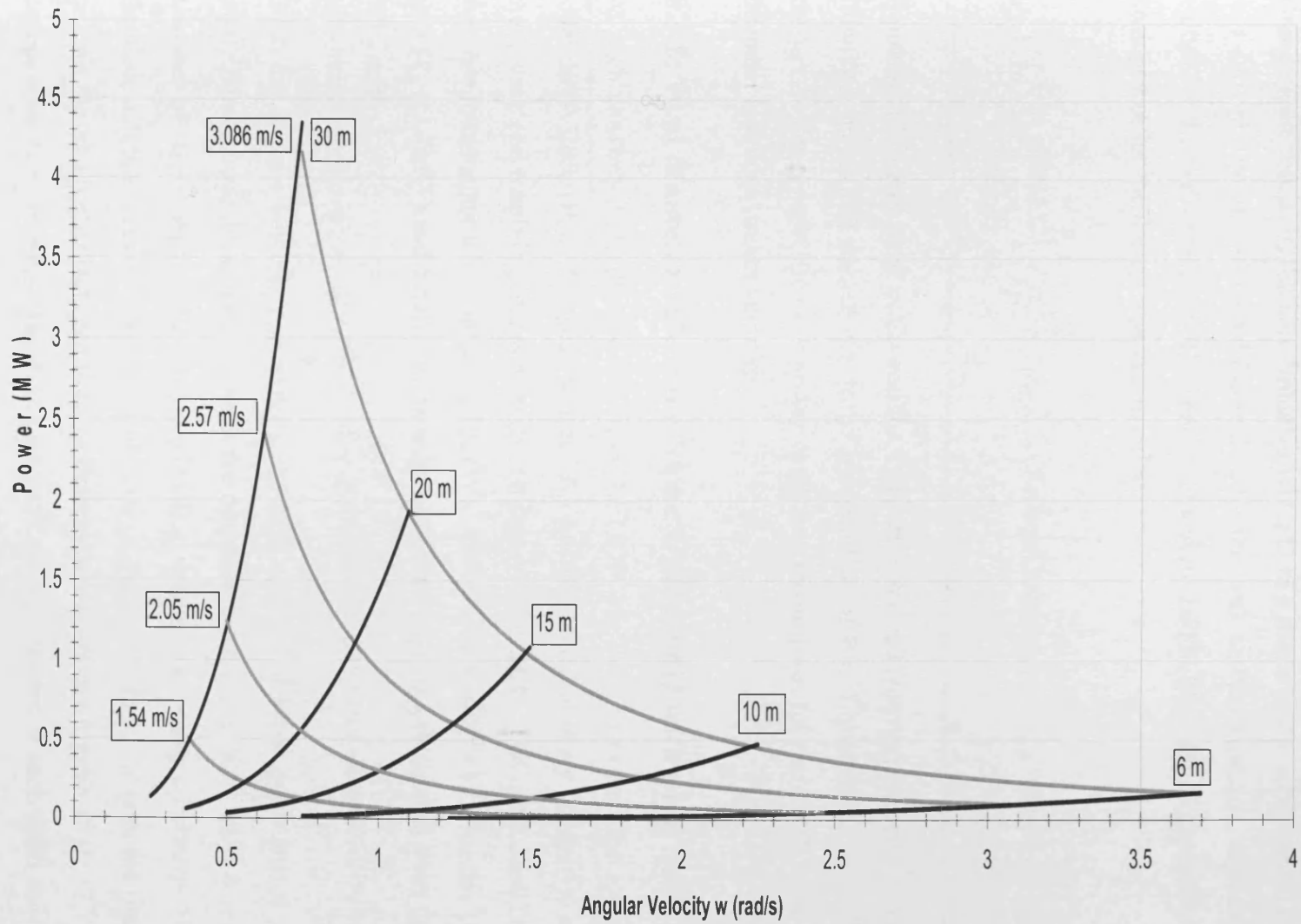


Figure 8.15: Design specific Peak power curves with increasing diameter and tidal velocity with a maximum tidal velocity of 3.08 m/s

8.3.1: Peak power calculations

Based on the results of the non-dimensional CFD and flume study, an empirical expression was derived from the measured flume data for the peak power extraction. By substituting values for the average $C_p = 0.41$ (Table 6.1) and $\rho = 1000 \text{ kg/m}^3$ into Equation 4.44 the peak power for the design was expressed as:

$$P_p = 20.13D^5 \left(\frac{2V}{D} \right)^3 \Rightarrow P_p = 161(D^2 V^3) \quad (8.1)$$

Equation 8.1 is empirical as C_p and the TSR were derived from experimentation under plug flow and via scaling was shown to be independent of Re . Equation 8.1 could be used to predict the design specific peak power extraction capabilities for the HATT with changes in diameter and tidal stream velocity.

8.3.2: 10 m diameter reference frame CFD model with plug flow

At each converged steady-state solution the UDF was used to extract the torque (T) and axial thrust force (F_T). The peak torque (T_p) was calculated at every converged solution by integrating and resolving forces at each cell face via the UDF. The product of $T\omega$ (W) was then use to calculate the peak power P_p (W). The power available (P_a) for the 10 m swept area ($P_a = 1.2\text{MW}$) and finally the power coefficient (C_p) was calculated from the quotient of P_p and P_a .

From the angular velocity (ω) sweeps run over a range of blade pitch angles a series of power curves were developed to check the optimum pitch angle of 6° while using a HATT diameter of 10 m. Again, the pitch angle (θ) is defined as the angle between the chord of the blade and the normal to the rotational axis of the turbine hub. As with the flume model, to limit the number of runs required to determine the optimum pitch angle (θ_p), coarse ω sweeps were run. Figure 8.16, shows the peak power obtained at each pitch angle over the angular velocity sweep.

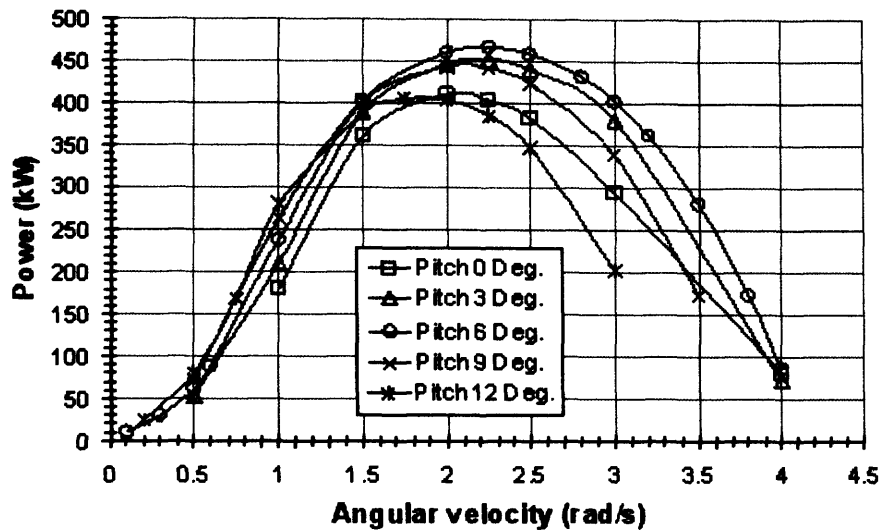


Figure 8.16: Power curves with blade pitch variation for 10 m diameter turbine

The result for the 10m diameter HATT gives a peak power extraction at a blade pitch of 6° matching the 0.5m reference and flume CFD models. Although the power curves are coarse it is evident that the angular velocity at which peak power occurs shifts with changes in θ . This is clearly seen for a blade pitch of 12° where the angular velocity at peak power is approximately 1.8 rad/s. For the 3.08 m/s tidal flow used in the model the TSR has shifted from 3.6 at 6° to 2.92 at 12° indicating that at larger pitch angles the rotational velocity of the turbine must decrease to obtain optimum power, as evident in the non-dimensional curves.

Further data were generated by incrementing ω to add further detail to the power curve and to include torque and axial thrust profiles under the same peak flow conditions. Figure 8.17 gives the full performance characteristic for the 10 m HATT at the V_{msp} tidal velocity of 3.08 m/s under plug flow conditions. The torque generated for the stationary turbine (start-up) is approximately 96 kNm which increases to a maximum of 275 kNm at 1.3 rad/s. After approximately 1.5 rad/s the torque decreases approximately linearly to zero. In reality however the torque can only approach zero at high rotational velocity since zero torque would imply no lift forces and hence zero angular velocity through stall. The turbine will remain just below the complete stall angular velocity at a free wheeling state. The general shape of the power curve is “parabolic” in nature except for a slight ‘tail’

towards lower rotational velocities, in this case between 0 and 0.6 rad/s. Following the relatively linear decrease in torque after its peak at 1.3 rad/s the power maintains a steady increase to a maximum of approximately 466 kW at a rotational velocity of 2.25 rad/s, which was around 1 rad/s above the peak torque.

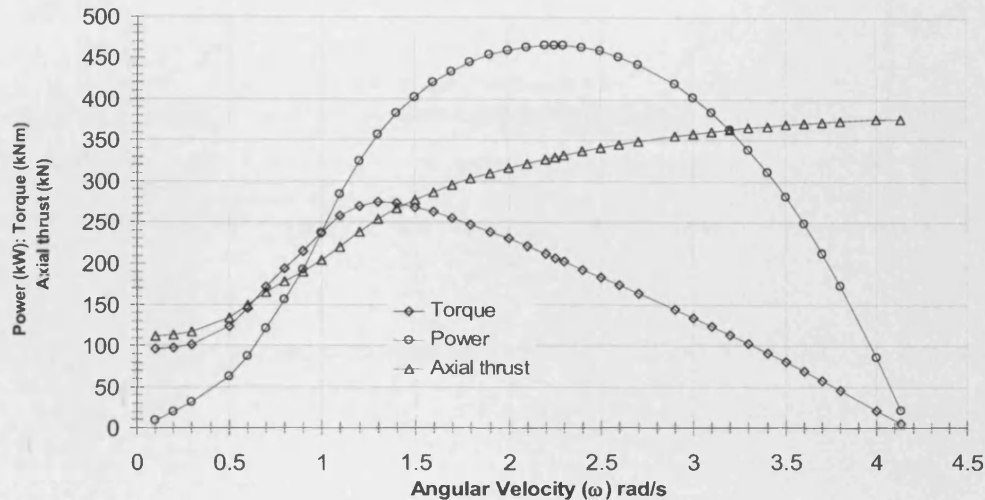


Figure 8.17: Performance characteristics for 10 m diameter HATT plug flow with a $V = 3.08$ m/s

Figure 8.18 plots the C_p and C_T against the TSR. The maximum C_p of 0.4 occurred at a TSR of 3.6 with a corresponding C_T of 0.86. Taking the value of peak torque at $\omega = 1.3$ rad/s from Figure 8.13, peak torque occurs at a TSR of 2.1 with a C_T of 0.66. With a C_T reaching 0.98 and a C_p approaching zero the turbine starts to freewheel at a TSR of approximately 6.7. The possibility of mitigating extreme loading during spring tides was investigated by normalising the power and thrust data with the peak power extraction and axial thrust at freewheeling, respectively. Figure 8.19 shows how C_T and C_p are affected as θ is varied with V_{msp} of 3.08 m/s. Again peak C_p occurs at $\theta_p = 6^\circ$. A greater rate of decay in power extraction is indicated as θ approaches 0° with a 23% reduction in peak C_p , however as θ approaches 12° , C_p is only reduced by 13%. As for C_T , it varies between 0.58 and 1 for angles of θ between 0° and 12° . Therefore, as θ approaches 12° a 33% reduction in C_T is realised while maintaining a C_p of approximately 35%.

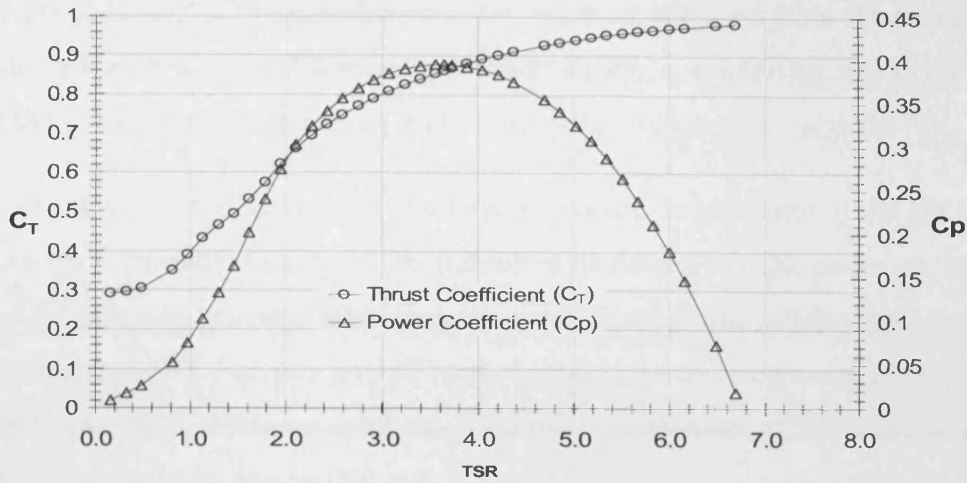


Figure 8.18: Performance characteristics for 10 m diameter HATT to the base TSR

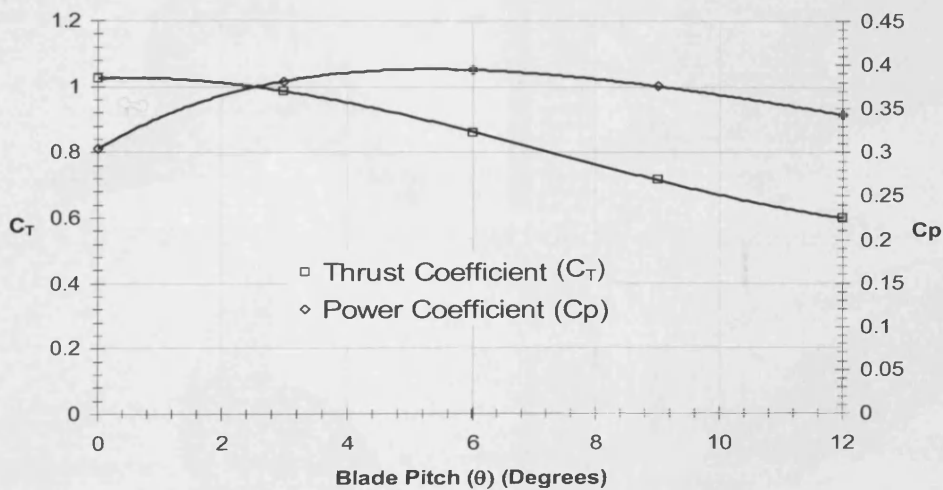


Figure 8.19: Variation in C_T and C_p with blade pitch angle (θ)

Varying the blade tip angle (θ) between 0° to 12° had little effect on C_p over the range of tide velocities. It is, however, clear that thrust loading (F_T) on a HATT is considerable and that a reduction in C_p may be beneficial to C_T when running at peak spring tide velocities. The degree to which this will have an impact is of course site dependent. Within the pitch angle range selected for the study, an 11% increase in torque was also obtained at a blade pitch angle of 12° allowing an increase in torque at start-up under low tide velocity if the device was to be designed to make use of variable blade pitch (Mason-Jones et al, 2008).

Figures 8.20, 8.21 and 8.22 show downstream pathlines released from the surface of each blade coloured with axial wake velocity. Each figure is related to the key operational stages of the HATT for the reference CFD model with a blade pitch angle of 6° .

Figure 8.20 shows the formation of a stable wake vortex downstream of the HATT at peak torque. As the rotational velocity of the turbine is increased to peak power extraction with a $TSR = 3.6$ the vortex becomes stretched, however its rotational component remains stable and can, as discussed in Section, extend a considerable distance downstream of the HATT. The vortex elongation increases until the rotational component of the wake is practically removed at freewheeling, where $TSR = 6.7$.

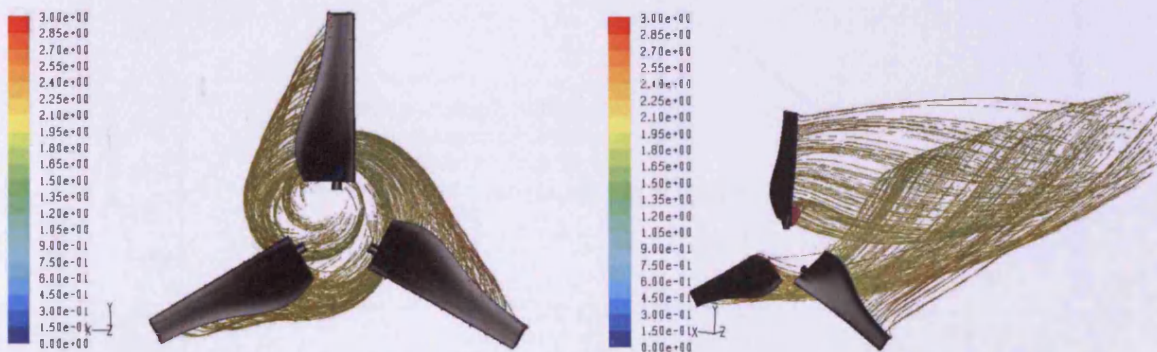


Figure 8.20: Pathlines coloured with axial velocity at peak torque $TSR = 2.1$ [A]

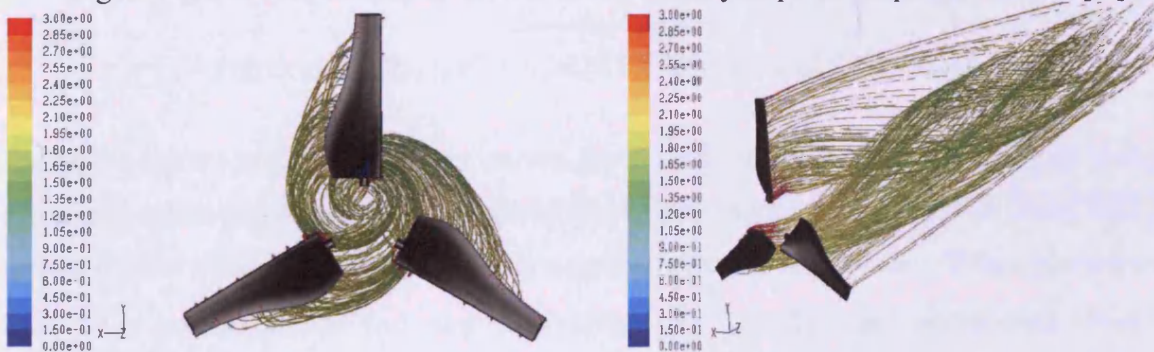


Figure 8.21: Pathlines coloured with axial velocity at peak power $TSR = 3.6$ [B]

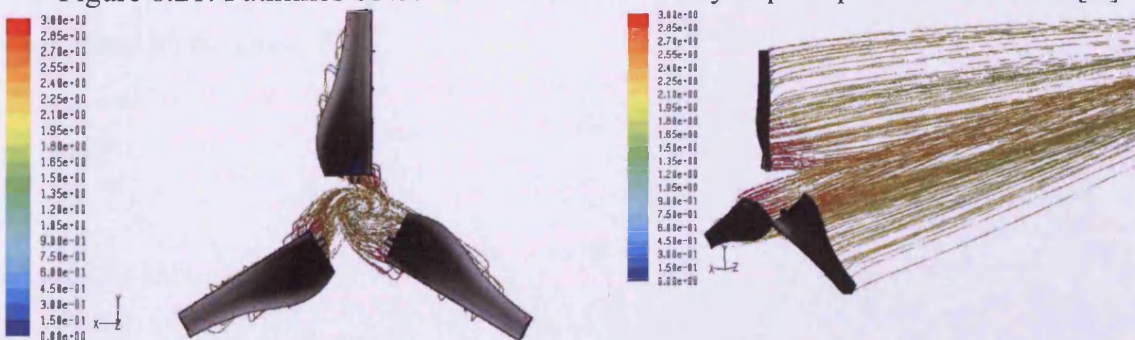


Figure 8.22: Pathlines coloured with axial velocity at freewheeling $TSR = 6.7$ [C]

8.3.3: Tidal velocity effects on peak power

By running further reference domain models at 1.5 m/s, 2 m/s and 3.08 m/s the peak power (P_p) was studied. As expected, the power extraction increased and decreased with tide velocity, however the θ_p proved to be insensitive to changes in velocity, at least within the specified range. This can be clearly seen in the normalised curve for all 3 tide velocities, Figure 8.23, and suggests that it is acceptable to maintain θ_p at a constant 6° for the range of tidal velocities proposed.

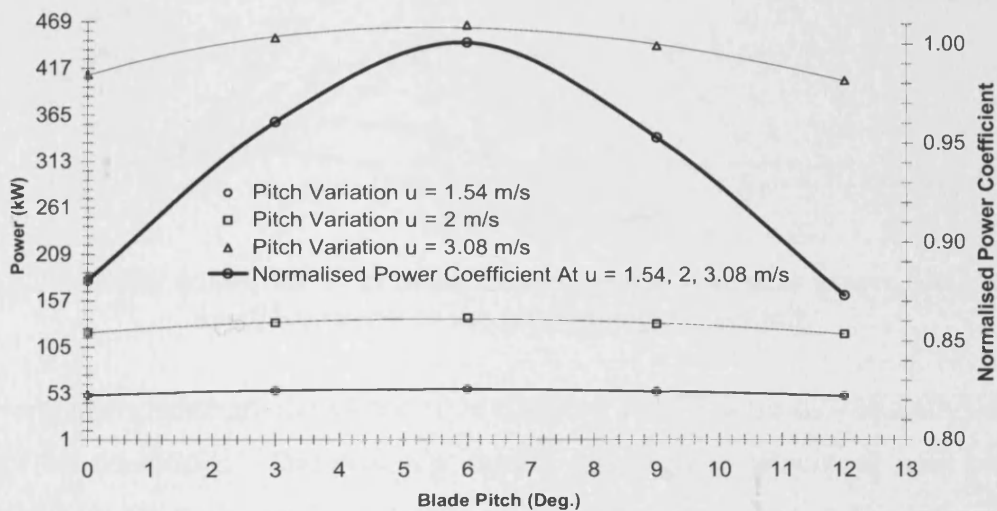


Figure 8.23: Peak power with blade pitch and tidal velocity

Figure 8.24 gives a series of power curves generated for five peak tide velocities using the 10 m reference CFD model. The available power, theoretical extraction limit and peak power (P_p) extracted by the turbine via equation fits are also given. When plotted to the base of angular velocity (ω) and decreasing tide velocity the operational range and magnitude of P_p extracted by the turbine reduces. P_p can be seen to follow a power law as represented by Equation 8.2:

$$P_p = k\omega^3 \quad (8.2)$$

Where $k=37356$

Figure 8.24 also shows the points A, B and C that coincide with the pathlines given previously in Figures 8.20, 8.21 and 8.22 for a tidal velocity of 3.08 m/s.

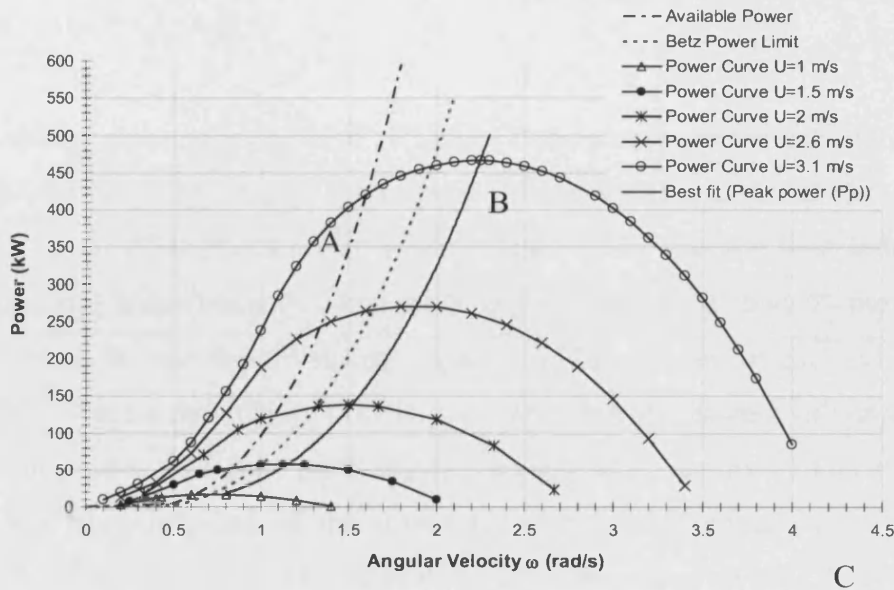


Figure 8.24: Power curves for 10 m diameter turbine showing peak power, Betz limit and available power to the base of angular velocity

The performance characteristics of the 10 m diameter HATT were subsequently established for plug flow conditions. The peak C_p , torque and angular velocity at peak power was established at a blade tip pitch angle (θ) of 6° . A maximum C_p of approximately 0.4 occurred at 2.25 rad/s and a tip speed ratio (TSR) of 3.6. The peak torque occurred at $\omega = 1.3$ rad/s with a TSR of 2.1. The HATT starts to freewheel at $\omega = 4.13$ rad/s and a TSR of approximately 6.7. As a first order approximation the results compare well with power measurements made on a 6 m diameter turbine (Egarr et al, 2003).

8.4: Wake recovery for 10 m diameter reference frame CFD model plug flow

Downstream wake velocities were also studied by plotting the axial velocity along the rotational axis of the turbine as the blade pitch angle is varied between 0° and 12° , Figure 8.25. The axial velocity directly behind the turbine drops from the upstream velocity of 3.08 m/s to around 2.2 m/s. Between 2 m and 182 m downstream of the turbine there is a considerable difference in the velocity recovery rates of the wake. At a pitch angle of 0° a

minimal downstream wake velocity of 0.81 m/s occurred, using Equation 8.4 this equates to a velocity deficit of 74 % at approximately 5 turbine diameters (5 D) downstream.

$$V_{\text{def}} = 1 - \frac{V_w}{V_o} \quad (8.4)$$

For the remaining pitch angles of 3°, 6°, 9°, and 12° the maximum velocity deficits of 61 %, 50 %, 41 % and 32 % occurred at downstream distances of 5.6 D, 6.1 D, 5.4 D and 3.4 D, respectively. It would seem then that the pitch angle of 12° has the least influence on the downstream axial wake velocity. For pitch angles between 0° and 9° the downstream distance at which the minimum velocity occurs is within a metre of each other between a minimum of 5 D and a maximum of 6.1 D. At a downstream distance of approximately 18 D the axial velocities for all the pitch angles converge at a velocity deficit of 29 % or 2.2 m/s. Beyond this point each of the curves recovers at approximately the same rate to around 90 % of the upstream velocity at 40 D. While subject to plug flow and minimal boundary effects the wake induced from power extraction can travel a considerable distance downstream as originally mentioned in Section 8.3.3. Higher blade pitch angles however can improve recovery rates as previously stated with minimal effects on the power extraction efficiency. Figure 8.26 shows the recovery of the wake with C_T . At a C_T of 0.47 (below peak torque) the wake recovery along the rotational axis of the HATT approaches that of a stationary turbine. The axial velocity along the rotational axis shows a rapid drop up to around 0.6 D downstream. The recovery rate is then steady extending the length of the CFD domain up to 40 D. At peak torque the minimum axial velocity occurs at around 1.2 D. Figure 8.20 previously showed that at peak torque the downstream vortex is stable with and therefore influences the velocity at the core of the vortex. This reduces the axial velocity immediately downstream of the HATT. Beyond a wake length of around 12 m (1.2 D) the wake recovers steadily with a similar profile to that of a stationary HATT. At peak power extraction the wake recovery is the same as that previously discussed. However, as C_T is increased towards freewheeling, the HATT's ability to extract power is reduced as the hydrodynamic performance of the blades is compromised through near surface vortex shedding, which in turn reduces the lift forces while at the same time increasing drag forces. The axial wake velocity along the rotational centre drops to a minimum at around 170 m (17 D) downstream of the HATT then gradually increases to a

maximum of 2.66 m/s or 86 % of the upstream velocity. Higher rotational velocities have a significant influence on downstream wake velocities. These influences however are small near to peak power extraction, such that there is little advantage to running the HATT at angular velocities above the optimum TSR of 3.6 ($C_T = 0.86$) without excessive increases in axial thrust loads and a rapid decay in power extraction when compared to any benefits gained from faster wake recoveries. It should be noted however that the wake recovery is influenced by the value of the turbulence intensity upstream of the turbine. For the results given in this study a TI of 5% was used. It is postulated that with increasing turbulence intensity (TI), the recovery rate of the wake will correspondingly increase. Although the study cannot be directly compared, due to differences in the experimental setup, Myers et al, (2008), showed that the wake recovery at 18 diameters downstream had recovered to approximately 90 % with a turbulence intensity of around 7 %. The Myers et al, (2008) experimental results will be discussed further in Chapter 9.

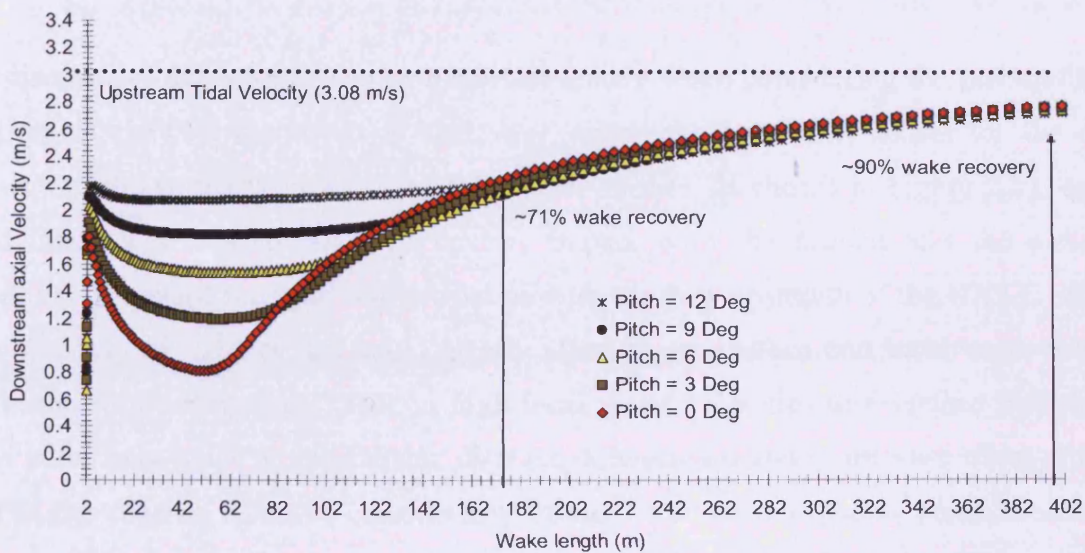


Figure 8.25: Downstream axial velocity recovery with pitch angle variation for 10 m diameter turbine (reference model: $V = 3.08$ m/s : $TI = 5\%$)

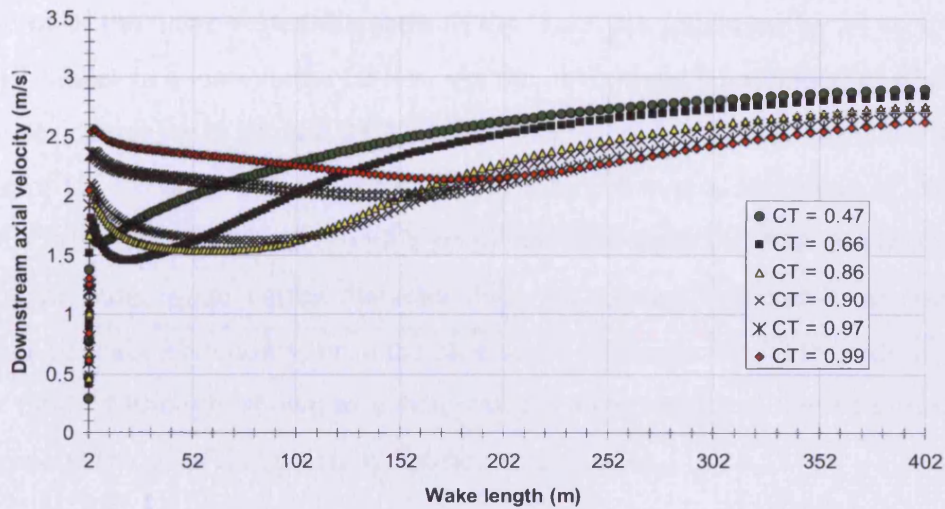


Figure 8.26: Downstream axial velocity recovery with increasing axial thrust CT
For 10 m diameter turbine
(reference model: $V = 3.08$ m/s : $TI = 5\%$)

The diameter of the wake is also an important feature when considering the positioning of an array of HATTs, moreover, in shallower waters the possibility exists for the outer diameter of the vortex wake to contact the water surface, as shown in Figure 2.21, and or more likely with seabed mounted devices impact with the seabed and the resulting possibility of surface scouring and interaction with the flow upstream of the HATT. With a large numbers of turbines this could greatly affect water surface and local wave patterns within the surrounding area. Due to high local water velocities this surface disturbance could potentially travel a considerable distance downstream and in the case of an array of HATTs the distance could be considerably further. For all the models considered in the thesis the CFD domain downstream distance from the HATT was limited to 400 m, both to maintain consistency and to limit the number cells in the main flow field of the CFD models. For purpose of this discussion the diameter of the wake at 400 m, which also represents the outlet pressure boundary for the models, represents the maximum wake diameter.

Figures 8.27, 8.28 and 8.29 indicates that the outer vortex diameter of the wake, 400 m downstream of the HATT, increase as the blade pitch angle is decreased. At a blade pitch angle of 0° the outer vortex diameter of the wake has increased by 24 m from leaving the HATT blades to a maximum of 34 m. As the pitch angle is increased to 6° the vortex wake diameter decreases to around 28.4 m, and finally, with a further decrease of 6° to a pitch angle of 12° the outer vortex diameter reduces by 2.4 m to a maximum of 26 m. Therefore, for the reference CFD model, with a rotational axis depth of 25 m and total water depth of 50 m the outer wake vortex diameter does not expand sufficiently to contact either the surface or seabed boundary, or in the case of the reference model the side walls of the main flow field. Although, shown in a different plane the results of these figures clearly follow the general trends of that given by Fabrice et al, (2008).

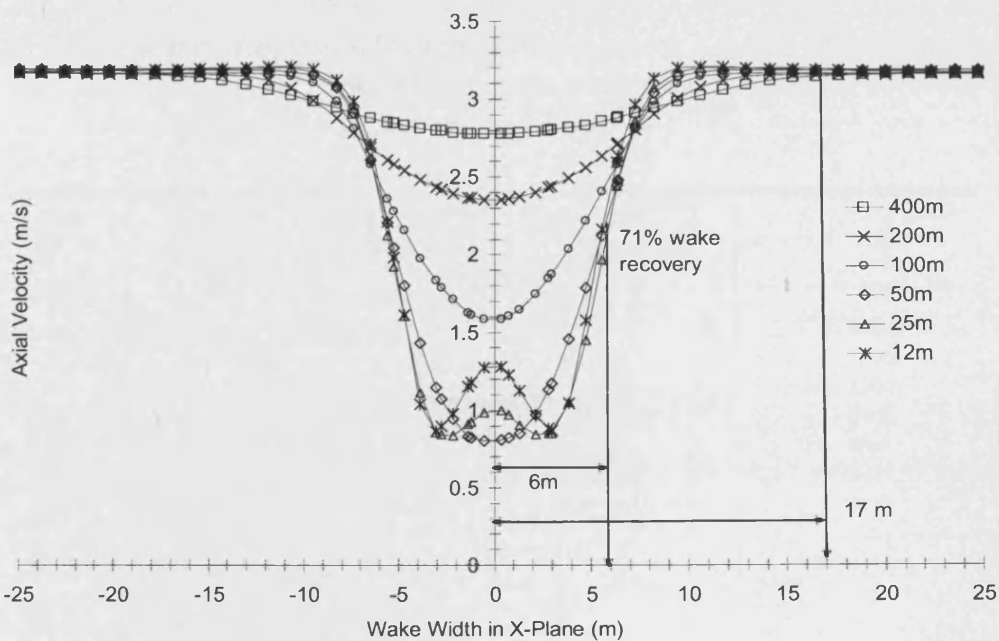


Figure 8.27: Wake recovery and vortex diameter across X-plane of reference domain with a blade pitch angle of 0°

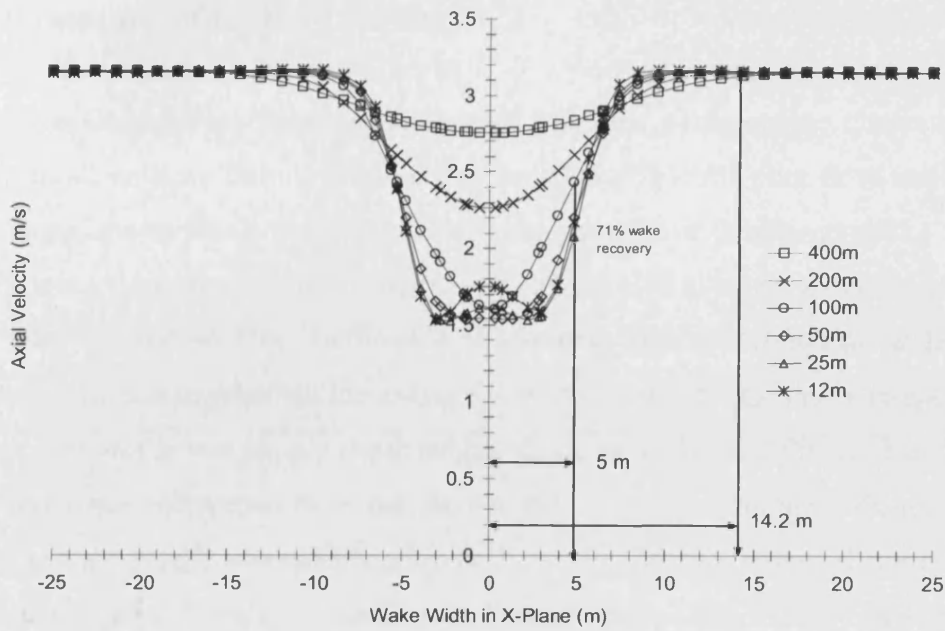


Figure 8.28: Wake recovery and vortex diameter across X-plane of reference domain with a blade pitch angle of 6°

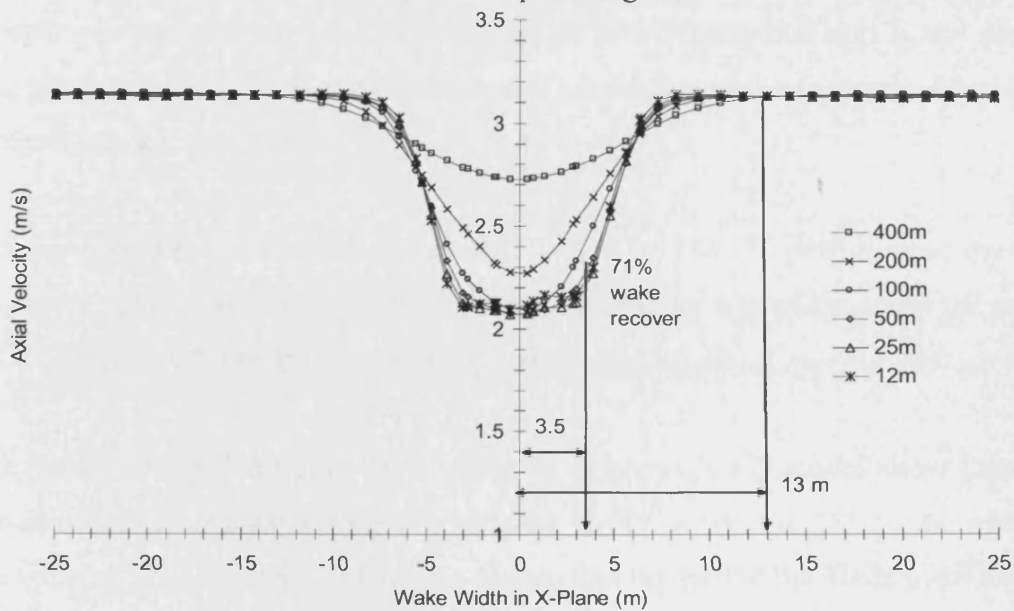


Figure 8.29: Wake recovery and vortex diameter across X-plane of reference domain with a blade pitch angle of 12°

8.5: Summary of turbine scaling

Using non-dimensional analysis, the scaled HATT's performance characteristics were shown to all collapse onto a single curve, indicating that for plug flow and a fixed blade pitch angle, the turbine's performance was independent of the Re number. Therefore, the turbine's key performance characteristics could be scaled to larger models and with varying tidal velocities and profiles. In the case of a velocity profile through the water column two methods were used to establish the average velocity across the turbine's swept area. Firstly, the velocity profile was simply depth averaged across the turbine diameter and secondly, by calculating the volumetric flow rate across the swept area of the turbine. The average velocity of the profile was calculated to be 2.2 m/s while that obtained from the volumetric calculation was 2.07 m/s for the Severn Estuary data. The average velocity, calculated from the volumetric flow across the turbine area, gave a reasonable correlation to the assumption that the turbine's key performance characteristics are independent of the Re number. It was also shown that a new set of non-dimensional curves are required with changes to the blade pitch angle because the geometric similarity required for dimensional analysis was not preserved.

A series of power curves were also plotted to give the HATTs performance over a range of diameters, tidal velocities and velocity ranges providing a useful method for matching the HATT's peak performance characteristics to site conditions.

The results obtained from the 10 m diameter reference CFD model show that there are a number of clear advantages to not running the HATT at what would be considered to be its peak operation parameters. It has been shown that increasing the blade pitch from 6° to 12° reduces the coefficient of thrust C_T by 30.6 % with only a 13 % reduction in its power coefficient C_p . This has clear advantages in reducing the device's axial load with a relatively small sacrifice in power extraction.

When considering placement in an array the advantage of increasing the rate of wake recovery and the downstream vortex diameter, are also realised with a pitch angle of 12°.

Optimal performance characteristics are very much case and site specific, the results of the optimisation study have shown that even under ideal conditions, with plug flow and no interference from surface and seabed boundaries there may be clear advantages to running the device below its optimal hydrodynamic performance.

As the HATT is positioned closer to the seabed, as in some of the full scale prototype devices as discussed in Section 2.2.3, Figure 2.9 (d), other factors come into play, such as flow concentration between the swept area and the seabed and more importantly the rate of decay associated with the velocity profile at greater depths. HATT performance, with power attenuation through the depth, will be discussed in Chapter 9.

9: Power attenuation through depth using Severn Estuary ADCP data

From the flume model, flume reference model and scaled model results, the maximum C_p of the HATT was shown to be circa 0.4. Due to the flow concentration between the seabed and the HATT the energy extracted is increased by approximately 2 % with a C_p of around 0.42. Typically, C_p is calculated from the available resource upstream of the turbine and if a plug flow is assumed C_p is unambiguous as the velocity is constant throughout the water column, with only a slight attenuation towards the seabed from near wall boundary conditions. However, when considering a profiled flow the choice of upstream tidal velocity has a direct effect on how C_p is calculated. If, for example, the maximum upstream velocity is taken, then the available energy density is calculated from the velocity typically 1 m below the water surface. This has a significant effect on the performance estimates of the turbine since it does not occupy the higher portion of the water column. Ignoring the shipping requirements discussed earlier, the HATT was modelled at various depths. Figure 9.1, shows the normalised power (P_n) through the water column, where P_n is normalised to the maximum power obtained at 3.08 m/s. The same normalisation procedure is applied to both the site and reference CFD domains; each point represents the rotation centre of the HATT as it is theoretically lowered through the water column.

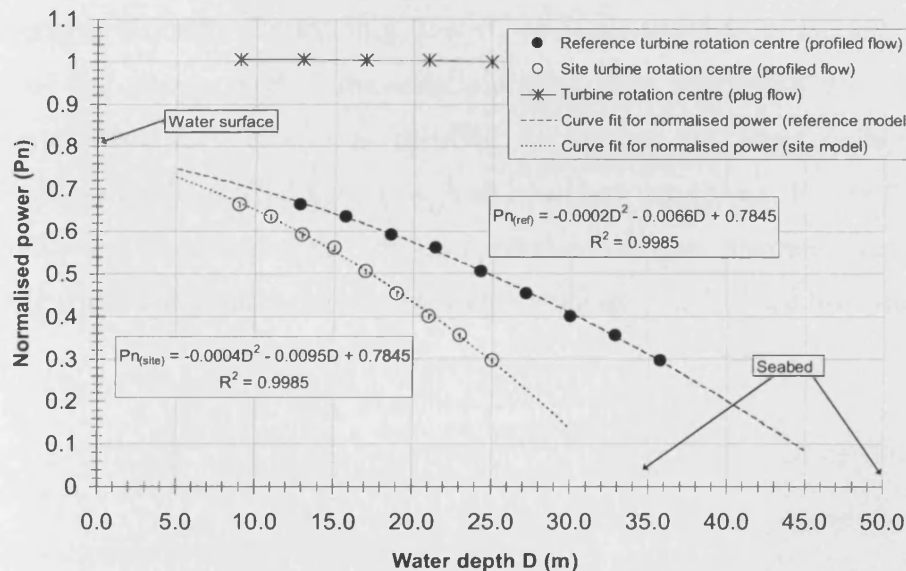


Figure 9.1: Normalised power (P_n) attenuation through water column with plug and profiled upstream velocity profiles for the site and reference CFD models.

Since the CFD model of the HATT occupies a cylindrical MRF which has a diameter slightly greater than the turbine diameter, gaps are left between the water and seabed boundaries. In reality if the turbine were to be positioned too high in the water column the turbine blades would start to break the water surface, in this case starting at a depth of 5 m. Any higher than this the turbine would be operating in partial submersion. With increasing depth, in this case below 30 m, the turbine would make contact with the seabed. It is also clear from Figure 9.1 that power density calculations based on the tidal velocity just below the water surface is misleading. For example, for the site under consideration the portion of the velocity profile 10 m below the surface is optimum, if the turbine rotation centre were to be positioned at this depth the power extracted by the HATT would be reduced by a factor of 0.65 and 0.7 for the site and reference CFD models, respectively.

9.1: Upstream velocity and power definition using Severn Estuary data

Figure 9.2 shows the power and torque curves for the HATT positioned 25 m below the water surface when subject to plug and profiled tidal flow using the Severn Estuary data. This again illustrates the reduction in power extracted due to the lower average velocity across the HATT diameter at that depth. As previously stated the operational efficiency of the HATT is therefore affected by the upstream velocity used when calculating the available energy density. Under plug flow C_p was calculated from the available resource upstream of the turbine and if the idealised plug flow conditions are assumed, C_p is unambiguous since the velocity is constant throughout the water column with slight attenuation towards the seabed from near wall boundary conditions, Figure 9.3. Again, the power coefficient calculation can be compromised by the upstream calculation used. Specifically when using the maximum upstream velocity in a profiled flow field.

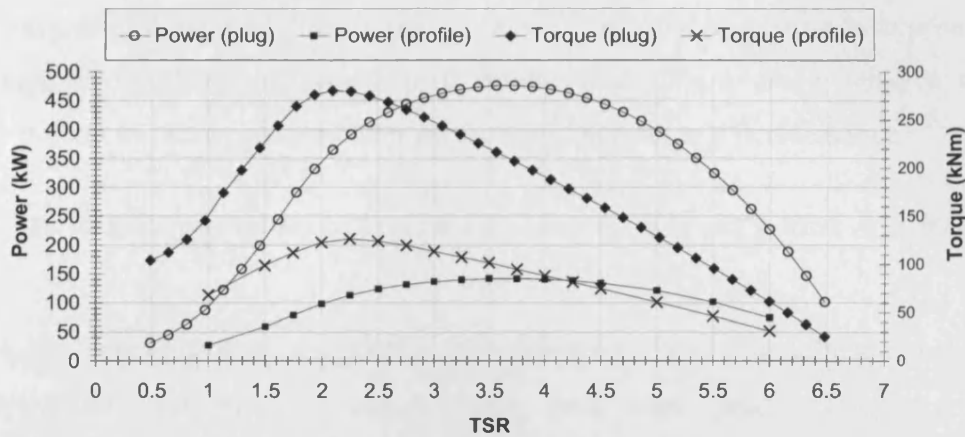


Figure 9.2: Power and torque curves for reference and site domains with plug and profiled flows

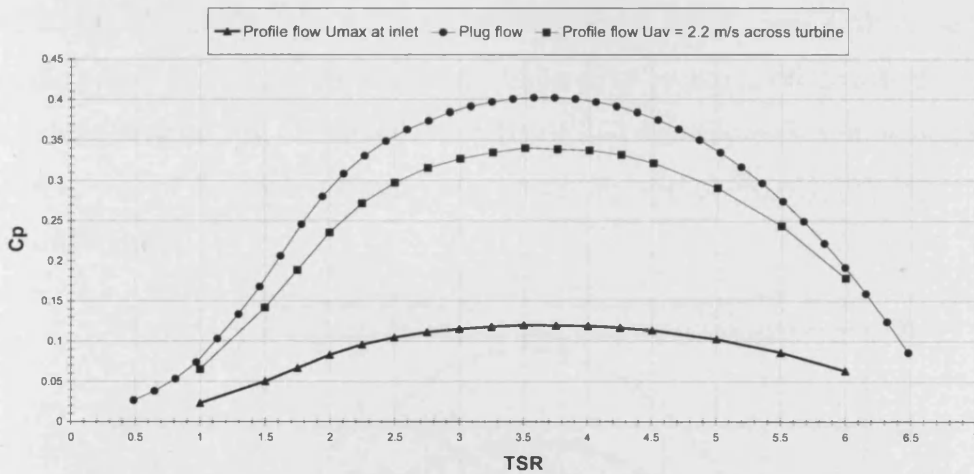


Figure 9.3: Dependency of power coefficient on upstream flow definition

For a true representation of turbine performance the tidal velocity should be monitored between 2 and 5 turbine diameters upstream of the HATT and at the depth of its rotation axis. It was shown that by using the peak upstream near surface tidal velocity (3.08 m/s) C_p reduced to 0.12. However, if the average flow velocity across the turbine diameter is used $C_p = 0.34$. Using the volumetric calculated average velocity (2.09 m/s), the maximum C_p returns to approximately 0.4 This clearly illustrates the need to clarify the operational boundaries to which the HATT is matched and how its performance is monitored during operation. As discussed in Chapter 4 it is suggested that a better estimate of the turbine's

performance can be gained by using the average of the velocity profile at approximately 3 m upstream of the turbine. It was shown, however, that the average velocity, calculated from the volumetric flow, gave a better measure of the turbine's performance.

9.1.1: Power comparisons between the Severn Estuary and Anglesey site 2 data

With the idealised plug flow of 3.08 m/s the reference site CFD model gave peak power of 466 kW, which was equal to the reference deep water model. However, with the introduction of the profiled velocity flow, derived from the ADCP site data, the power density at 25 m below the water surface is considerably reduced and thus the torque and power extracted by the HATT are reduced. As previously stated, for the Severn estuary site, the peak power at this depth was 142 kW.

When the velocity profiles for the two sites were scaled to the same peak velocity and water depth, the power and torque curves were compared to each other to assess the effects of the profile shape, Figure 9.4. It should be clarified that the Anglesey site velocities are much higher than that of the Severn Estuary site producing approximately 30% more power, with a peak of 185 kW.

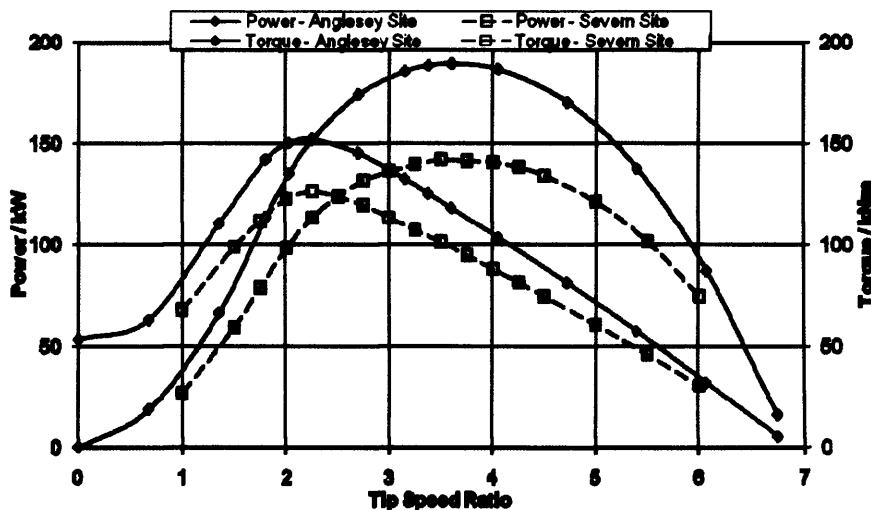


Figure 9.4: Torque and power curves for Severn and Anglesey site 2

The turbine at either site has a peak power at a TSR of ~ 3.6 , with the peak torques occurring at a TSR of ~ 2.2 . Interestingly, the average velocity over the turbines only varies by a small amount with the average velocity for the Severn site being 2.20 m/s and that for

the Anglesey site being 2.23 m/s. Hence the distribution of the velocity over the swept area is critical. One way to increase the C_p value would be to place the turbine at a higher position in the water column, though the shipping requirements discussed earlier would have to be ignored, the effects of depth positioning were shown in Figure 9.1 using the Severn Estuary velocity profile. Figure 9.5, compares the power curves for both the Severn Estuary site and Anglesey site 2. Also shown is a power curve generated using the $1/7^{\text{th}}$ power law. The figure clearly shows the a significant over estimate on the power extracted by the HATT when using the $1/7^{\text{th}}$ power when compared to the power curves calculated from both the Severn and Anglesey velocity profiles. All these however are significantly below the curve calculated from the 3.08 m/s plug flow. The power curves generated from the Severn and Anglesey site 2 data show a difference in peak power extraction of around 50 kW whereas the $1/7^{\text{th}}$ power law shows an increase of 80 kW above the Anglesey site 2 curve and 128 kW above the Severn Estuary curve. Given the assumed re-scaled curves the $1/7^{\text{th}}$ power law has the potential to over estimate the power extracted for the Severn and Anglesey sites by 89.9 % and 42.2 %, respectively, at the defined depth and velocity profile bounded by the HATT diameter.

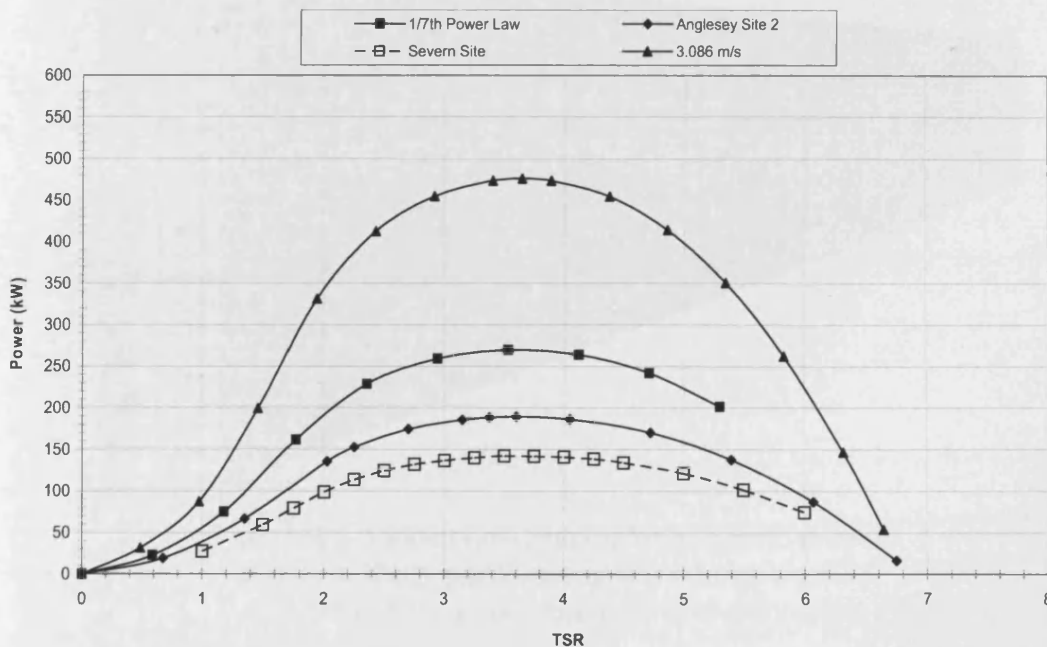


Figure 9.5: Comparison between Anglesey, Severn and $1/7^{\text{th}}$ power law: 3.08 m/s plug flow and scaled profiled flow. U_{av} @ Anglesey = 2.23 m/s ; U_{av} @ Severn = 2.2 m/s

The velocity at the Severn estuary site is unlikely to provide a suitable level of power to be viable if the un-scaled tidal velocity of 1.8 m/s were used in this study. The Anglesey site however would meet the economically viable velocity of 2-3 m/s. Due to the velocity profile through the water column in both cases however the power developed would be significantly less, i.e 30-40 % of that assumed if the near surface velocity is considered (466 kW at 3.08 m/s plug flow).

9.2: Contour of wake z-axis velocity with plug flow for 50 m depth CFD model

The velocity profile up to 400 m downstream of the HATT under plug and profiled flow for both the reference and site models were plotted along a vertical plane passing through the rotational centre of the hub. Figure 9.6, gives the velocity profile under plug flow conditions with a peak upstream velocity of 3.086 m/s for the reference CFD model. As a result of partial blockage effects induced by power extraction the water upstream of the turbine can be seen to slow. For all the CFD models at peak power extraction this typically occurred at around 5 m upstream of the HATT hub cone.

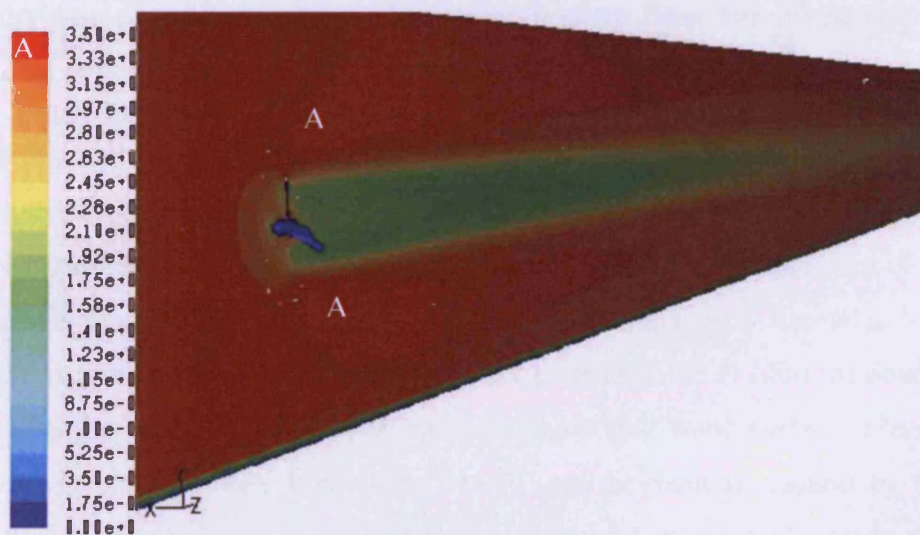


Figure 9.6: Velocity magnitude for reference domain z-axis velocity profile along central depth plane with plug -flow at velocity-inlet boundary (m/s)

The water then accelerates to the sides, above and below the HATT. Due to the application of a zero shear stress at the surface boundary the accelerated flow field extends to the

surface. Whereas towards the seabed a profile is induced by the application of the no-slip boundary condition. The velocity of the water above and below the HATT is approximately 3.5 m/s, which is around 0.5 m/s greater than the upstream water velocity. Even though the turbine rotational axis is positioned 2.5 diameters below the surface it is clear that some form of surface interaction would occur immediately downstream of the HATT. The velocity immediately downstream of the turbine can be seen to reduce from 3.08 m/s to approximately 1.65 m/s along the rotational centre line. With little influence from the surface and seabed boundaries the wake extends to the full 400 m length of the CFD domain. As suggested by Myers et al, (2008) the slower moving core of the wake is surrounded by the faster flowing free stream water velocity. In order to conserve momentum as the wake moves downstream it progressively expands forming a divergent cone. If the domain length were longer, turbulent mixing at the boundary between the wake and the faster flowing free stream would eventually break down the outer wake boundary as it becomes reenergised returning the wake to the velocity and turbulence intensity of the upstream flow.

9.2.1: Contour of wake z-axis velocity with plug flow for 35 m depth CFD model

Figure 9.7 shows the wake recovery for the site CFD model with plug flow at 3.086 m/s. With the turbine positioned 25 m below the surface boundary similar features as in the reference CFD model can be seen such as the slower axial velocity upstream of the HATT and the acceleration of the water above and below of the HATT diameter. The downstream wake is stable and symmetrical and finally extends to 40 D (400 m) downstream to the pressure outlet boundary. Figure 9.7 also indicates that some surface interaction may occur as the velocity directly behind the HATT can be seen to extend to the surface boundary, however, all the reference and site models used in the analyses do not account for a free surface.

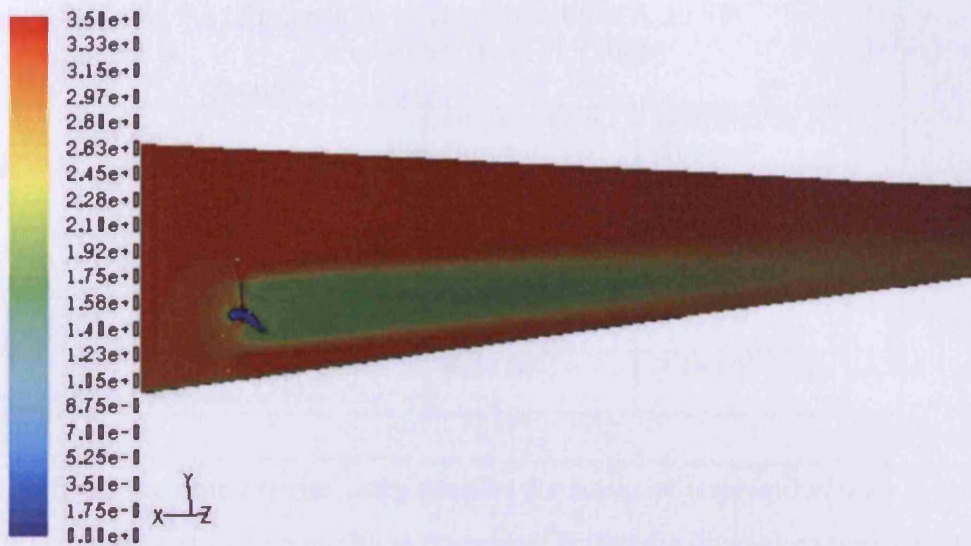


Figure 9.7: Velocity magnitude for site domain z-axis velocity profile along central depth plane with plug flow at velocity-inlet boundary (m/s)

As no wake velocity measurement were made during the flume testing similar measurements from literature were used for comparison, at least on a qualitative level has no free surface was included in the study. Table 9.1 gives the dimensions of flume facilities as presented by Myers et al, 2008, also shown are the depth averaged Froude and Reynolds numbers. Both of these studies used actuator discs to simulate the downstream wake characteristics of a HATT. The latter cited work showed the principle differences between wakes generated from semi-porous meshes (actuator discs) and horizontal axis turbines. At both facilities the depth from the surface to the centre of the disc was maintained constant, however due to the larger dimensions of facility B two different depths were studied. This latter feature enabling the visualisation of any effects associated with flow concentration between the disc and flume floor. For facility A a well defined varying velocity profile was demonstrated for the study. The velocity profile for facility B was similar to that of A, however, the disc in facility B occupied a smaller portion of the water column and thus experienced less variability in velocity with depth.

Table 9.1: Dimensions of flume facilities A and B
Source: Myers et al, (2008)

Facility	A	B
	Chilworth flume	IFREMER channel
Total water depth	4 Diameters	20 Diameters
Channel width	13 Diameters	40 Diameters
Disk centre from surface	2 Diameters	2 Diameters
Depth-Averaged Froude No.	0.118	0.113
Depth-averaged Reynolds No.	9.2×10^4	9.9×10^5

Figure 9.8 shows the downstream wake profiles for series of tests undertaken at locations A and B. What is apparent when studying the wakes is that the downstream recovery distance for the deeper water at facility B is far longer than that of facility A. The wake in facility B can be seen to traverse up to 20 disc diameters (D) downstream whilst at location A the wake shows a much greater degree of velocity recovery. For a velocity deficit of approximately 0.4 the downstream distances are around 6 D for facility A and 12 D for B. The experimental results presented by Myers et al, (2008) show that the wake length in facility A was shortened as the water accelerated around the disc and, via mixing, it was stated that this phenomenon helped to break up the downstream wake. Myers et al, (2008) attributed the longer wake in facility B to a lack of flow acceleration between the disc and the flume bed, which then allowed the wake to remain stable for longer. In contrast to the above, computational analyses using an in-house developed code, MacLeod et al, (2002) concluded that the wake velocity deficits are barely affected by the depth of submergence when modelled using semi-permeably membranes to simulate power extraction. To investigate the reference and site models further velocity deficit plots were generated with both plug and profiled flows. The profile used was that obtained from the Severn Estuary data.

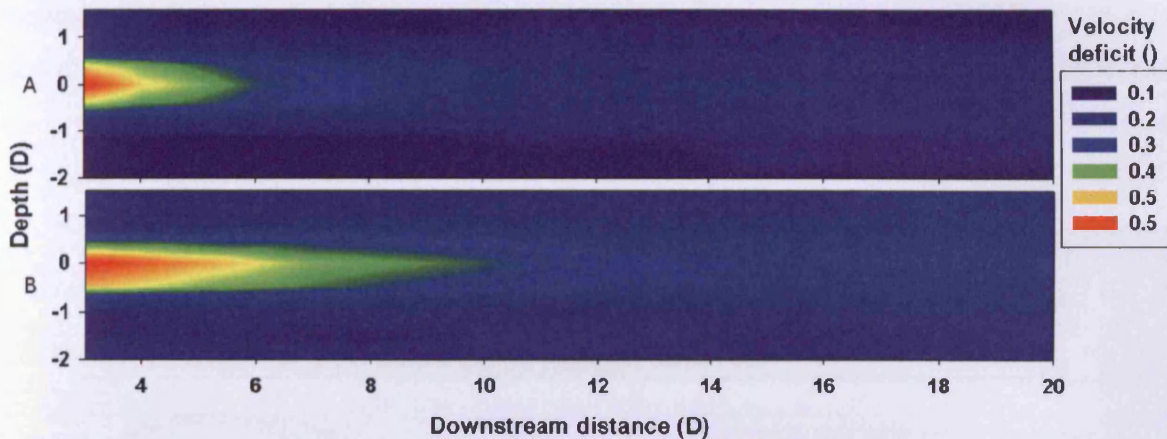


Figure 9.8: Centre plane velocity deficit profiles; Chilworth (A) and IFREMER (B).
Source: Myers et al, (2008)

With a plug flow, Figure 9.9 shows the wake deficits for the reference model, where the turbine's rotational axis is positioned 25 m below the surface, in a total depth of 50 m. The mid depth position leaves 20 m between both the surface and seabed boundaries and the outer swept area of the blades. For the site model, Figure 9.10, the turbine's rotational axis is positioned 25 m below the surface, in a total depth of 35 m. The lower positioning, in the shallower depth, leaves 20 m above and 5 m below the turbine's swept area. Also shown in both Figures 9.9 and 9.10 are contour plots coloured with axial velocity.

From Figures 9.9 and 9.10 there can be seen to be an increase in the velocity deficit for the reference model when compared with the site model. From the work of Myers et al, (2008) the increased wake deficit in facility B can be seen to show some similarity with the reference model with larger depths below the turbine. For the reference model, the velocities above and below the turbine's swept area, Figure 9.9, are equal in magnitude and are approaching the upstream velocity of 3.08 m/s. In the site model, Figure 9.10, the close proximity of the turbine to the lower boundary results in an increase in velocity and a shortening of the wake when compared to the reference model. However, this cannot be directly compared to facility A due to the differences in depth above and below the swept area. However, what it does show is that an increase in velocity between the disc/turbine and boundaries (surface and bed) increases mixing resulting in a faster breakdown of the wake structure. There is a noticeable curvature of the wake for the site model under plug flow, Figure 9.10. Due to the close proximity of the HATT to the seabed as the wake

expands it starts to contact the seabed. This is seen to occur at around 252 m (25.2 D) downstream. Beyond this point the wake starts to move towards the seabed which in turn imparts increased shear that helps to break up the wake.

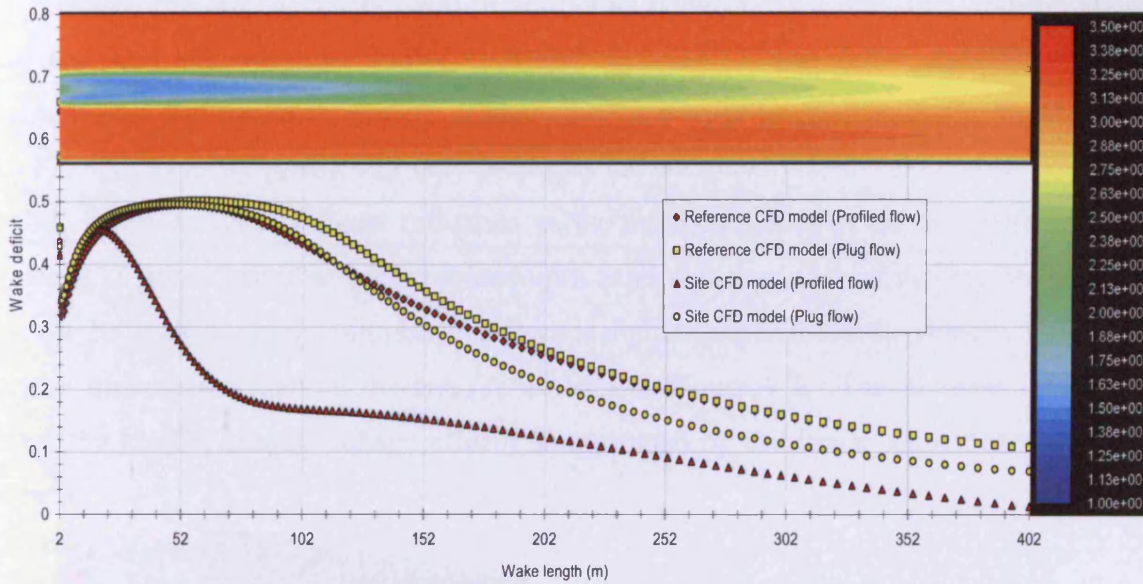


Figure 9.9: Wake deficits for Reference and site CFD models with plug and profiled flow. Plus contour plot coloured with axial velocity for reference CFD model with plug flow

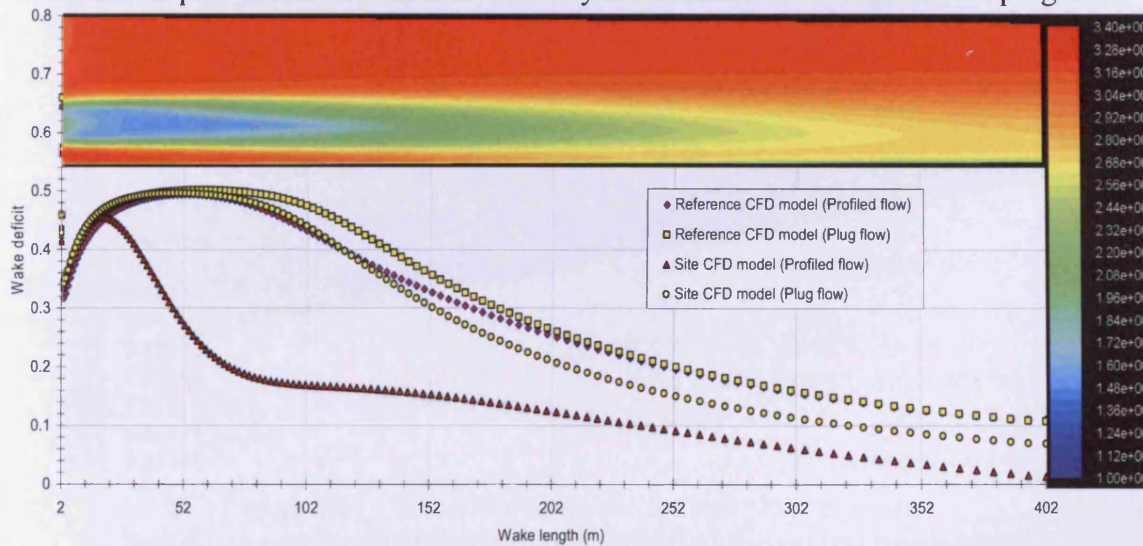


Figure 9.10: Wake deficits for Reference and site CFD models with plug and profiled flow. Plus contour plot coloured with axial velocity for reference CFD model with profiled flow

9.2.2: Contour of wake z-axis velocity with profiled flow (Severn data) for 50 m depth CFD model

With the introduction of the velocity profile derived from the Severn Estuary data, the water below the HATT can be seen to accelerate between its swept area and the slower moving fluid towards the seabed. Above the HATT the faster moving water is uninterrupted and continues to flow at much the same axial velocity as that upstream of the HATT. The velocity profile not only increases the complexity of the flow upstream of the HATT, it also has a significant influence on the hydrodynamics of the downstream wake. Figure 9.11 gives a contour plot coloured with axial velocity. One of the key observations that can be made from this figure is that there is no increase in the wake velocity toward the surface immediately behind the HATT, as seen in Figure 9.7. The increase in velocity above the HATT, from blockage effects, is swamped by the larger velocities toward the surface.

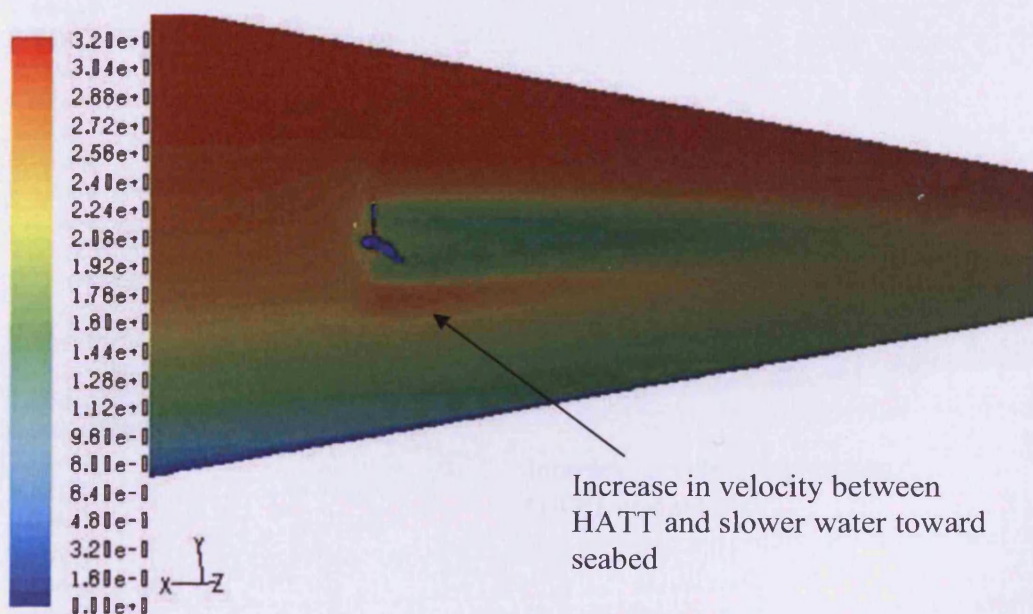


Figure 9.11: Velocity magnitude for reference domain z-axis velocity profile (Velocity magnitude) along central depth plane with profiled flow at velocity-inlet boundary (m/s)

9.2.3: Contour of wake z-axis velocity with profiled flow (Severn data) for 35 m depth CFD model

With the HATT positioned 25 m below the surface the effects of the velocity profile are magnified downstream. In much the same way as for the reference model the water velocity increases around the HATT. Figure 9.12 shows a similar increase in the axial velocity below the blade tip diameter and the slower moving water towards the seabed boundary. Again, no visible interaction with the surface is noticeable as the faster moving water towards the surface boundary suppresses the velocity increase above the turbine. If Figures 9.13 and 9.14 are compared with the profiles shown in Figures 9.9 and 9.10 a slight curvature can be seen in the wake. The magnitude of the curvature can be seen to increase in the site model.

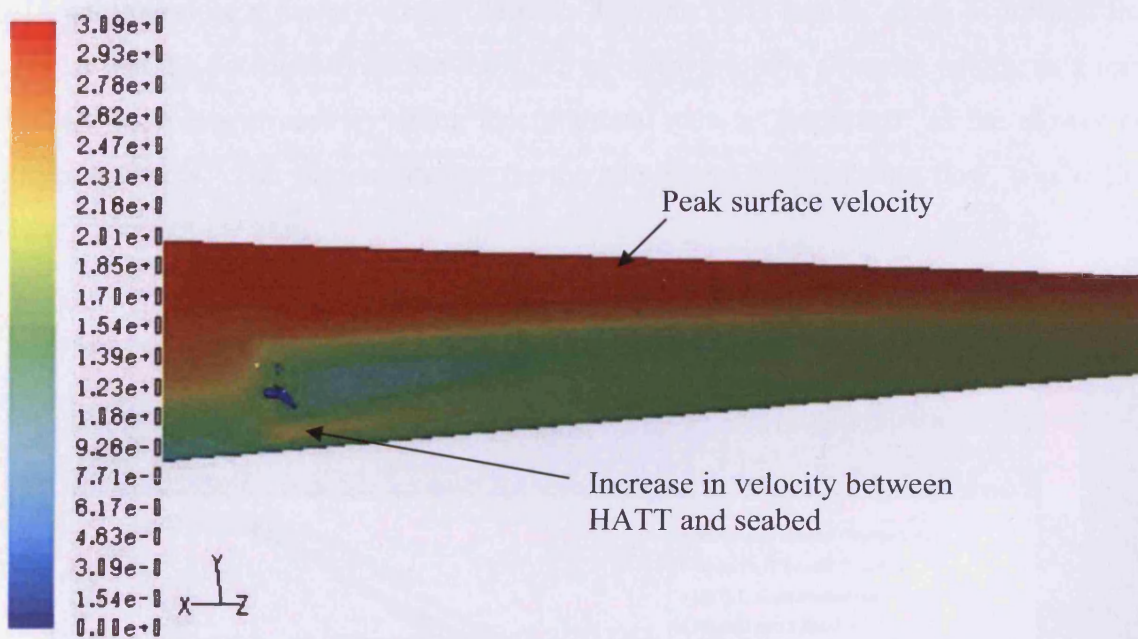


Figure 9.12: Velocity magnitude for site domain
z-axis velocity profile along central depth plane with profiled
flow at velocity-inlet boundary (m/s)

Figures 9.13 and 9.14 elucidate the curvature further by placing the contour plane in line with the axial velocity deficit curves. The difference between the downstream axial wake

velocities, along the rotational axis of the HATT, for the site and reference models are now more pronounced.

Plotting the axial wake velocity along the rotational axis of the HATT is now misleading since the core of the wake curves above the rotational axis between 2 m (0.2 D) and 102 m (10.2 D) downstream. For the site model, the curvature is further magnified by the close proximity to the seabed. This can be seen in the site CFD model with profiled flow curve Figure 9.14. At around 20 m (2 D) downstream of the HATT the curve shows a rapid decay in the axial velocity deficit up to approximately 90 m (9 D) beyond which the flow recovers to the upstream axial velocity. The increase in velocity below the swept area and the faster moving water above has a significant effect on the shape of the downstream wake. However, if a HATT were to be positioned at the same height downstream it would in effect be exposed to the flow along the axis of the velocity deficit curve shown in Figure 9.14 and therefore a lower velocity deficit. The site CFD results, using a profiled flow, suggest that the potential exists for the wake to be asymmetric along its length; as a result, the rate of velocity recovery along the rotational axis is 'improved' as the slower core curves upwards. The velocity deficit for the site model, using a plug flow, was reduced along the rotational axis.

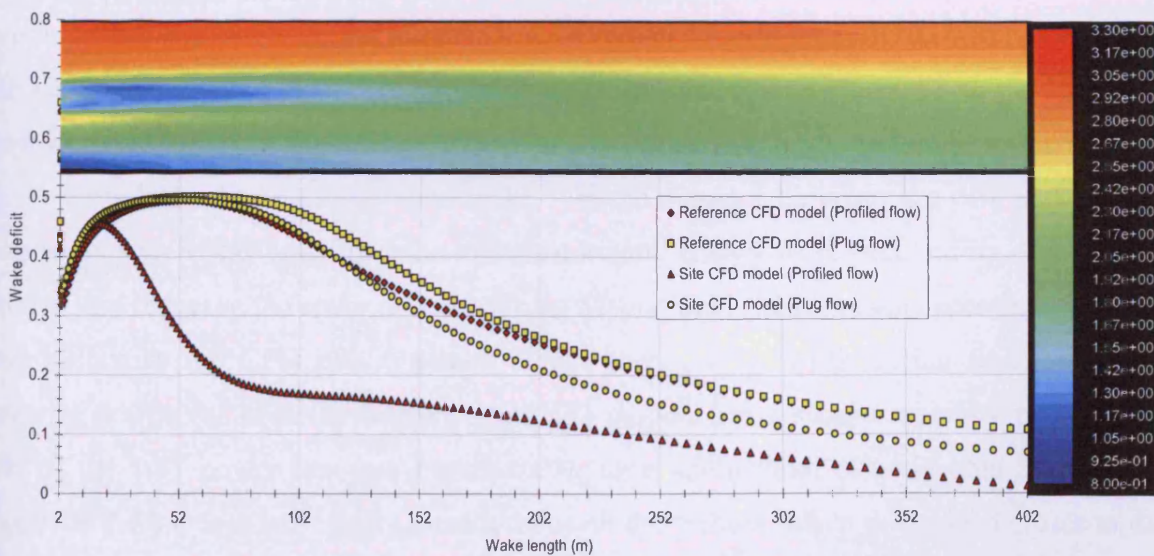


Figure 9.13: Wake deficits for Reference and site CFD models with plug and profiled flow. Plus contour plot coloured with axial velocity for site CFD model with plug flow

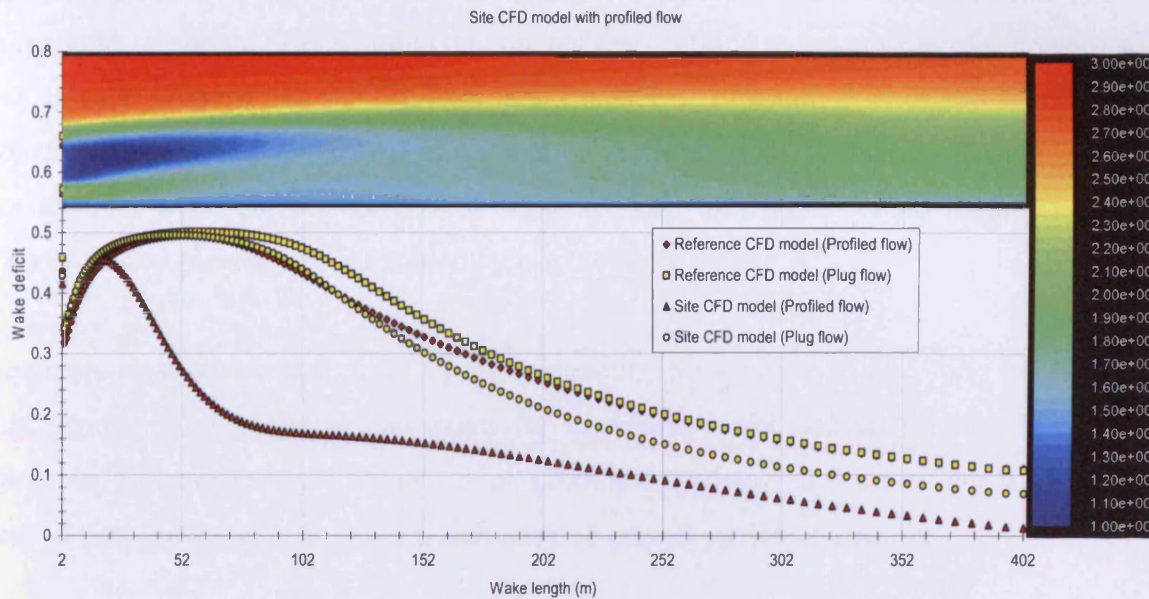


Figure 9.14: Wake deficits for Reference and site CFD models with plug and profiled flow. Plus contour plot coloured with axial velocity for site CFD model with profiled flow

In contrast to the CFD results presented in this thesis, experimental results presented by Myers² et al, (2008), using mesh discs, showed that the wake velocity deficit increased with close proximity to the lower boundary. In total 4 depths were studied with disk centres at 0.33d, 0.50d, 0.66d and 0.75d. The velocity profile for the experiments approximated to a 1/8th power law. It was shown that the velocity deficit at near surface (0.75d) and mid depth (0.50d) exhibited similar magnitudes. At greater depths (0.33d) the wake deficit was shown to increase and extended further downstream. This was attributed to the low mass flow rate and turbulent kinetic energy beneath the disc, which resulted in a re-energisation of the flow beneath the downstream wake. As the distance between the disc and the bed was increased, it was noted that the turbulent kinetic energy increased, aiding downstream mixing and reducing the wake deficit. Whilst Myers² et al (2008) results present a different conclusions to the CFD data obtained in this thesis, it is worth noting that the inflow velocity profile for both the reference and site models has a steeper velocity profile than that of the 1/8th power law, see Figure 6.23. One feature that is noticeable in the CFD results is the increase in velocity directly beneath the turbine, when positioned closer to the lower boundary. This is more apparent with the profiled inlet flow. It is proposed that this is the key feature of the simulated flow that contributes to the reduction in the downstream

wake. It is also proposed that this feature maybe a function of the initial upstream velocity magnitude. It should also be noted that the solidus (defined as the portion of the swept area that is solid. For the HATT definition see Chapter 3, Equation 3.2) of the Myers² et al, (2008) and the 3 bladed HATT discussed in this thesis are different. To compare the downstream wake characteristics it is suggested that the HATT would require 5 blades. This increased blockage could indeed reduce the wake deficit.

There are clear advantages, from a power extraction perspective, to operating the HATT at mid depths. The potential also exists for improving wake deficits through blade pitch variation. As suggested by Myers² et al, (2008), the relative position of the HATT to the seabed may induce longer wakes which have an impact on device spacing.

9.2.4: Comparison of wake vortex with plug and profiled flow

Figures 9.15 and 9.16 show pathlines released from a surface 25 m below the water surface along the axis of rotation for both plug and profiled flow for the site CFD model. With plug flow at the inlet, the pathlines clearly show a stable vortex formation downstream of the turbine that reaches the outlet boundary 400 m (40 D) downstream of the turbine. With a profiled flow the downstream vortex collapses significantly sooner resulting in a faster wake velocity recovery. The wake also exhibits vortex asymmetry with bias toward the negative x- axis. The full implications of this will be discussed later. It appears that with the introduction of a profiled velocity flow, the length, and hence the recovery rate of the wake is improved in both shallow and deep water scenarios, although its complexity is also increased in terms of flow direction. While a plug flow has the advantage of symmetry and the associated benefit of maximising power extraction, as suggested by the CFD data it would clearly be a disadvantage in the development of arrays as it exhibits greater velocity deficits.

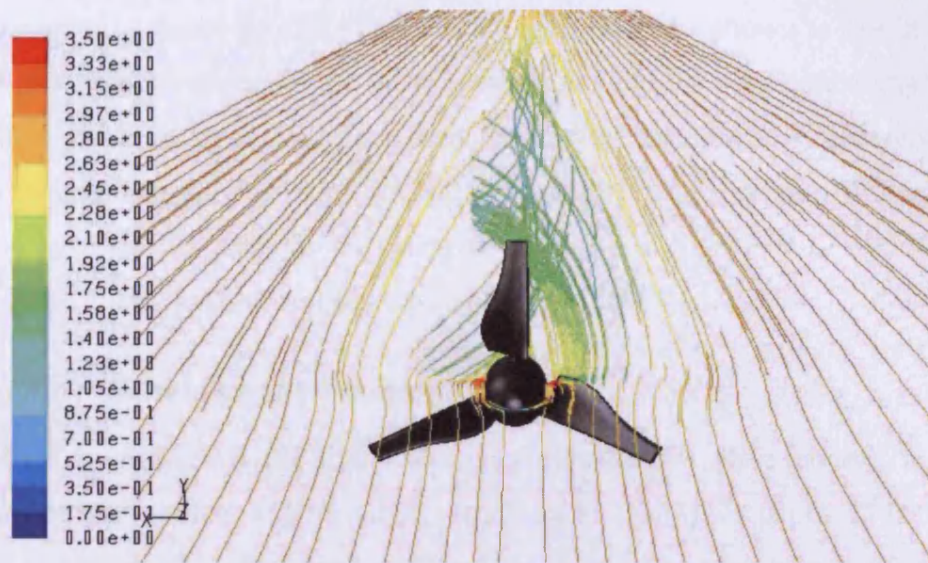


Figure 9.15: Stable downstream vortices with upstream plug flow (m/s)



Figure 9.16: Disrupted downstream vortices with upstream profiled flow (m/s)

It is proposed that while subject a profiled flow, the wake length is shortened due to the velocity differential above and below the wake. Under a profiled flow the wake does not expand symmetrically as it moves downstream, as a result the divergent cone, which would exist with a plug flow, is suppressed. In the near wake, this would help to collapse the rotational component of the vortex as it rotates between the slower and faster moving component of the main flow surrounding the wake. It is proposed that for extreme velocity profiles the greater asymmetry of the wake. The effect of an extreme velocity profile on the wake of a wind turbine was shown by Sezer-Uzol and Uzol, (2009). Using steady and transient modelling, the study showed that the asymmetry of the wake increased with an

extreme upstream velocity profile. The downstream wake was shown to rise in the vertical direction directly downstream of the turbine, at which point the rotational component of the wake also starts to collapse. Whilst it is noted that the models have differences in their boundary conditions and therefore do not show a direct comparison, the noted feature shows some similarities with the curvature of the wake in Figures 9.13 and 9.14 and the collapse of the vortex has shown between Figures 9.15 and 9.16.

9.3: Turbine stanchion interaction

As proposed in Section 4.12, five basic geometric shapes were chosen to study the interaction of the turbine with a single stanchion in the 35 m depth CFD domain, as presented in Figure 4.17. By using pathlines coloured with velocity magnitude (m/s) the level of downstream disturbance emanating from each stanchion surface can be shown. Figures 9.17 to 9.26 show the increase in flow disturbance as the stanchion geometry is changed between ellipse, hydrofoil, circular, diamond and finally square. Figures 9.17 and 9.18 show pathlines of velocity magnitude (m/s) for the elliptical cross section.

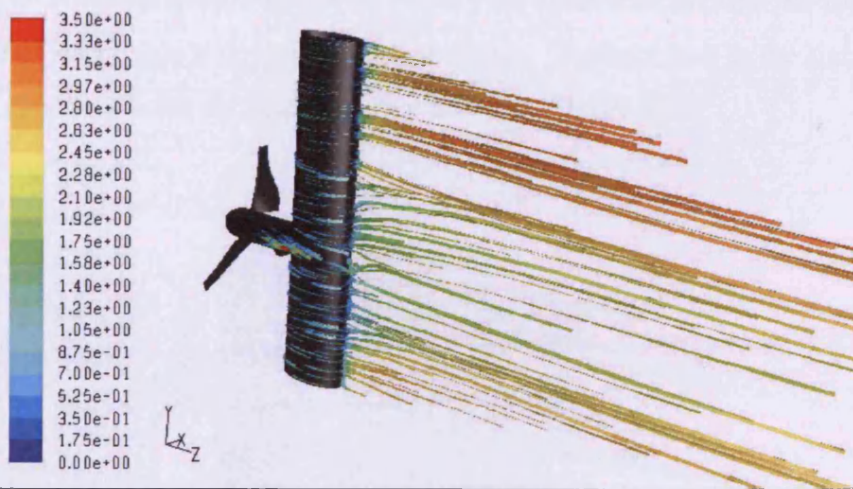


Figure 9.17: Pathlines coloured by velocity magnitude with elliptical stanchion cross section



Figure 9.18: Plan view of Pathlines coloured by velocity magnitude with elliptic cross section

In both Figures the pathlines show the flow following the contour of the surface of the stanchion and show very little disturbance downstream. From the plan view in Figure 9.18 the wake shows a bias to the right hand side of the rear of the stanchion.

The hydrofoil cross section in Figures 9.19 and 9.20 again indicate that the flow follows the contour of the profile into a downstream disturbance. A slight bias to the right hand side of the wake is also noticed as in the ellipse in plan view, Figure 9.20.

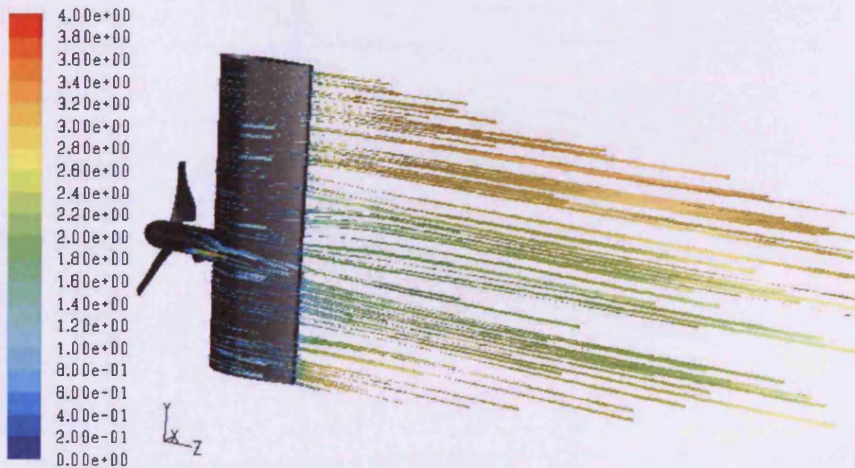


Figure 9.19: Pathlines coloured by velocity magnitude with profiled stanchion cross section

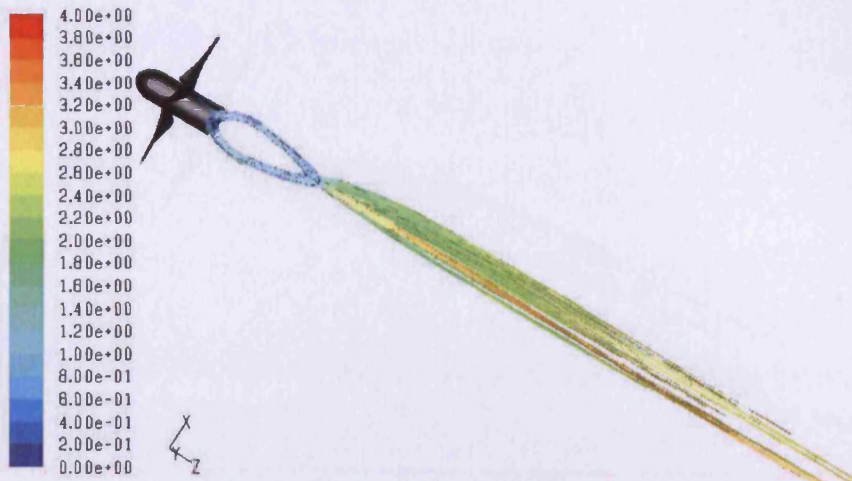


Figure 9.20: Plan view of Pathlines coloured by velocity magnitude with profiled cross section

With the use of a circular cross section, Figures 9.21 and 9.22, vortex eddies can be seen developing as the pathlines pass around the rear of the stanchion. The vortices dissipate at approximately 1.5 hub diameters downstream, starting from the downstream stanchion diameter. Along the upstream face of the stanchion, however, the flow remains close to the surface. Again, as in the other cases above, the flow in plan view shows a bias towards the right hand side of the stanchion, but with an increase in magnitude.

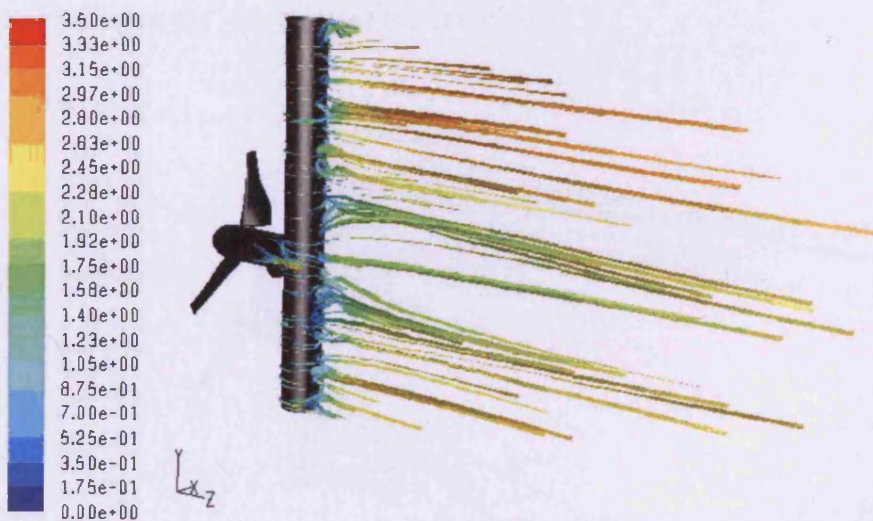


Figure 9.21: Plan view of Pathlines coloured by velocity magnitude with circular cross section

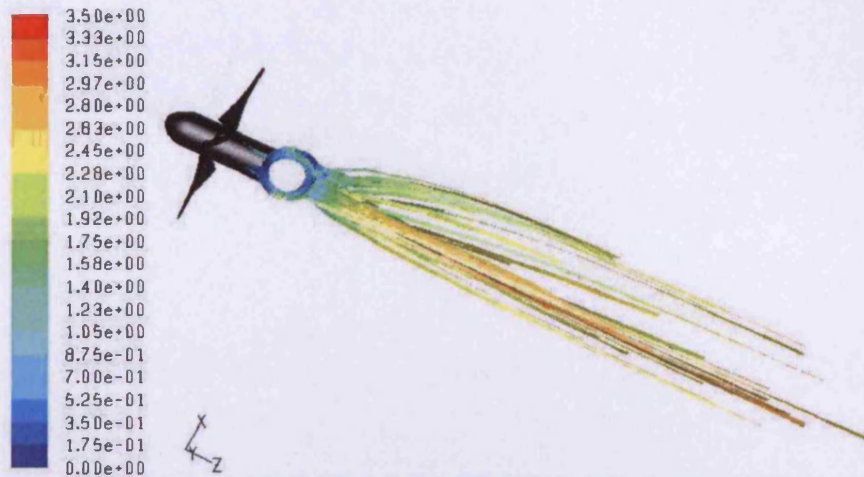


Figure 9.22: Plan view of Pathlines coloured by velocity magnitude with circular cross section

Figures 9.23 and 9.24 show the results for the diamond cross section. The pathlines in this case indicate that the disturbance in the flow field downstream of the stanchion has increased significantly. Figure 9.23 shows the formation of large eddies in both the vertical and horizontal planes. In the plan view as given by Figure 9.24 two main areas of vortex intensity can be seen either side of the central axis of the stanchion when viewed along the Z-axis. The downstream vortices travel a distance of around 4.1 hub diameters downstream starting at the rear edge of the stanchion.

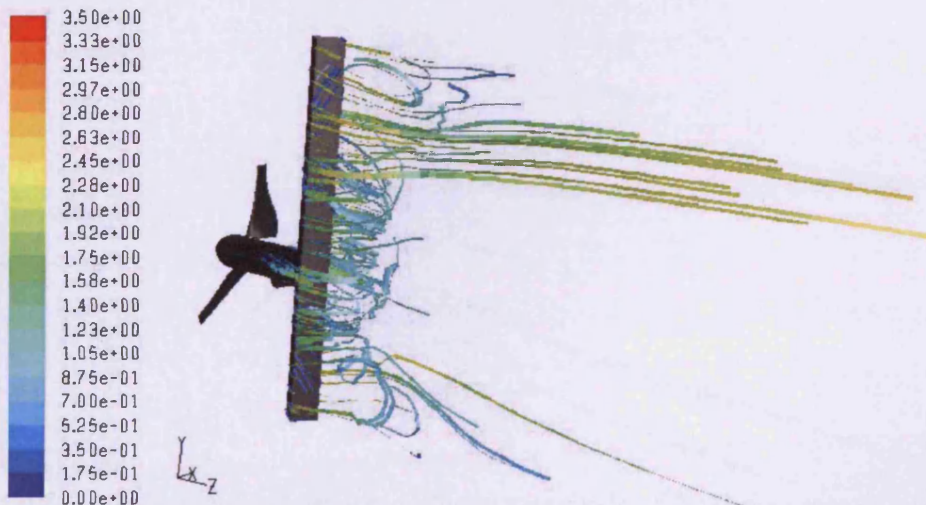


Figure 9.23: Pathlines coloured by velocity magnitude with diamond stanchion cross section



Figure 9.24: Plan view of Pathlines coloured by velocity magnitude with diamond cross section

For the final square cross section, Figures 9.25 and 9.26, the vortices are again formed in both the vertical and horizontal plains with a similar separation plane along the central Z-axis of stanchion as in the diamond cross section. When viewed from above, Figure 9.26, the vortices can be seen to extend around 4 hub diameters downstream of the stanchion. From a flow perspective, the elliptical and hydrofoil cross sections give the best downstream flow characteristic when compared in terms of flow disturbance.

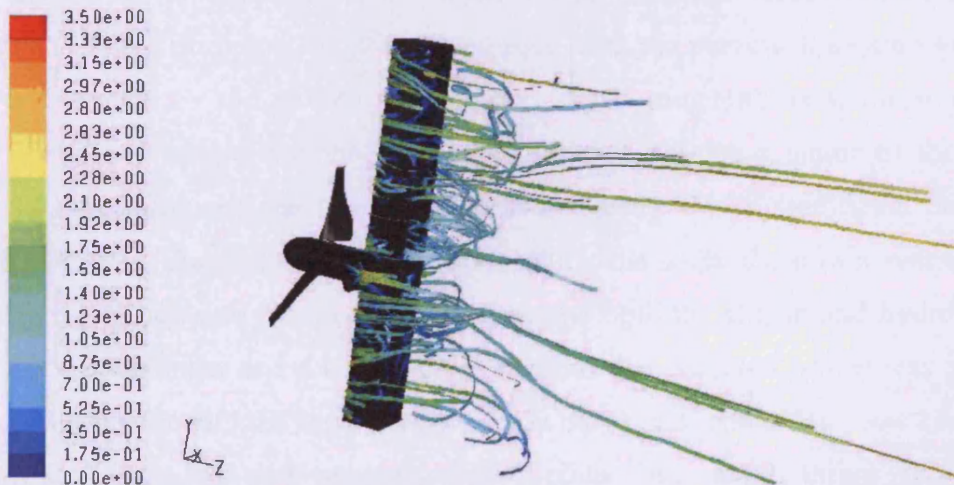


Figure 9.25: Pathlines coloured by velocity magnitude with square cross section

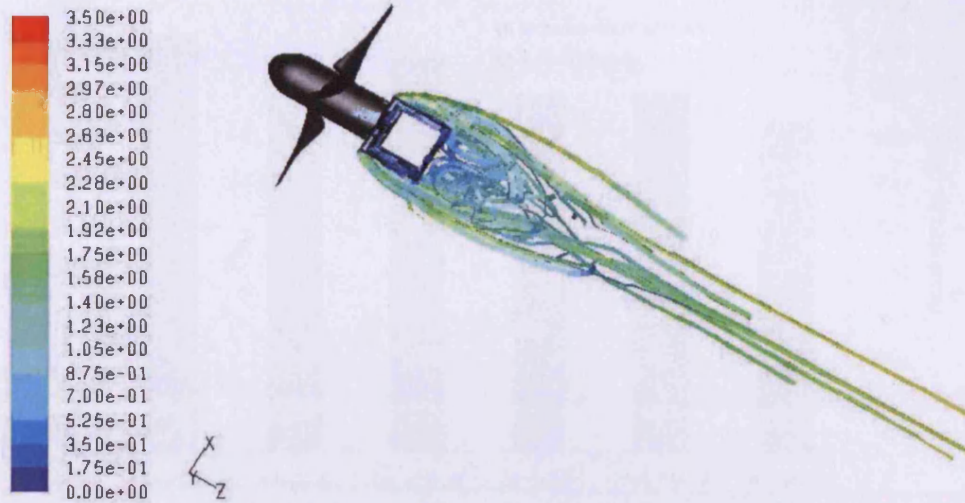


Figure 9.26: Plan view of Pathlines coloured by velocity magnitude with square cross section

Their application is however problematic given their shape in relation to a flow field that changes direction as the tide ebbs and flows. The only possible solution would be to rotate the whole stanchion between the two tidal cycles. This would be more so in the case for the hydrofoil cross section as its shape is directional specific. Out of the remaining three geometries studied the next cross section with the least downstream flow disturbance was the circular cross section. For both the Seaflow and Seagen projects (MCT, 2008) a tubular pile was used to fix the turbine assembly to the seabed. It is also clear from the histogram in Figure 9.27 that with increased flow disturbance from the varying stanchion geometries the power extracted by the turbine is attenuated as the stanchion axial thrust increases. Whilst it is acknowledged that the level of disturbance will be a factor of the distance between the stanchion and the turbine the results indicate that a significant decrease in energy is possible. For the 2 hub diameters used in this study the power extraction was reduced by 6.4 % between the no stanchion case and both the ellipse and hydrofoil cross sections. For the circular and diamond cross sections the extracted power was attenuated by 15 %. And finally with the square cross section the overall power loss was 21.2 %. For the remaining diamond and square cross sections the axial thrust increases by approximately 25 % and 37 %, respectively from the circular cross section.

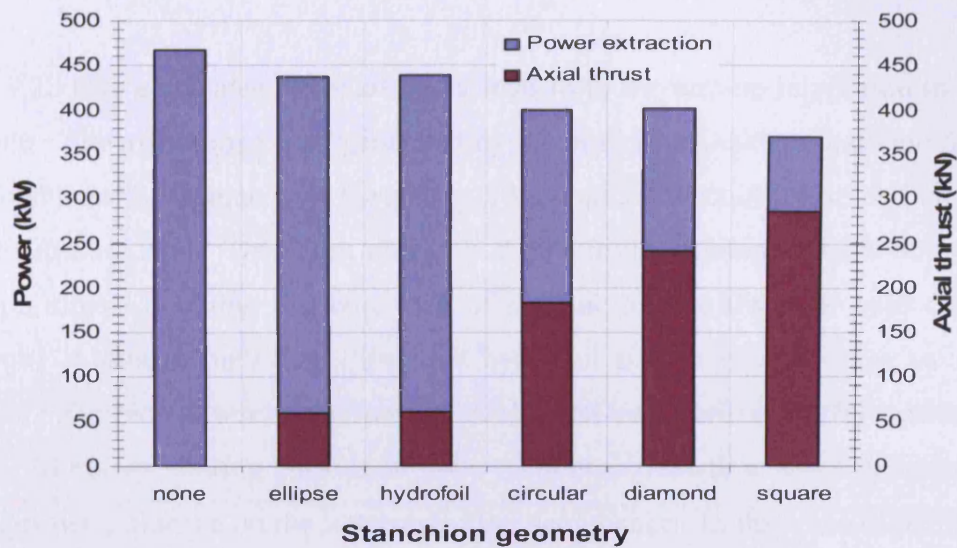


Figure 9.27: Effect of stanchion geometry on turbine power extraction with increasing stanchion axial thrust
 $V = 3.08 \text{ m/s}$

Figure 9.28 shows the individual axial thrust load for the turbine in isolation, the stanchion and when the two are combined. It is clear from Figure 9.28 that the axial thrust load from the turbine drops along with the power extracted, Figure 9.27. The maximum drop in turbine axial thrust load is around 50 kN from the base case without a stanchion to the use of the circular and square cross sections.

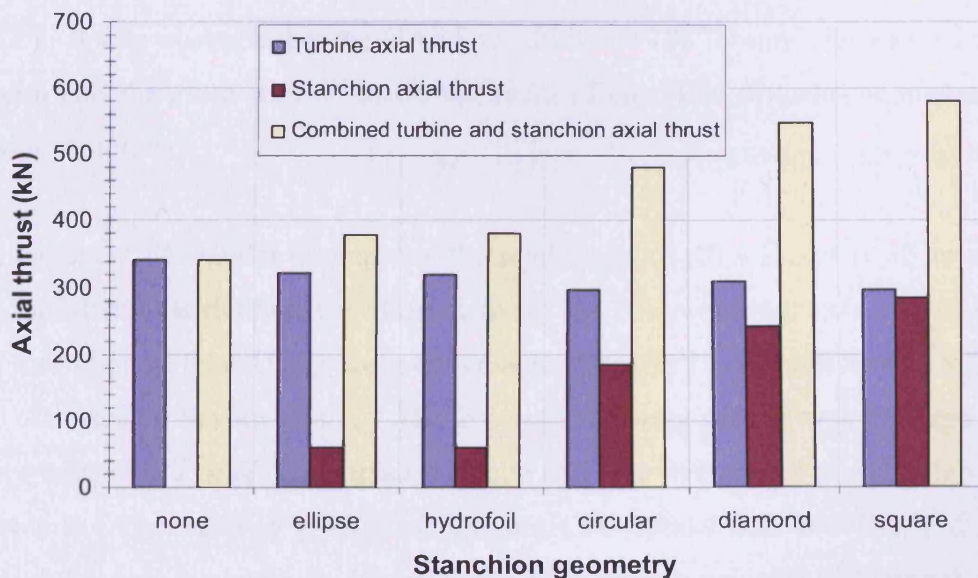


Figure 9.28: Turbine and stanchion axial thrust variation with stanchion geometry
 $V = 3.08 \text{ m/s}$ (plug)

Figure 9.28 also elucidates the axial thrust load from the turbine in relation to that of the stanchion. The axial thrust load generated by the circular stanchion is around 63 % of the thrust load from the turbine. For the square cross section the axial thrust load increase to 97 % of the turbine load. The result of this is shown in the combined loads with the square stanchion almost doubling the axial load of a single turbine from the base case with no stanchion. Although both the ellipse and hydrofoil stanchion geometries have the least influence on turbine power extraction and axial thrust load, their geometry is more complex to form. Moreover, during periods of none rectilinear tidal flow these geometries would have a greater influence on the intensity of the disturbance. In this case of the hydrofoil it would be necessary to rotate the stanchion so that the profile can be correctly aligned with the upstream flow. The circular geometry was therefore chosen above the diamond and square geometries due to their high loading and negative influence on power extraction.

9.3.1: Effect of stanchion on HATT power under site conditions

Using the methodology discussed in Section 4.13, torque, power and axial load curves were generated for each turbine blade through 360° of rotation. A quasi-static approach was used to approximate temporal motion initially with no stanchion (Case.1.) and then finally with a circular cross-section stanchion placed 2 hub diameters downstream of the turbine (Case.2.). It was assumed that the HATT would rotate 180° around the vertical axis of the stanchion and therefore would remain upstream of any flow disturbance emanating from the fixing structure.

Using the site CFD model dimensions the total water depth was set at 35 m and due to vessel hull depth restrictions, the 10 m diameter HATTs rotational axis was situated 25 m below the water surface. Using these dimensions the HATT occupied 28.6% of the overall depth. The scaled Severn Estuary ADCP current velocity profile was also applied to the velocity-inlet with a peak near surface velocity of 3.086 m/s and an average depth velocity of 2.24 m/s. The velocity profile for the site CFD model was previously discussed in Section 6.3.3 and is shown in Figure 6.19. The current velocity differential across the turbine diameter was 38.5% with a peak of 2.4 m/s and a minimum of 1.5 m/s.

9.3.2: Performance curves through 360° of rotation (no stanchion) with profiled flow

Under plug flow with the HATT located in such a position as to be unaffected by flow concentration (between the HATT swept area and slower moving water or proximity to seabed under the HATT) the vortices formed in the downstream wake by each blade are symmetrical, Figure 9.15. However, to maintain flow continuity as the turbine is positioned closer to the seabed the water velocity between the swept area of the HATT and the seabed increases, as shown in Figure 9.12.

With the introduction of a profiled velocity at the inlet-boundary the downstream wake can be seen to curve upward downstream of the turbine in the site model, Figure 9.14. This phenomenon was also observed as the HATT was rotated through 360°. With no stanchion in place, Figure 9.29 gives the torque generated by blade 1 (B1), blade 2 (B2) and blade 3 (B3) as they move between the higher velocity water at the top of the HATT and slower velocities towards the seabed. Intuitively, the maximum torque and hence power should occur at 0° (TDC) since at this point in the rotational cycle each blade would be subjected to the maximum velocity at that depth followed by a minimum at 180°.

Under profiled flow a similar phenomenon occurs due to the slower moving fluid beneath the HATT. The curvature in the downstream wake is shown in Figures 9.13 and 9.14. If under this set of conditions the torque, power and axial load curves are plotted for B1, B2 and B3 to the base of rotation angle, the maximum for the torque, power and axial thrust appears to move out of phase. If, for the sake of discussion the path of B1 is followed the phase shift is approximately -72°. As the HATT is rotated through one revolution the cyclic shape of each curve is symmetrical following a sinusoidal pattern. Curves B1, B2 and B3 with no stanchion pass through points of torque as generated by 9 steady-state models each with the turbine advanced in a clockwise direction by 40°, Figure 9.29. The -72° phase shift moves the maximum torque for B1 to approximately 288° and the minimum by -65° to around 115°. The corresponding maximum and minimum torque at these angles were 36 kNm and 30.6 kNm, respectively, with a peak torque oscillation of 15%. At 0° and

180° the torques are 33.9 kNm, 32.1 kNm with a torque oscillation of 5.3% clearly indicating that the maximum and minimum torque occur before 0° and 180°. This will be discussed further later in the Chapter.

Using the product ($T\omega$) the power curves for B1, B2 and B3 were then calculated using the torque data shown in Figure 9.30 and a constant ω of 1.47 rad/s, as applied to the CFD model. The maximum and minimum powers occur at approximately the same rotational angles with magnitudes of 52.3 kW and 44.6 kW, respectively and a percentage variation across the diameter of around 15%. The power oscillation across the turbine between 0° and 180° was 4.3 % with a maximum of 49.3 kW and a minimum of 47.2 kW.

For axial thrust loads a slight shift in the maximum and minimum load angle was noted with the peak and minimum axial load taking place at rotation angles of 270° and 110° with corresponding magnitudes of 53 kN and 51.6 kN. The axial thrust variation across the turbine diameter was approximately 3%. Between 0° and 180° the axial load oscillation was close to zero with a value of around 52.3 kN, Figure 9.31.

The total torque, power and axial load from each blade is also shown in Figures 9.29, 9.30 and 9.31, with magnitudes of 99 ± 0.182 kNm, 144.5 ± 0.175 kW and 157 ± 0.104 kN, respectively. The maximum and minimum torque, power and axial thrust for blades B2 and B3 also occur at the same angles but advanced by 120° and 240°, respectively.

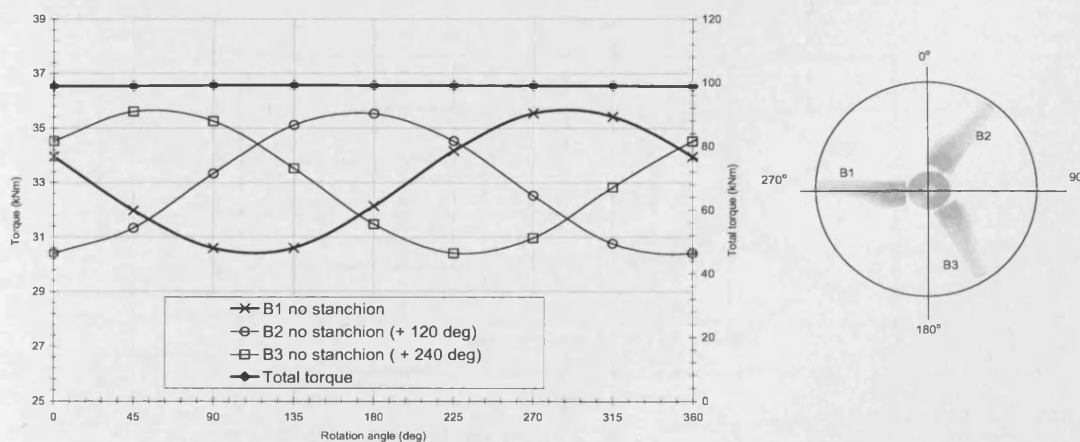


Figure 9.29: Torque variation for B1, B2 and B3 through 360° with no stanchion

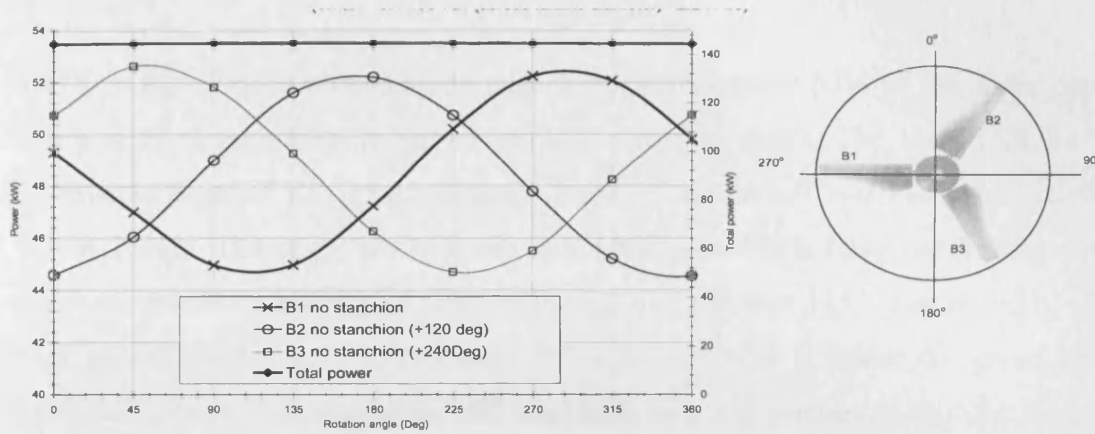


Figure 9.30: Power variation for B1, B2 and B3 through 360° with no stanchion

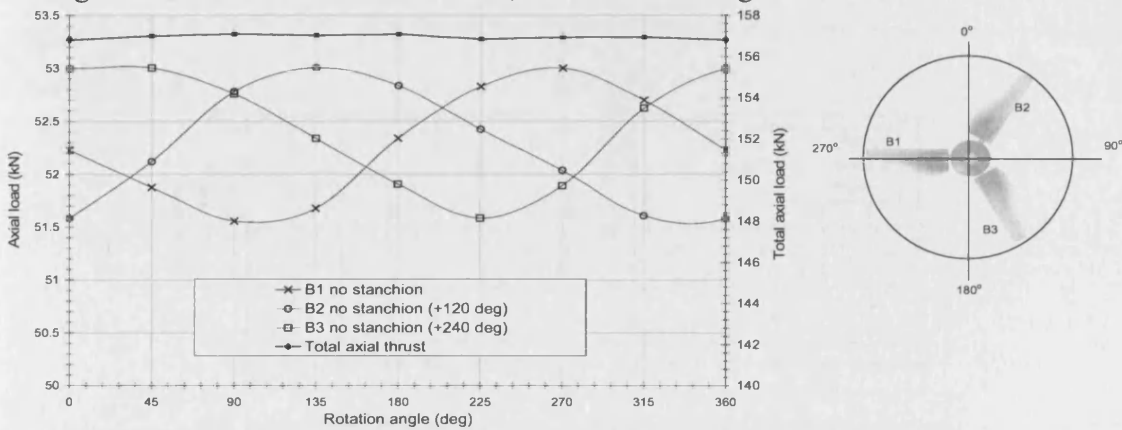


Figure 9.31: Axial thrust variation for B1, B2 and B3 through 360° with no stanchion

Batten et al, (2008) using a velocity profile based on the 1/7th power, Equation 6.4, studied power and axial thrust variability through 360° for a 20 m diameter 3 bladed HATT in a water depth of 30 m and a peak tidal speed of 2 m/s, Figure 9.32.

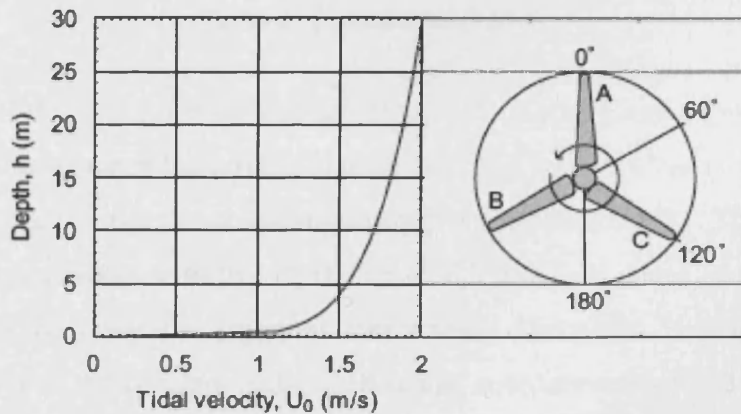


Figure 9.32: Example of current velocity profile and turbine rotation Source: Batten et al, 2008

The HATT in the aforementioned study occupied approximately 67% of the water depth, resulting in a 20 % reduction in current velocity across its depth. The local TSR for the HATT shown in Figure 9.32 varied between 6.2 and 7.7 between 0° and 180° , with a design TSR = 6 at 2 m/s. The study also showed individual axial blade force oscillations up to 3%, matching the 3% obtained at rotation angles of 288° and 115° , Figure 9.31. The maximum power, Figure 9.33 a, and axial thrust, Figure 9.33 b, under the given set of conditions, are clearly shown to occur at 0° and 360° with a minimum at 180° for blade A. Also shown are the sum of the power and axial thrust for all the blades, Figure 9.33, c and d, respectively.

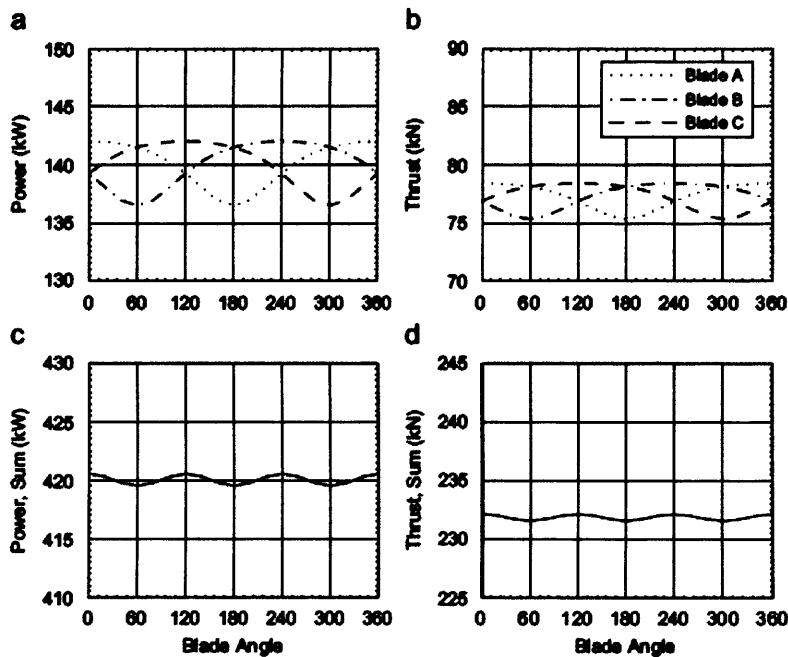


Figure 9.33: Individual blade and total power and thrust curves through 360° of rotation:
Source: Batten et al, (2008)

When combined the data from each steady-state CFD model gives a quasi-static picture on the macro physics between the turbine and surrounding water and in general the magnitude of the power extracted and thrust loading through 1 rotational cycle. The data presented in this thesis are comparable with that of Batten et al, (2008), in terms of the magnitudes and shape. There is however the question surrounding the blade position at which these magnitudes occur as the negative phase shift seems counterintuitive and non-physical given

the boundary conditions that define the velocity profile. A clue to the cause could be in the wake curvature shown in the 2D contour plot, Figure 9.14.

With closer inspection of the downstream wake vortex and its interaction with the velocity field upstream and downstream of the HATT a hypothesis for the physics leading to the phase shift in the location of the peak hydrodynamic performance is proposed.

Figure 9.34 shows pathlines coloured by velocity magnitude (m/s) released from a horizontal plane 28 m below the surface boundary and from the surface of B1 while positioned at a rotation angle of 315° . As previously stated the turbine is positioned with its rotational axis 10 m from the seabed boundary increasing the velocity of the water via flow restriction. For the given set of conditions at approximately 8 m downstream of the turbine the pathlines generated on the 28 m depth horizontal plane rise and contact the wake generated by B3 causing an upward swell and an increase in the corresponding vortex radius.

The magnitude of the velocity in m/s at the onset of the up flow is given by the arrow and annotated by the letter A. Depending on the rotational direction of the turbine the upward flow of water, indicated by the rising pathlines along the 28 m plane, can either increase or decrease the downstream blade vortex radius as measured from the rotational axis of the turbine. This can be seen to occur at approximately 9 m downstream as the up flow pathlines interact with those generated from the trailing edge as B1 advances in a clockwise direction. While at the same (B1) rotational angle the vortex radius generated by B3 is increased by the up flow, thereby forming an asymmetric wake.

The increased vortex radius between 0° and approximately 110° directly influences the velocity field upstream of the turbine. Figures 9.36 and 9.37 show the addition of pathlines released from horizontal plains at depths of 27 m and 22 m, respectively and their subsequent interaction with the downstream wake. On the right hand side of the turbine, Figure 9.36, the pathlines can be seen to pass over the raised vortex, whereas on the left hand side, Figure 9.37, they pass beneath the vortex but with less variance to their original

path indicating that the asymmetry of the wake on the right hand side of Figure 9.36 has an influences on the upstream water velocity.

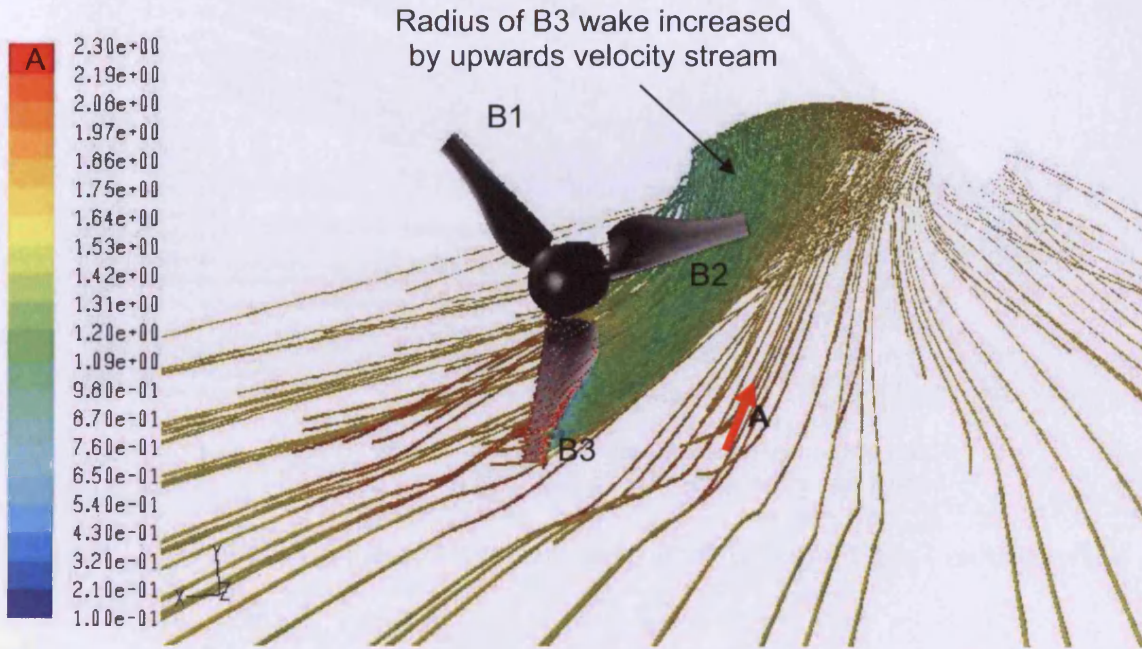


Figure 9.34: Pathlines coloured by velocity magnitude (m/s) Case.1 right view

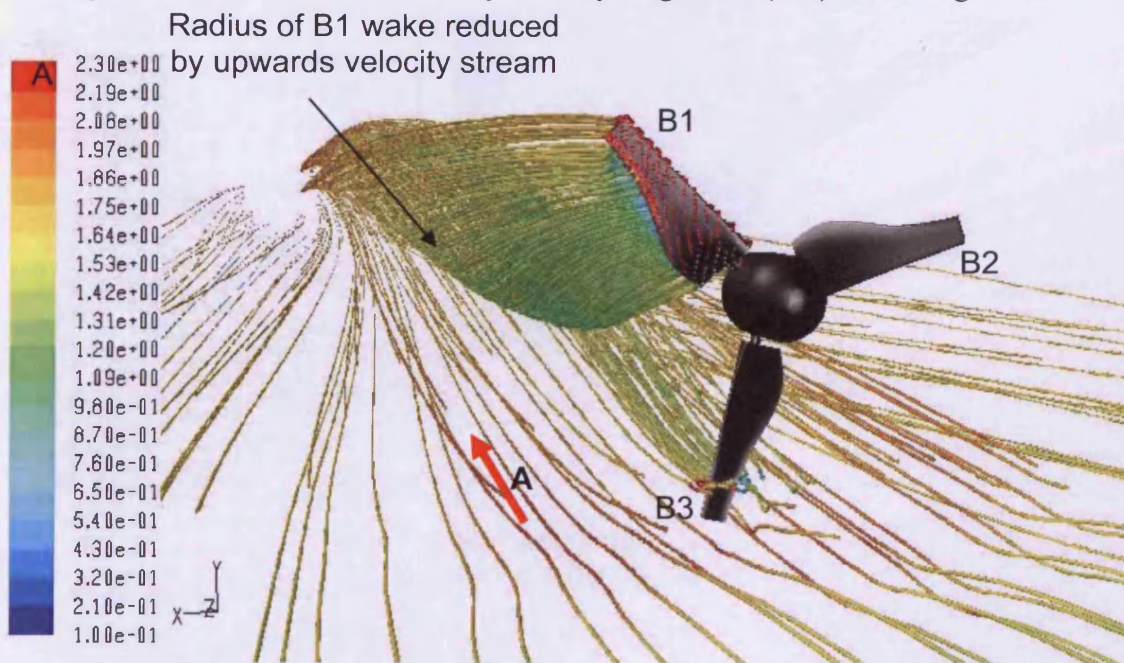
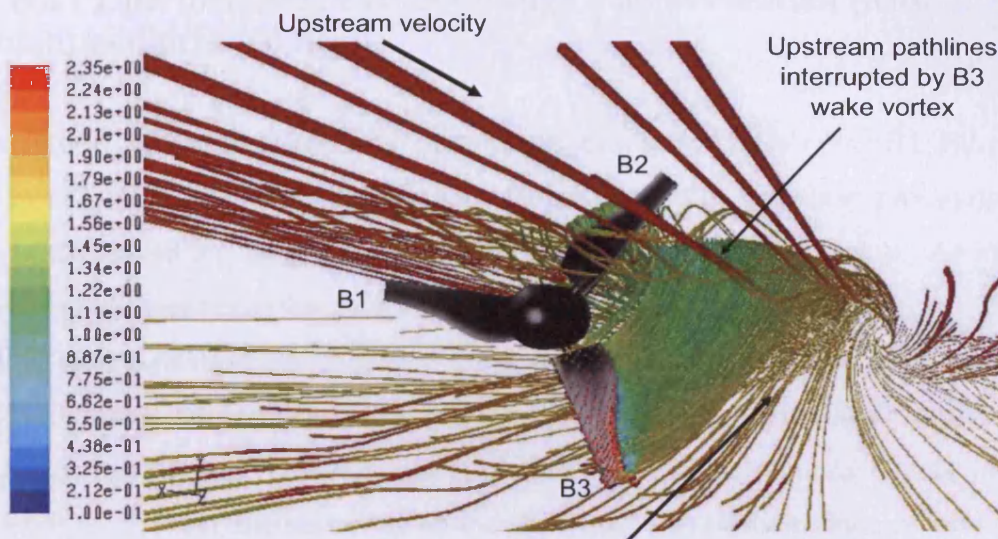
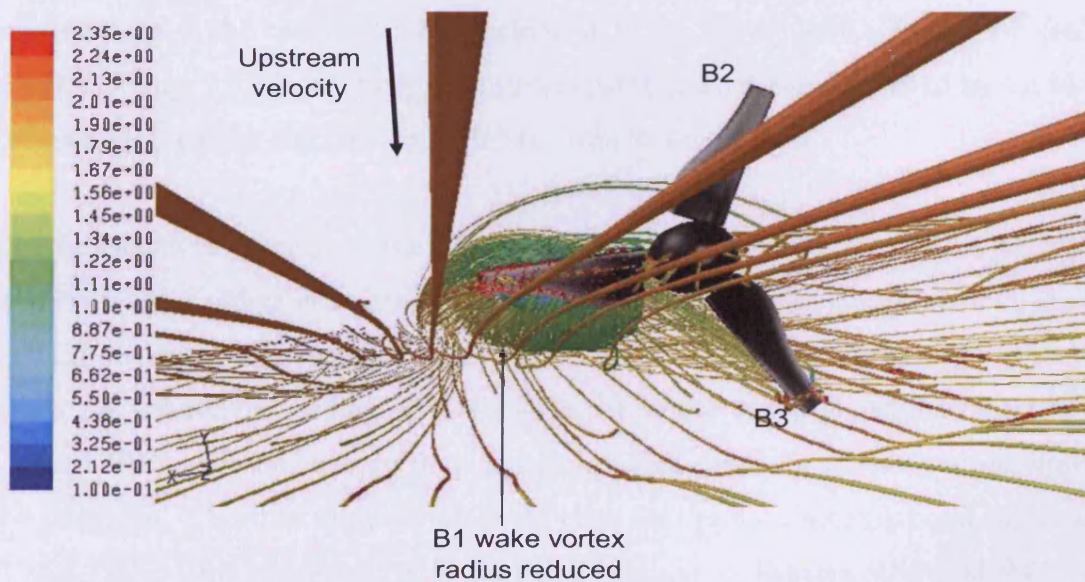


Figure 9.35: Pathlines coloured by velocity magnitude (m/s) for Case.1 left view



B3 vortex radius increased by up flow due to Flow restriction between turbine and seabed

Figure 9.36: Pathlines coloured by velocity magnitude (m/s) for Case.1 reduced wake



B1 wake vortex radius reduced

Figure 9.37: Pathlines coloured by velocity magnitude (m/s) for Case.1 increased wake

9.3.3: HATT performance curves through 360° of rotation (with stanchion) and profiled flow

The magnitude of symmetric and asymmetric vortices released from either B1, B2 or B3 as shown in Figures 9.38 to 9.41 for Case.1. However, due to the close proximity of the turbine to the seabed the same upward flow of water can be seen to develop. As in Case.1 the vortex radius generated by each turbine blade is again either increased or decreased depending on its rotation direction. If the rotational direction is clockwise, the vortex radius is increased and reduced by the upward flow in exactly the same manner as in Case.1. Between 0° and 110° the upstream water velocity is reduced due to increased interference for the asymmetric vortex on the right hand side of the turbine as the pathlines following the up flow interact with those released from B3. Figure 9.38 shows pathlines released from a plane 2.5 m above the turbine rotational axis and how they are influenced by the downstream wake within the vicinity of the turbine. Here the pathlines directly are influenced upstream by the vortex. On the left hand side of the turbine, pathlines pass beneath B1 with less interference from the vortex since again its radius is reduced by the upward flow, as in the case with no stanchion in place, Figure 9.36. Above the leading edge of B1, Figure 9.39 shows that the upstream pathline lines are unaffected by the vortex generated by B1 and B2 and pass downstream virtually unaffected.

Due to the clockwise rotation of the turbine the vortex generated by B1 leaves the trailing edge of B1 with its radius increasing outward (or at this location in the rotational cycle in a downward direction) influencing the flow field as in the Case.1, as previously discussed. The flow field above the leading edge is unaffected by the vortex generated by B2 as it is still in part effected by the upward flow, but more significantly by the obstruction imposed by the stanchion. This then allows a relatively clear flow path between B1 and B2 between 270° and 315°. This phenomenon is further illustrated in Figures 9.40 and 9.41, with pathlines generated from a plane 2.5 m above the rotational axis. Here the asymmetry of the vortex downstream of the turbine is clear with the increased radius on the right hand side of the turbine. Points A and B annotate the difference in velocity magnitude 3 m

upstream of the hub tip. Point A has a velocity magnitude between 2.13 m/s and 2.01 m/s and B 1.9 m/s and 1.79 m/s, representing an average difference in velocity magnitude of around 0.23 m/s across the width of the turbine (X-axis) between rotation angles 90° and 270°.

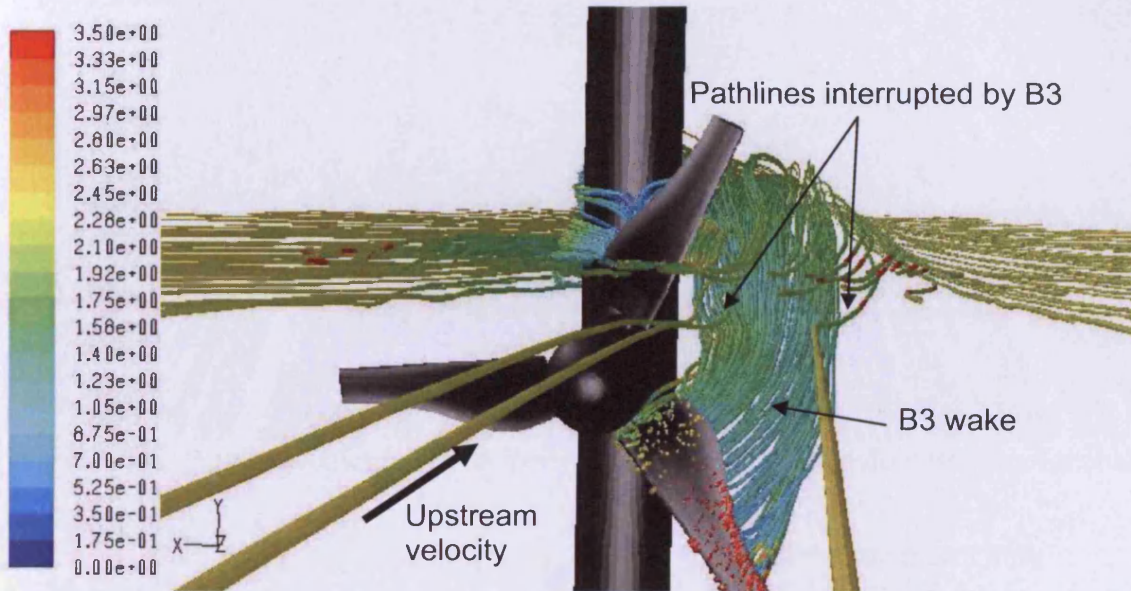


Figure 9.38: Upstream pathline contacting B3 wake along a plain at 32 m depth coloured with velocity magnitude (m/s) and B1 at 263° rotation angle

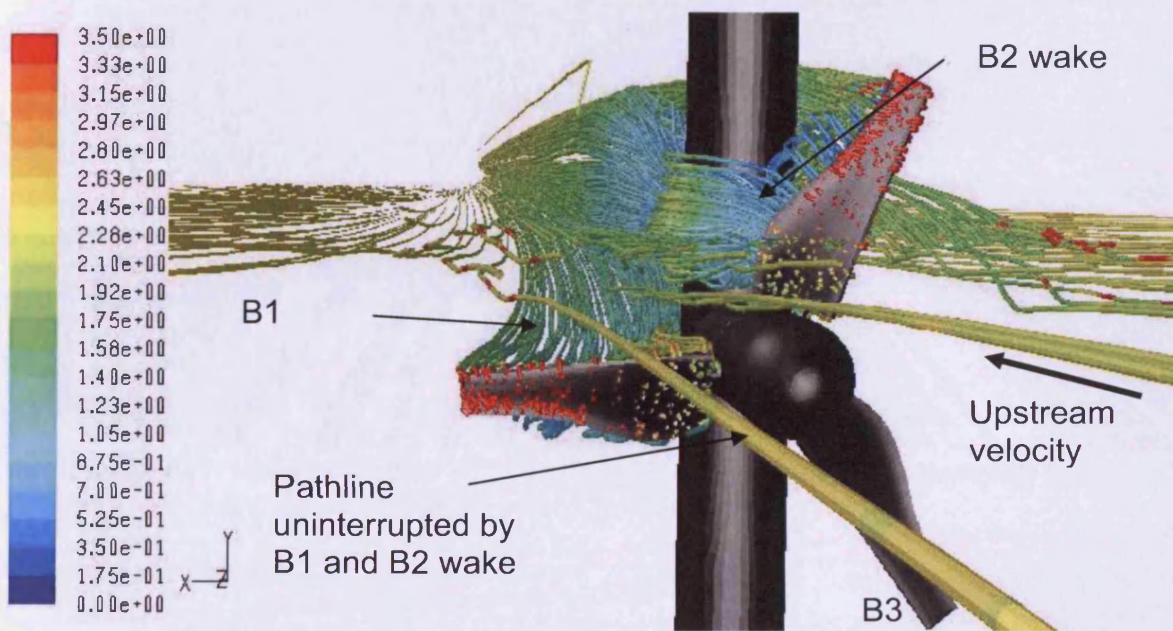


Figure 9.39: Upstream pathline missing B1 and B2 wake along a plain at 32 m depth coloured with velocity magnitude (m/s) and B1 at 263° rotation angle



Figure 9.40: Pathlines coloured by velocity magnitude (m/s) with downstream stanchion

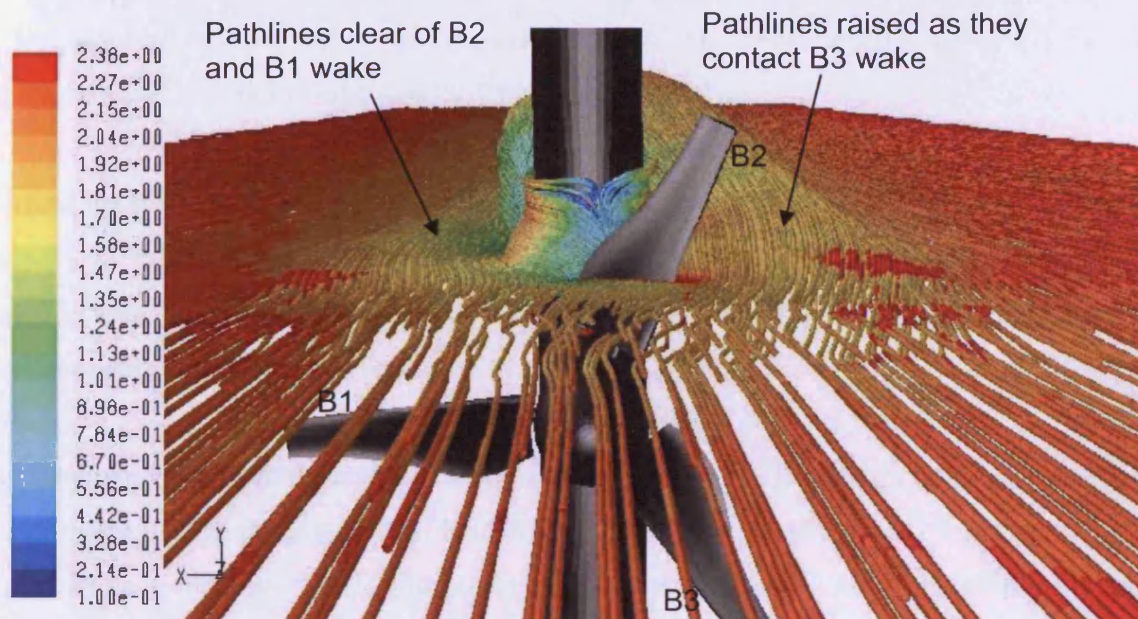


Figure 9.41: Pathline plain at 32 m depth coloured with velocity magnitude (m/s) with B1 at 263° rotation angle

Both Figure 9.40 and 9.41 also show the decrease in velocity between the turbine and the upstream edge of the stanchion. With a distance of 2 m downstream, the velocity at the

central distance between the rear of the hub and front edge of the stanchion was reduced from an average upstream velocity of 2.2 m/s to 1.2 m/s.

As the HATT is rotated through one revolution for Case.2 a cyclic shape is formed for each curve, however the sinusoidal pattern that was previously observed in Case.1 is interrupted at 180° and 0° . Curves B1, B2 and B3, with a stanchion in the downstream position, pass through points of torque again generated by 9 steady-state models each with the turbine advanced in a clockwise direction, with increments of 24° , Figure 9.42. The rotation resolution was increased to capture any effects associated with turbine to stanchion interaction.

For Case.2 a phase angle of -96° moves the maximum torque for B1 to approximately 264° and the minimum to angle of around 130° with a phase angle of 50° . The corresponding maximum and minimum torque at these angles are 33 kNm and 25 kNm, respectively with a torque oscillation of 24%. Between 0° and 180° the torque oscillation is 9.3 % with maximum and minimum values of 29.1 kNm and 26.4 kNm.

The power curve was calculated using the torque data shown in Figure 9.42 and a constant ω of 1.47 rad/s, Figure 9.43. The maximum and minimum power occurs at the same rotational angles with magnitudes of 48.6 kW and 37.1 kW, respectively and a percentage power oscillation of around 15%.

As for Case.1 the axial thrust loads show a slight shift in the maximum and minimum axial thrust angles. The maximum axial load was noted at approximately 242° and the minimum thrust angle at 0° or 360° as B1 moves in front of the stanchion. A similar effect is seen at 180° again as B1 passes upstream of the stanchion, Figure 9.44. For B1 the axial thrust magnitudes at 180° , 242° and 360° were 45.6 kN and 49.4 kN and 44.7 kN, respectively. Between the peak axial thrust of 49.4 kN at 242° and the minimum 44.7 kN at 360° the axial thrust oscillation was shown to be 9%, double that previously calculated and given by Batten et al, (2008), Figure 9.32. As before the total torque, power and axial thrust from each blade is given in Figures 9.42, 9.43 and 9.44, with average magnitudes of 87.1 ± 1.31

kNm, 128 ± 1.92 kW and 139.8 ± 0.92 kN. As mentioned for Case.1 the maximum and minimum torque, power and axial thrust for blades B2 and B3 also occur at the same angles but advanced by 120° and 240° , respectively.

Under profiled flow for Case.1 the power extracted by the turbine was 144 kW and for Case.2 the total power extracted was 128 kW giving a power reduction of 16 kW. The maximum axial load for Case.1 was 157 kN and 139.8 kN for Case.2 giving a axial load reduction of 17.2 kN.

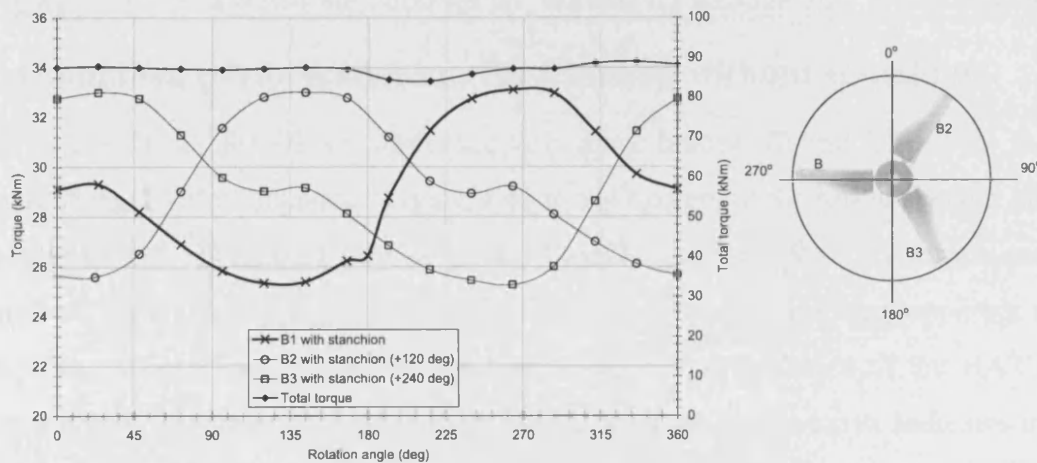


Figure 9.42: Torque variation for B1, B2 and B3 through 360° with stanchion

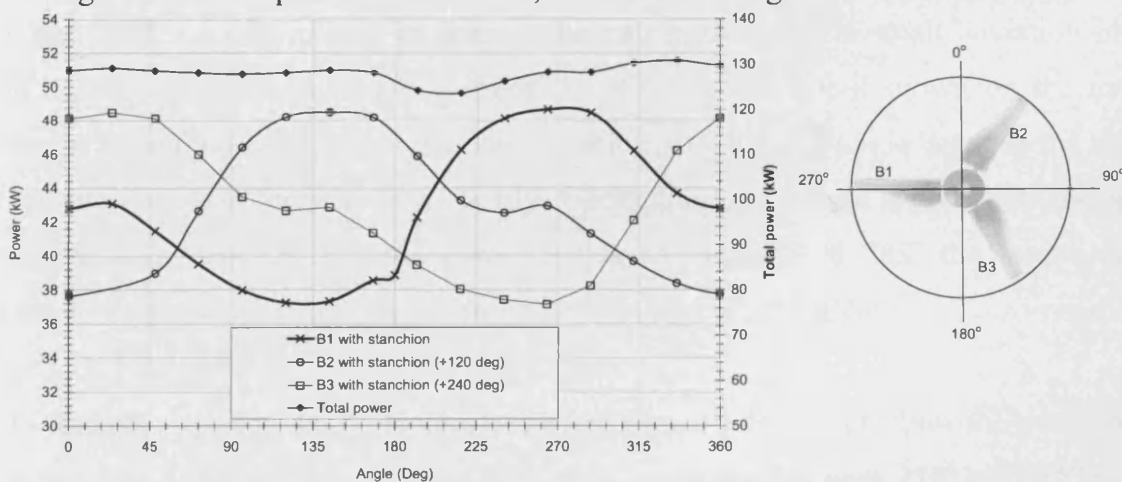


Figure 9.43: Power variation for B1, B2 and B3 through 360° with stanchion

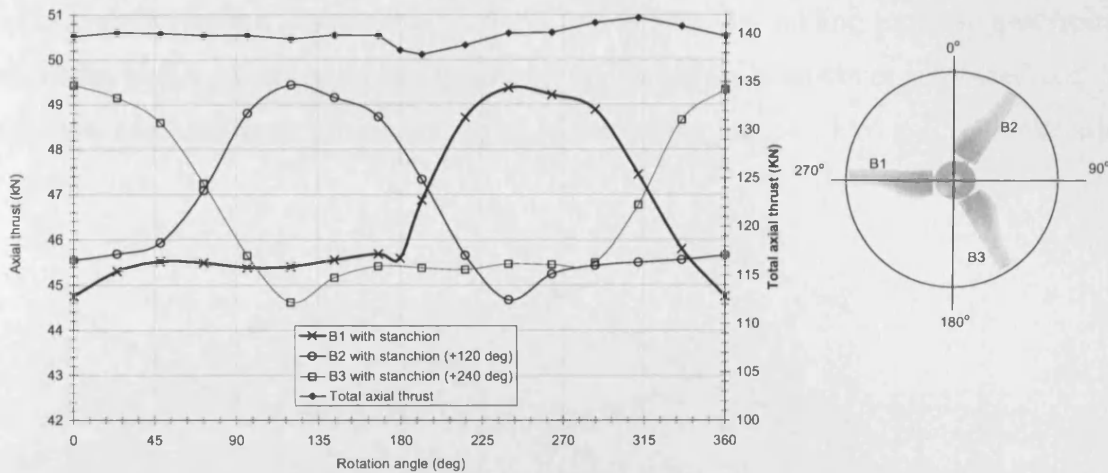


Figure 9.44: Axial thrust variation for B1, B2 and B3 through 360° with stanchion

9.3.4: Combined performance curves with and without stanchion

For clarity the curves for B1 are discussed only since blades B2 and B3 follow the same pattern 120° and 240° in advance. Figure 9.45 to 9.47 compare the torque, power and axial load curves for B1, B2 and B3 for Case.1 and Case.2. In Figure 9.45 the torque generated through 360° for B1 is highlighted for both Case.1 and Case.2. It is very apparent that the stanchion has a significant impact on the hydrodynamic performance of the HATT when the torque curves are compared. Moreover, the shape of the torque curve indicates the level of interaction between the stanchion and the HATT blades, most notably at rotation angles of 0° and 180°. As B1 passes in front of the stanchion at 180° a small deviation in the curve can be seen also annotated by point A. This feature is not shown on the torque curves for B2 and B3 because of insufficient resolution. The 120° angle between the blades and the angles chosen for each of the steady-state models this feature is essentially skipped. Within the last ¼ of the rotation cycle starting at an angle of 288° the torque curve decreases sharply toward a minimum at 360° and a value of 29.1 kNm.

These features are also seen in the power curves, Figure 9.46, which show the peak power extraction for Case.1 and Case.2, these once again, occurring between 270° and 315° with a minimum between 90° and 135°. For Case.2 the power extracted by B1 is reduced throughout the 360° rotation with a reduction in peak extraction to 486 kW from 523 kW in Case.1. The minimum power output from Case.1 is approximately 449 kW giving a power fluctuation of around 74 kW. With a minimum power extraction of 371 kW for Case.2 the

peak power fluctuation is increased by 54 % to 114 kW. By adding in the output from B2 and B3 the power fluctuation experienced by the generator is however smoothed out. The maximum and minimum power delivered to the motor are 145 kW and 144 kW with a 0.5% variance.

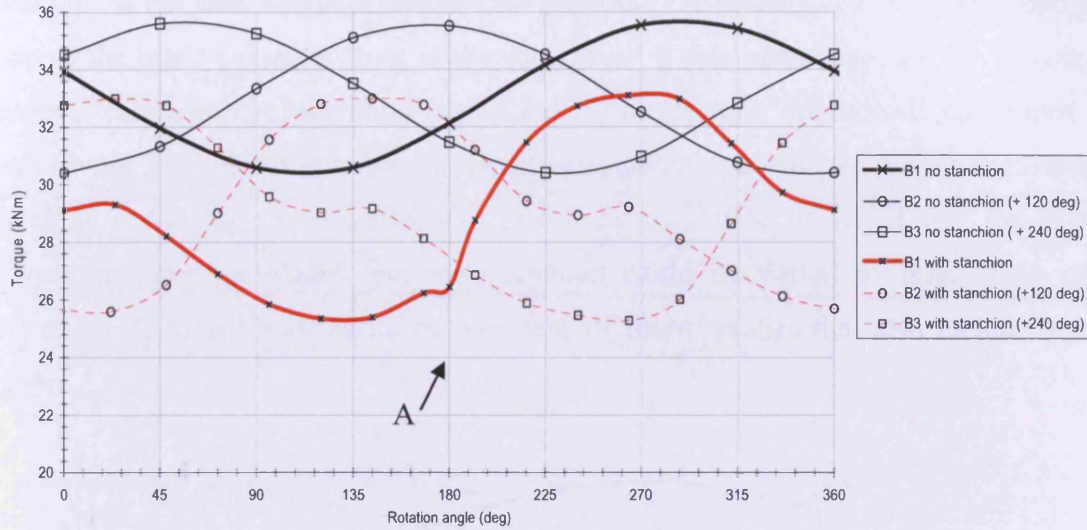


Figure 9.45: Combined torque variation for Case.1 and Case.2.

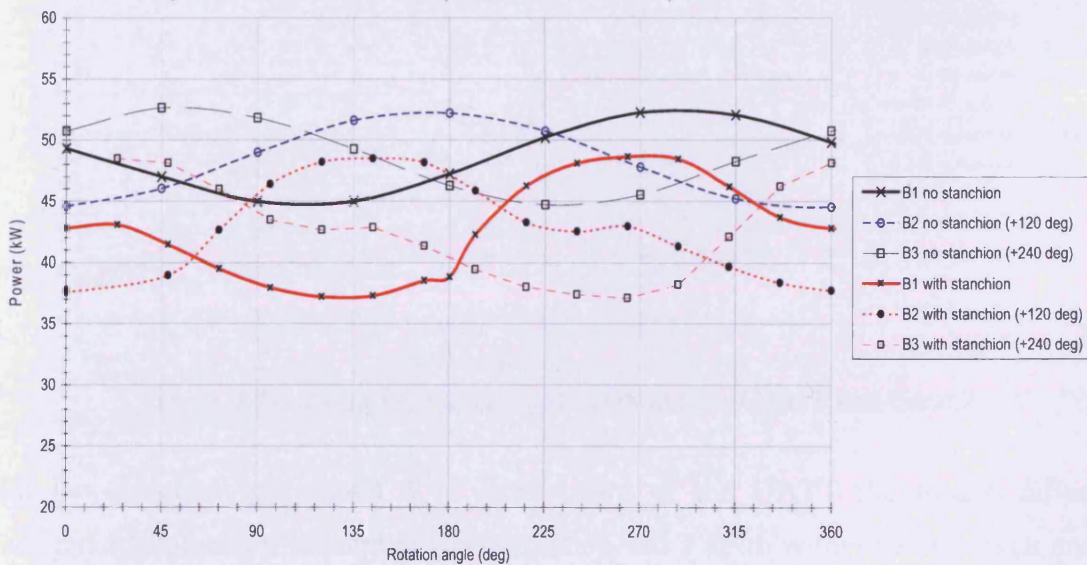


Figure 9.46: Combined power variation for Case.1 and Case.2

From Figure 9.47 it is clear then that the stanchion increases the difference between the maximum and minimum performance characteristics of the HATT increasing problems associated with cyclic power generation and axial thrust loading.

One interesting feature in the axial thrust curve with stanchion, Figure 9.47 is the relatively flat portion of the curve between 0° and 180° and the sudden rise again towards peak power extraction. The relatively flat portion coincides with the portion of the rotation cycle where the minimum flow velocity occurs, this is also true for the sudden rise to peak power extraction as the peak occurs between 216° and 188° . Following 188° the axial load drops again as the blade passes in front of the stanchion. If this phenomenon truly represents a physical feature of the operation of the HATT under such operational conditions then further work is required involving physical measurement as well as further mathematical modelling. Although not included in this study, it should be noted that the distance between the passing blades and the stanchion could be varied to limit some of the differences discussed and should be the focus of future studies that also include velocity profiles.

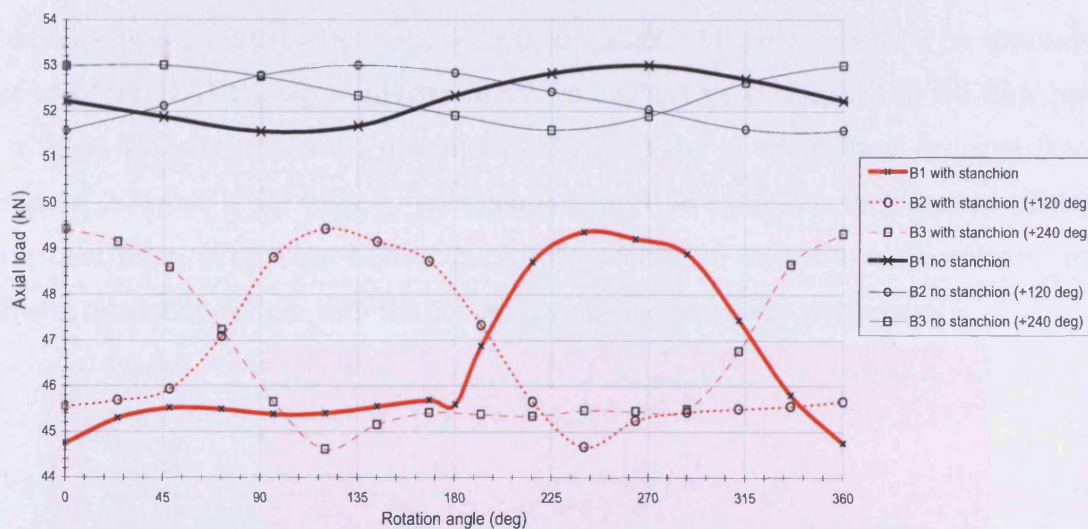


Figure 9.47: Combined axial load variation for Case.1 and Case.2

With the stanchion positioned 2 m downstream of the HATT the torque difference generated at peak and minimum power extraction was 5 kNm without a stanchion and 7.7 kNm with. The peak and minimum differential in power at the same points in the rotational cycle was 7.3 kW and 11 kW. Finally, the turbine axial thrust load differential was 1.4 kN without the stanchion and 4.6 kN with.

9.3.5: Contour plots of asymmetric flow

The asymmetry in the torque, power and axial thrust curves and in the pathlines can also be seen in the contour planes downstream and upstream of the HATT. Figure 9.48, a and b gives contour plots of velocity magnitude (m/s) at upstream locations 8 m, 6 m. Figure 9.49, a and b show the velocity profile at 1 m, and at 0.5 m downstream. Contour plots at 1 m and 0.5 m pass through the MRF. At 6 m and 8 m upstream the velocity profile through the depth again indicates that a peak power should occur for each turbine blade at a 0° rotation angle and a corresponding minimum at 180° . A slight shift however can be seen in the velocity profile contour lines at 8 m upstream, Figure 9.48 a. The approximate location of the HATT is illustrated by the circle. The contour lines here can be seen to rise towards a clockwise 45° rotation angle. At 6 m upstream the velocity contours can be seen to rotate further, the velocity magnitude through the Y-axis is now asymmetric with the lower velocity contours raising to the 45° rotation angle of Figure 9.48 b. The approximate location of the HATT is again illustrated by the circle. Due to the shift in the flow pattern the average velocity across the diameter of the HATT 6 m upstream is reduced from an average of 2.15 m/s at the velocity-inlet boundary to 1.84 m/s. This then greatly affects the power coefficient (C_p) when basing the power calculation on the average velocity of the profile at the defined depth with the potential to underestimate its performance.

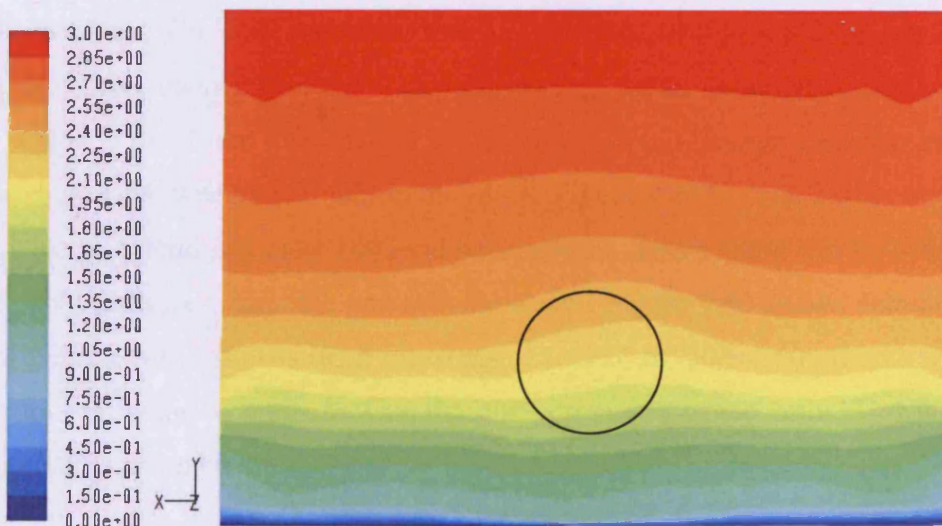
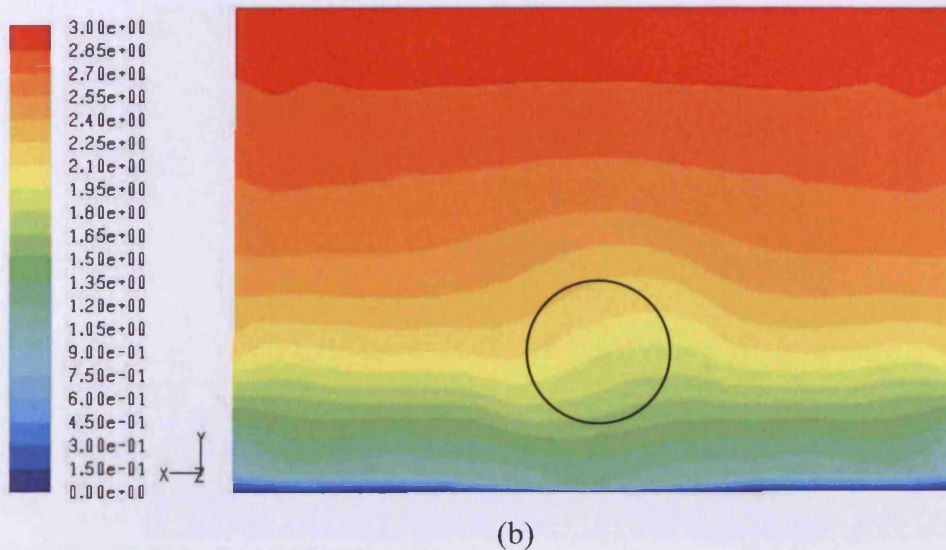


Figure 9.48 (a)



(b)
Figure 9.48: Contours coloured with velocity magnitude (m/s) at (a) 8 m and (b) 6 m upstream of the HATT

As the contour planes approach the turbine and the MRF the rotation in the contours can be seen to intensify with increasing asymmetry. At an upstream location of 1 m the contour plane coloured by velocity magnitude falls within the MRF and clearly shows a shift in the peak velocity toward the left hand side of the turbine within a rotation angle lying between 270° and 315° , Figure 9.49 a. If the velocity profile through the column depth is now compared with that of the horizontal x-axis, the averaged differences are 0.15 m/s and 0.45 m/s, respectively. The corresponding peak velocity magnitudes are 2.03 m/s at 0° and 2.2 m/s at -90° thus again indicating increased asymmetry in velocity magnitude within the MRF. Outside the direct influence of B1, B2 and B3 this feature can also be seen 0.5 m downstream of the turbine still within the MRF, Figure 9.49 b. The higher velocity profile can be seen to extend just after 180° and before 360° . This feature can be seen to extend a considerable distance within the downstream wake. Figure 9.50 shows velocity magnitude contour patterns for 5 downstream locations at 3m, 20 m, 50 m, 100m and 150 m. Using this contour progression it can be seen that the asymmetry of the velocity starts to decrease at around 20 m downstream.

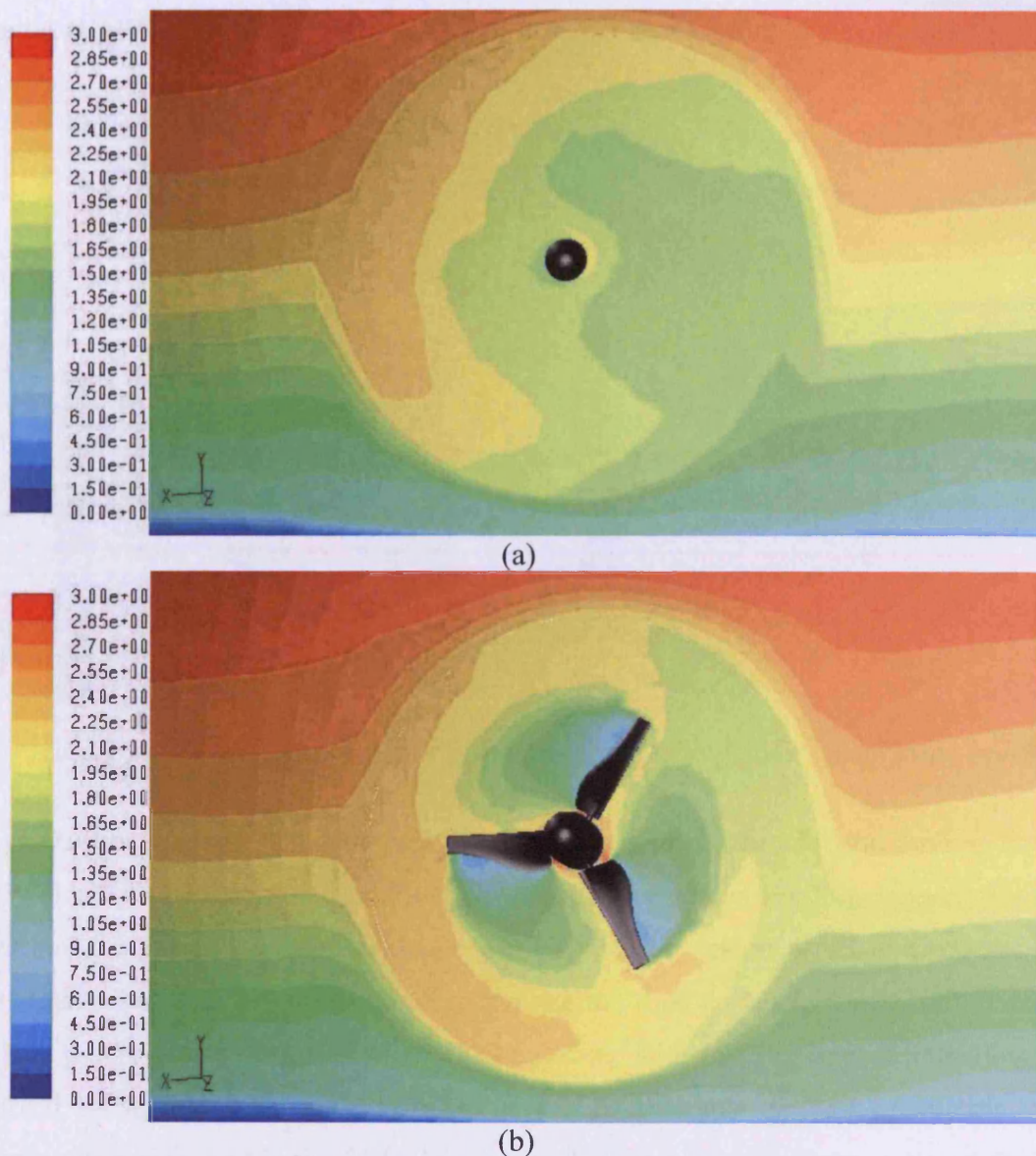


Figure 9.49: Contours coloured with velocity magnitude (m/s) at (a) 1 m upstream and (b) 0.5 m downstream of the HATT

As the wake moves downstream it also expands, the contours also show the rise in the wake downstream. The core of the vortex can also be seen to move upward and to the left of Figure 9.50, indicating that the wake has the potential not only to increase in height but to shift along the x-axis, in this case at around 100 m downstream. Given a flat seabed this indicates that the flow complexity of the wake can be increased when operated close to the seabed and within the lower flow boundaries. Given shipping restrictions this then has the

potential to eliminate large portions of the Severn Estuary from the placement of HATT arrays.

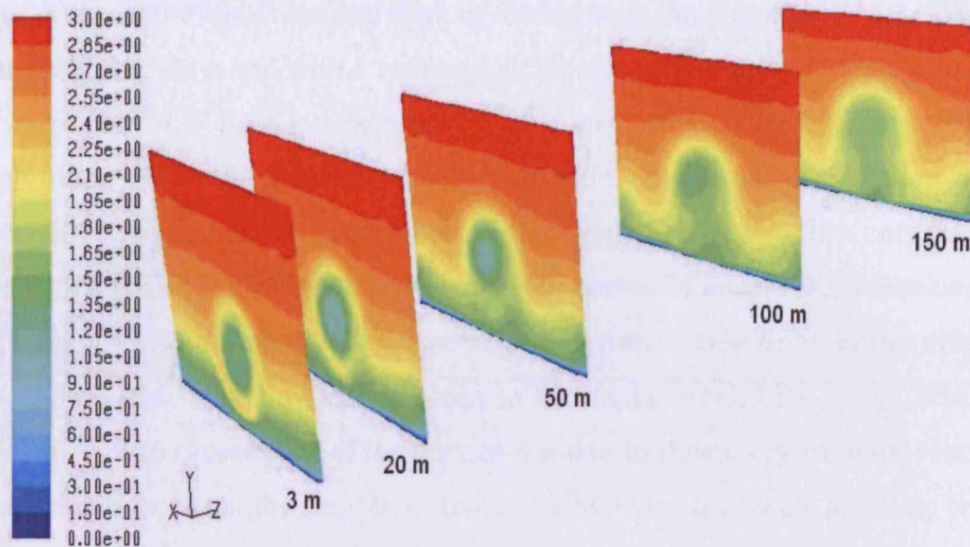


Figure 9.50: Downstream contour planes coloured with velocity magnitude (m/s)

It is interesting to note that although this scenario is unsuitable for the Severn Estuary, mainly due to a combination of relatively low surface velocities and high velocity shear the operation of a HATT in the latter may still be a viable option at other locations if the operational parameters are clearly understood and the final design is configured to account for them, such as the structure of the blades along with bearing and seal loading. As discussed in Section 2.3.6 there is potentially a considerable amount of energy flux at depths > 50 m even within the 25 % lower boundary that could be extracted and therefore should be part of future studies.

9.4: Example of possible asymmetric wake interaction for a modular array

The close proximity of HATTs to the seabed has the potential to introduce complexity to the wake, which may have a significant effect on neighbouring turbines. In a study by O'Doherty² et al, (2009) the axial thrust loading and possible wake interaction between turbines was studied for a modular frame using FLUENTTM. Although a constant velocity profile was assumed for the study, to simulate a worse case scenario for axial thrust loads,

the results give an indication to the potential problems faced if asymmetry in the wake is introduced via close proximity to the seabed and a high velocity shear. Figure 9.51 a and b show an iso contour of velocity magnitude (1.3 m/s) with flow entering the triangular horizontal frame at the apex base and apex of the frame as the direction of the tide changes. While under a plug flow and with a turbine rotational centre at approximately 50 % of the overall water depth (25 m) the wakes generated from turbines 1 to 5 show no interaction with each other. With the exception of the supporting frame this observation applies in both flow directions. This is largely due to the symmetry of the flow upstream of the structure which helps develop a stable downstream vortex. Figure 9.52 shows contours of velocity magnitude at the rotational centre of each turbine. Due to blockage effects from turbines 4, 3, 2 and 1 the flow can be seen to accelerate around the swept area of each turbine. This in turn causes each of the upstream wakes to flow away from the rear turbines while the velocity between the devices increases. If however the whole structure were to be position within the lower 25 % of the depth and a extreme velocity profile, some of the dynamics discussed in Sections 9.3.4 and 9.4.5 could potentially arise allowing the turbine wakes to interact due to horizontal and vertical asymmetry in the flow. However, if the magnitude of the wake asymmetry is known, better estimates on parameters such as lateral and horizontal spacing could be made. It is proposed that the work carried out in this thesis should be extended to include the array structure shown in Figures 9.51 and 9.52 in conjunction with the velocity profiles.

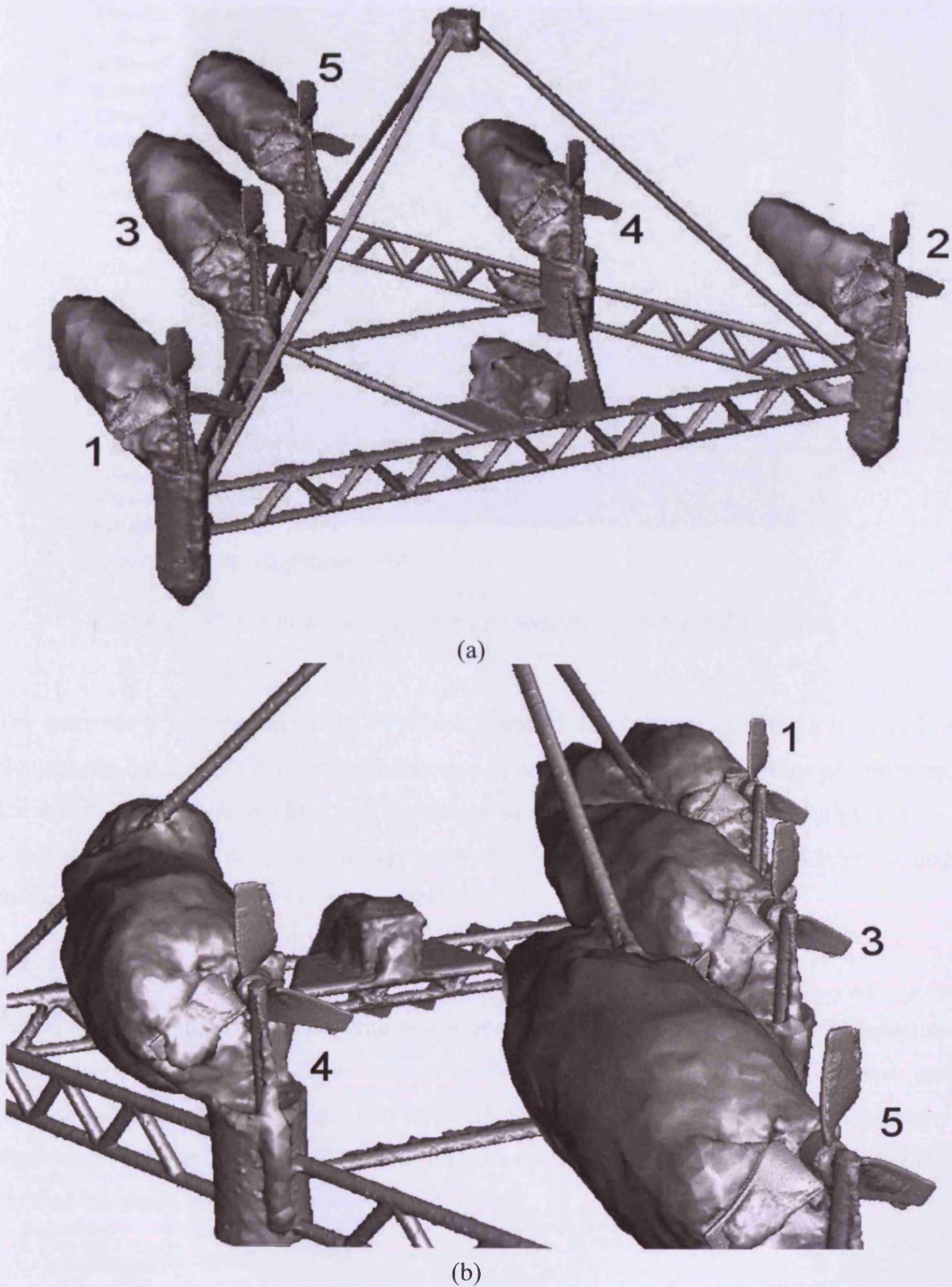
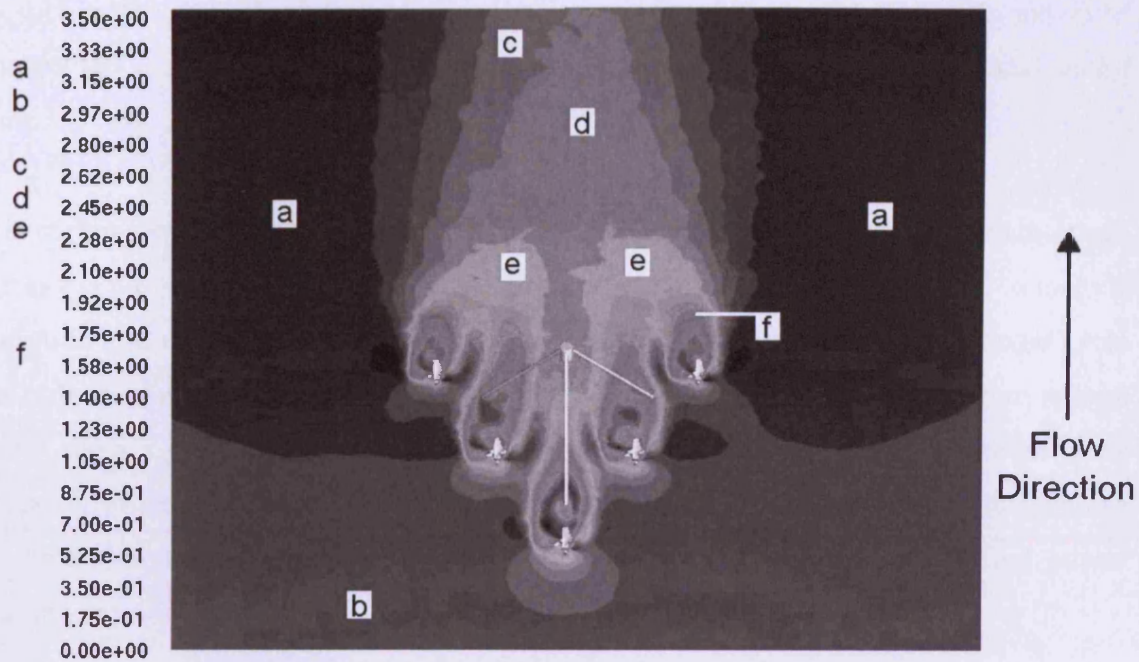


Figure 9.51: Iso contour (1.3 m/s) with flow entering at the apex frame base (a) and at the apex (b)

Source: O'Doherty et al, (2008)



Contours of velocity magnitude, / m/s

(c)

Figure 9.52: contours of velocity magnitude (m/s) entering frame apex.

Source: O'Doherty et al, (2008)

The complexity of operating a HATT in the lower 25 % of the water column is therefore challenging but given the potential resource at greater depths the possibility of operating turbines in such a harsh environment should not be ruled out. Indeed operating higher in the water also pose other problems such as reactive torque with free floating and large turning moments with seabed fixed tower arrangements.

9.5: Summary for power attenuation

This chapter as attempted to deal with power attenuation from turbine stanchion interaction and that imposed by water depth velocity profiles derived from the Severn Estuary and Anglesey Skeries. Although from two very different locations, these profiles showed many similarities, such as a high velocity shear towards the seabed, typically approaching the last 25 % of the depth, as stated by Brydon et al, (1998).

It was also shown that the potential exists for the downstream wake of the HATT to interact with the flow upstream when the HATT is positioned closer to the seabed under a profiled

flow such as that measured at the Seven Estuary and Anglesey sites. This was shown to influence the rotational angle at which peak torque, peak power and peak axial thrust occurs.

Power curves were also generated demonstrating the degree to which power attenuation can occur as the turbine is positioned lower in the water column. This was extended to include variation in turbine performance through a rotational cycle. By comparing a rotational cycle for a turbine operating in deep water with a plug flow and one operating within a high velocity shear a greater degree of complexity in the torque, power and axial thrust loads was shown to result. The complexity of these parameters was further shown to increase with the addition of a stanchion along with increased cyclic axial thrust load and power extraction amplitudes.

Finally, a practical example of how these complexities could influence the operation of a proposed modular frame was given. It was hypothesised that the symmetrical flow characteristics shown under plug flow and at mid depth could be compromised for the given turbine spacing both laterally and horizontally. This then implying that a greater possibility exists for the wake of an upstream HATT to impact the performance of those downstream, specifically in close proximity such as the array design proposed here.

10: Conclusions and recommendations

10.1: Conclusions

- The performance characteristics of the prototype turbine were measured in a recirculating water flume at the University of Liverpool and are presented in Chapter 6. Limitations in the data were discussed, particularly the angular velocity. It was proposed, that the close proximity of the turbine to the support stanchion induced pulsing with the passing of each blade (section 6.1). However, due to the sample rate of 1.2 Hz (Section 7.4.1), it was not possible to confirm this hypothesis with the current data set. Linear regression was then applied to the averaged angular velocity from the 6 tests that was then used to validate the CFD performance data.
- By comparing torque and power curves from the flume tests, Chapter 6, with the CFD models discussed in Chapter 7, it was shown that the hydrodynamic performance of the HATT could be predicted with reasonable accuracy using a lower order discretisation scheme and the RSM viscous model, with y^+ values in region of 300 to 500. The wake and axial thrust characteristic were not validated during the flume tests and therefore relied on comparisons with similar studies in literature. Chapter 7, Section 7.2.3 presented the argument that the turbulent length scales vary between the near and far wake, indicating that the relationship between the turbulence dissipation and turbulence intensity, as they progress downstream, are key factors to predicting wake deficit attenuation.
- To assess the economic performance of the prototype HATT under estuarine and or oceanic conditions, it was necessary to scale the 0.5 m diameter prototype turbine. The prototype HATT's performance characteristics were non-dimensionalised from the flume measurements and CFD models and are presented in Chapter 8. As a result of local shipping restrictions and the local water depth of approximately 35 m, a HATT diameter of 10 m was selected. While using a plug flow ($V = 3.08$ m/s), it was shown in Section 8.2.1 that all the non-dimensional performance characteristics collapsed onto a single curve. This was also true for the characteristics resulting from a profiled flow (Section 8.2.2). It was shown that the latter only occurred if

the average velocity was calculated using the volumetric flow rate across the turbine's swept area. The collapse of the non-dimensional performance curves indicate that the scaling of an HATT is independent of the Reynolds number.

- Section 8.2.5 show the non-dimensionalised data obtained from the flume tests, these data have a reasonable correlation with the CFD reference and flume model curves, and therefore also confirming independence from Reynolds number. A change in the turbine geometry including the blade pitch angle does, however, result in a new set of non-dimensionalised characteristic curves, as discussed in Section 8.2.4.
- From Chapter 6, Section 6.3.3, the ADCP study showed that local velocity profiles can vary considerably from that typically calculated using the $1/7^{\text{th}}$ power law. The magnitude of the performance characteristics can also be significantly affected by the depth of the water column, i.e. where the turbine diameter can occupy a large percentage of the flow profile.
- It was found that the peak power extracted under plug flow was circa 470 kW for both reference and site CFD models. However, with the velocity profile scaled, to have the peak velocity equal to the plug flow value, the power extracted was shown to reduce to 142 kW for the Severn Estuary and 190 kW for the Anglesey site. A considerable reduction in power extraction from what could be classified as an initial estimate of the sites resource.
- In Chapter 9 the scaled 10 m diameter turbine was placed in a high velocity shear environment, where the Severn Estuary velocity profile was applied to a depth of 35 m. The cyclic power extraction (without a stanchion) of each blade was discussed in Section 9.3.2. It was shown that the trend of the cyclic torque, power and axial thrust curves were similar to those presented in literature. However, it was shown that the point of peak power extraction, through a rotational cycle, was advanced from TDC. It was shown in Sections 9.3.2 and 9.3.3 that the downstream wake asymmetry influenced the upstream flow field, resulting in a rotation. With the addition of a stanchion (Section 9.3.3), the amplitudes of the peak torque, power and axial thrust was shown to increase although at lower average values.
- Chapter 9 shows that with the use of quasi-static lower order models, the high

velocity shear was shown to increase the HATT's interaction with the ocean seabed, via the downstream wake. The asymmetry of the wake was shown to affect the hydrodynamic power extraction and axial thrust via upstream rotation in the main flow field. These latter operational features are of prime importance if the lower 25 % of the water column is to be considered.

10.2: Specific Observations

- As with the furling of wind turbines, as the blade pitch angle was increased the leading edge of the blade was aligned with the upstream flow field, thereby reducing the blade's effective blockage and the hydrodynamic efficiency of the turbine. Figures 4.15 and 8.25 and 8.29 show that larger blade pitch angles can reduce the axial thrust and length of the downstream wake, respectively. The reduction in axial thrust was accompanied by a minimal reduction in the power extraction coefficient. The lowest axial thrust and wake deficit was achieved with a blade pitch of 12°
- The Anglesey site was shown to meet the economically viable velocity of 2-3 m/s. It also showed a similar trend to the Severn Estuary site with regards to power attenuation with depth. Specifically if subject to the same depth restrictions as the Severn site. The hydrographic and hydrodynamic high resolution SWATH bathymetric survey and a vessel-mounted ADCP surveys produced excellent data to investigate the feasibility of installing a HATT in the inner Bristol Channel and the Anglesey Skerries. The bathymetric survey provided accurate and detailed bathymetry of the sites, thus allowing the identification of a potential location to site a HATT.
- Resource estimates based on near surface velocity measurements typically at surface or at most 1 m to 3 m below the water surface overestimate the local energy flux. Given the results of the Severn Estuary and Anglesey Skerries surveys the actual near surface velocities of 1.8 m/s and 2.14 m/s, respectively reduce to 1.62 m/s and 1.96 m/s at mid depth. If shipping requirements are imposed to the same level as required for the Severn Estuary site these velocities are further reduced to 1.31 m/s and 1.88 m/s for the Severn and for Anglesey site, respectively. These

latter velocities are very close to the lower tidal velocity for economic power extraction.

- For a true representation of turbine performance the tidal velocity should be monitored between 2 and 5 turbine diameters upstream of the HATT and at the depth of its rotation axis. It was shown that by using the peak upstream near surface tidal velocity (3.1 m/s) C_p was reduced to 0.12. However, if the average flow velocity across the turbine diameter is used $C_p = 0.34$. This clearly illustrates the need to clarify the operational boundaries to which the HATT is matched and how its performance is monitored during operation.

10.3: Recommendations and future work

- To mitigate problems associated with the coupling between the 0.5 m diameter prototype HATT and the servomotor, it would be desirable to develop a water-tight container to house the servomotor, thereby allowing a direct connection below the water surface during testing.
- An alternative to a seabed mounted turbine is a free floating tethered system using counter rotating turbines (Clarke et al, 2008). A series of counter rotating steady-state CFD models could be developed with varying axial spacing. This would generate useful comparative data.
- Modelling the life expectancy for both singular and array based turbines, using Fixed-Space is not practical therefore coupled Fluid-Structural-Interfaces FSI are required. Although Fixed-Space fluid modelling of a HATT captures hydrodynamic interactions, it neglects the impact of blade deformation; subsequent loses in efficiency and a potential increase in component mean stress levels. Therefore FSI could be used to model a turbine aligned symmetrically and asymmetrically with the tidal flow. Blade deformation and its effects on power prediction and downstream wake recovery could be studied with variation in blade stiffness.
- A temporal study of blade loading should be included in any future work that considers blade structure interaction.

- In order to ascertain the HATT CFD model's ability to accurately predict the downstream wake, longitudinal, perpendicular and lateral measurements of its velocity and turbulence intensities are required.
- A temporal study should also be undertaken on the rotation of the blade and their interaction with a stanchion. This would generate useful data for comparison and validation of the steady-state data generated for this thesis.
- Finally, to ascertain whether or not the steep velocity attenuation reported in this study is typical of other locations further ADCP measurements are required in higher local tidal flows. The quasi-static approach used in this thesis should be extended to include a temporal study of the resulting asymmetric wake formation and phase shift in peak power extraction.

References

Abuelsamid, S., (2007). 1.2 MW Tidal Turbine to be installed off Northern Ireland. Autobloggreen. <http://www.autobloggreen.com/2007/06/16/1-2-mw-tidal-turbine-to-be-installed-off-northern-ireland/> [12 April 2009]

ABP mer (npower juice). Quantification of exploitable tidal energy resources in UK waters. Vol. 1: Main text and appendices. Project ref: R/3671/4. Report No: R.1349. July (2007)

Althaus, D., Wortmann, F.X., Stuttgarter Profilkatalog I. (Stuttgart Profile Catalog I.) Friedr. Vieweg & Sohn (Braunschweig), 1981.

Anderson, K., Bows, A., A response to the Draft Climate Change Bill's carbon reduction targets. Tyndall Briefing Note 17. March 2007.
http://www.tyndall.ac.uk/publications/briefing_notes/bn17.pdf [January 2009]

Arnott, S., (2008) The Independent, Business. Winds of change: A beacon of optimism
<http://www.independent.co.uk/news/business/analysis-and-features/winds-of-change-a-beacon-of-optimism-968693.html> [15th April 2009]

Ashton, T. S., The Industrial Revolution, 1760-1830. London, 196. (1998)

Atwater, J.F., Lawrence, G.A., Limitations on tidal power generation in a channel. Proc. World Renewable Energy Congress (WRECX). pp. 947-952. (2008).

Auld, T., (TAuld@abports.co.uk) 2008. Vessel draft. 20th March. Email to: Paul Evans, School of Earth, Ocean and Planetary Sciences, Cardiff University.

Black and Veatch. Tidal Stream Energy Resource and Technology Summary Report. Carbon Trust. (2005).

Black and Veatch. Phase II, UK Tidal stream energy resource assessment. Marine energy challenge. Carbon Trust. (2004)

Bahaj, A.S., Batten, W.M.J., McCann. G., Experimental verification of numerical predictions for the hydrodynamic performance of horizontal axis marine current turbines. Renewable Energy 32 (2007). pp. 2479-2490.

Bahaj, A.S., Myers, L.E., Analytical estimates of the energy yield potential from the Alderney Race (Channel Islands) using marine current energy converters. Renewable Energy 29 (2004). pp.1931-1945.

Bahaj, A.S., Myers, L.E. Fundamentals applicable to the utilisation of marine current turbines for energy production. Renewable Energy 28 (2003). pp. 2205-2211.

References

- Bahaj, A.S., Molland, A.F., Chaplin, J.R., Batten, W.M.J.**, Power and thrust measurements of marine current turbines under various hydrodynamic flow conditions in a cavitation tunnel and a towing tank. *Renewable Energy* 32 (2007) 407-426.
- Baker, C., Walbancke, J., Leach, P.**, Tidal Lagoon Power Generation Scheme in Swansea Bay. A report on behalf of the Department of Trade and Industry and the Welsh Development Agency. AEA Technology Contract numbers: 14709570 and 14709574. URN number: 06/1051. (2006)
- Baldor motion products.** MintMT Help files. Version 2005-02 ©Baldor 2005
- Barltrop, N., Varyani, K.S., Grant, A., Clelland, D., Pham, X.** Wave-current interactions in marine current turbines. *Proc. IMechE Vol. 220 Part M: J. Engineering for the Maritime Environment* (2006).
- Batten, W.M.J., Bahaj, A.S., Molland, A.F., Chaplin, J.R.**, The prediction of the hydrodynamic performance of marine current turbines. *Renewable Energy* 33 (2008). pp. 1085-1096.
- Bedard, R., Previsic, M., Polagye, B. Casavant, A.**, North America Tidal In-Stream Energy Conversion Technology Feasibility Study. Electrical Power Research – Institute (EPRI). EPRI TP-0080NA (June 2006)
- BERR.** The Energy Challenge, Energy review report, DTI. (2006).
<http://www.berr.gov.uk/files/file31890.pdf> [10 January 2009]
- BERR¹** (Department for Business Enterprise and Regulatory Reform). Atlas of Marine Renewable Energy Resources: Atlas Pages, A Strategic Environmental Assessment Report. ABPmer The Met Office, Proudman Oceanographic Laboratory. March 2008.
- BERR².** **UK renewable Energy Strategy, Consultation**, Department for Business Enterprise and Regulatory Reform. The UK Renewable Energy Strategy Consultation – full document. (2008).
http://www.decc.gov.uk/en/content/cms/consultations/cons_res/cons_res.aspx
[23 July 2009]
- BERR³** (Department for Business Enterprise and Regulatory Reform). Meeting the energy challenge. A white paper on nuclear power January 2008.
<http://www.berr.gov.uk/files/file43006.pdf> [20th October 2008]
- Betz, A.**, Introduction to the Theory of Flow *Machines*. (D. G. Randall, Trans.) Oxford: Pergamon Press. (1966)
- BWEA (British Wind Energy Association).** UKWED (UK Wind Energy Database) data base for wind energy projects in the UK. www.BWEA.com/UKWED/index.asp
[05 December 09]

References

Blue Energy Technology, Blue Energy International Inc #204, 2060 Comox Street, Vancouver, BC V6G 1R8. Canada. <http://www.bluenergy.com/technology.html> [25 November 08]

Blunden, L.S., Bahaj, A.S. Flow through large arrays of tidal energy converters: is there an analogy with depth limited flow through vegetation? Proc. World Renewable Energy Congress (WRECX). pp. 1091-1096. (2008).

Blunden, L.S., Bahaj, A.S. Initial evaluation of tidal stream energy resources at Portland Bill, UK. *Renewable Energy* 31 (2006) 121-132.

Boud, R., Graham, S., Savage, A., Watt, T., Donohew, A., Tait, L., Final Report, Tidal Technologies Overview. Contract 2. Sustainable Development Commission. Entec UK Limited. May 2007.

Bows, A., Calverley, D., Broderick, J., Anderson, K., 2009. Making a climate commitment: Analysis of the first report (2008) of the UK committee on climate change. Tyndall Centre for climate change research. A research report by the Tyndall Centre, University of Manchester.
http://www.tyndall.ac.uk/publications/Tyndall_Review_of_CCC_Report.pdf
[4th October 2008]

Bradshaw, P., (1971). An introduction to turbulence and its measurement. Elsevier. ISBN-10: 0080166210. ISBN-13: 978-0080166216

Bryden, I.G., Naik, S., Fraenkel, P., Bullen, C.R., Matching tidal current plants to local flow conditions. *Energy* Vol. 23, No. 9, pp. 699-709, 1998.

Bryden, I.G., Couch, S.J., How much energy can be extracted from moving water with a free surface: A question of importance in the field of tidal current energy? *Renewable Energy* 32 (2007) 1961-1966.

Bryden, I.G., Couch, S.J., ME1- marine energy extraction: tidal resource analysis. *Renewable Energy* 31 (2006) 133-139.

Bryden, I.G., Macfarlane, D.M., The utilisation of short term energy storage with tidal current generation systems. *Energy* 25 (2000). pp. 893-907.

Burton, T., Sharpe, D., Jenkins, N., Bossanyi, E., (2001). Wind energy: handbook. John Wiley and Sons. ISBN 0471489972, 9780471489979

CBC News., Kyoto and beyond., 2007. <http://www.cbc.ca/news/background/kyoto/#s5>
[January 2009]

Carbon Trust. Tidal stream and tidal stream energy device design. Website URL: http://www.carbontrust.co.uk/technology/technologyaccelerator/ME_guide3.htm
[December 2009]

References

- Carbon Trust.** United Kingdom Wave and Tidal Energy Study. Variability of UK marine resources. Final Report. 2005
- Carbon Trust,** Future Marine Energy. Results of the Marine Energy Challenge: Cost competitiveness and growth of wave and tidal stream energy. 20 January 2006.
- Carlton, J.,** (2007), Marine Propellers and Propulsion. Butterworth-Heinemann, ISBN 0750681500, 9780750681506
- Chaney, K., Eggers, A.J.,** Expanding wake induction effects on thrust distribution on a rotor disc. *Wind Energy*, (2001)(5): pp 213-226.
- Charhate, S.B., Deo, M.C., Kumar, V.S.,** Soft and hard computing approaches for real-time prediction of currents in a tide-dominated coastal area. *Proc. IMechE Vol. 221 Part M: J. Engineering for the Marine Environment*. pp. 147-165. (2007)
- Charlier, R.H.,** A “sleeping” awakes: tidal current power. *Renewable and Sustainable Energy Reviews*. 7 (2003) 515-529.
- Clarke, J., Connor, G., Grant, A., Johnstone, C., Ordonez-Sanchez, S.,** Contra-rotating marine current turbines: performance in field trials and power train developments. *World Renewable Energy Congress (WRECX)*. pp.1049-1054. (2008).
- Clarke, J.A., Conner, G., Grant, A.D., Johnstone, C.M., Mackenzie, D.,** Development of a contra-rotating tidal current turbine and analysis of performance. 7th European Wave and Tidal Energy Conference. Porto, Portugal, September, (2007)
- Clarke, J.A., Connor, G., Grant, A.D., Johnstone, C.M., Mackenzie, D.,** Design and initial testing of a contra-rotating tidal current turbine, *Proc. World Renewable Energy Congress*, Florence, 19 -25 Aug. (2006)
- Collinson, S.,** Obama to world: We will lead on climate change. AFP Online news. http://uk.news.yahoo.com/18/20090126/tpl-obama-to-world-we-will-lead-on-climate-10170b4_2.html [January 2009]
- Connel, J.R., George, R.L.,** The wake of the MOD-0A1 wind turbine at two rotor diameters downwind on 3 December 1981, Report no. PNL-4210, Pacific Northwest Laboratory, Battelle, U.S, (1982)
- CCC (Committee on Climate Change).** Building a low-Carbon economy – the UK’s contribution to tackling climate change. Chapter 5: Decarbonising electricity generation. (2008).
<http://www.theccc.org.uk/pdf/7980-TSO%20Book%20Chap%205.pdf> [27 April 2009]

References

- Cotrell, J.**, The mechanical design, analysis and testing of a two-bladed wind turbine hub. National Renewable Energy Laboratory. Technical report. NREL/TP-500-26645. (2002). <http://www.nrel.gov/docs/fy02osti/26645.pdf> [6 April 2009]
- Couch, S.J., Bryden, I.**, Tidal current energy extraction: hydrodynamic resource characteristics. Proc. IMechE Vol. 220 Part M:J. Engineering for the Maritime Environment (2006).
- Defra.**, Key Facts about: Supplementary Information. Electricity generation by renewable sources: (1996) and (2006). (2008). <http://www.defra.gov.uk/environment/statistics/supp/spkf19.htm> [January 2009]
- Douglas, C.A., Harrison, G.P., Chick, J.P.**, Life cycle assessment of the Seagen marine current turbine. Proc. IMechE Vol. 222 Part M: J. Engineering for the Maritime Environment (2007).
- Douglas, J.F., Gasiorek, J.M., Swaffield, J.A., Lynne, B.J.**, Fluid Mechanics. Fifth edition, Harlow, England. Pearson, (2005). ISBN 13:978-0-13-129293-2
- DTI**, The potential for the use of marine current energy in Northern Ireland, Department of Trade and Industry; Department of Enterprise, Trade and Investment; and Northern Ireland Electricity.(2003). <http://www.detini.gov.uk/cgibin/moreutil?utilid=41&site=5&util=2&fold=&.2005-08-29>
- DTI, Sustainable Energy Programme.** Tidal turbine installation at fixed navigation marks. ETSU T/05/00214/REP. DTI/Pub URN 01/1516 (2001) <http://www.berr.gov.uk/files/file18031.pdf>
- DTI¹**, SEAFLOW Marine Current Turbine. Project Summary No. PS244. 2006
- DTI²**. Final report on preliminary works associated with 1MW tidal turbine. Project Reference T/06/00233/00/00. URN 06/2046. (2006)
- DTI³**. Tidal Lagoon Power Generation Scheme in Swansea Bay. A report on behalf of the Department of Trade and Industry and the Welsh Development Agency. AEA Technology Contract No: 14709570 and 14709574. URN No. 06/1051. (2006)
- DTI**, Economic viability of a simple tidal stream energy capture device. DTI project No. TP/3/ERG/6/1/15527/REP URN 07/575. (2007)
- Egarr, D.A., O'Doherty, T., Morris, S., Ayre, R.G.**, Feasibility study using Computational Fluid Dynamics for the use of a turbine for extracting energy from the tide. Proc. 15th Australasian Fluid Mechanics Conference. The University of Sydney, Sydney, Australia. 13th-17th December (2004).

References

- Edwards, R.**, (2007). UK backs new generation of nuclear reactors. NewScientist. <http://www.newscientist.com/article/dn11913-uk-backs-new-generation-of-nuclear-reactors.html> [15th April 2009]
- Egarr, D.A., O'Doherty, T, Morris, S, Bacon, P.**, Experimental and computational study of tidal turbines as a renewable energy source, Proceedings of the Institution of Mechanical Engineers, Part A, Journal of Power and Energy (2005) (submitted)
- EIA (Energy Information Administration).** International Energy Outlook. Chapter 1 – World Energy Demand and Economic Outlook. Report #:DOE/EIA-0484. (2008) <http://www.eia.doe.gov/oiaf/ieo/world.html> [3rd May 2009]
- EIA (Energy Information Administration).** International Energy Outlook 2008, Report #: DOE/EIA-0484 (2008)
- Environmental Audit Committee.** (2007). Government targets in climate change bill need to be toughened. Lessons of Stern Review have still to be learned. (http://www.parliament.uk/parliamentary_committees/environmental_audit_committee/eac_19_03_07.cfm). [January 2009]
- ETSU (Energy Technology Support Unit).** The Severn Barrage project-detailed report, 5 volumes, ETSU TID 4060. Technology Support Unit, UK Department of Energy, Abingdon, UK. (1990).
- Encyclopaedia Britannica, USA,** (1965). Ocean - Density and Pressure. <http://hypertextbook.com/facts/2002/EdwardLaValley.shtml> [Accessed: 17 April 08]
- Fabrice, M., Grégory, P., Grégory, G., Elie, R.**, Numerical simulation of the wake of marine current turbines with particle methods. Proc.World Renewable Energy Congress (WREC) (2008). pp 1055-1060
- Friends of the Earth.** 2004. A Severn barrage or tidal lagoons? A comparison. http://www.foe.co.uk/resource/briefings/severn_barrage_lagoons.pdf [21st October 2008]
- Fluent Inc.**, Fluent documentation, (2006)
- Fluent Inc.**, Introductory Fluent Notes. FLUENT v6.2. (2005)
- Fraenkel P. L.**, Marine Current Turbines: An emerging technology, Hydraulic aspects of renewable energy, 16th Annual Seminar, Scottish Hydraulics Study Group, Glasgow, March (2004)
- Francis, M., Hamilton, M.**, SRTT floating tidal turbine production design study with independent verification. BERR, Contract number: T/06/00245/00/REP URN: 07/1463. (2007). <http://www.berr.gov.uk/files/file41865.pdf> [8th February 09]

References

Fujita Research., Wave and Tidal power, Web version updated July (2000), www.fujitaresearch.com/reports/tidalpower.html, [5 March 2004]

Greenpeace UK. (2009). Nuclear power. <http://www.greenpeace.org.uk/nuclear> [April 15th 2009]

Gupta, A.K., Lilley, D.G., (1985). Flow field modelling and diagnostics, Energy and Engineering Science Series, Abacus Press.

Hagerman, G., Fader, G., Bedard, R., New Brunswick tidal in-stream energy conversion (TISEC): Survey and characterisation of potential project sites. EPRI North American tidal flow power feasibility demonstration project. EPRI TP-003 NB Rev 1 (October 2006)

Hagerman², G., Polagye, B., Bedard, R., Previsic, M., EPRI., REV 2 DRAFT., Methodology for estimating tidal current energy resources and power production by Tidal In-Stream Energy Conversion (TISEC) devices. EPRI-TP-001 NA Rev 2. (2006)

Hallback, M., Johansson, A.V., Modeling of pressure-strain rate in homogeneous turbulence. Applied Science Research 51: pp. 495-499. (1993)

Hansen, M.O.L., Aerodynamics of wind turbines : Rotors, loads and structure. (2001), London; James & James (Science publishers) Ltd. ISBN 1902916069

Hardisky, J., Power intermittency, redundancy and tidal phasing around the United Kingdom. The Geographic journal, Vol. 174, No. 1, (2008). pp. 76-84

Harrison. P., EU warns climate may need bolder action. REUTERS. <http://uk.news.yahoo.com/22/20090128/twl-uk-eu-climate-bd5ae06.html> [January 2009]

Hau, E., (2006), Wind turbines: fundamentals, technologies, application, economics. Edition 2. ISBN .3540242406, 9783540242406

Hinze, J.O., (1987), Turbulence, McGraw-Hill

Holman, J.P., (2001). Experimental methods for engineers. McGraw-Hill. ISBN 978-0-07-118165-5

House of Lords. (2008). The EU's target for renewable energy: 20% by 2020. Volume I: Report. 27th report of session 2007-08. Pub. House of Lords. <http://www.publications.parliament.uk/pa/ld200708/ldselect/ldeucom/175/175.pdf> [10th October 2008]

Ingram, G., (2005). Wind turbine blade analysis using the blade element momentum method. School of Engineering, Durham University. http://www.dur.ac.uk/g.l.ingram/download/wind_turbine_design.pdf [August 2007]

References

- Jackson, I., Jackson, S.**, Siting new nuclear power stations: available and option for government, Discussion paper for DTI expert group. Final Paper. 26th April (2006).
- Jones, W.P., Launder, B.E.**, (1972). The prediction of laminarization with a two-equation model of turbulence , international Journal Heat and Mass Transfer, vol. 15, pp 301-314
- Jha, A.**, (2008). Second generation tidal turbines promise cheaper power. The Guardian. <http://www.guardian.co.uk/environment/2008/sep/04/waveandtidalpower.renewableenergy> [4 March 2009]
- Jo, C.H.**, Recent development of ocean energy in Korea. Proc. World Renewable Energy Congress (WRECX). pp. 911-916. (2008).
- Kerr, D.**, Marine energy. Philosophical Transcripts of the Royal Society A. 365, pp 971-992. (2006).
- Kirkup, L.**, (1994). Experimental methods. An introduction to the analysis and presentation of data. Wiley Ltd. ISBN 978-0-471-33579-5.
- Kleinbaum, D.G., Kupper, L.L., Muller, E.**, (1988). Applied regression analysis and other multivariable methods. Duxbury press Belmont, California. ISBN 0-87150-123-6.
- Kostaschuk, R., Best, J., Villard, P., Peakall, J. and Franklin, M.**, (2005) 'Measuring flow velocity and sediment transport with an acoustic Doppler current profiler' Geomorphology, 68 (1-2), pp. 25–37
- Kumar, S.**, (2008). THWAT: Next generation underwater turbines from Oxford. <http://www.ecofriend.org/entry/eco-energy-thwat-next-generation-underwater-turbines-from-oxford/> [4 March 2009]
- Launder, B.E.**, Second-moment closure and its use in modelling turbulent industrial flows. International Journal for Numerical Methods in Fluids Volume 9, Issue 8, pp 963 – 985, (2005)
- Leishman, J.G.**, (2006). Principles of helicopter aerodynamics. Cambridge University Press. ISBN 0521858607, 9780521858601
- MacLeod, A.J., Barnes, S., Rados, K.G., Bryden, I.G.**, Wake effects in tidal current turbine farms. Proceedings of the International Conference on Marine Renewable Energy, pp. 49-53, (2002).
- Maitre, T., Guittet, L., Achard, J-L., Ploesteanu, C.**, Marine turbine development: Numerical and experimental investigations. Transactions on Mechanics, Fascicola 2, (2005)

References

- Marine Currents**, EU JOULE contract JOU2-CT94-0355, Technomare SpA, IT Power, (1996).
- Maslin, M.**, Global Warming: A Very Short Introduction. Oxford University Press. (2004)
- Mason-Jones¹, A., O'Doherty, T., O'Doherty, D.M., Evans, P., Wooldrigde, C.F.**, Charaterisation of a HATT using CFD and ADCP site data. Proceedings of World Renewable Energy Congress (WREC), Glasgow (Sayigh, A., (ed)). (2008), pp. 941-946
- Mason-Jones², A., Evans, P., Wooldridge, C.E., O'Doherty, D.M., O'Doherty, T., Fryett, I.**, The use of ADCP data from the Inner Bristol Channel, UK and CFD to study power attenuation effects on HATT performance. Proceedings the 16th European-Based Biennial Conference of the International Federation of Hydrographic Societies (Hydro 8), Liverpool (Etkinson, H, (ed)), (2008)
- Massey, B.S.**, (1989). Mechanics of Fluids, 6th ed. Chapman and Hall, London. ISBN 0-412-34280-4
- Masters, I., Chapman, J., Orme, J.**, A three dimensional tidal stream turbine hydrodynamic performance model. Proceedings of the World Renewable Energy Congress (WRECX). pp. 923-928. (2008).
- McCombes, T., Grant, A., Johnstone, C.**, Unsteady hydrodynamic modelling of rotor systems used in marine current turbines. Proceedings of the World Renewable Energy Congress (WRECX), pp.1043-1048. (2008).
- MCT**, Sea Generation Ltd, The Court, The Green, Stoke Gifford, Bristol, South Gloucestershire, BS34 8PD. http://www.marineturbines.com/18/projects/20/the_skerries/ [18 January 09]
- MCT**. Marine Current Turbines outline plans for SeaGen's installation in Strangford Lough.(2008).
<http://www.seageneration.co.uk/media/080207%20MCT%20Press%20Release%207%20Feb%202008.pdf> [12 April 2009]
- Miller, B.G.**, (2005), Coal Energy Systems. Academic Press. ISBN 0124974511, 9780124974517
- Murtagh, B.J., Basu, B., Broderick, B.M.**, Along-wind response of a wind turbine tower with blade coupling subjected to rotationally sampled wind loading. Engineering Structures 27 (2005) pp 1209-1219
- Myers, L.E, Bahaj, A.S.**, Wake studies of a 1/30th scale horizontal axis marine current turbine. Ocean Engineering 34 (2007) 758-762.

References

- Myers, L.E, Bahaj, A.S.**, Power output performance characteristics of a horizontal axis marine current turbine. *Renewable Energy* 31 (2006). pp. 197-208.
- Myers, L.E, Bahaj, A.S.**, Simulated electrical power potential harnessed by marine current turbines in the Alderney Race. *Renewable Energy* 30 (2005). pp. 1713-1731.
- Myers, L.E, Bahaj, A.S., Germain, G., Giles, J.** Flow boundary interaction effects for marine current energy conversion devices. *Proceedings of the World Renewable Energy Congress (WRECX)*. (2008).
- Myers, L.E., Bahaj, A.S., Rawlinson-Smith, R.I., Thomson, M.**, The effect of boundary proximity upon the wake structure of horizontal axis marine current turbines. *Proceedings of the 27th International Conference on Offshore Mechanics and Arctic Engineering. OMAE* (2008) - 57667
- Nakanishi, N.**, Scottish power says Britain needs backup for wind. Reuters. (2009)
<http://uk.news.yahoo.com/22/20090422/tuk-uk-britain-power-wind-fa6b408.html> [24 April 2009]
- NIA (Nuclear Industry Association)**. (2009). EDF Energy nominates sites for new nuclear build.
<http://www.niauk.org/news/news-stories/edf-energy-nominates-sites-for-new-nuclear-build-1501-95.html> [15th April 2009]
- Nicholls-Less, R.F., Turnock, S.R.**, The use of Computational Fluid Dynamics in the optimisation of marine current turbines. *NUTTS* (2007)
- Nielsen, M. H.**, "Baroclinic surface currents in the Kattegat," *Journal of Marine Systems*, pp. 97-121, (2005).
- Non Nuclear Energy - JOULE II**, Wave energy project results, The Exploitation of Tidal Marine Currents," EU JOULE contract JOU2-CT94-0355, (1996).
- NOAA National Ocean Service Education: Tides and Water Levels**. (2008).
http://oceanservice.noaa.gov/education/kits/tides/tides07_cycles.html [4 March 08]
- Oberthür, S., Ott, H., Tarasofsky, R.G., von Weizsäcker, E.U.**, The Kyoto Protocol: international climate policy for the 21st century. Translated by von Weizsäcker, E.U., Springer, (1999). ISBN 354066470X, 9783540664703.
- O'Doherty¹, T., Mason-Jones, A., O'Doherty, D.M., Byrne, C.B., Owen, I., Wang, Y.**, Experimental and computational analysis of a model horizontal axis tidal turbine. To be presented at the 8th European Wave and Tidal Energy Conference, Uppsala, Sweden. (2009).

References

- O'Doherty², T., Egarr, D.A., Mason-Jones, A., O'Doherty, D.M.**, An assessment of axial loading on a 5 turbine array. Proceedings of the Institution of Civil Engineers (ICE), Energy 162, EN2. (2009)
- Orme, J.A.C., Masters, I.**, Design and testing of a direct drive tidal stream generator. Proc. MAREC (Institute of Marine Engineering, Science and Technology, (2004). pp 108-115
- Owen, I.**, Private communication relating to the turbulence intensity and near wall boundary conditions of the water flume at Liverpool University. September 08.
- Parsons Brinckerhoff.** DECC, analysis of options for tidal power development in the Severn Estuary. Interim options analysis report. Volume 1, 2008.
http://severntidalpowerconsultation.decc.gov.uk/supporting_documents [22 April 2009]
- Patankar, S.V., Spalding, D.B.**, (1970). Heat and mass transfer in boundary layers, 2nd Ed., Intertext, London.
- Pegnamenta, R.**, (2009). Experts warn of 'energy shortfall' as nuclear sites revealed. Times Online. <http://www.timesonline.co.uk/tol/news/environment/article6099637.ece> [15th April 2009]
- Previsic, M.**, System level design, performance, cost and economic assessment – San Francisco Tidal In-Stream Power Plant. EPRI. (2006)
- Pugh, D.**, Changing sea levels, effects of tides weather and climate. Cambridge University Press, (2004).
- Rados, K.G., Prospathopoulos, J.M., Stefanatos, N.Ch., Politis, E.S., Chaviaropoulos, P.K., Zervos, A.**, CFD modelling issues of wind turbine wakes under stable atmospheric conditions. Europe's premier wind energy event (EWEC), Parc channot, Marseille, France (2009).
- Robinson, E., Harnett, K., Byrne, G.**, Predicting annual output for tidal turbine technology. Proc. World Renewable Energy Congress (WRECX). pp. 964-968. (2008).
- ReVelle, P., ReVelle, C.**, The Global Environment: Securing a Sustainable Future. Jones & Bartlett Publishers. ISBN 0867203218, 9780867203219, (1992)
- Russ, P., Wiesenthal, T., van Regemorter, D., Ciscar, J. C.**, Global Climate Policy Scenarios for 2030 and beyond. Analysis of Greenhouse Gas Emissions Reduction Pathway Scenarios with the POLES and GEM-E3 models. JRC European Commission. October (2007).
- Rodi, W.**, (1982). Examples of turbulence models , AIAA J., vol. 20. pp. 872-879

References

- Salter, S.H.** DTI Energy Review Question 2. Possible under-estimation of the UK tidal resource. (2007)
- SeaGen, Sea Generation Ltd,** The Court, The Green, Stoke Gifford, Bristol, South Gloucestershire, BS34 8PD. <http://www.seageneration.co.uk/seagen-installation.asp> [18 January 09]
- Sezer-Uzol, N., Uzol, O.,** Effect of steady and transient wind shear on the wake structure and performance of a Horizontal Axis Wind Turbine rotor. Proceedings of the American Institute of Aeronautics and Astronautics. AIAA-2009-1406. Jan (2009).
- SDC (Sustainable Development Commission),** (2007). Tidal Technologies Research Report 2., Tidal Power in the UK.
<http://www.sd-commission.org.uk/pages/tidal-power.html>
- Snodin, H.,** (2001). Scotland's renewable resource. Volume II: Context.
<http://www.scotland.gov.uk/Resource/Doc/47176/0014635.pdf> [27 April 2009]
- Somers. D.M., Maughmer. M.D.,** Theoretical Aerodynamic Analyses of Six Airfoils for Use on Small Wind Turbines. National Renewable Energy Laboratory (NREL), Subcontractor Report. NREL/SR-500-33295. June (2003).
- Soares, C.,** Tidal Power: the next wave of electricity, 7/01/02, Pollution Engineering, www.pollutionengineering.com, [5 March 2009]
- Soerensen, H. C., Hansen, L.K., Hansen, R.,** Environmental Impact, WP 3.3 Final report. European Thematic Network on wave energy (2003). NNE5-1999-00438
- Stern, N.,** The Economics of Climate Change. The Stern Review. *Cabinet Office - HM Treasury* (ISBN-13: 9780521700801). (2005)
- Strathclyde, University of Strathclyde.** Marine current resource and technology methodology. Environment: Significant Impact Factor (SIF).
http://www.esru.strath.ac.uk/EandE/Web_sites/05-06/marine_renewables/envimpact/sif.htm
[December 2009]
- Strong, B., Brumely, B., Terray, E.A., Stone, G.W.,** The performance of ADCP-derived wave spectra and comparison with other independent measurements. Oceans 2000 MTS/IEEE Conference and Exhibition. pp 1195-1203. Vol.2. (2000)
- Summers., D., Carrington, D.,** (2008). Government pledges to cut carbon emissions by 80% by 2050. New climate change secretary Ed Miliband sets new goal to replace former target of 60%. The Guardian. <http://www.guardian.co.uk/politics/2008/oct/16/greenpolitics-edmiliband> [January 2009]

References

Sun, X., Chick, J.P., Bryden, I.G., Laboratory-scale simulation of energy extraction from tidal currents. *Renewable Energy* 33 (2008) pp 1267-1274

Sustainable Development Commission¹, (2007). Turning the tide. Tidal power in the UK. <http://www.sd-commission.org.uk/publications.php?id=607> [4 March 2009]

Sustainable Development Commission², (2007). Tidal power in the UK. Research report 3 – Severn barrage proposals. http://www.sd-commission.org.uk/publications/downloads/TidalPowerUK3-Severn_barrage_proposals.pdf [3rd April 2009]

Teoria Aeronáutica. Perfis Wortmann.
<http://www.aerodesign.ufsc.br/teoria/perfis/wort/wortmann.htm#> [16 March 2009]

TGL (Tidal Generation Ltd). SETsquared Business Acceleration Centre, University Gate East, Park Row, Bristol. BS1 5UB
<http://www.tidalgeneration.co.uk/background.html> [29 June 2009]

Thomas, K., Low Speed Energy Conversion from Marine Currents. Digital Comprehensive Summaries of Uppsala Dissertations from the Faculty of Science and Technology 383. ISBN 978-91-554-7063-0. (2007)

Vermeer, L.J., Sørensen, J.N., Crespo, A., Wind turbine wake aerodynamics. *Progress in Aerospace Sciences* 39 (2003) pp 467-510

Vermuelen, P.E.J., Mixing of simulated wind turbine wakes in turbulent shear flow, TNO report 79-09974, (1979)

Versteeg, H.K., Malalasekera, W., (1995). An introduction to CFD – The finite volume method, Longman Scientific and Technical.

Watson, R.T., and the core Writing Team (Eds)., IPCC Third Assessment Report: Climate Change. Climate Change (2001): Synthesis Report, Stand0alone edition, IPPCC, Geneva, Switzerland. Pp. 184
<http://www.ipcc.ch/ipccreports/tar/vol4/english/pdf/wg1ts.pdf> (18/10/08) [November 2008]

White, F.M., Fluid Dynamics, McGraw-Hill, New York, (1999), ISBN 0-07-116848-6

WHOI (Woods Hole Oceanographic Institution). Acoustic Doppler Current Profiler (ADCP). <http://www.whoi.edu/page.do?pid=11195&tid=282&cid=819> [January 2009]

Wortmann, P., Wortmann FX 63-137 profile.
<http://www.aerodesign.ufsc.br/teoria/perfis/wort/wortmann.htm> [October 2008]

References

Zahle, F., Johansen, J., Wind turbine rotor-tower interaction using an incompressible overset grid method. 45th AIAA Aerospace Science Meeting and Exhibit, 8 – 11 January (2007), Reno, Nevada. AIAA 2007 - 425

APPENDIX 1: BEM code

```
%-----  
% Input variables  
%-----  
w=11.5; V=1; B=3;  
gamma=84.00; c=0.0295; r=0.24725;  
gamma2=83.75; c2=0.03165; r2=0.228;  
gamma4=82.75; c4=0.035; r4=0.209;  
gamma6=80.81; c6=0.03904; r6=0.19;  
gamma8=78.48; c8=0.04525; r8=0.171;  
gamma10=75.59; c10=0.056; r10=0.152;  
gamma12=72.4; c12=0.0635; r12=0.1325;  
gamma14=68.71; c14=0.07; r14=0.1135;  
gamma16=64.14; c16=0.0745; r16=0.0945;  
gamma18=57.99; c18=0.0755; r18=0.0755;  
gamma20=50.11; c20=0.075; r20=0.0565;
```

The Local blade pitch angle (γ) in Degrees, local chord length in Metres (c) and local segment radius in Metres (r) are input by the user here.

```
Nseg=11
```

```
delta_aprime=1;con_a=1;con_ap=1;d_beta_i=1;  
a_old=.5;ap_old=.5;d_beta_i_old=1;  
d_beta_i_new=1;CL2deg=.5;
```

```
delta_aprime2=1;con_a2=1;con_ap2=1;d_beta_i2=1;  
a_old2=.5;ap_old2=.5;d_beta_i_old2=1;  
d_beta_i_new2=1;CL2deg2=.5;
```

```
delta_a4=1;delta_aprime4=1;con_a4=1;con_ap4=1;  
d_beta_i4=1;a_old4=.5;ap_old4=.5;  
d_beta_i_old4=1;d_beta_i_new4=1;CL2deg4=0.5;
```

```
delta_a6=1;delta_aprime6=1;con_a6=1;con_ap6=1;  
d_beta_i6=1;a_old6=.5;ap_old6=.5;  
d_beta_i_old6=1;d_beta_i_new6=1;CL2deg6=0.5;
```

```
delta_a8=1;delta_aprime8=1;con_a8=1;con_ap8=1;  
d_beta_i8=1;a_old8=.5;ap_old8=.5;  
d_beta_i_old8=1;d_beta_i_new8=1;CL2deg8=0.5;
```

```
delta_a10=1;delta_aprime10=1;con_a10=1;con_ap10=1;  
d_beta_i10=1;a_old10=.5;ap_old10=.5;  
d_beta_i_old10=1;d_beta_i_new10=1;CL2deg10=0.5;
```

```
delta_a12=1;delta_aprime12=1;con_a12=1;con_ap12=1;  
d_beta_i12=1;a_old12=.5;ap_old12=.5;  
d_beta_i_old12=1;d_beta_i_new12=1;CL2deg12=0.5;
```

Initial guess for the axial induction factor (a), rotational induction factor (a') and relative flow angle (b). Also included are the initial guesses for the convergence residuals.

APPENDIX 1: BEM code

```
delta_a14=1;delta_aprime14=1;con_a14=1;con_ap14=1;
d_beta_i14=1;a_old14=.5;ap_old14=.5;
d_beta_i_old14=1;d_beta_i_new14=1;CL2deg14=0.5;
```

```
delta_a16=1;delta_aprime16=1;con_a16=1;con_ap16=1;
d_beta_i16=1;a_old16=.5;ap_old16=.5;
d_beta_i_old16=1;d_beta_i_new16=1;CL2deg16=0.5;
```

```
delta_a18=1;delta_aprime18=1;con_a18=1;con_ap18=1;
d_beta_i18=1;a_old18=.5;ap_old18=.5;
d_beta_i_old18=1;d_beta_i_new18=1;CL2deg18=0.5;
```

```
delta_a20=1;delta_aprime20=1;con_a20=1;con_ap20=1;
d_beta_i20=1;a_old20=.5;ap_old20=.5;
d_beta_i_old20=1;d_beta_i_new20=1;CL2deg20=0.5;
```

```
m=0;n=0;n1=0;p=0;q=0;s=0;t=0;u=0;x=0;x2=0;x4=0;x6=0;
x8=0;x10=0;x12=0;
```

As above: initial guess for the axial induction factor (a), rotational induction factor (a') and relative flow angle (b). Also included are the initial guesses for the

Zeroing of convergence count

```
CD2deg=0.0;
CD2deg2=0.0;
CD2deg4=0.0;
CD2deg6=0.0;
CD2deg8=0.0;
CD2deg10=0.0;
CD2deg12=0.0;
CD2deg14=0.0;
CD2deg16=0.0;
CD2deg18=0.0;
CD2deg20=0.0;
```

Drag coefficient CD assumed to be zero

```
%-----
%iteration for tip segment
%-----
%-----
% Initial guess tip segment
%-----
```

```
lamdaR = (w*r)/V;
sig=(B*c)/(2*pi*r);
beta=1.5707-((2/3)*atan(1/8));
irad=(gamma*0.0174533)-beta;
ideg=irad*57.29577951;
```

Calculation for Local: TSR, Local solidity factor, Relative flow angle, Angle of incidence.

```
if (ideg >= -7) && (ideg <= 23);
```

APPENDIX 1: BEM code

```
CL2deg=-0.0002*(ideg^3)-(0.0013*ideg^2)+0.1095*ideg+0.7458;

elseif (ideg < -7);
    CL2deg=0.00001;
else (ideg > 23);

    CL2deg=0.0001;
    %CD2deg=0;
end

a1t=4*((cos(2*beta)+1)*0.5);
a1b=sig*CL2deg*sin(beta);
a1=(1+(a1t/a1b))^-1;
aprime1=(1-3*a1)/(4*a1-1);

aprime_i=aprime1;
a1_i=a1;

%iteration for tip segment

while (con_a > 0.00001) && (con_ap > 0.00001) && (n < 1000000);

beta_i=atan(lamdaR*((1+aprime_i)/(1-a1_i)));
irad=(gamma*0.0174533)-beta_i;
ideg=irad*57.29577951;

if (ideg >= -7) && (ideg <= 23);
    CL2deg=-0.0002*(ideg^3)-(0.0013*ideg^2)+0.1095*ideg+0.7458;

elseif (ideg < -7);
    CL2deg=0.00001;
else (ideg > 23);

    CL2deg=0.0001;
    %CD2deg=0.015;
end

n=n+1;

beta_i_deg = beta_i*57.29577951;

a1_i_T=sig*(CL2deg*sin(beta_i)+CD2deg*cos(beta_i));
a1_i_B1=(cos(2*beta_i)+1)/2;
a1_i_B2=4*(a1_i_B1)+sig*(CL2deg*sin(beta_i)+CD2deg*cos(beta_i));
a1_i=a1_i_T/a1_i_B2;
```

*Initial guess for
CL based on curve
fit to Wortmann
FX 63-137 profile*

*Calculation of axial and rotational
induction factors based on initial
guesses*

*Areas of code marked A
to B are the iterative
calculation to establish
the axial and rotational
induction factors at the
blade tip. The relative
flow angle, incidence
angle and CL are
updated each iteration
until the residual
tolerances con_a and
con_ap reach reached.*

A

APPENDIX 1: BEM code

```

apprime_i_T=(sig*(CL2deg*cos(beta_i)-CD2deg*sin(beta_i))*(1-a1_i);
apprime_i_B=4*lamdaR*((cos(2*beta_i)+1)/2);
apprime_i=apprime_i_T/apprime_i_B;

```

```

delta_a=abs(a_old - a1_i);
delta_aprime=abs(ap_old - aprime_i);

```

```

con_a=delta_a/a_old;
con_ap=delta_aprime/ap_old;

```

```

a_old=a1_i;
ap_old=apprime_i;

```

```

Yo1=(1-((CD2deg/CL2deg)*tan(beta_i)));
Yo=lamdaR^3*apprime_i*(1-a1_i)*Yo1;

```

```
end
```

```

%-----
%iteration for 2nd segment
%-----
%-----
% Initial guess 2nd segment
%-----

```

```

lamdaR2 = (w*r2)/V;
sig2=(B*c2)/(2*pi*r2);
beta2=1.5707-((2/3)*atan(1/8));
irad2=(gamma2*0.0174533)-beta2;
ideg2=irad2*57.29577951;

```

```

if (ideg2 >= -7) && (ideg2 <= 23);
    CL2deg2=-0.0002*(ideg2^3)-(0.0013*ideg2^2)+0.1095*ideg2+0.7458;

```

```

elseif (ideg2 < -7);
    CL2deg2=0.00001;

```

```
else (ideg2 > 23);
```

```
    CL2deg2=0.00001;
```

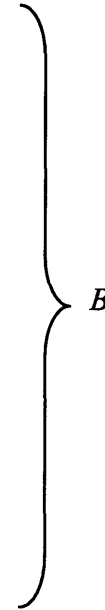
```
    %CD2deg2=0;
```

```
end
```

```

a1t2=4*((cos(2*beta2)+1)*0.5);
a1b2=sig2*CL2deg2*sin(beta2);
a12=(1+(a1t2/a1b2))^-1;
apprime12=(1-3*a12)/(4*a12-1);

```



For blade segments 2 to 20 the procedures shown for the first blade segment are repeated.



APPENDIX 1: BEM code

```
apprime_i2=apprime12;
a1_i2=a12;

%iteration for tip segment

while (con_a2 > 0.00001) && (con_ap2 > 0.00001) && (m < 1000000);

beta2_i=atan(lamdaR2*((1+apprime_i2)/(1-a1_i2)));
irad2=(gamma2*0.0174533)-beta2_i;
ideg2=irad2*57.29577951;

if (ideg2 >= -7) && (ideg2 <= 23);
    CL2deg2=-0.0002*(ideg2^3)-(0.0013*ideg2^2)+0.1095*ideg2+0.7458;

elseif (ideg2 < -7);
    CL2deg2=0.00001;
else (ideg2 > 23);

    CL2deg2=0.00001;
    %CD2deg2=0;
end
m=m+1;

beta_i_deg2 = beta2_i*57.29577951;

a1_i_T2=sig2*(CL2deg2*sin(beta2_i)+CD2deg2*cos(beta2_i));
a1_i_B12=(cos(2*beta2_i)+1)/2;
a1_i_B22=4*(a1_i_B12)+sig2*(CL2deg2*sin(beta2_i)+CD2deg2*cos(beta2_i));
a1_i2=a1_i_T2/a1_i_B22;

apprime_i_T2=(sig2*(CL2deg2*cos(beta2_i)-CD2deg2*sin(beta2_i)))*(1-a1_i2);
apprime_i_B2=4*lamdaR2*((cos(2*beta2_i)+1)/2);
apprime_i2=apprime_i_T2/apprime_i_B2;

delta_a2=abs(a_old2 - a1_i2);
delta_apprime2=abs(ap_old2 - aprime_i2);

con_a2=delta_a2/a_old2;
con_ap2=delta_apprime2/ap_old2;

a_old2=a1_i2;
ap_old2=apprime_i2;

Y21=(1-((CD2deg2/CL2deg2)*tan(beta2_i)));
```

APPENDIX 1: BEM code

```
Y2=lamdaR2^3*aprimel_i2*(1-a1_i2)*Y21;

end

%-----
%iteration for 4th segment
%-----
%-----
% Initial guess 4th segment
%-----
lamdaR4 = (w*r4)/V;
sig4=(B*c4)/(2*pi*r4);
beta4=1.5707-((2/3)*atan(1/8));
irad4=(gamma4*0.0174533)-beta4;
ideg4=irad4*57.29577951;

if (ideg4 >= -7) && (ideg4 <= 23);
    CL2deg4=-0.0002*(ideg4^3)-(0.0013*ideg4^2)+0.1095*ideg4+0.7458;

elseif (ideg4 < -7);
    CL2deg4=0.00001;
else (ideg4 > 23);

    CL2deg4=0.00001;
    %CD2deg4=0;
end

a1t4=4*((cos(2*beta4)+1)*0.5);
a1b4=sig4*CL2deg4*sin(beta4);
a14=(1+(a1t4/a1b4))^-1;
aprimel14=(1-3*a14)/(4*a14-1);

aprimel_i4=aprimel14;
a1_i4=a14;

%iteration for tip segment

while (con_a4 > 0.00001) && (con_ap4 > 0.00001) && (q < 1000000);

beta4_i=atan(lamdaR4*((1+aprimel_i4)/(1-a1_i4)));
irad4=(gamma4*0.0174533)-beta4_i;
ideg4=irad4*57.29577951;

if (ideg4 >= -7) && (ideg4 <= 23);
```

APPENDIX 1: BEM code

```
CL2deg4=-0.0002*(ideg4^3)-(0.0013*ideg4^2)+0.1095*ideg4+0.7458;

elseif (ideg4 < -7);
    CL2deg4=0.00001;
else (ideg4 > 23);

    CL2deg4=0.00001;
    %CD2deg4=0;

end

q=q+1;

beta_i_deg4 = beta4_i*57.29577951;

a1_i_T4=sig4*(CL2deg4*sin(beta4_i)+CD2deg4*cos(beta4_i));
a1_i_B14=(cos(2*beta4_i)+1)/2;
a1_i_B24=4*(a1_i_B14)+sig4*(CL2deg4*sin(beta4_i)+CD2deg4*cos(beta4_i));
a1_i4=a1_i_T4/a1_i_B24;

aprime_i_T4=(sig4*(CL2deg4*cos(beta4_i)-CD2deg4*sin(beta4_i)))*(1-a1_i4);
aprime_i_B4=4*lamdaR4*((cos(2*beta4_i)+1)/2);
aprime_i4=aprime_i_T4/aprime_i_B4;

delta_a4=abs(a_old4 - a1_i4);
delta_aprime4=abs(ap_old4 - aprime_i4);

con_a4=delta_a4/a_old4;
con_ap4=delta_aprime4/ap_old4;

a_old4=a1_i4;
ap_old4=aprime_i4;

Y41=(1-((CD2deg4/CL2deg4)*tan(beta4_i)));
Y4=lamdaR4^3*aprime_i4*(1-a1_i4)*Y41;

end
%-----
%iteration for 6th segment
%-----
% Initial guess 6th segment
%-----
lamdaR6 = (w*r6)/V;
sig6=(B*c6)/(2*pi*r6);
beta6=1.5707-((2/3)*atan(1/8));
```


APPENDIX 1: BEM code

```
irad6=(gamma6*0.0174533)-beta6;
ideg6=irad6*57.29577951;

if (ideg6 >= -7) && (ideg6 <= 23);
    CL2deg6=-0.0002*(ideg6^3)-(0.0013*ideg6^2)+0.1095*ideg6+0.7458;

elseif (ideg6 < -7);
    CL2deg6=0.00001;
else (ideg6 > 23);

    CL2deg6=0.00001;
    %CD2deg6=0;
end

a1t6=4*((cos(2*beta6)+1)*0.5);
a1b6=sig6*CL2deg6*sin(beta6);
a16=(1+(a1t6/a1b6))^-1;
aprime16=(1-3*a16)/(4*a16-1);

aprime_i6=aprime16;
a1_i6=a16;

%iteration for tip segment

while (con_a6 > 0.00001) && (con_ap6 > 0.00001) && (t < 1000000);

beta6_i=atan(lamdaR6*((1+aprime_i6)/(1-a1_i6)));
irad6=(gamma6*0.0174533)-beta6_i;
ideg6=irad6*57.29577951;

if (ideg6 >= -7) && (ideg6 <= 23);
    CL2deg6=-0.0002*(ideg6^3)-(0.0013*ideg6^2)+0.1095*ideg6+0.7458;

elseif (ideg6 < -7);
    CL2deg6=0.00001;
else (ideg6 > 23);

    CL2deg6=0.00001;
    %CD2deg6=0;
end

t=t+1;

beta_i_deg6 = beta6_i*57.29577951;
```

APPENDIX 1: BEM code

```
a1_i_T6=sig6*(CL2deg6*sin(beta6_i)+CD2deg6*cos(beta6_i));
a1_i_B16=(cos(2*beta6_i)+1)/2;
a1_i_B26=4*(a1_i_B16)+sig6*(CL2deg6*sin(beta6_i)+CD2deg6*cos(beta6_i));
a1_i6=a1_i_T6/a1_i_B26;

aprime_i_T6=(sig6*(CL2deg6*cos(beta6_i)-CD2deg6*sin(beta6_i)))*(1-a1_i6);
aprime_i_B6=4*lamdaR6*((cos(2*beta6_i)+1)/2);
aprime_i6=aprime_i_T6/aprime_i_B6;

delta_a6=abs(a_old6 - a1_i6);
delta_aprime6=abs(ap_old6 - aprime_i6);

con_a6=delta_a6/a_old6;
con_ap6=delta_aprime6/ap_old6;

a_old6=a1_i6;
ap_old6=aprime_i6;

Y61=(1-((CD2deg6/CL2deg6)*tan(beta6_i)));
Y6=lamdaR6^3*aprime_i6*(1-a1_i6)*Y61;

end
%-----
%iteration for 8th segment
%-----
%-----
% Initial guess 8th segment
%-----
lamdaR8 = (w*r8)/V;
sig8=(B*c8)/(2*pi*r8);
beta8=1.5707-((2/3)*atan(1/8));
irad8=(gamma8*0.0174533)-beta8;
ideg8=irad8*57.29577951;

if (ideg8 >= -7) && (ideg8 <= 23);
    CL2deg8=-0.0002*(ideg8^3)-(0.0013*ideg8^2)+0.1095*ideg8+0.7458;

elseif (ideg8 < -7);
    CL2deg8=0.00001;
else (ideg8 > 23);

    CL2deg8=0.000001;
    %CD2deg8=0;
end

a1t8=4*((cos(2*beta8)+1)*0.5);
```

APPENDIX 1: BEM code

```
a1b8=sig8*CL2deg8*sin(beta8);
a18=(1+(a1t8/a1b8))^-1;
aprime18=(1-3*a18)/(4*a18-1);

aprime_i8=aprime18;
a1_i8=a18;

%iteration for tip segment

while (con_a8 > 0.00001) && (con_ap8 > 0.00001) && (x < 1000000);

beta8_i=atan(lamdaR8*((1+aprime_i8)/(1-a1_i8)));
irad8=(gamma8*0.0174533)-beta8_i;
ideg8=irad8*57.29577951;

if (ideg8 >= -7) && (ideg8 <= 23);
    CL2deg8=-0.0002*(ideg8^3)-(0.0013*ideg8^2)+0.1095*ideg8+0.7458;

elseif (ideg8 < -7);
    CL2deg8=0.00001;
else (ideg8 > 23);

    CL2deg8=0.000001;
    %CD2deg8=0;
end

x=x+1;

beta_i_deg8 = beta8_i*57.29577951;

a1_i_T8=sig8*(CL2deg8*sin(beta8_i)+CD2deg8*cos(beta8_i));
a1_i_B18=(cos(2*beta8_i)+1)/2;
a1_i_B28=4*(a1_i_B18)+sig8*(CL2deg8*sin(beta8_i)+CD2deg8*cos(beta8_i));
a1_i8=a1_i_T8/a1_i_B28;

aprime_i_T8=(sig8*(CL2deg8*cos(beta8_i)-CD2deg8*sin(beta8_i)))*(1-a1_i8);
aprime_i_B8=4*lamdaR8*((cos(2*beta8_i)+1)/2);
aprime_i8=aprime_i_T8/aprime_i_B8;

delta_a8=abs(a_old8 - a1_i8);
delta_aprime8=abs(ap_old8 - aprime_i8);

con_a8=delta_a8/a_old8;
con_ap8=delta_aprime8/ap_old8;
```

APPENDIX 1: BEM code

```
a_old8=a1_i8;
ap_old8=apime_i8;

Y81=(1-((CD2deg8/CL2deg8)*tan(beta8_i)));
Y8=lamdaR8^3*apime_i8*(1-a1_i8)*Y81;

end
%-----
%iteration for 10th segment
%-----
%-----
% Initial guess 10th segment
%-----
lamdaR10 = (w*r10)/V;
sig10=(B*c10)/(2*pi*r10);
beta10=1.5707-((2/3)*atan(1/8));
irad10=(gamma10*0.0174533)-beta10;
ideg10=irad10*57.29577951;

if (ideg10 >= -7) && (ideg10 <= 23);
    CL2deg10=-0.0002*(ideg10^3)-(0.0013*ideg10^2)+0.1095*ideg10+0.7458;

elseif (ideg10 < -7);
    CL2deg10=0.00001;
else (ideg10 > 23);

    CL2deg10=0.00001;
    %CD2deg10=0;
end

a1t10=4*((cos(2*beta10)+1)*0.5);
a1b10=sig10*CL2deg10*sin(beta10);
a110=(1+(a1t10/a1b10))^-1;
apime110=(1-3*a110)/(4*a110-1);

apime_i10=apime110;
a1_i10=a110;

%iteration for tip segment

while (con_a10 > 0.00001) && (con_ap10 > 0.00001) && (x2 < 1000000);

beta10_i=atan(lamdaR10*((1+apime_i10)/(1-a1_i10)));
irad10=(gamma10*0.0174533)-beta10_i;
```


APPENDIX 1: BEM code

```
ideg10=irad10*57.29577951;

if (ideg10 >= -7) && (ideg10 <= 23);
    CL2deg10=-0.0002*(ideg10^3)-(0.0013*ideg10^2)+0.1095*ideg10+0.7458;

elseif (ideg10 < -7);
    CL2deg10=0.00001;
else (ideg10 > 23);

    CL2deg10=0.000001;
    %CD2deg10=0;
end

x2=x2+1;

beta_i_deg10 = beta10_i*57.29577951;

a1_i_T10=sig10*(CL2deg10*sin(beta10_i)+CD2deg10*cos(beta10_i));
a1_i_B110=(cos(2*beta10_i)+1)/2;
a1_i_B210=4*(a1_i_B110)+sig10*(CL2deg10*sin(beta10_i)+CD2deg10*cos(beta10_i))
;
a1_i10=a1_i_T10/a1_i_B210;

aprime_i_T10=(sig10*(CL2deg10*cos(beta10_i)-CD2deg10*sin(beta10_i)))*(1-a1_i10);
aprime_i_B10=4*lamdaR10*((cos(2*beta10_i)+1)/2);
aprime_i10=aprime_i_T10/aprime_i_B10;

delta_a10=abs(a_old10 - a1_i10);
delta_aprime10=abs(ap_old10 - aprime_i10);

con_a10=delta_a10/a_old10;
con_ap10=delta_aprime10/ap_old10;

a_old10=a1_i10;
ap_old10=aprime_i10;

Y101=(1-((CD2deg10/CL2deg10)*tan(beta10_i)));
Y10=lamdaR10^3*aprime_i10*(1-a1_i10)*Y101;
end
%-----
%iteration for 12th segment
%-----
%-----
% Initial guess 12th segment
%-----
lamdaR12 = (w*r12)/V;
```

APPENDIX 1: BEM code

```
sig12=(B*c12)/(2*pi*r12);
beta12=1.5707-((2/3)*atan(1/8));
irad12=(gamma12*0.0174533)-beta12;
ideg12=irad12*57.29577951;

if (ideg12 >= -7) && (ideg12 <= 23);
    CL2deg12=-0.0002*(ideg12^3)-(0.0013*ideg12^2)+0.1095*ideg12+0.7458;

elseif (ideg12 < -7);
    CL2deg12=0.00001;
else (ideg12 > 23);

    CL2deg12=0.00001;
    %CD2deg12=0;
end

a1t12=4*((cos(2*beta12)+1)*0.5);
a1b12=sig12*CL2deg12*sin(beta12);
a112=(1+(a1t12/a1b12))^-1;
aprime112=(1-3*a112)/(4*a112-1);

aprime_i12=aprime112;
a1_i12=a112;

%iteration for tip segment

while (con_a12 > 0.00001) && (con_ap12 > 0.00001) && (x4 < 1000000);

beta12_i=atan(lamdaR12*((1+aprime_i12)/(1-a1_i12)));
irad12=(gamma12*0.0174533)-beta12_i;
ideg12=irad12*57.29577951;

if (ideg12 >= -7) && (ideg12 <= 23);
    CL2deg12=-0.0002*(ideg12^3)-(0.0013*ideg12^2)+0.1095*ideg12+0.7458;

elseif (ideg12 < -7);
    CL2deg12=0.00001;
else (ideg12 > 23);

    CL2deg12=0.000001;
    %CD2deg12=0;

end

x4=x4+1;
```

APPENDIX 1: BEM code

```
beta_i_deg12 = beta12_i*57.29577951;

a1_i_T12=sig12*(CL2deg12*sin(beta12_i)+CD2deg12*cos(beta12_i));
a1_i_B112=(cos(2*beta12_i)+1)/2;
a1_i_B212=4*(a1_i_B112)+sig12*(CL2deg12*sin(beta12_i)+CD2deg12*cos(beta12_i))
;
a1_i12=a1_i_T12/a1_i_B212;

aprime_i_T12=(sig12*(CL2deg12*cos(beta12_i)-CD2deg12*sin(beta12_i)))*(1-a1_i12);
aprime_i_B12=4*lamdaR12*((cos(2*beta12_i)+1)/2);
aprime_i12=aprime_i_T12/aprime_i_B12;

delta_a12=abs(a_old12 - a1_i12);
delta_aprime12=abs(ap_old12 - aprime_i12);

con_a12=delta_a12/a_old12;
con_ap12=delta_aprime12/ap_old12;

a_old12=a1_i12;
ap_old12=aprime_i12;

Y121=(1-((CD2deg12/CL2deg12)*tan(beta12_i)));
Y12=lamdaR12^3*aprime_i12*(1-a1_i12)*Y121;

end
%-----
%iteration for 14th segment
%-----
%-----
% Initial guess 14th segment
%-----
lamdaR14 = (w*r14)/V;
sig14=(B*c14)/(2*pi*r14);
beta14=1.5707-((2/3)*atan(1/8));
irad14=(gamma14*0.0174533)-beta14;
ideg14=irad14*57.29577951;

if (ideg14 >= -7) && (ideg14 <= 23);
    CL2deg14=-0.0002*(ideg14^3)-(0.0013*ideg14^2)+0.1095*ideg14+0.7458;

elseif (ideg14 < -7);
    CL2deg14=0.00001;
else (ideg14 > 23);

    CL2deg14=0.000001;
```

APPENDIX 1: BEM code

```
%CD2deg14=0;
end

alt14=4*((cos(2*beta14)+1)*0.5);
alb14=sig14*CL2deg14*sin(beta14);
a114=(1+(alt14/alb14))^-1;
aprime114=(1-3*a114)/(4*a114-1);

aprime_i14=aprime114;
al_i14=a114;

%interation for tip segment

while (con_a14 > 0.00001) && (con_ap14 > 0.00001) && (x6 < 1000000);

beta14_i=atan(lamdaR14*((1+aprime_i14)/(1-al_i14)));
irad14=(gamma14*0.0174533)-beta14_i;
ideg14=irad14*57.29577951;

if (ideg14 >= -7) && (ideg14 <= 23);
    CL2deg14=-0.0002*(ideg14^3)-(0.0013*ideg14^2)+0.1095*ideg14+0.7458;

elseif (ideg14 < -7);
    CL2deg14=0.00001;
else (ideg14 > 23);

    CL2deg14=0.00001;
    %CD2deg14=0;
end

x6=x6+1;

beta_i_deg14 = beta14_i*57.29577951;

al_i_T14=sig14*(CL2deg14*sin(beta14_i)+CD2deg14*cos(beta14_i));
al_i_B114=(cos(2*beta14_i)+1)/2;
al_i_B214=4*(al_i_B114)+sig14*(CL2deg14*sin(beta14_i)+CD2deg14*cos(beta14_i))
;
al_i14=al_i_T14/al_i_B214;

aprime_i_T14=(sig14*(CL2deg14*cos(beta14_i)-CD2deg14*sin(beta14_i)))*(1-al_i14);
aprime_i_B14=4*lamdaR14*((cos(2*beta14_i)+1)/2);
aprime_i14=aprime_i_T14/aprime_i_B14;

delta_a14=abs(a_old14 - al_i14);
```


APPENDIX 1: BEM code

```
delta_aprime14=abs(ap_old14 - aprime_i14);

con_a14=delta_a14/a_old14;
con_ap14=delta_aprime14/ap_old14;

a_old14=a1_i14;
ap_old14=aprime_i14;

Y141=(1-((CD2deg14/CL2deg14)*tan(beta14_i)));
Y14=lamdaR14^3*aprime_i14*(1-a1_i14)*Y141;
end
%-----
%iteration for 16th segment
%-----
%-----
% Initial guess 16th segment
%-----
lamdaR16 = (w*r16)/V;
sig16=(B*c16)/(2*pi*r16);
beta16=1.5707-((2/3)*atan(1/8));
irad16=(gamma16*0.0174533)-beta16;
ideg16=irad16*57.29577951;

if (ideg16 >= -7) && (ideg16 <= 23);
    CL2deg16=-0.0002*(ideg16^3)-(0.0013*ideg16^2)+0.1095*ideg16+0.7458;

elseif (ideg16 < -7);
    CL2deg16=0.00001;
else (ideg16 > 23);

    CL2deg16=0.000001;
    %CD2deg16=0;
end

a1t16=4*((cos(2*beta16)+1)*0.5);
a1b16=sig16*CL2deg16*sin(beta16);
a116=(1+(a1t16/a1b16))^-1;
aprime116=(1-3*a116)/(4*a116-1);

aprime_i16=aprime116;
a1_i16=a116;

%iteration for tip segment

while (con_a16 > 0.00001) && (con_ap16 > 0.00001) && (x8 < 1000000);
```

APPENDIX 1: BEM code

```
beta16_i=atan(lamdaR16*((1+aprime_i16)/(1-a1_i16)));
irad16=(gamma16*0.0174533)-beta16_i;
ideg16=irad16*57.29577951;

if (ideg16 >= -7) && (ideg16 <= 23);
    CL2deg16=-0.0002*(ideg16^3)-(0.0013*ideg16^2)+0.1095*ideg16+0.7458;

elseif (ideg16 < -7);
    CL2deg16=0.00001;
else (ideg16 > 23);

    CL2deg16=0.00001;
    %CD2deg16=0;
end

x8=x8+1;

beta_i_deg16 = beta16_i*57.29577951;

a1_i_T16=sig16*(CL2deg16*sin(beta16_i)+CD2deg16*cos(beta16_i));
a1_i_B116=(cos(2*beta16_i)+1)/2;
a1_i_B216=4*(a1_i_B116)+sig16*(CL2deg16*sin(beta16_i)+CD2deg16*cos(beta16_i))
;
a1_i16=a1_i_T16/a1_i_B216;

aprime_i_T16=(sig16*(CL2deg16*cos(beta16_i)-CD2deg16*sin(beta16_i)))*(1-a1_i16);
aprime_i_B16=4*lamdaR16*((cos(2*beta16_i)+1)/2);
aprime_i16=aprime_i_T16/aprime_i_B16;

delta_a16=abs(a_old16 - a1_i16);
delta_aprime16=abs(ap_old16 - aprime_i16);

con_a16=delta_a16/a_old16;
con_ap16=delta_aprime16/ap_old16;

a_old16=a1_i16;
ap_old16=aprime_i16;

Y161=(1-((CD2deg16/CL2deg16)*tan(beta16_i)));
Y16=lamdaR16^3*aprime_i16*(1-a1_i16)*Y161;
end
%-----
%iteration for 18th segment
%-----
%-----
```

APPENDIX 1: BEM code

```
% Initial guess 18th segment
%-----
lamdaR18 = (w*r18)/V;
sig18=(B*c18)/(2*pi*r18);
beta18=1.5707-((2/3)*atan(1/8));
irad18=(gamma18*0.0174533)-beta18;
ideg18=irad18*57.29577951;

if (ideg18 >= -7) && (ideg18 <= 23);
    CL2deg18=-0.0002*(ideg18^3)-(0.0013*ideg18^2)+0.1095*ideg18+0.7458;

elseif (ideg18 < -7);
    CL2deg18=0.00001;
else (ideg18 > 23);

    CL2deg18=0.00001;
    %CD2deg18=0;
end

a1t18=4*((cos(2*beta18)+1)*0.5);
a1b18=sig18*CL2deg18*sin(beta18);
a118=(1+(a1t18/a1b18))^-1;
aprime118=(1-3*a118)/(4*a118-1);

aprime_i18=aprime118;
a1_i18=a118;

%iteration for tip segment

while (con_a18 > 0.00001) && (con_ap18 > 0.00001) && (x10 < 1000000);

beta18_i=atan(lamdaR18*((1+aprime_i18)/(1-a1_i18)));
irad18=(gamma18*0.0174533)-beta18_i;
ideg18=irad18*57.29577951;

if (ideg18 >= -7) && (ideg18 <= 23);
    CL2deg18=-0.0002*(ideg18^3)-(0.0013*ideg18^2)+0.1095*ideg18+0.7458;

elseif (ideg18 < -7);
    CL2deg18=0.00001;
else (ideg18 > 23);

    CL2deg18=0.00001;
    %CD2deg18=0;
end
```

APPENDIX 1: BEM code

```
x10=x10+1;

beta_i_deg18 = beta18_i*57.29577951;

a1_i_T18=sig18*(CL2deg18*sin(beta18_i)+CD2deg18*cos(beta18_i));
a1_i_B118=(cos(2*beta18_i)+1)/2;
a1_i_B218=4*(a1_i_B118)+sig18*(CL2deg18*sin(beta18_i)+CD2deg18*cos(beta18_i))
;
a1_i18=a1_i_T18/a1_i_B218;

aprime_i_T18=(sig18*(CL2deg18*cos(beta18_i)-CD2deg18*sin(beta18_i)))*(1-a1_i18);
aprime_i_B18=4*lamdaR18*((cos(2*beta18_i)+1)/2);
aprime_i18=aprime_i_T18/aprime_i_B18;

delta_a18=abs(a_old18 - a1_i18);
delta_aprime18=abs(ap_old18 - aprime_i18);

con_a18=delta_a18/a_old18;
con_ap18=delta_aprime18/ap_old18;

a_old18=a1_i18;
ap_old18=aprime_i18;

Y181=(1-((CD2deg18/CL2deg18)*tan(beta18_i)));
Y18=lamdaR18^3*aprime_i18*(1-a1_i18)*Y181;
end
%-----
%iteration for 20th segment
%-----
%-----
% Initial guess 20th segment
%-----
lamdaR20 = (w*r20)/V;
sig20=(B*c20)/(2*pi*r20);
beta20=1.5707-((2/3)*atan(1/8));
irad20=(gamma20*0.0174533)-beta20;
ideg20=irad20*57.29577951;

if (ideg20 >= -7) && (ideg20 <= 23);
    CL2deg20=-0.0002*(ideg20^3)-(0.0013*ideg20^2)+0.1095*ideg20+0.7458;

elseif (ideg20 < -7);
    CL2deg20=0.00001;
else (ideg20 > 23);
```


APPENDIX 1: BEM code

```
CL2deg20=0.00001;
%CD2deg20=0;

end

a1t20=4*((cos(2*beta20)+1)*0.5);
a1b20=sig20*CL2deg20*sin(beta20);
a120=(1+(a1t20/a1b20))^-1;
aprime120=(1-3*a120)/(4*a120-1);

aprime_i20=aprime120;
a1_i20=a120;

%iteration for tip segment

while (con_a20 > 0.00001) && (con_ap20 > 0.00001) && (x12 < 1000000);

beta20_i=atan(lamdaR20*((1+aprime_i20)/(1-a1_i20)));
irad20=(gamma20*0.0174533)-beta20_i;
ideg20=irad20*57.29577951;

if (ideg20 >= -7) && (ideg20 <= 23);
    CL2deg20=-0.0002*(ideg20^3)-(0.0013*ideg20^2)+0.1095*ideg20+0.7458;

elseif (ideg20 < -7);
    CL2deg20=0.00001;
else (ideg20 > 23);

    CL2deg20=0.000001;
    %CD2deg20=0;

end

x12=x12+1;

beta_i_deg20 = beta20_i*57.29577951;

a1_i_T20=sig20*(CL2deg20*sin(beta20_i)+CD2deg20*cos(beta20_i));
a1_i_B120=(cos(2*beta20_i)+1)/2;
a1_i_B220=4*(a1_i_B120)+sig20*(CL2deg20*sin(beta20_i)+CD2deg20*cos(beta20_i))
;
a1_i20=a1_i_T20/a1_i_B220;

aprime_i_T20=(sig20*(CL2deg20*cos(beta20_i)-CD2deg20*sin(beta20_i)))*(1-a1_i20);
aprime_i_B20=4*lamdaR20*((cos(2*beta20_i)+1)/2);
aprime_i20=aprime_i_T20/aprime_i_B20;
```

APPENDIX 1: BEM code

```
delta_a20=abs(a_old20 - a1_i20);  
delta_aprime20=abs(ap_old20 - aprime_i20);
```

```
con_a20=delta_a20/a_old20;  
con_ap20=delta_aprime20/ap_old20;
```

```
a_old20=a1_i20;  
ap_old20=aprime_i20;
```

```
Y201=(1-((CD2deg20/CL2deg20)*tan(beta20_i)));  
Y20=lamdaR20^3*aprime_i20*(1-a1_i20)*Y201;  
end
```



*End of blade
segment iterations*

```
f=(r-r2)/(2);  
f2=(r2-r4)/(2);  
f4=(r4-r6)/(2);  
f6=(r6-r8)/2;  
f8=(r8-r10)/2;  
f10=(r10-r12)/2;  
f12=(r12-r14)/2;  
f14=(r14-r16)/2;  
f16=(r16-r18)/2;  
f18=(r18-r20)/2;
```

```
g=Y0+Y2;  
g2=Y2+Y4;  
g4=Y4+Y6;  
g6=Y6+Y8;  
g8=Y8+Y10;  
g10=Y10+Y12;  
g12=Y12+Y14;  
g14=Y14+Y16;  
g16=Y16+Y18;  
g18=Y18+Y20;
```

```
ff=(8/lamdaR^2);
```

```
fg=f*g;  
f2g2=f2*g2;  
f4g4=f4*g4;  
f6g6=f6*g6;  
f8g8=f8*g8;  
f10g10=f10*g10;  
f12g12=f12*g12;
```

C

*Between C & D is the calculation of the
extracted power and Cp using equation 4.9
and the available power for the swept area.*

APPENDIX 1: BEM code

```
f14g14=f14*g14;  
f16g16=f16*g16;  
f18g18=f18*g18;
```

```
bn=fg;  
bn2=f2g2;  
bn4=f4g4;  
bn6=f6g6;  
bn8=f8g8;  
bn10=f10g10;  
bn12=f12g12;  
bn14=f14g14;  
bn16=f16g16;  
bn18=f18g18;
```

```
Cp=(bn+bn2+bn4+bn6+bn8+bn10+bn12+bn14+bn16+bn18)*ff;
```

```
Power=0.5*1000*pi*r^2*V^3;
```

```
PowerCp=Power*Cp;
```

```
Cp
```

```
Power
```

```
PowerCp
```

```
n
```

```
CL2deg
```

```
ideg
```

```
al_i
```

```
aprime_i
```



D

APPENDIX 2

Blade tip pitch angles for BEM study.

Blade pitch base line	2	3	4	5	5.5	6	6.5	7	7.5	8	9	10	Chord length m	Radius m
	Deg.	Deg.	Deg.	Deg.	Deg.	Deg.	Deg.	Deg.	Deg.	Deg.	Deg.	Deg.		
90	88	87	86	85	84.5	84	83.5	83	82.5	82	81	80	0.0295	0.24725
89.75	87.75	86.75	85.75	84.75	84.25	83.75	83.25	82.75	82.25	81.75	80.75	79.75	0.03165	0.228
88.75	86.75	85.75	84.75	83.75	83.25	82.75	82.25	81.75	81.25	80.75	79.75	78.75	0.035	0.209
86.81	84.81	83.81	82.81	81.81	81.31	80.81	80.31	79.81	79.31	78.81	77.81	76.81	0.03904	0.19
84.48	82.48	81.48	80.48	79.48	78.98	78.48	77.98	77.48	76.98	76.48	75.48	74.48	0.04525	0.171
81.59	79.59	78.59	77.59	76.59	76.09	75.59	75.09	74.59	74.09	73.59	72.59	71.59	0.056	0.152
78.4	76.4	75.4	74.4	73.4	72.9	72.4	71.9	71.4	70.9	70.4	69.4	68.4	0.0635	0.1325
74.71	72.71	71.71	70.71	69.71	69.21	68.71	68.21	67.71	67.21	66.71	65.71	64.71	0.07	0.1135
70.14	68.14	67.14	66.14	65.14	64.64	64.14	63.64	63.14	62.64	62.14	61.14	60.14	0.0745	0.0945
63.99	61.99	60.99	59.99	58.99	58.49	57.99	57.49	56.99	56.49	55.99	54.99	53.99	0.0755	0.0755
56.11	54.11	53.11	52.11	51.11	50.61	50.11	49.61	49.11	48.61	48.11	47.11	46.11	0.075	0.0565

Appendix 3: User Defined Function (UDF); torque, power, axial thrust and blade forces

```

/*****
/* UDF adapted by A. Mason-Jones */
*****/

/*****
/* UDF written for use with FLUENT 6.3 */
*****/

/*****
/* UDF to report the power, torque, angular velocity */
/* and forces in x,y and z */
*****/

#include "udf.h"

/*****
/*
*/
/* The following need to be defined*/
/*
*/

#define T1_WALLS 4 /* Number of walls forming the blades for turbine 1 */

static int T1wall_ids[T1_WALLS] = { 11, 12, 13, 14 }; /* Wall IDs for turbine blades
from fluent utility */

#define U_fs 0.7 /* Free stream velocity */
#define T1_Diameter 0.5 /* Diameter of turbine 1 */

#define T1_Domain 3 /* Domain ID for turbine 1 from fluent utility */

/*****

#define pi 3.141592654 /* pi() */

static real T1_centre_x; /* x coordinate of turbine 1 centre */
static real T1_centre_y; /* y coordinate of turbine 1 centre */
static real T1_centre_z; /* z coordinate of turbine 1 centre */

static real fluid_rho; /* Fluid density */

static real T1_torque; /* Torque on turbine 1 due to pressure and shear force on blades */
static real T1_Power; /* Turbine 1 power */
static real T1_Omega; /* Angular velocity of turbine 1 cell zone */

static real T1_Max_Power; /* Power available to the turbine */

static real efficiency; /* Efficiency of turbine */

DEFINE_ON_DEMAND(Powershort)
{
Domain *domain = Get_Domain(1);

```

Appendix 3: User Defined Function (UDF); torque, power, axial thrust and blade forces

```
Thread *T1ct = Lookup_Thread(domain,T1_Domain);    /* Looks up the thread pointer
                                                    to zone T1_Domain */

Thread *T1ft;  /* Pointer to face thread data type on turbine 1 */

face_t f;      /* Face data type */

int i;

/* Declaration of variables */
/* Turbine static pressure force */

real T1_tp_force[ND_ND];    /* Stores T1_tp_force in a matrix i.e. x, y and z components */

/* Declaration of variables */
/* Turbines shear stress force */

real T1_ts_force[ND_ND];    /* Stores T1_ts_force in a matrix i.e. x, y and z components */

/* Declaration of variables */
/* Force on turbines (sum of static and shear) */

real T1_Force[ND_ND];    /* Stores T1_Force in a matrix i.e. x, y and z components */

real f_A[ND_ND];    /* Stores f_A (face area) in a matrix
                    i.e. x, y and z components */

real f_cen[ND_ND];    /* Stores f_cen (face centroid) in a matrix
                    i.e. x, y and z components */

T1_torque = 0.0;    /* Initializes/Resets the torque to zero */

NV_S(T1_Force,=,0); /* Initializes/Resets the force vector to zero */

T1_Omega = THREAD_VAR(T1ct).fluid.omega; /* Sets T1_Omega equal to the the angular
                                           velocity defined in the boundary condition
                                           for turbine 1 */

T1_centre_x = THREAD_VAR(T1ct).fluid.origin[0];
T1_centre_y = THREAD_VAR(T1ct).fluid.origin[1];
T1_centre_z = THREAD_VAR(T1ct).fluid.origin[2];

fluid_rho = MATERIAL_PROP(THREAD_MATERIAL(T1ct),PROP_rho);

/* Turbine */
```

Appendix 3: User Defined Function (UDF); torque, power, axial thrust and blade forces

```

for (i=0;i<T1_WALLS;i++)
{
    T1ft=Lookup_Thread(domain,T1wall_ids[i]);
        /* Lookup the face threads for the wall ids on turbine 1 */

    begin_f_loop(f,T1ft) /* Loop over all face threads of the wall ids */
    {
        F_AREA(f_A,f,T1ft);
        /* Macro for face area containing pointers
            to face area, face and face thread */

        F_CENTROID(f_cen,f,T1ft);
        /* Macro for face centroid containing pointers
            to face centroid, face and face thread */

        /* Store shear force on turbine 1*/
        N3V_V(T1_ts_force,=,F_STORAGE_R_N3V(f,T1ft,SV_WALL_SHEAR));

        /* Store static pressure force on turbine 1*/
        T1_tp_force[0] = f_A[0]*F_P(f,T1ft); /* defines the tp_force in x-component */
        T1_tp_force[1] = f_A[1]*F_P(f,T1ft); /* defines the tp_force in y-component */
        T1_tp_force[2] = f_A[2]*F_P(f,T1ft); /* defines the tp_force in z-component */
        /* F_P(f,ft) is the face static pressure */

        /* For turbine axis in the x-component */
        /* T1_torque += (T1_tp_force[1]-T1_ts_force[1])*(f_cen[2]-T1_centre_z)
            - (T1_tp_force[2]-T1_ts_force[2])*(f_cen[1]-T1_centre_y); */

        T1_Force[0] += T1_tp_force[0] - T1_ts_force[0];

        /* For turbine axis in the y-component */
        /* T1_torque += (T1_tp_force[2]-T1_ts_force[2])*(f_cen[0]-T1_centre_x)
            - (T1_tp_force[0]-T1_ts_force[0])*(f_cen[2]-T1_centre_z); */

        T1_Force[1] += T1_tp_force[1] - T1_ts_force[1];

        /* For turbine axis in the z-component */
        T1_torque += (T1_tp_force[0]-T1_ts_force[0])*(f_cen[1]-T1_centre_y)
            - (T1_tp_force[1]-T1_ts_force[1])*(f_cen[0]-T1_centre_x);
        /* N.B. Shear force subtracted due to sign convention
            i.e. subtract a negative equals a plus */

        T1_Force[2] += T1_tp_force[2]-T1_ts_force[2];
        /* Force acting on blades in direction of flow */

    }
    end_f_loop(f,T1ft);
}

```

Appendix 3: User Defined Function (UDF); torque, power, axial thrust and blade forces

```

/* calculate available power and turbine efficiency */

T1_Max_Power = 0.5*fluid_rho*( (T1_Diameter/2.0)*(T1_Diameter/2.0)
)*pi*(U_fs*U_fs*U_fs);

T1_Power = fabs(T1_torque)*fabs(T1_Omega);

efficiency = 100.0*T1_Power/T1_Max_Power;

/* output turbine performance characteristics */

Message("\n *****");
Message("\n * WARNING: Did you set the correct zone IDs in the UDF? *");
Message("\n *****\n");

Message("\n *****");
Message("\n * Turbine Report                *");
Message("\n *                                *");
Message("\n * Turbine Torque:  %12.4e Nm        *", T1_torque);
Message("\n * Turbine Omega:   %12.4e rad/s     *", T1_Omega);
Message("\n * Turbine Power:   %12.4e W         *", T1_Power);
Message("\n * Power Available: %12.4e W         *", T1_Max_Power);
Message("\n * Turbine Efficiency: %g Percent    *", efficiency);
Message("\n *                                *");
Message("\n * Turbine Blade forces            *");
Message("\n * Force in x-comp.: %12.4e N       *", T1_Force[0]);
Message("\n * Force in y-comp.: %12.4e N       *", T1_Force[1]);
Message("\n * Force in z-comp.: %12.4e N       *", T1_Force[2]);
Message("\n * Turbine Force Magnitude: %12.4e N *", NV_MAG(T1_Force));
Message("\n *                                *");
Message("\n * Angle of Resultant Force, OX: %12.4e degrees *", (180/pi)*( acos(
T1_Force[0]/NV_MAG(T1_Force) ) ) );
Message("\n * Angle of Resultant Force, OY: %12.4e degrees *", (180/pi)*( acos(
T1_Force[1]/NV_MAG(T1_Force) ) ) );
Message("\n * Angle of Resultant Force, OZ: %12.4e degrees *", (180/pi)*( acos(
T1_Force[2]/NV_MAG(T1_Force) ) ) );
Message("\n *                                *");
Message("\n *****\n");

/* 'Message' prints the requested data to the Fluent window
%12.4e: 12:  the field width i.e. space for 12 characters
.4       reserves 4 charracters after the decimal place
e        defines scientific notation; useful for copying
the data into other programs e.g. Microsoft Excel */
}

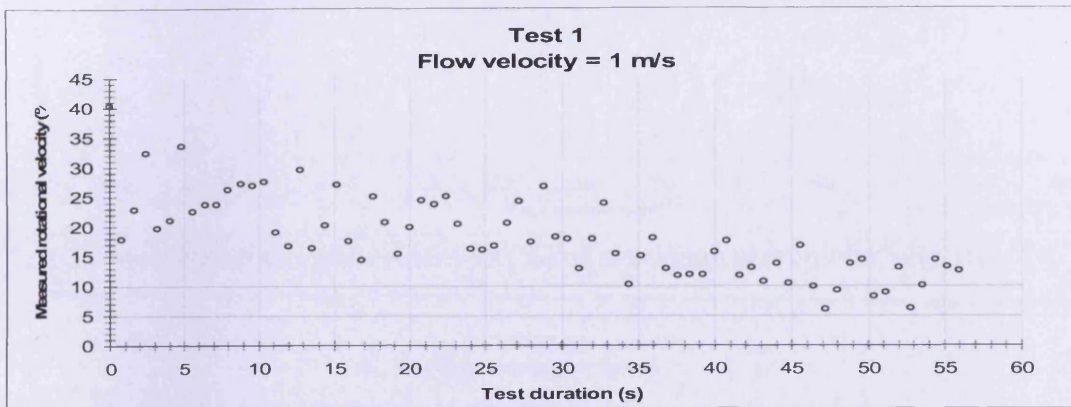
```


APPENDIX 4

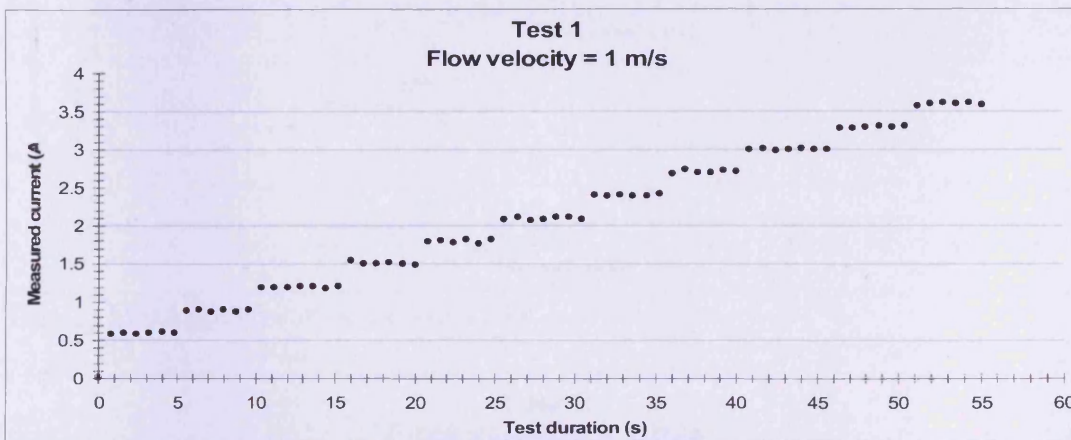
Measured data from flume tests at Liverpool University

(solid drive shaft).

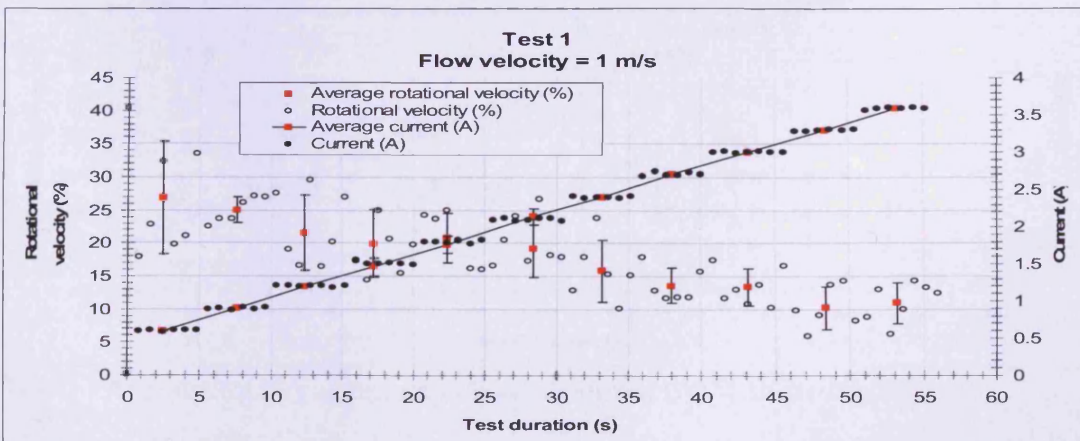
Test 1 data



Test 1 : Measured rotational velocity as (%) of maximum servomotor velocity.



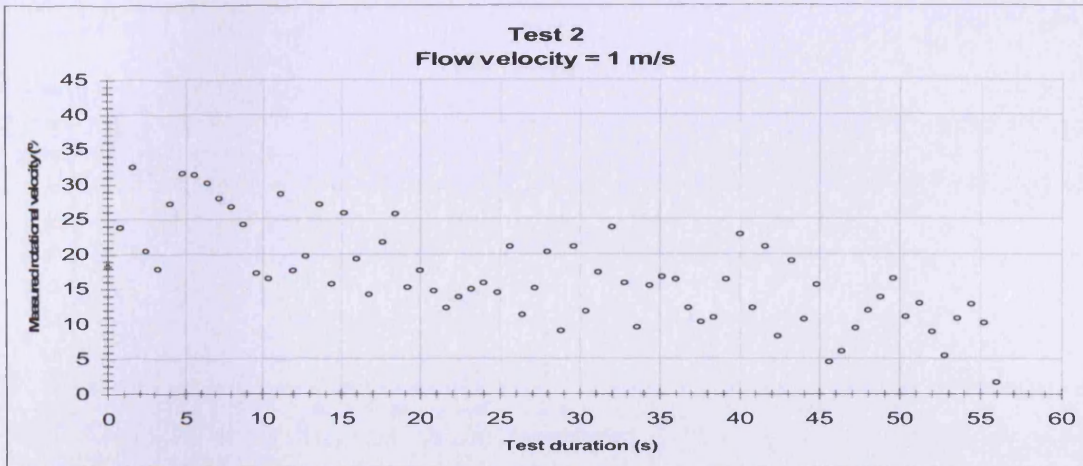
Test 1 : Measured servomotor current (A)



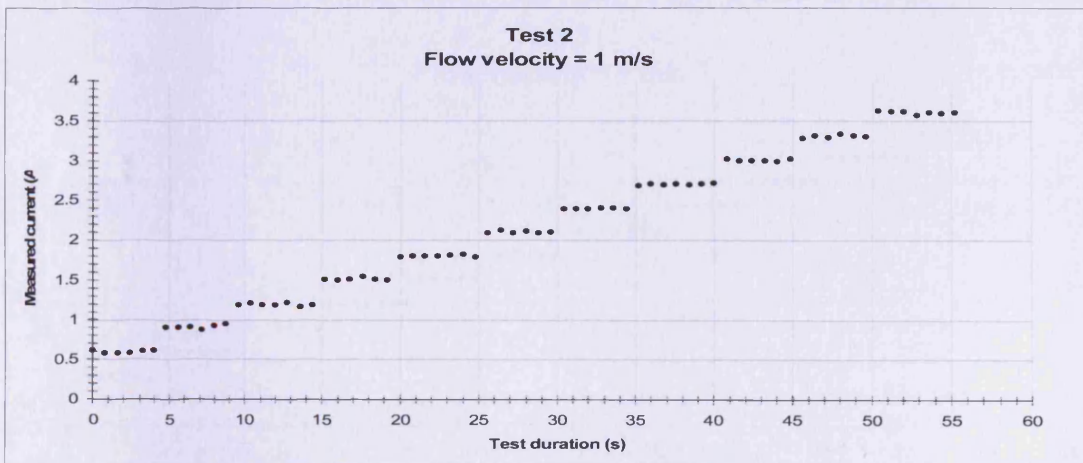
Test 1 : Average rotational velocity (%) and current (A) with error bars

APPENDIX 4: Flume data

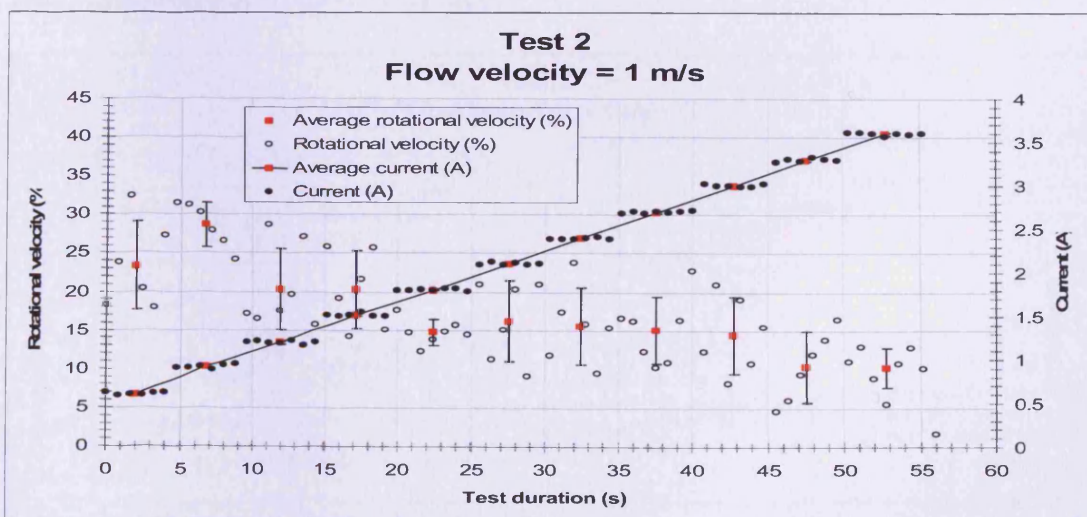
Test 2 data



Test 2 : Measured rotational velocity as (%) of maximum servomotor velocity.



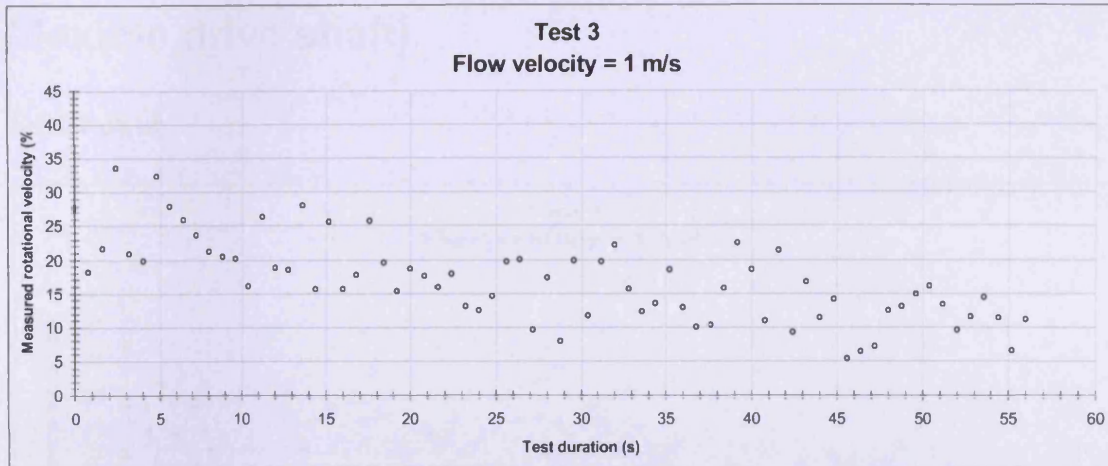
Test 2 : Measured servomotor current (A)



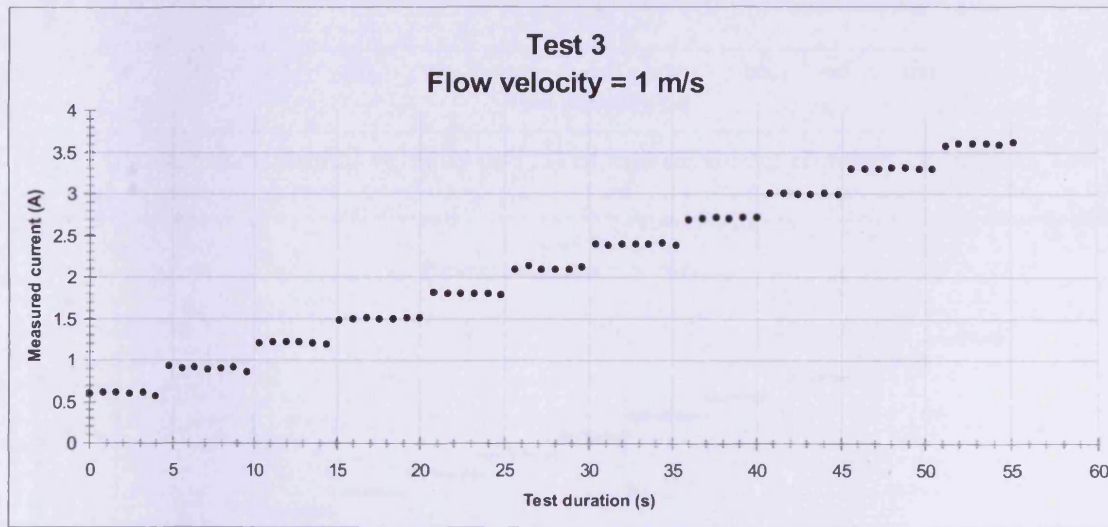
Test 2 : Average rotational velocity (%) and current (A) with error bars

APPENDIX 4: Flume data

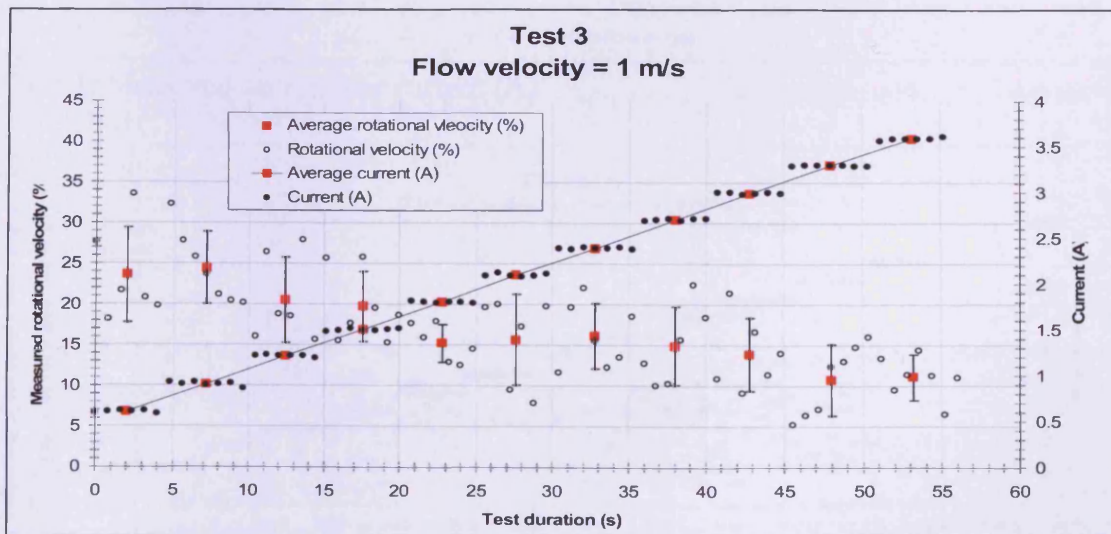
Test 3 data



Test 3: Measured rotational velocity as (%) of maximum servomotor velocity.



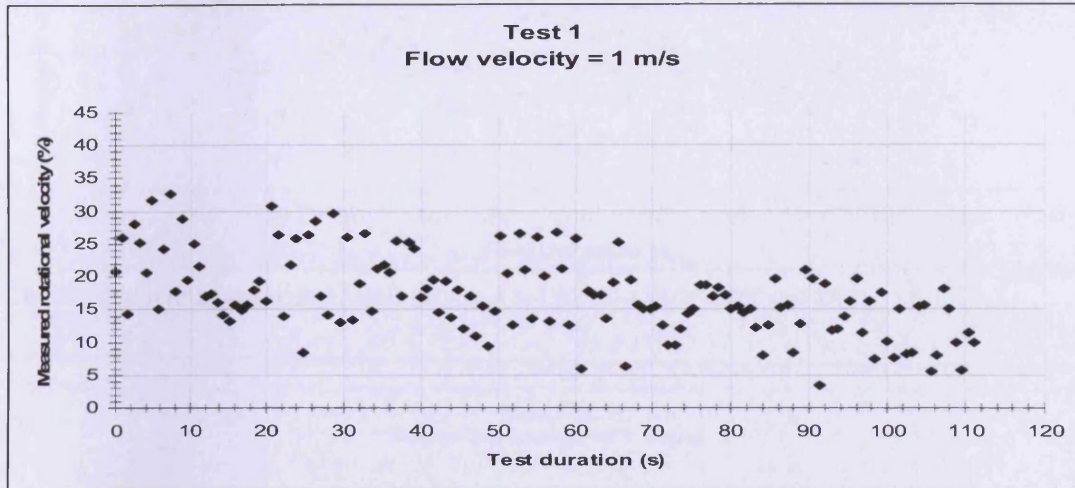
Test 3: Measured servomotor current (A)



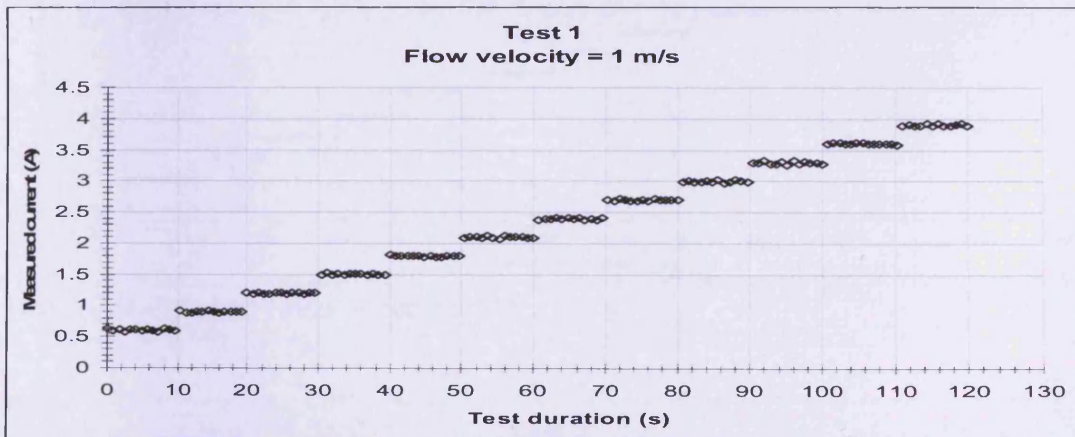
Test 3: Average rotational velocity (%) and current (A) with error bars

Measured data from flume tests at Liverpool University (flexible drive shaft).

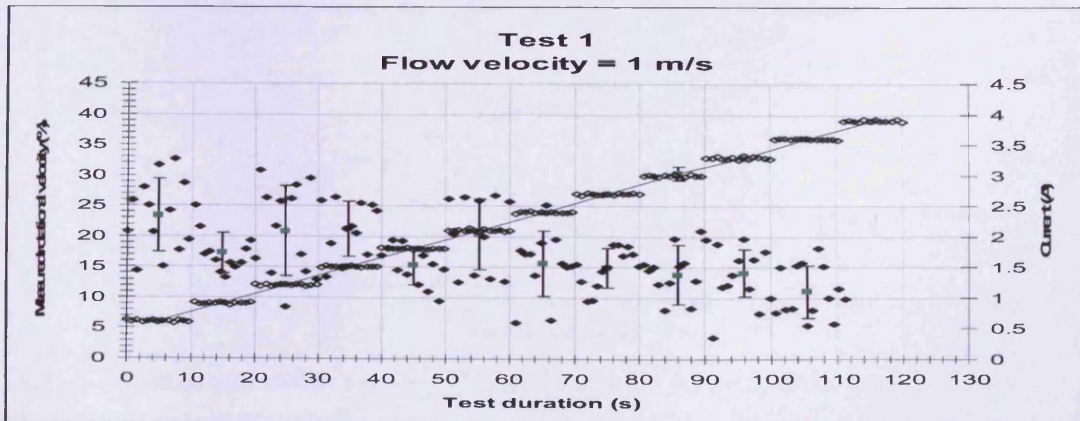
Test 1 data



Test 1: Measured rotational velocity as (%) of maximum servomotor velocity.



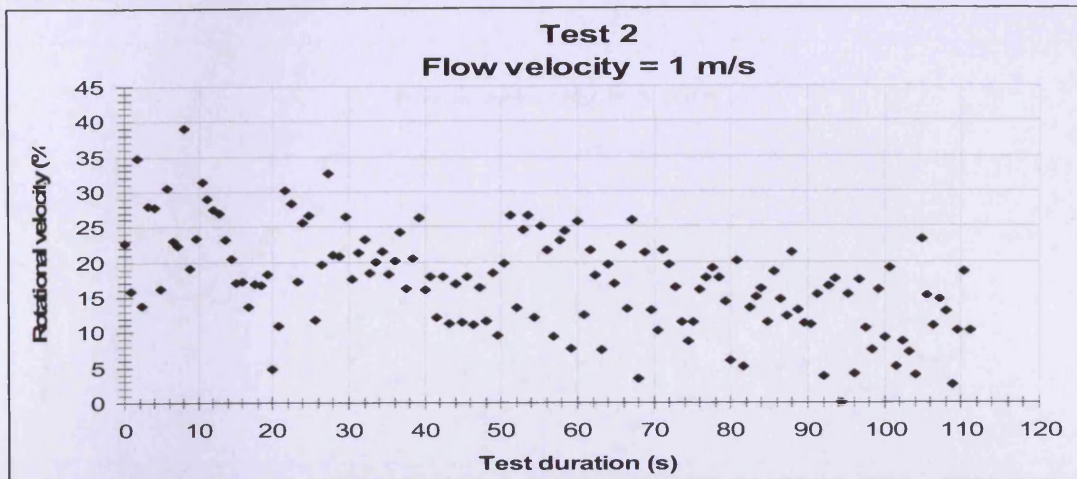
Test 1: Measured servomotor current (A)



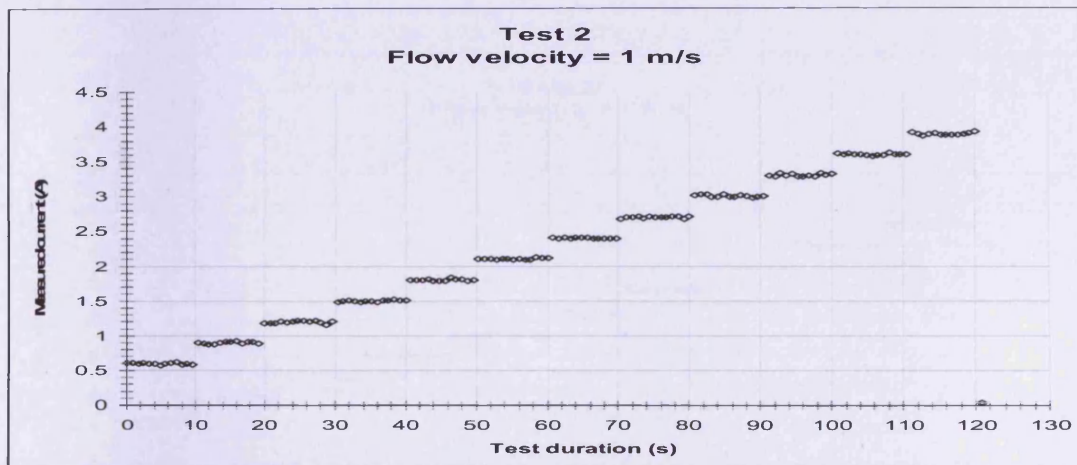
Test 1: Average rotational velocity (%) and current (A) with error bars

APPENDIX 4: Flume data

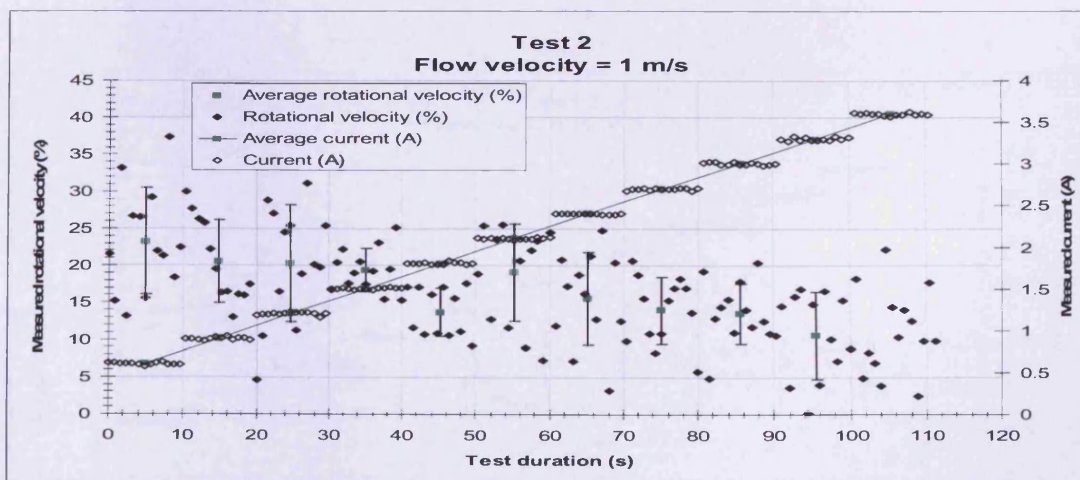
Test 2 data



Test 2: Measured rotational velocity as (%) of maximum servomotor velocity.



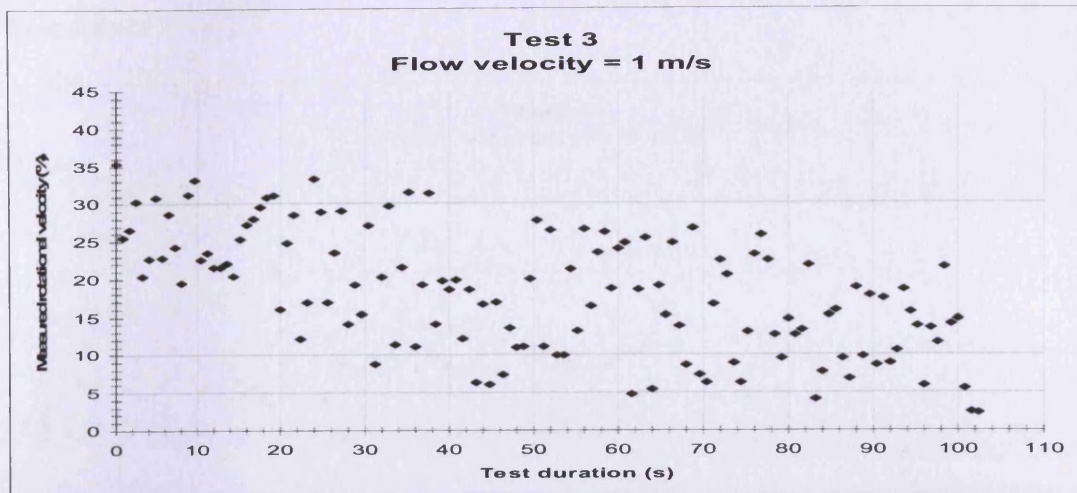
Test 2: Measured servomotor current (A)



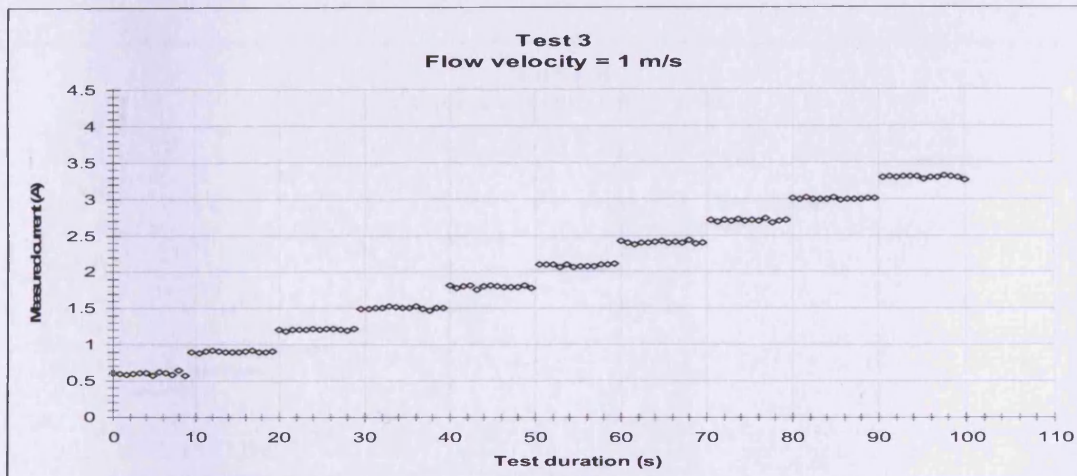
Test 2: Average rotational velocity (%) and current (A) with error bars

APPENDIX 4: Flume data

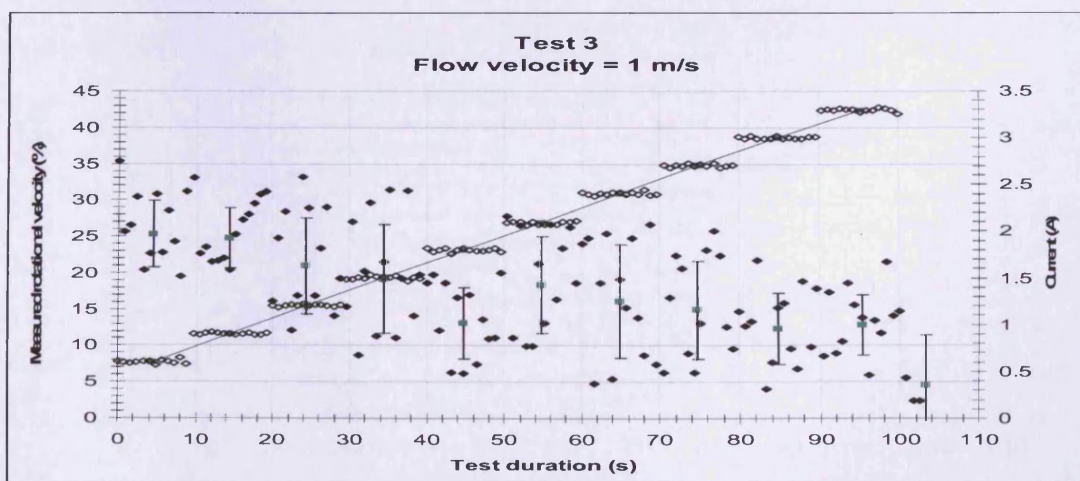
Test 3 data



Test 3: Measured rotational velocity as (%) of maximum servomotor velocity.



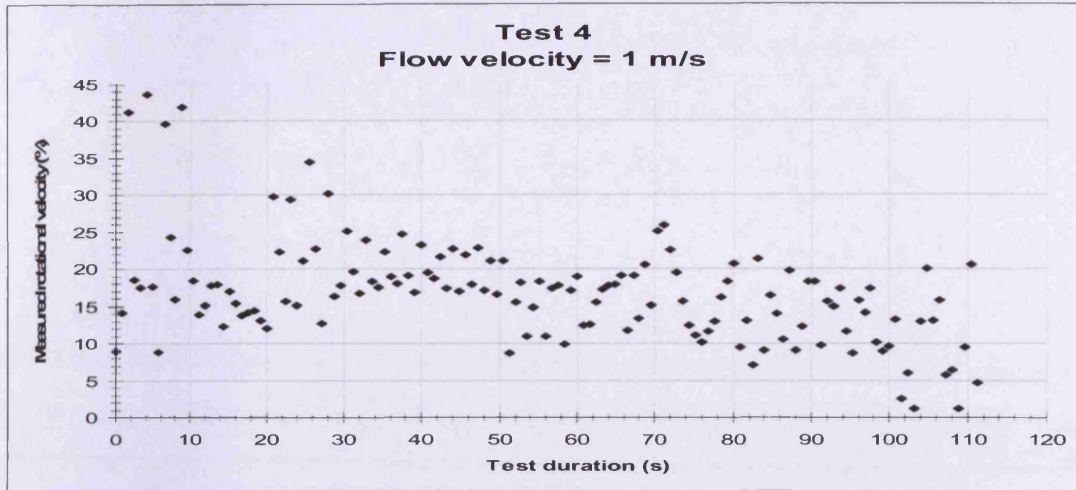
Test 3: Measured servomotor current (A)



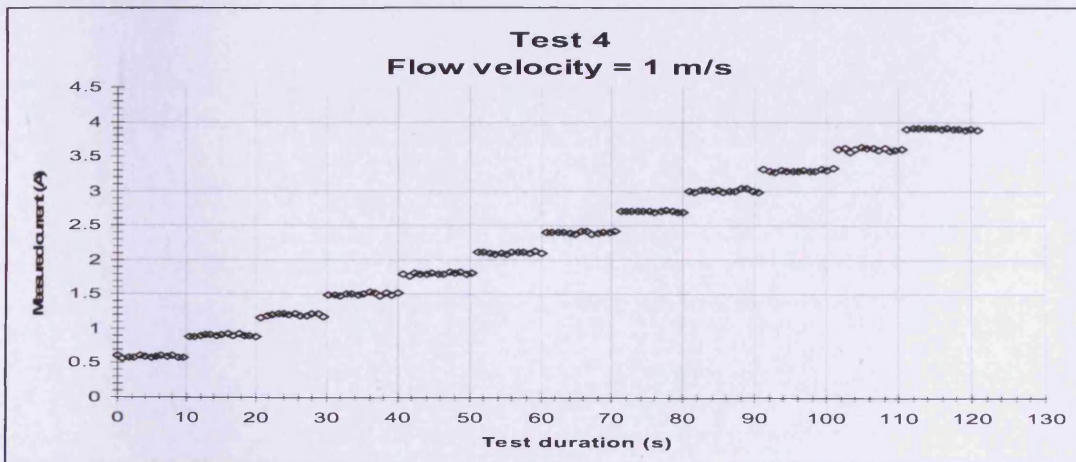
Test 3: Average rotational velocity (%) and current (A) with error bars

APPENDIX 4: Flume data

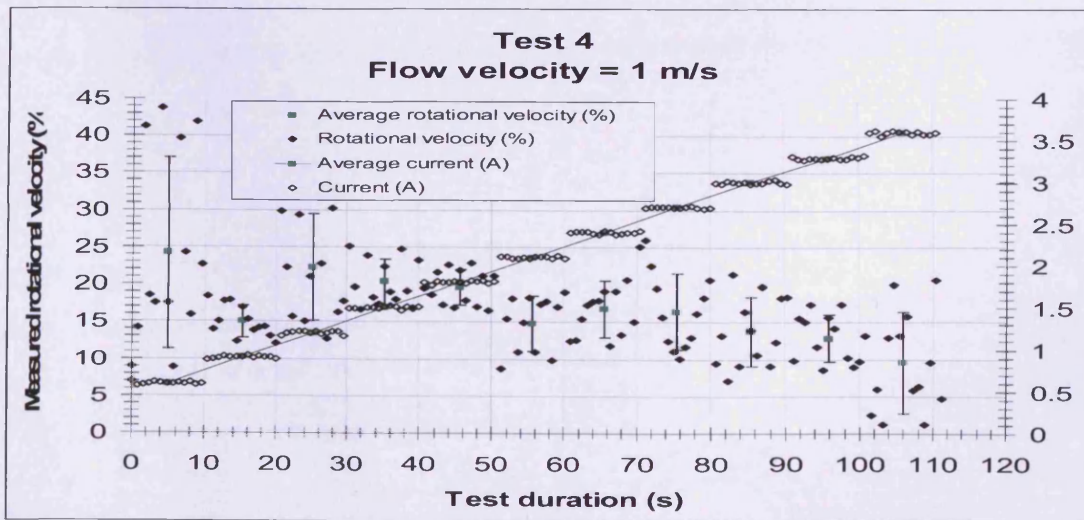
Test 4 data



Test 4: Measured rotational velocity as (%) of maximum servomotor velocity.



Test 4: Measured servomotor current (A)



Test 4: Average rotational velocity (%) and current (A) with error bars

APPENDIX 4: Flume data

